UNIVERSITY OF SOUTHAMPTON

FACULTY OF NATURAL AND ENVIRONMENTAL SCIENCES

Academic Unit – Chemistry

Supervisors – Dr. Simon Coles, Prof. Ian Sinclair, Dr. Ranko Vrcelj

Advisor – Prof. Andrew Hector

PhD

Mixing and Characterisation of Multi-Component Materials for Pyrotechnic Applications

By

Lisa Blair

Thesis for the degree of Doctor of Philosophy

July 2015

UNIVERSITY OF SOUTHAMPTON
ABSTRACT
FACULTY OF NATURAL AND ENVIRONMENTAL SCIENCES
ACADEMIC UNIT – CHEMISTRY
Doctor of Philosophy

MIXING AND CHARACTERISATION OF MULTI-COMPONENT MATERIALS FOR PYROTECHNIC APPLICATIONS

By Lisa Blair

This multidisciplinary research studied the relationship between components of a pyrotechnic product and how manufacturing, in particular the mixing method employed, affects its macroscopic structure and properties. For pyrotechnics to produce the desired effect the ingredients must be intimately mixed, however, the present physical mixing approach can lead to inconsistencies in performance between batches. X-ray computed tomography (CT) was used to investigate the distribution of components in a pyrotechnic mixture. Near-neighbour distances between particles were calculated and used to assess the homogeneity of the mixtures and the efficiency of combustion.

Another strand of this research to overcome batch inconsistencies was by chemically binding pyrotechnic ingredients rather than physically mixing them together. One method of achieving this was through incorporating two or more components within the same crystalline lattice. This may be achieved through co-crystallisation or coordination in functional frameworks, thereby reducing the number of components in a physical mixture and minimising the variation between batches.

Li *et al.* have investigated using metal-organic frameworks (MOFs) to stabilise energetic materials.[1] The research presented here uses MOFs to bring together fuels and oxidisers into one framework to create a so-called MOFirework. Numerous linkers and metal centres were investigated to build up a structural family to correlate structure with pyrotechnic function (*e.g.* changing burn colour; Sr = red, Ba = green). Both powder and single crystal X-ray diffraction were used to characterise the products. Differential scanning calorimetry was used to study the thermal profiles to investigate their possible uses as pyrotechnics. Lastly, a burn test was carried out to determine their pyrotechnic effect (*e.g.* gas, smoke, light, heat, colour, and sound) and quantitatively link this to structure.

---

[1] Li, S.; Wang, Y.; Qi, C.; Zhao, X.; Zhang, J.; Zhang, S.; Pang, S., *Angew. Chem. Int. Ed.* 2013, 52 (52), 14031-14035.

EXTENDED ABSTRACT

This multidisciplinary research is looking at the relationship between components of a pyrotechnic product and how manufacturing, in particular the mixing method employed, affects its macroscopic structure and properties. For pyrotechnics to produce the desired effect the ingredients must be intimately mixed, however, the present physical mixing approach can lead to inconsistencies in performance between batches. The aim of this research is to manufacture a pyrotechnic which is an improvement relative to its predecessors not only through refinement of the manufacturing process but also through control at the molecular level. This would be measured in terms of consistency of production, and pyrotechnic effect (which changes depending on the purpose of the composition; *e.g.* smoke composition, flare), amongst other parameters. This thesis aims to address questions relating to the mixing efficiency of pyrotechnic materials. It suggests a mechanism through which pyrotechnic mixtures can be characterised quantitatively. It also suggests another route to synthesise pyrotechnics in order to increase the intimate contact between the two main ingredients, the oxidiser and the fuel.

Firstly, **Chapter 1** details the background information associated with main areas of this research. The topics discussed include; pyrotechnics, granular materials, and the crystalline state (with a specific focus on crystal engineering tools such as co-crystals, and MOFs). Analytical techniques used in this work are also presented within this chapter. **Chapter 2** introduces the experimental methods used to manufacture pyrotechnic mixtures and synthesise co-crystals and MOFs. The analytical approaches used for characterisation and the assessment of the physical properties of these products are also provided.

Chapter 3 discusses the macroscopic characterisation of various combinations of group 1 metal nitrate oxidisers and α-lactose monohydrate using X-ray computed tomography (CT). Not only were the oxidisers varied between mixtures but so also was their particle size. In addition, the ratio of oxidiser to fuel was altered and investigated. The choice of oxidiser, its particle size, and the oxidiser/fuel ratio are all known to affect pyrotechnic performance. Another main contributor is mixture homogeneity. These factors are discussed and quantitatively linked to their impact on performance. Moving away from traditional manufacturing approaches, the next couple of chapters suggests a different means to make pyrotechnic products by using crystal engineering tools (co-crystals and MOFs) to ensure that both fuel and oxidiser ingredients are in intimate contact. Instead of physically mixing

pyrotechnic ingredients we propose chemically binding them. **Chapter 4** describes the crystal structures of several co-crystals, salts, and solvates which arose from combining three forms of fluorinated benzene dicarboxylic acid (oxidisers) with numerous nitrogen containing heterocycles (fuels) as well as their thermal properties. **Chapter 5** describes the characterisation of several MOFs which were the result of combining group 1 metal nitrates/group 2 metal nitrates with several diacids which are discussed in terms of their coordination and their dimensionality. Their pyrotechnic potential is highlighted throughout this chapter.

In conclusion, this thesis presents a means to quantitatively characterise pyrotechnic mixtures. Not only that, but it proposes a novel alternative approach to manufacture pyrotechnic materials through the use of co-crystals and MOFs.

Appendix 1 includes a case study of the CT analysis of pyrotechnic mixtures, tables detailing the outcome of co-crystal and MOF experiments as well as a list of their unit cell dimensions. PXRD patterns and DSC traces are also provided. A CD provided with this thesis includes derived raw data from CT collections, CIF files and PXRD raw files of the co-crystal and MOF products presented throughout this thesis.

CONTENTS LIST

CHAPTER 1 – Background Literature

CONTENTS

FIGURE LIST

TABLE LIST

EQUATION LIST

SCHEME LIST

APPENDIX LIST

DECLARATION OF AUTHORSHIP

I, Lisa Blair, declare that the thesis entitled:

Mixing and Characterisation of Multi-Component Materials for Pyrotechnic Applications

and the work presented in the thesis are both my own, and have been generated by me as the result of my own original research. I confirm that:

- this work was done wholly or mainly while in candidature for a research degree at this University;

- where any part of this thesis has previously been submitted for a degree or any other qualification at this University or any other institution, this has been clearly stated;

- where I have consulted the published work of others, this is always clearly attributed;

- where I have quoted from the work of others, the source is always given. With the exception of such quotations, this thesis is entirely my own work;

- I have acknowledged all main sources of help;

- where the thesis is based on work done by myself jointly with others, I have made clear exactly what was done by others and what I have contributed myself;

- parts of this work have been published as:

Blair, L. H.; Colakel, A.; Vrcelj, R. M.; Sinclair, I.; Coles, S. J., Chem. Commun. 2015, 51 (61), 12185-12188.

Signed: …………………………………………………………………..

Date:…………………………………………………………………….

ACKNOWLEDGEMENTS

CONTENTS

And where would I be without awesome characters like Louise 'Karen Genious' Karagiannidis, and Charlotte 'Lottie' Mardle by my side going through this PhD rollercoaster ride. You both are a true blessing.

ABBREVIATIONS

PXRD	Powder X-ray Diffraction
SXRD	Single Crystal X-ray Diffraction
DSC	Differential Scanning Calorimetry
CT	Computed Tomography
CoV	Coefficient of Variance
MOF	Metal-Organic Framework
CSD	Cambridge Structural Database
CIF	Crystallographic Information File

Pyr	2-Pyrrolidone	Im	Imidazole
MPyri	N-Methylpyrrolidine	2MI	2-Methylimidazole
Idn	2-Imidazolidone	4MI	4-Methylimidazole
DMIdn	1,3-Dimethyl-2-imidazolidone	1AI	1Acetylimidazole
Mo	Morpholine	NOI	4-Nitroimidazole
AMo	N-Acetylmorpholine	DMI	1,2-Dimethylimidazole
NPy	2-Aminopyridine	Tro	1,2,4-triazole
DNPy	2,6-Diaminopyridine	3NTro	3-Amino-1,2,4-triazole
3NONPy	3-Nitro-2-pyridinamine	5NOIn	5-Nitroindazole
5NONPy	5-Nitro-2-pyridinamine	MR	Methyl Red
DMNPym	4,6-Dimethyl-2-pyrimidinamine	S3	Sudan III
Az	Pyrazine	MO1	Mordant Orange 1
Tri	s-triazine		

OxA	Oxalic Acid	FmA	Fumaric Acid
MnA	Malonic Acid	BDC	Terephthalic Acid
ScA	Succinic Acid	isoBDC	Isophthalic Acid
GlA	Glutaric Acid	altBDC	Phthalic Acid
AdA	Adipic Acid	fBDC	Tetrafluoroterephthalic Acid
PmA	Pimelic Acid	isofBDC	Tetrafluoroisophthalic Acid
SbA	Suberic Acid	altfBDC	Tetrafluorophthalic Acid
LTA	L-Tartaric Acid	DMF	Dimethylformamide
MeA	Maleic Acid	TEA	Triethylamine

CONTENTS

CHAPTER 1

Background Literature

1.1 PYROTECHNICS

1.1.1 INTRODUCTION

"Pyrotechnics" originates from the two Greek words – πυρο (meaning fire) and τεχνι (meaning art).[1] Their discovery, originating in China around 8th century BC, was realised when the addition of saltpetre (potassium nitrate) to naturally occurring combustible materials resulted in an accelerated combustion reaction.[2] Since then the world has been captivated by fireworks. Today, their uses have extended beyond visual displays to various, complex technical applications such as airbags, fire extinguishers, flares, matches, and propellants. Their ongoing development and investigation continues to be carried out by many energetic material groups who are constantly discovering new applications and finding ways of improving pyrotechnic performance.

A pyrotechnic device is made up of two main constituents; an oxidiser and a reducing agent otherwise known as a fuel. Optional ingredients which can be included are binders, propellants, colouring agents, and sound or smoke producing agents.[3] Pyrotechnics are grouped alongside propellants and explosives and are termed as "Energetic Materials". In comparison to high explosives, which typically are single molecules containing both essential ingredients, pyrotechnics are mixtures of substances. As such pyrotechnic reactions are solid-state reactions. Essential factors to consider when designing a pyrotechnic device therefore include the identification of the optimum particle sizes of starting materials and also the homogeneity of the final compositions. Another difference to note between the kinds of energetic materials is the rate in which they release their energy. Explosives release their energy rapidly (TNT – 6950 m/s), whereas a pyrotechnic mixture releases it much more slowly (2.3×10^{-3} m/s). What most would not expect is that a pyrotechnic mixture can contain nearly twice the

energy per gram of material in comparison to an explosive. Pyrotechnic compositions have very useful properties; high energy density, long unattended storage life, resistance to radiation and EMP (electromagnetic pulse), low energy requirement. [2] Pyrotechnic mixtures are used to produce a "required effect" whether it be for the production of heat (*e.g.* match heads), light (*e.g.* signal flares), smoke (*e.g.* signalling and screening smoke), sound (*e.g.* stun grenades), gas (*e.g.* oxygen candles) or a mixture of all of these effects.

Traditional firework rockets or shells still utilise gunpowder (75% potassium nitrate, 15% charcoal, and 10% sulfur) as a basic ingredient although the composition tends to vary depending on the specific application (50-85% potassium nitrate, 0-30% charcoal, 0-50% sulfur). Military pyrotechnic applications include aerial countermeasures, camouflage and delusion devices, delay devices in blasting caps, flares, gas and smoke generators, igniters and initiators, incendiary devices, missile propellants, signal flares, and tracers. These types of products are made of components other than gunpowder to allow for improved performance. The development of these materials typically incurs higher costs and uses materials which are known to be slightly toxic. However, if their performance cannot be duplicated by a non-toxic, cheaper equivalent then they must continue using the existing product.

Figure 1.1.1 - Examples of Pyrotechnic Applications [4-7]

1.1.2   CONSTITUENTS OF PYROTECHNIC COMPOSITIONS

1.1.2.1   FUELS

The type of fuel (reducing agent) used is dependent on the intended pyrotechnic effect. Following in the footsteps of the discoverers, non-metals (charcoal, sulfur, and red phosphorus), metalloids (silicon and boron), and various other organic materials and natural products (flour and sugar), are all used as fuels. These materials are typically used for compositions which burn at lower temperatures. Metal powders are used to produce bright fireworks which burn at the higher end of the temperature scale, >3000K. The metals typically used include aluminium, copper, iron, magnesium (and the other alkaline earth metals), titanium, zinc, and zirconium. Due to its low cost, magnesium is one of the most common fuels used today. However, it possesses some unfavourable properties in terms of its associated hazards *e.g.* reactivity with water. Metal alloys, such as magnalium (Mg-Al 50:50), have been employed as a means to counteract the issues with using the single metal. Other alloys used are Zr alloys, and Ni-Fe alloys. Beryllium, chromium, nickel, and tungsten are also used as fuels but much less frequently.

1.1.2.2   OXIDISERS

1.1.2.2.1   CONVENTIONAL OXIDISERS

Traditional oxidisers include alkali and alkaline earth metal nitrates, perchlorates, and chlorates. Ammonium salts (nitrate and perchlorate) are also used. Organic compounds such as guanidinium nitrate can be used but are less frequently. Other oxidisers used include calcium and barium chromates, lead and potassium dichromates, and strontium and barium peroxides. Nitrates require higher temperatures to decompose and release their oxygen compared to perchlorates which decompose much more readily. Therefore nitrates are typically coupled with metal fuels.

Pyrotechnic formulations are thermodynamically meta-stable. Water and hygroscopic compounds are unacceptable in pyrotechnic compositions as water tends to inhibit pyrotechnic reactions but can in some cases lead to unintended hazardous reactions.[8]

The introduction of water to magnesium, as alluded to earlier, is undesirable due to its high reactivity.[9]

1.1.2.2.2 OXYGEN BALANCE

Oxygen balance (Ω) is a measure of the potential of an oxidiser in a mixture or an oxidising group in a compound. It represents the theoretical ability of a system to perform complete combustion, in other words residue-free consumption of the fuel. An oxygen balance of 0% indicates a stoichiometric mixture of fuel and oxidiser. A negative oxygen balance represents a system where atmospheric oxygen is required or where residual unburned fuel is still present. A positive oxygen balance indicates that there is an excess of oxygen in the system. A general oxygen balance, Ω, calculation for $C_aH_bN_cO_d$ with atomic mass M is given by:

$$\Omega = \frac{\left(d - 2a - \frac{b}{2}\right) \text{x } 16}{M} \quad \text{x } 100 \qquad \text{(Equation 1.1.1)}$$

The pyrotechnic reaction must be assessed in order to gain an understanding of the chemical reactions which are taking place. This information will be used to estimate the oxygen balance for that system. By varying the oxygen balance it is possible to alter the reaction rate and the heat of reaction.

1.1.2.2.3 ALTERNATIVE REDOX REACTIONS

Oxygen is not the only oxidising species used in pyrotechnic mixtures. Magnesium/Teflon/Viton mixtures, more commonly known as MTV, are used in many pyrotechnic applications including aerial countermeasures, signalling flares, and tracking flares.[10, 11] MTV is an example of an alternative redox pair based on metals and halogenated organic compounds or polymers. The redox reaction of its combustion is given in Equation 1.1.2.

$$(C_2F_4)n + 2nMg \rightarrow 2nC + 2nMgF_2 \qquad \text{(Equation 1.1.2)}$$
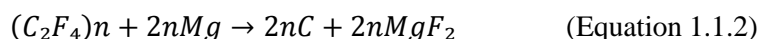
Compositions based on MTV use polychlorotrifluoroethylene (PCTFE), polycarbon monofluoride (PMF) in combination with magnesium or alternative fuels; boron, silicon

or silicon alloys, or titanium in place of the original polytetrafluoroethylene (PTFE). There are many other fluoroelastomers in addition to the ones mentioned which are being investigated to see how they influence pyrotechnic performance.[12]

1.1.2.3   COLOURING AGENTS

Colour can be introduced into a pyrotechnic through two mechanisms; 1) addition of a dye or 2) incorporation of metal or metal oxidisers which at high temperature emit light at a specific wavelength within the visible spectrum.
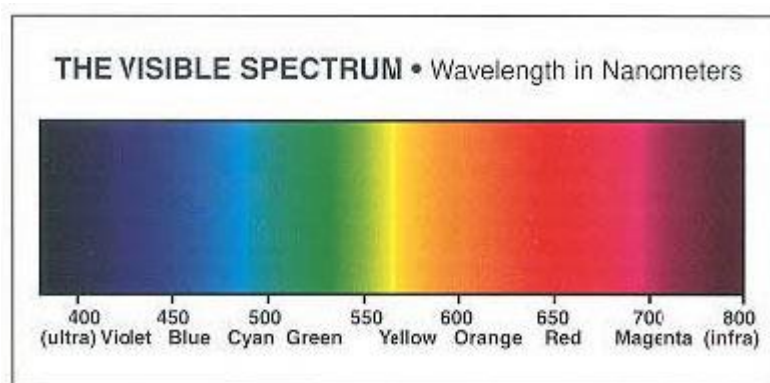
Figure 1.1.2 – Wavelengths of Visible Spectrum[13]

A dye would be used in cases where the pyrotechnic does not burn at a high temperature as most dyes tend to be organic compounds   *e.g.* Disperse red 9 (1-methylamino-anthraquinone) and Violet (1,4-diamino-2,3-dihydroanthraquinone) and will decompose at lower temperatures.[14] Dye materials used are typically low molecular weight (<400 g/mol) and tend not to include oxygen rich functional groups as they are likely to release their oxygen thus leading to oxidative decomposition.[15] Metal or metal compounds are used to impart colour at the other end of the scale. When coloured light is generated through the latter method, it is not monochromatic, because spectral components outside of the visual spectrum are also emitted. When excited by high temperatures (>3000 K), atoms and molecules produce numerous strong emission lines. Only a small number of elements emit lines which lie in the visible spectrum. Sodium produces yellow luminescence, strontium red, barium green, and copper green/blue.

Calcium and potassium, although less frequently used, produce red and violet luminescence, respectively.[15]

1.1.2.4   BINDERS

Binders are introduced into pyrotechnic composition to provide mechanical stability and to improve water resistance of the individual components by coating them. They help prevent the segregation of the components during processes such as manufacture, transport, and storage. They are there to ensure that the mixture remains homogeneous. They typically make up a large percentage of the final weight of a pyrotechnic. Improvements upon existing binders are required. Non-energetic binders can act as retardants and decrease reaction rates which is not always desirable. Both natural (*e.g.* acacia gum, acaroid resin, shellac, and corn starch), and synthetic (*e.g.* polyethylene, polyvinylchloride, and Viton®) binders are used.[16]

1.1.3   ISSUES FOR THE PYROTECHNIC INDUSTRY

1.1.3.1   ENVIRONMENTAL AND HEALTH CONCERNS

Some of the chemicals and heavy metals used in manufacturing pyrotechnic compositions are known pollutants.[17] Their use also deposits unfavourable decomposition materials which can be detrimental to the environment.[18] The low cost of these traditional pyrotechnic compositions makes it difficult for new "green" pyrotechnics to compete and consequently green pyrotechnics require financial backing to be developed further.[3]

1.1.3.1.1   HEAVY METALS

The main heavy metals used in the industry are barium, lead, and chromium. Barium compounds produce green luminescence *e.g.* barium nitrate (oxidiser and colouring agent). Ba(II) compounds, such as the pyrotechnic decomposition products BaCl and BaO, are water soluble and are very poisonous.[17] Lead compounds are used for various pyrotechnic applications *e.g.* burn rate catalysts, oxidisers, and initiators[19], however lead and lead containing compounds are poisonous. Micro-organisms may be wiped out

by high levels of lead concentrations. Accumulation of lead on plants prevents the plant from receiving the light it requires for photosynthesis.[19] Chromium is a toxic and carcinogenic material and its toxicity varies depending on its oxidation state. Its main form in pyrotechnics is as a chromate anion. It is typically coupled with metals such as barium and lead and is used as an oxidiser.[20, 21]

1.1.3.1.2 PERCHLORATES AND POLYCHLORINATED ORGANIC COMPOUNDS

Both potassium perchlorate and ammonium perchlorate are heavily used as oxidisers in the industry typically in applications such as military aerial decoy flares.[2] Perchlorate ions have been shown to be teratogenic and can cause hypothyroidism. They have contributed to a significant amount of groundwater contamination as a result of their intense use.[22] The combustion of organic matter (*e.g.* charcoal) in the presence of chlorine (*e.g.* chlorates, and perchlorates) can lead to the formation of toxic chlorinated organic compounds, such as polychlorinated dibennzo-p-dioxin (PCDD) and dibenzofurans (PCDF). These materials are toxic and environmental contaminants which are detectable in almost all compartments of the global ecosystems.[3]

1.1.3.1.3 SMOKE, PARTICULATES, AND GASEOUS POLLUTANTS

The generation of smoke is mainly attributed to the fuel within the pyrotechnic composition. Smoke, except in applications where this is the intended output, can pose problems in several ways. If too much smoke is present during a fireworks display the smoke can obscure the display but it can also affect the audience by acting as an irritant. Smoke may also contain small particulates which can themselves cause adverse health effects. A number of missile propellants used by the military are known to release a great deal of smoke which makes them detectable by satellites.[2] The main gaseous pollutants that arise from the decomposition of pyrotechnics are CO, NO_x and SO_x. These pollutants have contributed to the increase in number of adults with respiratory diseases such as asthma.[23]

1.1.3.1.4 POTENTIAL SOLUTION – 'GREEN PYROTECHNICS'

There is huge motivation to remove the use of heavy metals, perchlorates, and polychlorinated organic compounds from pyrotechnic compositions.[24-26] Simple changes have been suggested: replacing barium compounds with copper compounds. A particular drive in the development of green pyrotechnics has been to utilise nitrogen-rich materials. In comparison to traditional pyrotechnic compositions which gain their energy from the oxidation of the fuel, nitrogen rich materials gain their energy from their high heats of formation. Numerous nitrogen-rich materials (*e.g.* tetrazoles, aminotetrazoles, and tetrazines) are being investigated at present to assess their effect on pyrotechnic performance.[3, 25] These materials have several advantages; only or mostly gaseous products, high heats of formation, high propulsive power, high specific impulse and high flame temperatures.[3]

1.1.3.2   CONSISTENCY IN PYROTECHNIC PERFORMANCE

Pyrotechnic materials exist as mixtures of several ingredients and as such their performance is governed by solid state interactions. Factors which greatly influence the behaviour of the pyrotechnic include the particle sizes of each of the ingredients and the homogeneity of the resultant compositions when ingredients are mixed together.[16] By having numerous ingredients, the complexity of the composition is increased and multiple components introduce greater variation in the pyrotechnics' performance.[27]

1.1.3.2.1 INFLUENCE OF PARTICLE SIZE AND CRYSTAL DEFECTS

The particle sizes of the main ingredients of a composition, especially the oxidiser, greatly influence the performance of a pyrotechnic. It particularly affects its conversion rates, the pressure rise and the maximum pressure obtained within closed volumes.[28] Extensive research has been carried out to assess the influence of particle sizes within a range of 1-100 μm.[29] Smaller oxidiser particles breakdown more rapidly to release an oxidising atmosphere and smaller metallic fuel particles are consumed faster.[30, 31] Optimum particle sizes will vary and are dependent on the specific ingredients.[9, 32] Increasing the particle size for a pressed non-metallic mixture increases the burning

rate. This phenomenon occurs because of the void space formation which increases with increased particles sizes. The hot gases (flame front) travelling through the pyrotechnic mixtures will find more voids which in turn results in a reduced burn time.[1] Numerous pyrotechnic ingredients exist in crystalline form which is beneficial for those attempting to relate a structure with its physical properties. However, crystals rarely form perfectly and typically include crystal defects. These are highly undesirable in the energetic materials field, mainly when these defects are at least 5 μm in size, as they can cause 'hot spots' within the system which can increase their sensitivity making them more easily ignitable.

1.1.3.2.2   IMPACT OF MIXING METHOD

The 'required effect' of a pyrotechnic is influenced by how well the pyrotechnic ingredients are mixed. When handling powders, segregation becomes a key issue as it can result in changes in the ingredients ratio which consequently alters the bulk density of pressed compositions. This can happen when sieving together the ingredients to make a pyrotechnic composition or when transferring a composition to a pressing mould to be pressed. Segregation not only changes the mass of the material but also changes its pressing behaviour. This can detrimentally affect the pyrotechnics' burning rate and also increase its ease of ignition (sensitivity), both whilst the composition is being pressed and afterwards if it does not ignite whilst in the press.[2]

1.1.3.2.3   POTENTIAL SOLUTIONS - IMPROVING MIXING CONSISTENCY

To maintain a consistent particle size within a composition ingredients are sieved to a specific particle size and then additionally sieved using a smaller mesh sized sieve to collect 'fines' which would otherwise have increased the burning rate. Binders are used to minimise powder segregation. These are mixed with the oxidisers and fuels and activated in a variety of ways (*e.g.* heating, cooling, and UV etc.). More recently, the use of nanometer-size metal particle fuels has been investigated for pyrotechnic applications specifically for infrared countermeasures. The fine metal powders are introduced into the pores of nanostructured metal oxides *e.g.* iron oxides produced during sol-gel processes.[16] This approach improves the homogeneity of the fuel and

oxidiser ingredients. It also has resulted in improved performance and lowered sensitivities of the pyrotechnic materials.

One of the main aims of this work is to address inconsistencies in pyrotechnic performance attributed to the mixing quality of pyrotechnic compositions.

1.2   GRANULAR MATERIALS

1.2.1   INTRODUCTION

In process engineering terms, mixing is a unit operation. It involves the manipulation of a heterogeneous physical system to create a system which is more homogeneous. An everyday example is to consider the simple task of baking a cake. Ingredients are added to a bowl and then *stirred* to create a smooth mixture. Mixing tends to be more complicated for manufacturing companies as most processes are done on a much larger scale.

Mixing can be a challenge for many industries especially the pyrotechnic industry and the pharmaceutical industry. Companies strive for a mixing method that will produce a homogeneous mix, which will have more predictable properties. Understanding the raw materials is very important as not all powders act in the same way. Each powder may have different properties.[33] They must be assessed in order to get an idea of how they should behave whilst being mixed. The characteristics typically examined are as follows:

- Particle Size Distribution
- Particle Morphology
- Surface Roughness
- Cohesiveness
- Density
- Stability
- Static Charge
- Moisture Content
- Friability

There are a number of other factors to consider: sequence of addition of ingredients, type of mixer used and mixing time and efficiency.[29] The sequence in which ingredients are added to a mix is very important both in terms of safety and achieving homogeneity of the mix. For instance the addition of fine particles before coarse particles or vice

versa will determine the flow behaviour of the mixture and affect its mechanical properties (*e.g*. shear strength and hardness).[34] An appropriate mixer will be selected if the relationship of energy vs. mixing, the segregation phenomenon and impact mixing vs. shear mixing are all understood.[35] In terms of business it is also important to take into account the processing requirements, such as the time required to mix, the power requirements and cost of maintenance.[36]

1.2.2   MIXING METHODS

There are two categories into which mixers can be split: batch mixers or continuous mixers. The pyrotechnic industry typically uses batch mixers over continuous mixers due to the sensitive nature of the materials they handle. The pharmaceutical industry and the pyrotechnic industry are not all that different. They both use similar materials *e.g*. lactose. It is only its purpose which changes. The pharmaceutical industry uses it as a binder and an excipient [37] where the pyrotechnic industry uses it as a fuel. It should come as no surprise that they can utilise similar mixing methods.

Materials can be either dry or wet mixed.[38] Dry mixing involves 'Turbula' mixers which are typically used when the materials are very energetic and are likely to ignite violently. The process involves tumbling together dry powders.[39] Sieve mixing is another way that dry powders can be mixed. Each component of a mixture is sieved separately and then together to create a mixture.[40] Wet mixing uses a range of horizontal and vertical mixers including anchor blade, change-can, helical-blade, and double-arm kneading mixers. End runner and edge runner mixers are other types of mixers, which act more like a pestle and mortar. Water is added and acts as both a mixing aid and as a desensitiser.[2] Banbury mixers and roll mills are more intensive forms of batch mixers.[29] More intense mixing can lead to improved properties including higher mechanical strength and increased burning rate.

Cohesive and electrostatic powders are problematic; they have a tendency to agglomerate, thereby the agglomerates are mixing rather than the particles. Milling is

used under these circumstances. The operation is used to overcome the forces of cohesion between powder particles.[37]

The mixing time and efficiency is critical. The mechanical properties will vary depending on the efficiency of the whole mixing process. The mixing time is an important factor. If the mixing time is too long the individual particles can break down, whereas if it is too short the mix will not be sufficiently homogeneous.[34, 41]

1.2.3   OTHER FACTORS

Other mixer selection criteria which should be considered are the cycle time/capacity, the mixing accuracy, cleanability, filling & discharging rates, maximum temperature allowed, residue between two batches, safety requirements (mitigation measures for explosives, emission rate, pressure design) and the heating/cooling accuracy.[35]

As with any laboratory based experiment the pressure and temperature values play an integral part in the success of the experiment. These values should be at their optimum for the mixing process to be consistently successful. Slight fluctuations do occur in the burn rates of pyrotechnic mixtures, typically due to changes in humidity which arise from changes in temperature of the environment.

1.3   THE CRYSTALLINE STATE

1.3.1   INTRODUCTION

Molecular crystals are supramolecules. They are made up of molecules which are held together in a periodic arrangement by various interactions including short-range and directional interactions (*e.g.* hydrogen bonds), and lower range and formally non-directional interactions (*e.g.* van der Waals). These interactions are responsible for molecular recognition and complexation. The properties of these solid state materials are due to the intricate interplay between the different types of interactions present in a material. Supramolecular chemistry is referred to as the 'chemistry beyond the molecule'. This concept was coined by Lehn and involves the chemistry of molecular assemblies held together by intermolecular forces.[42, 43] This research is concerned with understanding the properties of pyrotechnic materials and how they can be altered and so it is necessary that these interactions be discussed.

1.3.2   INTERMOLECULAR INTERACTIONS

Intermolecular interactions are the fundamental bases for crystallisation and dissolution of organic molecules. They are responsible for the presence or absence of characteristic geometrical patterns in crystals which relate to the symmetry elements associated with a crystal. The shape and conformation of a molecule (*e.g.* DNA helix) is defined by these interactions. Intermolecular interactions include electrostatic interactions (ion-ion, ion-dipole, dipole-dipole, and quadrupole-quadrupole), hydrogen bonding, van der Waals, and aromatic interactions (π-π).[44] They all influence the potential energy of a crystal. The distance dependence and directionality of these interactions are the two most meaningful measures for classifying the strength of an interaction. Intermolecular interactions may be attractive or repulsive and the energy associated with them changes with r^{-n} (r = distance between selected non-bonded atoms, n = positive integer). In order to predict the properties of crystals and understand the crystal design process it is imperative that these interactions be taken into account.[45]

1.3.2.1   VAN DER WAALS INTERACTIONS AND CLOSE PACKING

Van der Waals forces are composed of dispersive and repulsive forces. Dispersive forces are one of the most important long-range forces as they contribute significantly to the stabilisation of non-polar molecules. They are attractive in nature and arise as a result of the interaction of the fluctuating multipoles of adjacent molecules. Repulsive forces balance the dispersive forces at short range and control the equilibrium distances between molecules. Kitaigorodskii's[46, 47] close packing principle is a natural consequence of the atom-atom potential method.[47, 48] The close packing principle considers that the volume of a molecule within a crystal can be considered as a system of intersecting spheres which represent individual atoms. The size of sphere is equivalent to the van der Waals radii of the atom. The molecules will tend to pack effectively and fill the space as tightly as possible. Kitaigorodskii's principle makes the assumption that as molecules tend towards equilibrium positions that the systems potential energy is minimised. This translates to the maximum number of intermolecular contacts being achieved.[44]

1.3.2.2   HYDROGEN BONDING

The hydrogen bonding concept dates back to the early nineteenth century but was not defined until much later. Pauling provides a unique definition for hydrogen bonds, 'under certain conditions an atom of hydrogen is attracted by rather strong forces to two atoms, instead of only one, so that it may be considered to be acting as a bond between them'.[49] Pimental and McClellan developed the following definition: 'a hydrogen bond is said to exist when 1) there is evidence of bond formation (association or chelation) and 2) there is evidence that this sterically involves a hydrogen atom already bonded to another atom.[50] The term 'hydrogen bridging' is sometimes used in place of hydrogen bonding.[51]

Hydrogen bonding occurs between a proton-donor group (D-H) and a proton-acceptor group (A). Donor atoms include O, N, S, X (F, Cl, Br, I) or C, whilst the acceptor group is either a lone pair of an electronegative atom or a π bond from an unsaturated system. Examples include N-H···O and O-H···O hydrogen bonds where the donors and acceptors

are activated. More recent examples of hydrogen bonding which have been found includes C-H···O and C-H···π.[52-56]

The most frequently encountered non-van der Waals interaction in molecular crystals is hydrogen bonding. It is the most reliable anisotropic interaction in supramolecular chemistry.[57] It is composed of electrostatic forces, covalency, dispersion-repulsion forces, and polarisation forces. The most predominant force is the electrostatic forces. Both strong, (20–40 kJ mol^{-1}) and weak (2–20 kJ mol^{-1}) hydrogen bonds are known to exist. Strong hydrogen bonds occur when electron density is pulled from the hydrogen atom by a highly electronegative hydrogen bond donor inducing a positive charge (*e.g.* N-H···O). This causes a shortening in the bond length between the donor and acceptor atoms in relation to the predicted van der Waals radii. The weak hydrogen bonds (*e.g.* C-H···O and C-H···π) are made up of dispersive and repulsive forces but the electrostatic values associated are much lower in comparison to the stronger hydrogen bonds.[58]

Hydrogen bonding plays a vital role in the stabilisation of biomolecules and a key role in crystal design.[59, 60] It has been used to design structures of clathrates, molecular complexes of cyclodextrins, quinones, and phenols.[44] It can be used to assess the likelihood of co-crystal formation which is one of the main focus areas in this study.

1.3.2.3   OTHER INTERACTIONS

Halogens (Cl, Br, and I) may form short contacts to heteroatoms such as N, O, and S. They also form hydrogen-bond like interactions with N-H, O-H, and C-H groups.[61] There were questions as to the strength of interaction. It was initially considered as a weak interaction. The perception changed when a number of structures, containing halogens, were analysed. The halogens arranged themselves in a characteristic way. There are noticeable differences between symmetrical (Cl-Cl) and unsymmetrical (Cl-Br) interactions which show that atomic polarisation is a factor.

π-π interactions arise amongst aromatic sections of molecules. The polarisable π-electron density contributes to the stabilisation of the dispersion interactions between the aromatic molecules. The interaction is anisotropic as a consequence of the

electrostatic component which provides directionality. In aromatic hydrocarbons, a multipole is introduced by the small polarisation of the C-H bond. The hydrogen atoms are slightly positive in relation to the π-bonded core which is partially negative.[44]

1.3.3   CRYSTALLISATION

An article entitled '*Black crystal arts – The secret tricks needed to coax out crystals hark back to our alchemical past*' from the *Chemistry World* magazine sums up this process perfectly.[62] All chemists consider this a basic skill but how many have been able to comprehend or appreciate the full value of this technique. It is commonly used to improve the purity of compounds, create new materials, and as a preparation for characterisation. There are various types of crystallisation techniques including cooling, evaporative, anti-solvent, reactive, and melt, but there are only two stages involved – nucleation and growth. The conditions (solvent, temperature, pressure etc.) of the crystallisation system dictate which propagating pattern of crystal growth will be followed, which will inevitably result in the creation of the final crystal form.

1.3.3.1   CRYSTALLISATION TECHNIQUES

Crystallisation from solution is one of the most popular methods used in both research and industry however there are other possibilities including crystallisation from a melt, from a vapour and from a gel. The standard methods are cooling and evaporative crystallisations but when these fail more complex methods should be trialled. It is important to note there is no fail-safe recipe for success. The techniques used are as follows:

- Cooling crystallisations
- Evaporative crystallisations
- Mixed solvents
- From melt

- Solvent diffusion (Layered Solvents)
- Vapour diffusion
- Gel diffusion
- Sublimation

- Seeding

1.3.4 *CRYSTAL ENGINEERING*

Crystal engineering is a research area which is of substantial value to a wide range of disciplines including chemistry, physics, biology, engineering to name but a few. '*The field has evolved from designing structures to designing properties*'.[63] There are two main crystal engineering tools which have been utilised throughout this work; co-crystals/binary compounds and metal-organic frameworks. These will be discussed in more detail in the following sections.

1.3.4.1 CO-CRYSTALS

1.3.4.1.1 *INTRODUCTION*

Co-crystals are very valuable as they can show improved properties over a mixture of single parent compounds.[64] A co-crystal is a single crystal in which the unit cell is made up of two or more components. Co-crystallisation is still in its infancy. The pharmaceutical industry have been the main contributors to this area of research as it can show improved properties of active pharmaceutical ingredients (API) in terms of solubility and hence bioavailability.[53, 65, 66] The energetic materials groups have also began investigating this topic to improve properties such as the performance, sensitivity, and stability of their products.

1.3.4.1.2 *CO-CRYSTAL DESIGN*

The main forms of bonding that are attributed to the making of a co-crystal are $\pi \cdots \pi$ stacking interactions, hydrogen bonding, and van der Waals forces. The design of a co-crystal begins by looking at the intermolecular interactions which control the formation and breakage of non-covalent bonds. This means looking at the forms of bonding previously mentioned, as well as electrostatic interactions and halogen bonding.[61] '*Supramolecular synthon*' is a term commonly used in this field of research.[67] These synthons are building blocks which can be assembled by known, plausible synthetic operations which involve intermolecular interactions. The initial step in designing an API co-crystal is to begin by selecting and gathering research of an API whose

performance requires improvement. A *co-crystal former*, or *co-former,* will then be selected. This has been the main difficulty- however there now exists a library of co-crystal formers which have been developed, based on information provided by the Cambridge Structural Database (CSD).[68, 69] The library includes a multitude of functional groups which have been classified based on the way in which they contribute to a crystal packing arrangement. The theory of how the components should combine must be thought out. After the theory is understood co-crystal screening can take place. Any co-crystals which form can be characterized and then their performances assessed.[70]

Co-crystal screening is carried out as compounds which come from the same homologous series do not always exhibit the same reactivity towards co-crystal formation. A study, by Fábián, was carried out to look at factors outside synthon matching to draw conclusions about which factors contribute to the success or failure of co-crystallisation experiments. His results showed that molecular polarity and the shape and size of the molecules had a direct effect on the success of the experiment. He also saw that there was a correlation between the negative molecular surface and number of hydrogen bond donors of a molecule. He also showed that the formation of synthons was directed by the strength of hydrogen bonds between the co-crystal formers rather than the number of hydrogen bond donors/acceptors each had.[71] Put simply, materials should co-crystallise if they have a suitable geometry (shape complimentarity) and/or have a high likelihood of hydrogen bonding between the fuel and oxidiser (molecular complimentarity).
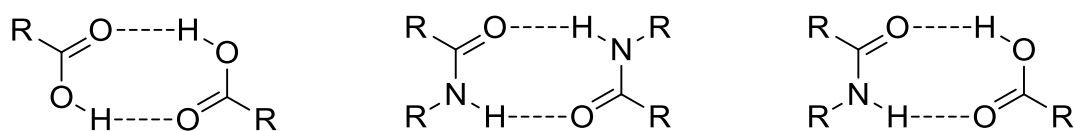
Figure 1.3.1– Typical H-bonding constructs

Pharmaceutical companies have limitations in terms of the materials they can use to create a co-crystal. The co-former must be generally recognised as safe (GRAS)[72] and must be more soluble than the API in order to attempt to improve the solubility and

therefore the bioavailability of the drug. The energetic materials industry have similar restrictions as they must abide by REACH regulations (Registration, Evaluation, Authorisation & restriction of Chemicals) as they inform what materials they can use within the synthesis and manufacture of energetic materials and products.[73] The following partial structure is a real example of an energetic-energetic co-crystal, composed of CL-20 and TNT.[74]
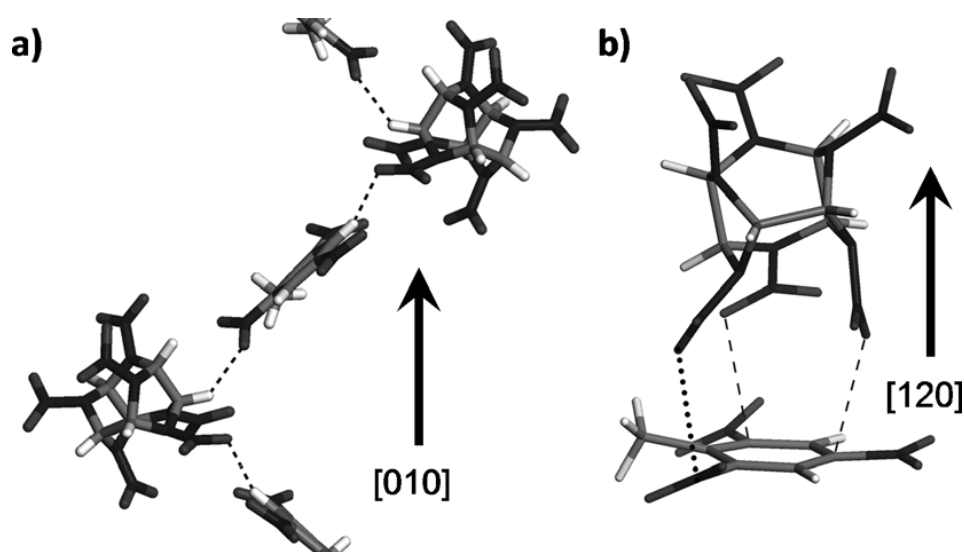
Figure 1.3.2 - Interactions between CL-20 and TNT[74]

1.3.4.1.3 CO-CRYSTALLISATION METHODS

There has been an array of methods reported which can be used to produce co-crystals. These include a number of solution based methods including evaporation of a heteromeric solution, reaction crystallisation and cooling crystallisation. In order to create a co-crystal the energetics must be more favourable than for the parent molecules to form together, to create a heteromeric solid, rather than to form separately. The components used to make a co-crystal must have similar solubilities in the solvent selected, otherwise the materials are likely to form separate species.[69] Solution methods are of great value; most of the known crystals which qualify for analysis by single crystal diffraction are prepared in this way.[66] Grinding methods are suitable alternative methods and have had well reported success. These include neat grinding and solvent drop grinding.[75] There are other methods which use supercritical fluids, hot stage

microscopy, and ultrasound to encourage co-crystallisation.[58, 64, 76] The most popular method is solvent drop grinding, not only because of its huge success, but because of what it could mean for the industry in terms of reducing costs and creating a more efficient synthesis. The costs will be reduced in terms of amount of raw materials which are required for the synthesis, and in turn this will reduce waste solvent. Improvements in this area are ongoing.

1.3.4.2   METAL-ORGANIC FRAMEWORKS (MOFs)

1.3.4.2.1   INTRODUCTION

A Metal-Organic Framework (MOF) is an infinitely extended framework constructed by metal nodes and bridging ligands. Work published by Robson, Moore, Yaghi, and Zaworotko highlighted their vast potential for creating new material structures and properties due to the wide range of metals and infinite choice and design of ligands that could be used to create them.[77-80] A broad range of structural, electrical, magnetic, optical, and catalytic properties may be explored through the use of these materials.

MOFs have been classified into many different categories such as IRMOF (Isoreticular Metal-Organic Frameworks), MOP (Metal-Organic Polyhedra), ZIF (Zeolitic-Imidazolate Frameworks), CP (Coordination Polymers), and PCP (Porous-Coordination Polymers) to name but a few. Although there are numerous categories they all alluded to the same metal-ligand compounds which extend into one, two, and three dimensions (1D, 2D, 3D).

1.3.4.2.2   PRINCIPLES IN MOF SYNTHESIS

An interest in polymeric structures constructed by metal ions and organic bridging ligands sparked in the early 1990s. Since then, the number of papers which use the term 'Metal-Organic Frameworks' or 'coordination polymer' has vastly increased.

These materials offer huge potential because there are an infinite number of MOFs which can be made due to the wide range of ingredients which are accessible. The dimensionality of the final structure can be tuned depending on the combination of

ingredients used. There also lies the potential to modify the linker when it is already within a framework to create a new structure allowing very different properties to be realised.

The final assembly, dimensionality, and porosity of a MOF are dependent on numerous factors namely: a) coordination potential of metal centres and ligands, b) synthetic method employed, c) solvent(s) used. The use of templates may also be required to allow formation.[81, 82] Understanding the coordination potential of both metal centres and ligands is integral in order to design MOFs and obtain specific geometries. Metal ions come in many sizes, and possess different coordination numbers and coordination geometries, which is why the choice of metal ion greatly affects the outcome of a MOF synthesis. The most common utilised set of metals for MOF synthesis are the transition metals. Their coordination numbers range from 2 to 6 and have coordination geometries of linear, square planar, tetrahedral, square pyramidal and octahedral. Higher coordination numbers (7-10) may be accessed by using alkaline earth metals or lanthanides which have higher coordination potentials.

linear   trigonal planar   tetrahedral   square planar   trigonal bypyramidal   square pyramidal

octahedral   trigonal prismatic   pentagonal bypramidal   trigonal prismatic, square face monocapped   square antiprism   tricapped trigonal prismatic
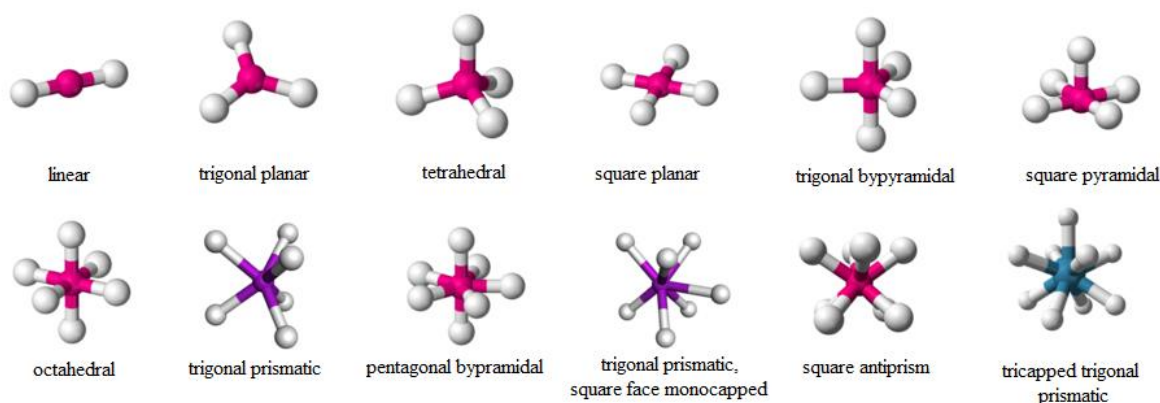
Figure 1.3.3 - Coordination geometries of transition metals and rare earth metals - lanthanides

Organic linkers commonly used to construct MOFs require ligands which have at least two different functionalities *e.g.* two carboxylates, one carboxylate and one pyridine, or bipyridine to generate an infinite structure. The dimensionality of these materials can be further extended by non-covalent interactions such as hydrogen bonding and π-π

stacking. Polycarboxylates (aromatic or aliphatic), imidazole, and bipyridine (can be used as either ligand or template) are most often used (Figure 1.3.4).

oxalic acid	fumaric acid	terephthalic acid	imidazole	pyrazine

benzene-1,3,5-tricarboxylic acid	benzene-1,2, 4,5-tetracarboxylic acid	4,4 bipyridine
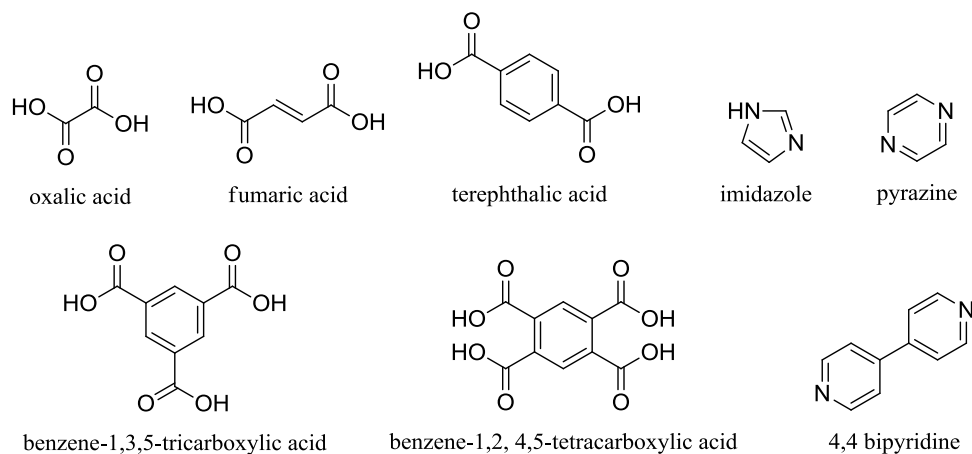
Figure 1.3.4 - Examples of organic bridging ligands

As previously stated, the dimensionality (1D, 2D, or 3D) of these materials is affected by the choice of metal centres and organic linkers because of their coordination capabilities. A brief discussion of the motifs generated by 1D, 2D, and 3D frameworks observed from the literature will be discussed here.
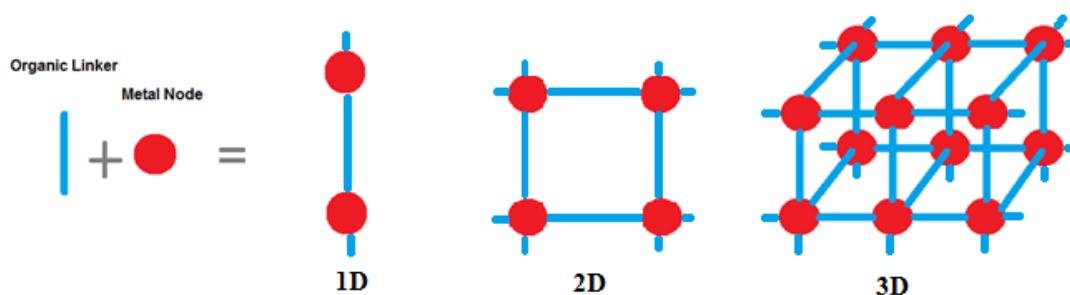
Figure 1.3.5 – Simplified representation of the formation of metal-organic frameworks (MOFs).

1D structures are created when a metal centre is coordinated to two ligand molecules such that 1D linear, zigzag, helical, or double-chain like motifs form. The metal coordination environment is completed by solvent molecules, and more often than not these tend to be water molecules. An example of a 1D structure is [Cu(tda)(phen)]1.5H$_2$O which contains two organic ligands tda (thiodibenzoic acid) and phen (phenanthroline).[83] Copper ions are four coordinated. The coordination

23

environment around Cu(II) is a distorted square planar geometry forming a [CuN$_2$O$_2$] unit. Copper ions, tda and phen ligands are combined together via the carboxylate oxygens to form a polymeric chain which result in a 3-D supramolecular architecture via weak C-H···π interactions of the phenyl rings to the benzene rings of the tda ligand.
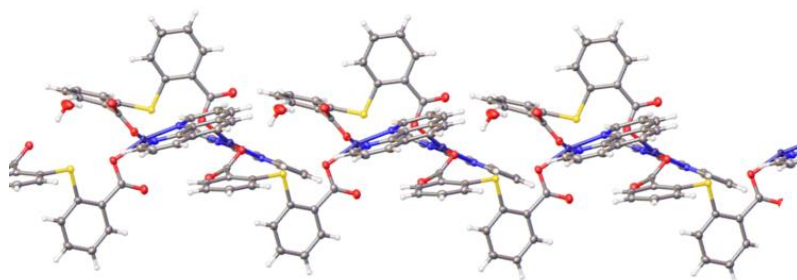
Figure 1.3.6 - Example of 1D MOF structure [Cu(tda)(phen)]1.5H$_2$O[83]

In 2D structures metal centres coordinate to three or four ligand molecules to form square grids, rhombic grids, honeycomb grids or brick wall-like structures. An example of a 2D structure is [Cd(4,4′-bpy)](NO$_3$)$_2$ (bpy = bipyrdine).[84] Cadmium ions are six coordinate. The coordination environment around Cd(II) is that of a distorted octahedral with four pyridyl groups occupying the equatorial positions whilst the nitrate anions occupy the apical sites. Cd(II) ions and bpy bond in two directions to make up square grids. Dibromobenzene molecules are present between the layers of Cd(II) ions and bpy ligands.
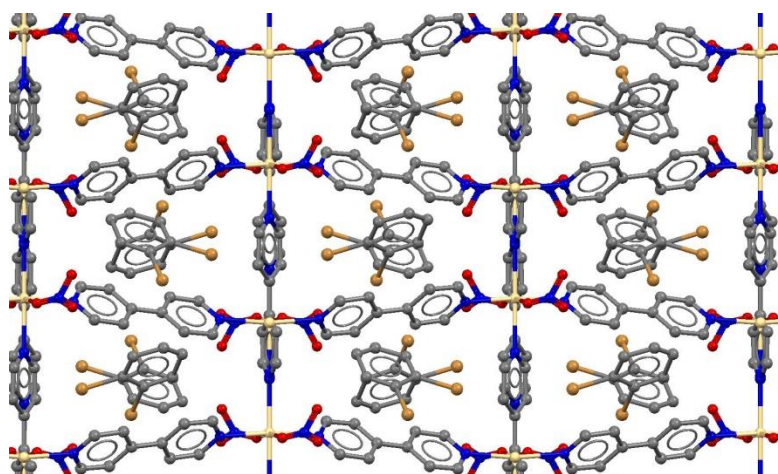
Figure 1.3.7 - Example of 2D MOF structure [Cd(4,4′-bpy)](NO$_3$)$_2$

Higher coordination numbers (4 or more) and multidentate ligands allow the formation of 3D structures which form octahedral, cubic, diamondoid or NbO networks. MOF-5, one of the most well-known MOFs and one which inspired part of this work, is an example of a 3D cubic MOF.[85] It comprises $Zn_4O(CO_2)_6$ clusters which are bridged by 1,4-benzenedicarboxylate (bdc).
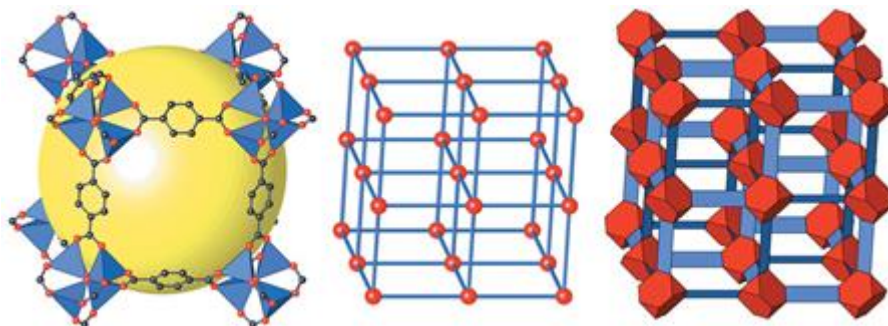
Figure 1.3.8 - Example of 3D structure MOF-5[78]

The concept of 'Reticular Chemistry' was coined soon after the synthesis of MOF-5 by Yaghi and O'Keefe.[78] They postulated that ordered, porous structures could be predicted and manufactured by the use of metal cations paired with well-defined, rigid organic ligands.

1.3.4.2.3 POTENTIAL MOF APPLICATIONS

The ability to design and functionalise these types of materials has caused numerous potential applications to be discovered. The applications which have been realised are mainly attributed to the porosity of the structures which can be generated. Porous MOFs can be used for CO_2 capture,[86] gas storage (H_2 and CH_4),[87] gas separation,[88] catalysis,[89-93] sensing,[94-97] and drug delivery.[98] A brief summary shall be given for applications which are or could be useful to the energetic materials field namely sensing, nanoparticle encapsulation, and post synthetic modification MOFs.

1.3.4.2.3.1 Sensing

The use of MOFs in the energetic materials field was unknown until recent explosive chemical sensors developments where the porosity of the framework absorbs and traps explosive compounds and triggers a detectable response.[94-97, 99]

1.3.4.2.3.2 Encapsulation of Nanoparticles

Nanoparticles (Pd) are typically used within MOFs to improve the selective catalytic activity of materials.[100, 101] However the encapsulation of metallic nanoparticles, such as Mg or Al, within these types of materials could be useful if the MOF itself was considered as an oxidiser. It would be interesting to compare systems based on this design approach along with those products which result from sol-gel processes where metal nanoparticles (fuel) are introduced into the pores of metal oxides (oxidiser).[16]

1.3.4.2.3.3 Post Synthetic Modification

The opportunity to alter a MOF material even after it has newly formed into an entirely different structure could be promising for the energetic materials field. Specifically regarding cation exchange, if one cation did not produce a satisfactory performance it could be substituted directly rather than initiating the whole synthesis once again.[102]

1.4   ANALYTICAL TECHNIQUES

1.4.1   INTRODUCTION

In this section, the analytical tools applied during this study are discussed.

1.4.2   X-RAYS

As X-rays are utilised by several techniques (CT, SXRD, PXRD) in this work a brief description is given for them. X-rays are a form of electromagnetic radiation with a wavelength of ~ 1Å. They are found between ultra violet rays and gamma rays in the electromagnetic spectrum. X-rays were discovered by Wilhelm Konrad von Röntgen (1845-1923) in 1895. This discovery led to him winning the Nobel Prize in 1901. His colleague, Max Theodor Felix von Laue (1897-1960) recognised that crystalline solids caused X-rays to diffract possibly due to the wavelength of X-rays being the same order of magnitude as the interatomic distances in crystals. His work on the theory of X-ray diffraction led to him receiving the Nobel Prize in 1914.[45]

X-rays are produced when a beam of accelerated electrons are directed onto a metal target, typically molybdenum or copper. When the high energy electrons hit the metal target, X-rays are created in two ways; 1) radiation is released over a continuous range of wavelengths (known as Bremsstrahlung), 2) energetic electrons expel inner 1s electrons which cause electrons from the outer shells (2p or 3p) to drop down to fill in the gap which in turn causes the release of X-ray photons. X-ray radiation of a specific wavelength can be chosen from the range of wavelengths by passing the radiation through a monochromator (*e.g.* graphite crystal).[103, 104]

When X-rays are directed through an object, photons can interact with the particles of matter and their energy can be absorbed or scattered. This is known as attenuation. The materials atomic number, density, thickness as well as the energy of the individual photons will dictate the number of photons which are transmitted through the object.

1.4.3   COMPUTED X-RAY TOMOGRAPHY (CT)

Computed axial tomography, usually referred to as either CAT or CT, has received a great deal of interest in the past few decades. Its main use for a long time was in medical applications in hospitals, but it has now found its way into various other disciplines. Examples include archaeology (*e.g.* fossil and artefact analysis), oceanography (sediment analysis), geology (rock mechanics and soil analysis) and many more. It is an ideal analysis technique for so many different types of objects because it is non-destructive. Differing levels of density and atomic composition help to reveal the internal structures of objects. Materials which have different levels of density or atomic composition will consequently have different linear attenuation coefficients. X-rays will attenuate differently based on the atomic composition or on the magnitude of the density, thus helping to identify individual components in mixtures of materials.

1.4.3.1   X-RAY ATTENUATION

The total attenuation takes into account the sum of the attenuation based on the different types of absorption and scattering interactions. The type of material and X-ray energy used will determine the dominant type of interaction that takes place. The photoelectric effect is dominant when low X-ray energies (50-100keV) are used whereas when higher energies (500-1000keV) are utilised Compton scattering is more prominent.[105]
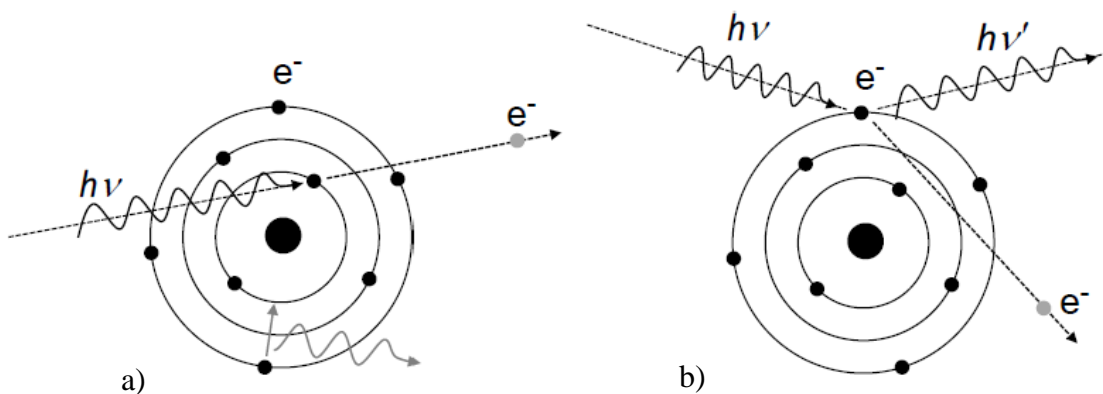
Figure 1.4.1 - a) Photo-electric effect b) Compton Scattering

The Beer-Lambert law describes the absorption of a monochromatic X-ray beam with intensity I passing through a homogenous material with respect to the distance travelled. The variation in intensity observed due to the passage of X-rays through the object under examination at distance *x* can be expressed as follows:

$$dI(x) = -I(x).\sigma_a.n_z.dx \qquad \text{Equation 1.4.1}$$

n_z is the number of atoms/cm^3, σ_z is a proportionality constant that indicates the total probability of a photon being scattered or absorbed and d_x is the incremental material thickness which X-rays have passed through. Integrating Equation 1.4.1 gives,

$$I = I_o exp[-\sigma_a n_z x] \qquad \text{Equation 1.4.2}$$

The linear attenuation coefficient μ is obtained by grouping n_z, σ_a. This is a material specific constant. When the X-rays are travelling through inhomogeneous matter as opposed to homogeneous the equation changes to:

$$I = I_o exp[\Sigma_i(-\mu_i x_i)] \qquad \text{Equation 1.4.3}$$

i corresponds to a single material with attenuation coefficient μ, over a linear range x_i. Commonly used reconstruction algorithms solve Equation 1.4.3, however, as there are other factors to consider such as the X-ray energy input, there are slight variations seen within reconstructed volumes. These are classed as imaging artefacts.

1.4.3.2   PRINCIPLE OF CT SCANNING

The word 'tomography' was derived from the Greek word *tomos* which means "a section" or "a cutting". X-ray tomography is a technique by which a single plane is imaged at any given time, whilst excluding all other planes. The images taken of each plane are collected and compiled to build up a 3D rendering of an object such that both an internal and external view of the object can be observed. [106] These 3D representations can then be inspected to identify the mechanical and physical properties of said object.

Conventional Tomography has many other names including planigraphy, stratigraphy, laminography, body section radiography, zonography and non-computed tomography.[107] One of the individuals who helped develop this technique was A.E.M. Bocage. In 1921, Bocage described an apparatus which had the capability to blur out structures above and below a plane of interest. The experimental setup comprised of an X-ray tube, an X-ray film, and a mechanical connection, which was of great importance, in order to ensure that synchronous movement of the X-ray tube and the film was achieved.

A CT system consists of a rotating stage, a radiation source, and a detector/imaging system. A computer-driven rotating stage and imaging system collects X-ray images and correlates them to the position of the test object. The detector collects the image of the test specimen. The rotating stage then moves the object to its next position to collect the next image. The degree of X-ray attenuation, as a result of coming into contact with an object, will vary depending on the density and atomic composition of the object, and the X-ray energy. 2D sinogram images are produced which are then converted into 2D radiographs and compiled together to produce a 3D volume rendering of the scanned object through the use of CT reconstruction software.

1.4.3.3 IMAGE RECONSTRUCTION

Image reconstruction from projections was attempted as early as 1940. Gabriel Frank describes the idea of tomography as it is used today in a patent granted to him in that year. This patent contained drawings of equipment which could be used to reconstruct images using optical backprojection techniques and sinogram (Radon transform data). Sinograms are representations of measurement data in terms of distance and angle (normally notated x and θ respectively). These are similar to radiographs, however these instead are in terms of planar distances (x vs. y). Numerous methods exist by which the X-ray attenuation can be converted into a reconstructed image; filtered backprojection appears to be most popular. Filtered backprojection is the process in which the image of a sample is formed by back-tracing the received radiation along its path of projection.[108] The linear data which is acquired at each angular orientation is collected and combined

with a specially designed filter and then backprojected across a pixel field at the very same angle.
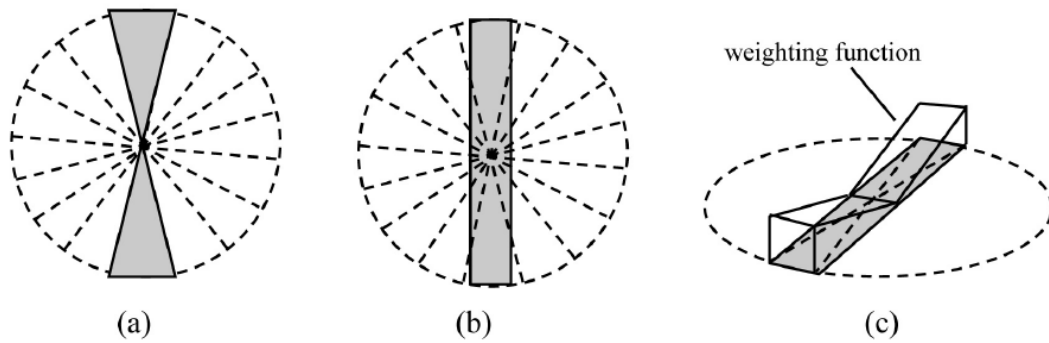
Figure 1.4.2 - Illustration of the filtered back projection concept, a) ideal frequency from one projection, b) actual frequency data from one projection c) weighting function in the frequency domain approximate to ideal conditions[106]

The grey regions within Figure 1.4.2 represent Fourier transforms of the acquired projections of an object being imaged (*e.g.* pyrotechnic composition). The ideal case means that when all Fourier transforms are combined that the object is evenly represented. Real Fourier transforms are represented by a strip rather than a pie slice and so when these are added the central region is effectively enhanced and the outer regions are understated. A reconstructed CT dataset is typically stored and shown as a 3D matrix of 'voxels' which are the equivalent 'pixels' in 2D images. In terms of CT, spatial resolution is quoted in voxels. In early days the technique proved very successful as it could resolve closely packed high contrast objects (*spatial resolution*), however it did have problems with distinguishing between low contrast objects and its background (*low contrast resolution*). Over time these parameters have improved. The technology involved has advanced dramatically in the past 30 years.

All of the advances have resulted in reduced scan time and better resolution, but there will always be obstacles associated with computed tomography: artefacts. The most common of these being beam hardening, which is a result of greater attenuation occurring in the centre of an object compared to its edge. This problem can be resolved by filtration and/or specialist software programs. There are four main categories of imaging artefacts; streaking, shading, rings and bands. Streaking appears as intense lines

(not all parallel) in the images collected. Shading appears near objects which are of high contrast. Rings and bands are artefacts mainly associated with 3rd generation scanners; they literally create rings in the images. Sophisticated software can be used to help minimise these artefacts so that clean and clear images can be observed. There are a number of different types of software available, which can be used to reconstruct images collected from a variety of different instruments not just CT. *Fiji, Avizo* and *VG Studio* are to name but a few.[109-112] These pieces of software can be used to enhance images in a multitude of ways, allowing both quantitative and qualitative information to be retrieved from data.

1.4.4   TESSELLATION TOOLS & STATISTICAL TOOLS

The 'required effect' of a pyrotechnic is influenced by how well the materials are mixed. The question pertains as to what makes a good mixture. This study aims to answer this question. Ordinarily mixtures are assessed visually, and the answer is necessarily subjective. A quantitative measure is required in order to obtain objective, comparable results.

In the book 'Spatial Tessellations – Concepts and Applications of Voronoi Diagrams', Okabe et al. reveals the use of tessellation throughout history dating as far back as the 15th century where a Voronoi-like diagrams were used to show the disposition of matter in the solar system. Peter Gustav Lejeune Dirichlet (1805-1859) and Georgy Fedoseevich Voronoy (Georges Voronoi) (1868-1908) both worked on positive definite quadric forms. It was these two men who developed the concept of Voronoi diagrams. Dirichlet tested both two and three dimensional cases where Voronoi kept his focus on m-dimensional scenarios.[113] A collection of points which are regularly spaced are produced by linear combination of m- linear independent vectors each having integer coefficients. The Voronoi diagram acts to partition the space into 'mutually congruent polyhedral'.[113] Voronoi showed that for an m-dimensional polyhedron when translation repetition of the (m-1)-dimensional facets occurred that a given space could be filled with no overlaps. One of its first applications was in crystallography. The concepts of

Voronoi diagrams and Delaunay tessellations lend themselves to a plethora of disciplines.
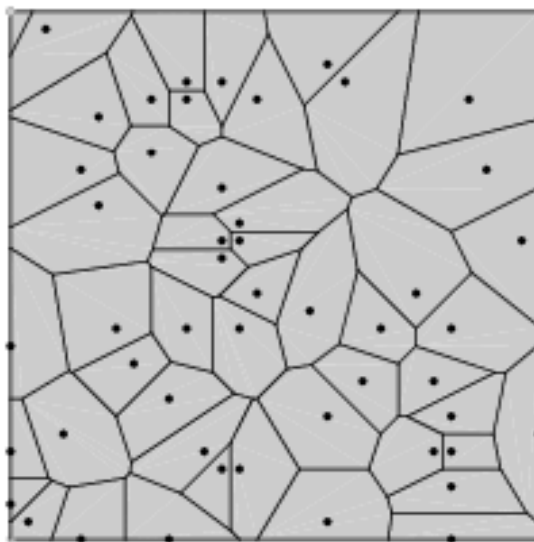
Figure 1.4.3 - Example of Voronoi Diagram[114]

Tessellation in this context refers to the complete filling of a given space. Here regions are grown from a particle, such that a cell is defined for each particle. Any point within a given cell is closer to the particle from which it originates than any other particle. They are useful tools as they help provide a mathematical description as to how data points are related to each other with respect to the regions of space they are associated with. This allows the distribution of data points to be explained. The most popular type of tessellation appears to be the Voronoi tessellations.[115] There are various types of these tools that have been developed for specific purposes. There are Delaunay tessellations, Dirichlet tessellations, Laguerre tessellations and geodesic centroidal tessellations to name just a few.[116-119] Occasionally the typical Voronoi tessellation technique is not sufficient to describe a dataset. It faces problems when describing an atomic structure as it assumes that all atoms are the same size. The Voronoi tessellation works by generating a convex polyhedron that splits the distance between two points. It is possible to define the convex polyhedron occupied by half planes between each point and its neighbouring points. [120, 121] The faces and edges of the polyhedrons can identify the structure of each atom within an atomic structure. There will be associated errors as

atomic sizes vary; extra calculations need to be applied to account for this. The type of tool utilised will depend on the type of data under analysis.

A number of different tools can be used to analyse a data set. In terms of this research understanding the distribution of the components in a pyrotechnic mixture is fundamental. One of the simplest ways of measuring the spread of data is by looking at the range of a data set, comparing the lowest value to the highest. *Standard deviation* is a familiar tool used commonly to assess the variation within a data set (See equation 1.4.4).

$$\sigma = \sqrt{\frac{1}{N}\sum_{i=1}^{N}(x_i - \overline{x})^2} \qquad \text{(Equation 1.4.4)}$$

where N = number of data points, x_i is the *i*th data point and $\overline{x}$ is the mean value of the data points. *Coefficient of variation (CoV)* is one of the most useful statistical methods as it is a normalized measure of the variation. CoV is the standard deviation divided by the mean.

$$c_v = \frac{\sigma}{\overline{x}} \qquad \text{(Equation 1.4.5)}$$

It is most useful when comparing data sets where they have different units or have very different mean values as the CoV is a dimensionless number. By comparison standard deviation is always put in context of the mean value.

1.4.5   CRYSTALLOGRAPHY

X-ray crystallography is a technique used to determine the atomic arrangement within a crystal. A beam of X-rays is fired through a single crystal as it is rotated through a number of different angles. The atomic structure of the lattice causes X-rays to scatter in a distinct way to produce a diffraction pattern. The electron density of the crystal may be worked out from the numerous diffraction patterns collected at various angles. The electron density map is used to find the positions of atoms, assign appropriate labels to these atoms, and determine the types of chemical bonds which exist within a crystal. This allows the accurate identification of a molecular structure. The physical properties of materials, such as melting point, hardness and density, are influenced by the assembly of these molecules and therefore it is important to have an understanding of crystal structures.[122]

Understanding the mechanical, performance and processing characteristics of pyrotechnic materials is of particular importance for this research and therefore it is useful to have a general knowledge of crystal structures and their interactions with X-rays.

1.4.5.1   SOLID FORM – CRYSTAL STRUCTURE

Molecules make up the basic structural design of crystalline solid materials. The molecules arrange themselves such that they create a regular array which is repeated by translation in three dimensions thus forming a lattice. The unit cell is the smallest collection of atoms which contains the overall symmetry of a crystal structure. It is a parallelepiped defined by sides of lengths a, b, and c as well as three angles α, β, and γ. The number of molecules within the unit cell is referred to as Z; the number of molecules within the asymmetric unit is referred to as Z′.

Only seven types of crystal systems exist. This is due to the restrictions on the unit cell parameters which arise because of both rotation and reflection symmetry. These are detailed in Table 1.4.1.

Crystal System	Unit Cell Restrictions	Essential Symmetry	Cell Types
Triclinic	none	none	*P*
Monoclinic	$\alpha = \gamma = 90°$	One 2-fold axis of rotation or one mirror plane	*P, C (I)*
Orthorhombic	$\alpha = \beta = \gamma = 90°$	Three 2-fold axes of rotation or one 2-fold axis of rotation and two mirror planes	*P, C (A), I, F*
Tetragonal	$a = b$; $\alpha = \beta = \gamma = 90°$	One 4-fold axes of rotation	*P, I*
Trigonal	$a = b \neq c$; $\alpha = \beta = 90°$; $\gamma = 120°$	One 3-fold axes of rotation	*P (R)*
Hexagonal	$a = b$; $\alpha = \beta = 90°$; $\gamma = 120°$	One 6-fold axes of rotation	*P*
Cubic	$a = b = c$; $\alpha = \beta = \gamma = 90°$	Four 3-fold axes of rotation	*P, I, F*

<u>Table 1.4.1 - The Seven Crystal Systems</u>[123]

There are four possible lattice types within these seven crystal systems: Primitive (*P*) face-centred (*F*), side –centred (*A, B,* or *C*) and body-centred (*I*). *R* stands for rhombohedral which is specific to trigonal structures.[123] The combination of the different lattice types and crystal systems create what are known as the Bravais lattices of which there are fourteen.[124] The associated symmetry operations (*e.g.* rotation, inversion) for a molecule is described by its relative point group and when combined with translational symmetry give rise to specific symmetry elements such as screw axes and glide planes. Space groups, of which there are 230, are generated by combining all of the symmetry elements and the Bravais lattices. The complete crystal structure can be acquired from the asymmetric unit and its relevant space group. Each of the space group's symmetry properties is well established and can be found in the *International Tables of Crystallography, Volume A*.[125] Each space group is denoted by a symbol consisting of a single capital letter showing the Bravais lattice type followed by lower case numbers and letters which show the presence of rotation, reflection, and inversion

symmetry in the structure. The numbers represent rotations (screw axes). The letters represent reflections (mirror and glide planes). The number of instances a space group is encountered varies for each group. Around a third of all crystal structures of molecular compounds have the space group $P2_1/c$ (Primitive unit cell with a screw axis parallel to the b-axis and a glide plane perpendicular to b with a translation along c).

1.4.5.2   THE LAUE EQUATIONS AND BRAGG'S LAW

Through his studies of diffraction patterns, Laue deduced three equations which were used to describe the diffraction of X-rays by crystals. The equations signify the three conditions needed for diffracted X-rays to interfere constructively. Each equation is associated with the diffraction conditions for an atom row in one specific direction.

$$a(\cos \alpha_0 - \cos \alpha) = h\lambda$$ ....(Equation 1.4.6)

$$b(\cos \beta_0 - \cos \beta) = k\lambda$$ .... (Equation 1.4.7)

$$c(\cos \gamma_0 - \cos \gamma) = l\lambda$$ .... (Equation 1.4.8)

Where α_0, β_0, and γ_0 are the angles between the incident X-ray beam and the unit cell axes a, b, and c. α, β, and γ are the corresponding angles for the diffracted beam. A diffracted beam will occur if the values of the six angles selected cause the h, k, and l parameters to be integers[126]. h, k, and l are Miller indices these represent the orientation of a plane, in three dimensional space, with respect to the three unit cell edges.

An alternative interpretation of diffraction was introduced by William Henry Bragg (1862-1942) and his son, William Lawrence Bragg (1890-1971). Their theory is much more commonly practiced today due to its simplicity. In 1913, Bragg and his son demonstrated that crystals could be considered as assemblies of parallel layers or planes through lattice points. Each layer acted as a semi-transparent mirror such that some X-rays were transmitted through the layer and some were reflected. William Lawrence Bragg contributed his knowledge of optics and the idea of reflection and his father developed the instrument, the X-ray spectrometer, which allowed their theory to be tested.[127]

X-ray beams are parallel and in phase until they strike the various layers of atoms. One beam will strike the top layer and hit a specific atom and produce scattering with an angle of reflection equivalent to the incident angle. The second beam will strike another atom on the second layer where again the reflection and incident angles are equal.
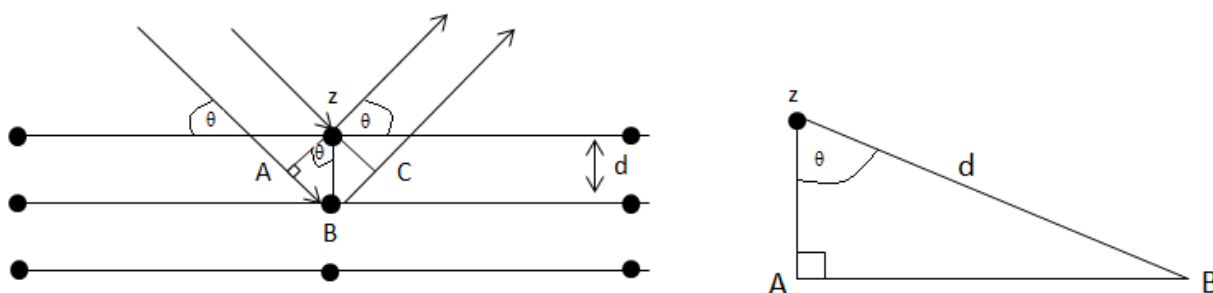
Figure 1.4.4 - Deriving Bragg's Law from Trigonometry

Interference effects occur due to the reflections of the adjacent planes. If the path length of each wave is an integer multiple of the wavelength then the scattered waves interfere constructively and are therefore in phase. Bragg, realising this, developed an equation which described this occurrence.

$$n\lambda = 2d_{hkl}sin\theta$$ (Equation 1.4.9)

n = integer (order of reflection)

λ = wavelength

d_{hkl} = interplanar spacing

θ = 'Bragg' angle or 'glancing angle'

The diffraction pattern is built up by these scattered waves as result of them interacting either constructively or destructively. The size/strength of various spots which appear in a diffraction pattern are a result of this interference. Crystal structure determination relies on the collection of as many diffraction points, *hkl*, as possible. The variation of d_{hkl} is representative of the orientation of the crystal in terms of the incident X-ray beam. This is varied whilst the wavelength is kept constant so the diffraction data from all relevant orientations can be collected.[103]

1.4.5.3   STRUCTURE FACTORS

Incident X-rays are diffracted by atoms resulting in reflections. A diffraction pattern is a collection of these distinct reflections. Each reflection is a wave which has its own amplitude and associated phase and each wave is built up of a sum of waves which are scattered by the individual atoms. The amount of scattering produced by the atoms is dependent on the scattering angle of the X-rays, the atomic number/electrons of the atom, and also the degree of atomic absorption. The whole crystal contributes to the diffraction and so the atomic scattering associated with all of the atoms must be taken into account. The scattering of the collection of atoms in a structure is known as the structure factor, (Fhkl) which is a complex number representing both the amplitude and phase for a specific h,k,l reflection. This is given by:

$$F_{hkl.} = \sum_{j=1}^{N} f_j exp\left[2\pi i\left(hx_j + ky_j + lz_j\right)\right]$$

(Equation 1.4.10)

f_j = atomic scattering factor for the jth atom in the unit cell

x_j, y_j, z_j = fractional co-ordinates

h, k, l = Miller indices

The equation represents the mathematical relationship between the crystal structure, in terms of electron density, and the diffraction pattern. It is known as the Fourier transform. The electron density can be realised from the structure factor since the scattering is caused by the electron density within the unit cell. Equation 1.4.10 represents the forward Fourier transform where equation 1.4.11 represents the reverse Fourier transform which allows the calculation of the electron density ($\rho(xyz)$) at any point x, y, z.

$$\rho(xyz) = \frac{1}{V}\sum_{hkl} F(hkl)\, exp\left[-2\pi i(hx + ky + lz)\right]$$

(Equation 1.4.11)

V = unit cell volume

This equation allows information in terms of reciprocal space (diffraction pattern) to be converted into information in real space (electron density).[123]

The complex structure factors are requisites for the Fourier transformation, however only their amplitude (magnitude), |F(hkl)|, is known and not their phase (direction). Therefore the calculation may not be performed directly from experimental measurements of the X-ray intensities. This is referred to as the phase problem.[128, 129] Fortuitously the phase angle can be isolated from the electron density leading to the following equation: |F(hkl)|

$$\rho(xyz) = \frac{1}{V} \sum_{hkl} |F(hkl)| \exp[i\phi(hkl)] \exp[-2\pi i(hx + ky + lz)]$$

(Equation 1.4.12)

This equation is useful as it treats the amplitudes and the phases separately. Using a computer, the observed values of the amplitudes (|F(hkl)|) can be combined with derived values for the phases (ϕ(hkl)) to create a trial density map. If the map appears reasonable then it may be refined. Direct methods use phase relationships based on observed intensities in the diffraction pattern to obtain approximate reflection phases. These probable phase values are estimated by analysing the intensities of the reflections and the trigonometric relationships between the amplitudes. The electron density maps are calculated using the best sets of phase values which are indicated by the figures of merit. Structure determination via direct methods has become popular as it is a simple method to use. The direct methods approach is most often used when the molecule contains atoms of approximately equal value such as C, N, and O. Molecules containing heavier elements, for instance organometallic compounds, tend to use the Patterson method. This study only employed the direct methods approach.[130]

1.4.5.4   POWDER X-RAY DIFFRACTION (PXRD)

PXRD is a complementary technique to SXRD. SXRD is a very valuable characterisation technique however it does have its drawbacks. A crystal suitable for SXRD must meet certain criteria before it can be put forward for analysis. An ideal

crystal should be crystalline, single, spherical, free from defects, free from strain and be of the correct size range 0.002 – 0.5mm. The other issue is that the crystal selected may not necessarily be a good representation of the whole batch. PXRD is valuable in that it evaluates the bulk material.[45] PXRD provides a means to identify crystalline phases and allow both qualitative and quantitative analysis of mixtures. In the process of SXRD, each reflection produces a single spot within a diffraction pattern. For PXRD many reflections attributed to the random arrangement of polycrystalline material results in a diffraction pattern which appears as a collection of rings rather than a collection of spots. The rings arise because the reflections overlap. The intensity of the diffracted beam is measured as a function of 2θ in one dimension.
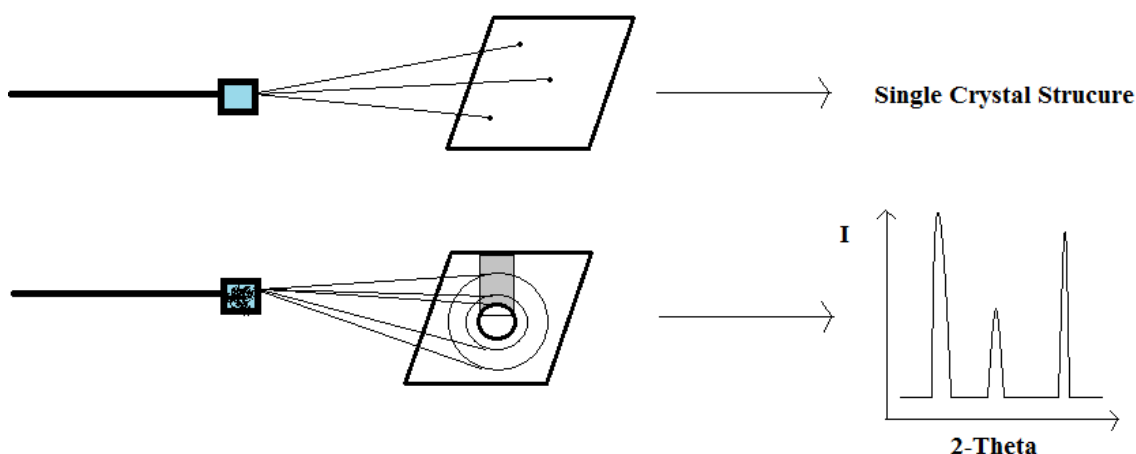
Figure 1.4.5 - Comparison of diffraction patterns resulting from PXRD and SXRD analysis

PXRD creates a pattern of peaks which are each associated with the periodic spacings of atoms in the solid state. Each peak is associated with a single reflection. It provides the data associated with the most strongly diffracting hkl planes of the sample. Unique patterns provide qualitative information allowing material phase identification. They also give quantitative data; crystallographic unit cell dimensions (based on the positions of the reflections), thermal properties, and lattice distortion.[131] The atomic/molecular arrangements within the unit cell may be identified however, this is more difficult to do compared with SXRD as the data is condensed from 3D to 1D. The Rietveld method is most commonly used to deduce the molecular structure within an unknown sample.[132,]

[133] It allows the determination of unknowns through structural refinements. The cell parameters and peak profiles are refined against calculated structure factors, which are provided from a structural model, using least squares refinements. PXRD also provides an indication of crystallite size, stress/strain, and defects by looking at the position and shape of the peaks in the patterns.

Appropriate sample preparation is the key to the success of a PXRD experiment. There are two main issues to consider when selecting sample preparation techniques; 1) large particle sizes translate to fewer particles being in the beam resulting in poor averaging, 2) preferred orientation of crystallites (plate or needle morphology) or textures which increases intensity of certain diffraction peaks in comparison to others causing problems in unit cell determination. The first issue can be minimised by sieving or grinding to achieve small uniform particles, however grinding must be considered carefully as it can induce a phase change and form a binary compound. To resolve the preferred orientation of crystallites the sample can be mounted in a capillary and rotated. [132, 134]

Structure determination from PXRD data can be carried out using programs such as DASH[135] which uses a simulated annealing algorithm. PXRD in comparison to SXRD has reduced dimensionality. It is a 1D pattern of intensity versus 2θ. This can create issues with overlapping reflections making it difficult to identify unit cell parameters and determine the intensity of each individual reflection. More complex structures will therefore be more problematic. Particle size correlates with peak width and therefore to minimise peak overlaps the particle size should be small.

1.4.6   THERMAL CHARACTERISATION METHODS

1.4.6.1   HOT-STAGE MICROSCOPY

This technique dates back to the 1880s, in the time of Otto Lehman[136], however it is both Ludwig and Adelheid Kofler who were credited with the development of the technique.[137] It is one of the oldest and simplest methods applied in the field of crystallography to monitor changes in the physical characteristics of a material with respect to temperature and time. A typical hot-stage microscope today includes an optical microscope, polarizer, hot and cold stage (heating stage and sample holder), digital programmable temperature controller, digital camera, computer and software used to capture images or videos during an experiment.

Hot-stage microscopy has many applications including the study and formation of polymorphs, solvates, co-crystals and stability. For example; some polymorphs which do not form readily through solvent recrystallization can be prepared using this technique. The yield is small - only a small number of seed crystals are likely to form, however they can be used to grow more crystals.

HSM and DSC are complimentary techniques. The analytical potential for HSM and DSC is further improved when the techniques are combined. The origin of an event on a DSC trace can be confirmed by HSM and *vice versa* thereby increasing the confidence in the result obtained.

1.4.6.2   DIFFERENTIAL SCANNING CALORIMETRY (DSC)

The technique is used to investigate certain effects and properties of materials such as their melting behaviour, heat of fusion, purity, polymorphism, phase diagrams, evaporation, interaction/compatibility, thermal and oxidation stability, kinetics of decomposition.   Polymorphism and pseudopolymorphism (hydrates or solvates of materials) typically result in a number of unique melting points. These melting points are associated with specific polymorphs. Some polymorphic materials are known to have as many as 17 different melting points, each corresponding to a specific

polymorph.[138] DSC is a very powerful technique, but a single method should not be relied upon to distinguish between phase transitions.
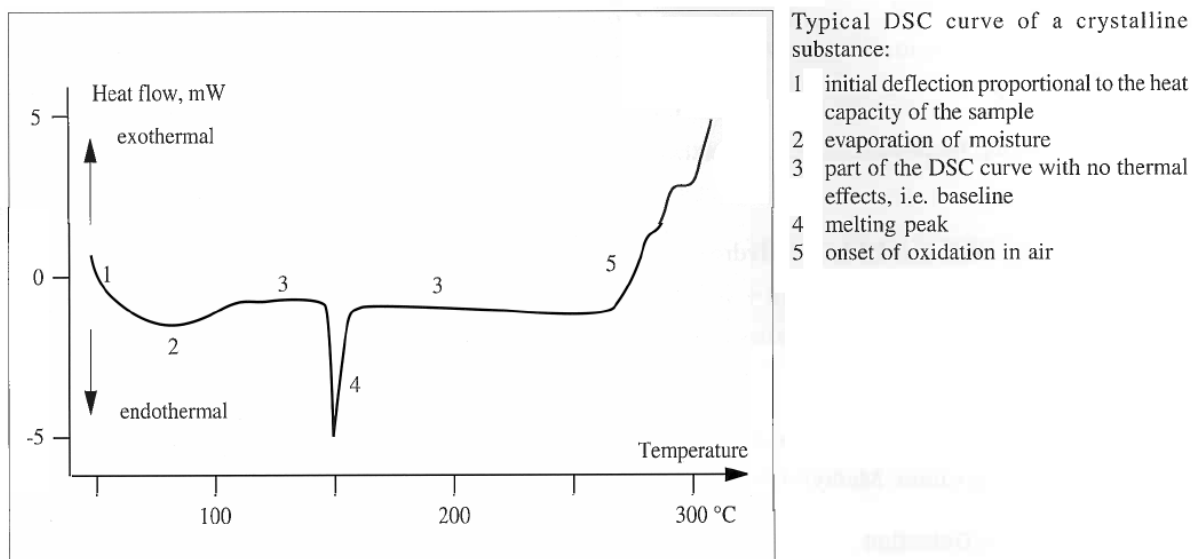
Figure 1.4.6 - Example of DSC Scan [139]

A DSC runs a pre-set temperature program on both a sample pan and a reference pan. It measures the difference in heat flow between the two pans. The heat flow relates to the transmitted power (measured in watts (W) and milliwatts (mW)). A quantity of energy is obtained (in joules or millijoules respectively) when the heat flow is integrated with respect to time. The measurements offer information on thermal effects, which are recognised by specific temperatures and by changes in enthalpy. Enthalpy measures whether a chemical process either absorbs or releases energy. This is accompanied by the reaction being endothermic or exothermic respectively.[140] The area enclosed under a DSC peak is proportional to the enthalpy of the reaction or other physical process taking place.

References

1. Hassell, C. D. *The Application of Solid State Physics Principles to Pyrotechnic Mixture Systems*; U. S. Army Armament Munitions Chemical Command: 1987.

2. Davies, N., *Pyrotechnics Handbook*. Cranfield University; Defence College of Management and Technology; Department of Applied Science, Security and Resilience: 2009.

3. Steinhauser, G.; Klapötke, T. M., *Angew. Chem. Int. Ed.* **2008,** *47* (18), 3330-3347.

4. DoD photo by Senior Airman Julianne Showalter, U. S. A. F., Hurlburt, A.-O., Ed. Wikimedia Commons: 2008; Vol. 4,200 × 2,592 pixels, pp An AC-130U Spooky Gunship from the 4th Special Operations Squadron jettisons flares over an area near Hurlburt Field, Florida, on August 20, 2008. The flares are used as a countermeasure to heat-seeking missiles that can track aircraft during real-world missions.

5. Kurume-Shimin, ColorfulFireworks, Ed. 2011; Vol. 1,599 × 967 pixels, pp 352nd Chikugo river Fireworks Festival which is held on 5th, Aug. 2011(Kurume, Fukuoka, Japan).

6. Tech Sgt Scott T Sturkol, U. S. A. F., Purple_smoke_grenade, Ed. Wikimedia Commons, 2006; Vol. 2918 × 2100 pixels, pp A student in the Air Mobility Warfare Center's Advanced Contingency Skills Training Course 06-5 at Fort Dix, N.J., deploys smoke during a training session at a tactical range there Sept. 18. More than 60 Airmen are participating in the training course, learning numerous combat-related skills including tactics, media skills, convoy operations, first aid, and field craft. The course is taught by the AMWC's 421st Combat Training Squadron. (U.S. Air Force photo/Tech. Sgt. Scott T. Sturkol).

7. The_Department_for_Culture_Media_and_Sport, Sparks_fly_from_Olympic_rings_suspended_from_the_roof, Ed. Wikimedia Commons: 2012; Vol. 4288 × 2848 pixels, p Sparks_fly_from_Olympic_rings_suspended_from_the_roof.

8. Vethathiri Pakkirisamy, S.; Mahadevan, S.; Suthangathan Paramashivan, S.; Asit Baran, M., *J. Loss. Prevent. Proc.* **2014,** (30), 275-281.

9. Hart, D.; Eppig, H. J. *Long Range Research on Pyrotechnics: Burning Characteristics of Binary Mixtures*; Picatinny Arsenal: 1947.

10. Koch, E.-C., *Propellants Explos. Pyrotech.* **2002,** *27* (5), 262-266.

11.   Christo, F. C. *Thermochemistry and Kinetics Models for Magnesium/Teflon/Viton Pyrotechnic Compositions*; Melbourne Victoria 3001 Australia, 1999; p 32.

12.   Koch, E.-C., *Metal-Fluorocarbon Based Energetic Materials*. Wiley-VCH Hoboken, NJ, USA 2012; p 362

13.   Gigahertz-Optik II Properties and Concepts of Light and Color. http://www.light-measurement.com/properties-and-concepts/ (accessed 21/03/2014).

14.   Eslami, A.; Hosseini, S., *J. Therm. Anal. Calorim.* **2011,** *104* (2), 671-678.

15.   Conkling, J. A., *Chemistry of pyrotechnics: basic priniciples and theory*. 10th ed.; M. Dekker: New York, 1985; p 190.

16.   Berger, B., *Propellants Explos. Pyrotech.* **2005,** *30* (1), 27-35.

17.   Steinhauser, G.; Sterba, J. H.; Foster, M.; Grass, F.; Bichler, M., *Atmos. Environ.* **2008,** *42* (37), 8616-8622.

18.   Moreno, T.; Querol, X.; Alastuey, A.; Cruz Minguillón, M.; Pey, J.; Rodriguez, S.; Vicente Miró, J.; Felis, C.; Gibbons, W., *Atmos. Environ.* **2007,** *41* (5), 913-922.

19.   Steinhauser, G.; Klapötke, T. M., *J. Chem. Educ.* **2010,** *87* (2), 150-156.

20.   Wise, S. S.; Schuler, J. H. C.; Katsifis, S. P.; Wise, J. P., *Environ. Mol. Mutagen.* **2003,** *42* (4), 274-278.

21.   Gouder, C.; Montefort, S., *Lung India : Official Organ of Indian Chest Society* **2014,** *31* (4), 375-379.

22.   Munster, J.; Hanson, G.; Jackson, W. A.; Rajagopalan, S., *Water, Air, Soil Pollut.* **2009,** *198* (1-4), 149-153.

23.   Becker, J. M.; Iskandrian, S.; Conkling, J., *Ann. Allerg., Asthma Im.* **2000,** *85* (6), 512-513.

24.   Sabatini, J. J.; Raab, J. M.; Hann, R. K.; Freeman, C. T., *Z. Anorg. Allg. Chem.* **2013,** *639* (1), 25-30.

25.   Sabatini, J. J.; Moretti, J. D., *Chem. Eur. J.* **2013,** *19* (38), 12839-12845.

26.   Case, F., A shade of green. *Chemistry World* 2011, pp 48-51.

27.   Koch, E.-C., *Propellants Explos. Pyrotech.* **2013,** (38), 603 – 604.

28.   Steinz, J. A.; Stang, P. L.; Summerfield, M. *Effects of Oxidizer Particle Size on Composite Solid Propellant Burning: Normal Burning, Plateau Burning and Intermediate Pressure Extinction*; Princeton University Princeton University 1967; p 18.

29.   Teipel, U., *Energetic Materials - Particle Processing and Characterization*. WILEY-VCH: 2005; p 621.

30. Fathollahi, M.; Pourmortazavi, S. M.; Hosseini, S. G., *Journal of Energetic Materials* **2007,** *26* (1), 52-69.

31. Ivanov, Y. F.; Osmonoliev, M. N.; Sedoi, V. S.; Arkhipov, V. A.; Bondarchuk, S. S.; Vorozhtsov, A. B.; Korotkikh, A. G.; Kuznetsov, V. T., *Propellants Explos. Pyrotech.* **2003,** *28* (6), 319-333.

32. Brown, M. E.; Taylor, S. J.; Tribelhorn, M. J., *Propellants Explos. Pyrotech.* **1998,** *23* (6), 320-327.

33. Ottino, J. M.; Khakhar, D. V., *Annu. Rev. Fluid Mech.* **2000,** *32*, 55 - 91.

34. Campbell, C. S., *Powder Technol.* **2006,** *162* (3), 208-229.

35. HosokawaMicronGroup Hosokawa Micron Powder Systems - Educational Center. http://www.hmicronpowder.com/pages/webinar.php?uid=48 (accessed 02/10/2012).

36. Lachman, L.; Lieberman, H. A.; Kanig, J. L., *The Theory and Practice of Industrial Pharmacy*. 2nd ed.; LEA & FEBIGER: 1976; p 787.

37. Carstensen, J. T., *Solid Pharmaceutics: Mechanical Properties and Rate Phenomena*. ACADEMIC PRESS, INC: 1980; p 259.

38. Iveson, S. M.; Litster, J. D.; Hapgood, K.; Ennis, B. J., *Powder Technol.* **2001,** *117* (1–2), 3-39.

39. Obadele, B. A.; Masuku, Z. H.; Olubambi, P. A., *Powder Technol.* **2012,** *230*, 169-182.

40. Liu, K., *Powder Technol.* **2009,** *193*, 208-213.

41. Khakhar, D. V., *Macromol. Mater. Eng.* **2011,** *296* (3-4), 278-289.

42. Desiraju, G. R., *The Crystal as a Supramolecular Entity, Perspectives in Supramolecular Chemistry*. Wiley: Chichester, 1995; Vol. 2, p 326.

43. Müller-Dethlefs, K.; Hobza, P., *Chem. Rev.* **1999,** *100* (1), 143-168.

44. Desiraju, G. R., *Crystal engineering: the design of organic solids*. Elsevier: 1989.

45. Seddon, K. R.; Zaworotko, M., *Crystal Engineering: The Design and Application of Functional Solids*. Kluwer Academic Publishers: 1999; p 512.

46. Kitaigorodsky, A. I., *Organic Chemical Crystallography*. Consultants Bureau: 1955.

47. Kitaĭgorodskiĭ, A. I., *Molecular crystals and molecules*. Academic Press: 1973.

48. Pertsin, A. J.; Kitaĭgorodskiĭ, A. I., *The atom-atom potential method: applications to organic molecular solids*. Springer-Verlag: 1987.

49. Pauling, L., *The Nature of the Chemical Bond and the Structure of Molecules and Crystals: An Introduction to Modern Structural Chemistry*. Cornell University Press: 1960.

50. Pimentel, G. C.; McClellan, A. L., *The hydrogen bond*. W.H. Freeman: 1960.

51. Desiraju, G. R., *Acc. Chem. Res.* **2002,** *35* (7), 565-573.

52. Gilli, G.; Gilli, P., *The Nature of the Hydrogen Bond: Outline of a Comprehensive Hydrogen Bond Theory*. Oxford University Press, USA: 2009.

53. Nishio, M., *CrystEngComm* **2004,** *6* (27), 130-158.

54. Desiraju, G. R., *Acc. Chem. Res.* **1991,** *24* (10), 290-296.

55. Desiraju, G. R., *Acc. Chem. Res.* **1996,** *29* (9), 441-449.

56. Taylor, R.; Kennard, O., *J. Am. Chem. Soc.* **1982,** *104* (19), 5063-5070.

57. Steiner, T., *Angew. Chem. Int. Ed.* **2002,** *41* (1), 48-76.

58. Callear, S. Preparation , Characterisation and Structural Assessment of Salts and Co-Crystals of Organic Compounds. University of Southampton, Southampton, 2008.

59. Etter, M. C., *The Journal of Physical Chemistry* **1991,** *95* (12), 4601-4610.

60. Aakeroy, C. B.; Seddon, K. R., *Chem. Soc. Rev.* **1993,** *22* (6), 397-407.

61. Metrangolo, P.; Neukirch, H.; Pilati, T.; Resnati, G., *Acc. Chem. Res.* **2005,** *38* (5), 386-395.

62. Jones, D., Black crystal arts. *Chemistry World* 2012, p 80.

63. Biradha. K; Su. Cheng-Yong; Vittal. J. J, *Cryst. Growth Des.* **2011,** *11* (4), 875-886.

64. Friscic, T.; Childs, S. L.; Rizvi, S. A. A.; Jones, W., *CrystEngComm* **2009,** *11* (3), 418-426.

65. Vishweshwar, P.; McMahon, J. A.; Peterson, M. L.; Hickey, M. B.; Shattock, T. R.; Zaworotko, M. J., *Chem. Commun.* **2005,** (36), 4601-4603.

66. Qiao, N.; Li, M. Z.; Schlindwein, W.; Malek, N.; Davies, A.; Trappitt, G., *Int. J. Pharm.* **2011,** *419* (1-2), 1-11.

67. Brittain, H. G., *Cryst. Growth Des.* **2012,** *12* (2), 1046-1054.

68. Springuel, G.; Norberg, B.; Robeyns, K.; Wouters, J.; Leyssens, T., *Cryst. Growth Des.* **2012,** *12* (1), 475-484.

69. Blagden, N.; Berry, D. J.; Parkin, A.; Javed, H.; Ibrahim, A.; Gavan, P. T.; De Matos, L. L.; Seaton, C. C., *New J. Chem.* **2008,** *32* (10), 1659-1672.

70. Miroshnyk, I.; Mirza, S.; Sandler, N., *Expert Opinion on Drug Delivery* **2009,** *6* (4), 333-341.

71. Fabian. L, *Cryst. Growth Des.* **2009,** *9* (3), 1436-1443.

72. U.S.DepartmentofHealth&HumanServices Database of Select Commitee on GRAS Substances (SCOGS) Reviews.

http://www.accessdata.fda.gov/scripts/fcn/fcnNavigation.cfm?rpt=scogsListing&display All=true (accessed 27/11/2012).

73. EuropeanChemicalsAgency REACH (Registration, Evaluation, Authorisation and restriction of Chemicals) http://www.hse.gov.uk/reach/about.htm.

74. Bolton, O.; Matzger, A. J., *Angew. Chem. Int. Ed.* **2011,** *50* (38), 8960-8963.

75. Karki, S.; Friscic, T.; Jones, W., *CrystEngComm* **2009,** *11* (3), 470-481.

76. Sander, J. R. G.; Bučar, D.-K.; Henry, R. F.; Zhang, G. G. Z.; MacGillivray, L. R., *Angew. Chem. Int. Ed.* **2010,** *49* (40), 7284-7288.

77. James, S. L., *Chem. Soc. Rev.* **2003,** *32* (5), 276-288.

78. Yaghi, O. M.; O'Keeffe, M.; Ockwig, N. W.; Chae, H. K.; Eddaoudi, M.; Kim, J., *Nature* **2003,** *423*, 705 - 714.

79. Rowsell, J. L. C.; Yaghi, O. M., *Microporous Mesoporous Mater.* **2004,** *73* (1–2), 3-14.

80. Perry Iv, J. J.; Perman, J. A.; Zaworotko, M. J., *Chem. Soc. Rev.* **2009,** *38* (5), 1400-1417.

81. de Lill, D. T.; Bozzuto, D. J.; Cahill, C. L., *Dalton Transactions* **2005,** (12), 2111-2115.

82. Zhang, Z.; Zaworotko, M. J., *Chem. Soc. Rev.* **2014,** *43* (16), 5444-5455.

83. Moosun, S. B.; Blair, L. H.; Coles, S. J.; Bhowon, M. G.; Jhaumeer-Laulloo, S., *Transition Met. Chem.* **2015,** *40* (2), 161-169.

84. Fujita, M.; Kwon, Y. J.; Washizu, S.; Ogura, K., *J. Am. Chem. Soc.* **1994,** *116* (3), 1151-1152.

85. Saha, D.; Deng, S.; Yang, Z., *J. Porous Mater.* **2009,** *16* (2), 141-149.

86. Lu, C.-M.; Liu, J.; Xiao, K.; Harris, A. T., *Chem. Eng. J.* **2010,** *156* (2), 465-470.

87. Czaja, A. U.; Trukhan, N.; Muller, U., *Chem. Soc. Rev.* **2009,** *38* (5), 1284-1293.

88. Barea, E.; Montoro, C.; Navarro, J. A. R., *Chem. Soc. Rev.* **2014,** *43* (16), 5419-5430.

89. Evans, J. D.; Sumby, C. J.; Doonan, C. J., *Chem. Soc. Rev.* **2014,** *43* (16), 5933-5951.

90. Falcaro, P.; Ricco, R.; Doherty, C. M.; Liang, K.; Hill, A. J.; Styles, M. J., *Chem. Soc. Rev.* **2014,** *43* (16), 5513-5560.

91. Lu, W.; Wei, Z.; Gu, Z.-Y.; Liu, T.-F.; Park, J.; Park, J.; Tian, J.; Zhang, M.; Zhang, Q.; Gentle Iii, T.; Bosch, M.; Zhou, H.-C., *Chem. Soc. Rev.* **2014,** *43* (16), 5561-5593.

92. McGuire, C. V.; Forgan, R. S., *Chem. Commun.* **2014**.

93. Mueller, U.; Schubert, M.; Teich, F.; Puetter, H.; Schierle-Arndt, K.; Pastre, J., *J. Mater. Chem.* **2006,** *16* (7), 626-636.

94. Banerjee, D.; Hu, Z.; Pramanik, S.; Zhang, X.; Wang, H.; Li, J., *CrystEngComm* **2013,** *15* (45), 9745-9750.

95. Gong, Y.-N.; Jiang, L.; Lu, T.-B., *Chem. Commun.* **2013,** *49* (94), 11113-11115.

96.   Hu, Z.; Deibert, B. J.; Li, J., *Chem. Soc. Rev.* **2014,** *43* (16), 5815-5840.

97.   Wang, G.-Y.; Song, C.; Kong, D.-M.; Ruan, W.-J.; Chang, Z.; Li, Y., *J. Mater. Chem. A.* **2014,** *2* (7), 2213-2220.

98.   Dey, C.; Kundu, T.; Biswal, B. P.; Mallick, A.; Banerjee, R., *Acta Crystallogr. Sect. B* **2014,** *70* (1), 3-10.

99.   Pramanik, S.; Hu, Z.; Zhang, X.; Zheng, C.; Kelly, S.; Li, J., *Chem. Eur. J.* **2013,** *19* (47), 15964-15971.

100. Lu, G.; Li, S.; Guo, Z.; Farha, O. K.; Hauser, B. G.; Qi, X.; Wang, Y.; Wang, X.; Han, S.; Liu, X.; DuChene, J. S.; Zhang, H.; Zhang, Q.; Chen, X.; Ma, J.; Loo, S. C. J.; Wei, W. D.; Yang, Y.; Hupp, J. T.; Huo, F., *Nat. Chem.* **2012,** *4* (4), 310-316.

101. Zhu, Q.-L.; Li, J.; Xu, Q., *J. Am. Chem. Soc.* **2013,** *135* (28), 10210-10213.

102. Brozek, C. K.; Dinca, M., *Chem. Soc. Rev.* **2014,** *43* (16), 5456-5467.

103. Clegg, W., *Crystal Structure Determination*. Oxford University Press: Oxford, 1998.

104. Littlejohn, D.; Cussen, E., Surface Analysis and X-ray Techniques - Lecture Course. Univeristy of Strathclyde, 2010.

105. Ahmed, S. An investigation of particle shape and fabric associated with railway ballast using X-ray CT and the discrete element method. University of Southampton, 2015.

106. Hsieh, J., *Computed Tomotgraphy - Principles, Practice, Artifacts & Recent Advances*. 2nd ed.; SPIE: 2009; p 560.

107. Morgan, C. L., *Basic Principles of Computed Tomography*. University Park Press: Baltimore, 1983.

108. Webb, S., *Brit. J. Radiol.* **1992,** *65*, 835-837.

109. Schindelin, J.; Arganda-Carreras, I.; Frise, E.; Kaynig, V.; Longair, M.; Pietzsch, T.; Preibisch, S.; Rueden, C.; Saalfeld, S.; Schmid, B.; Tinevez, J.-Y.; White, D. J.; Hartenstein, V.; Eliceiri, K.; Tomancak, P.; Cardona, A., *Nat. Meth.* **2012,** *9* (7), 676-682.

110. Schneider, C. A.; Rasband, W. S.; Eliceiri, K. W., *Nat. Meth.* **2012,** *9* (7), 671-675.

111. VisualizationSciencesGroup Avizo® Fire. http://www.vsg3d.com/avizo/fire (accessed 04/09/2012).

112. VolumeGraphicsGmbH VG Studio Max. http://www.volumegraphics.com/en/products/vgstudio-max.html (accessed 04/09/2012).

113. Okabe, A.; Boots, B.; Kokichi, S.; Chiu, S. N., *Spatial Tessellations Concepts Applications of Voronoi Diagrams Book* 2nd ed.; Wiley: 2000; p 696.

114. Weisstein, E. W. Voronoi Diagram.
      http://mathworld.wolfram.com/VoronoiDiagram.html.

115. Lautensack, C., *J. Appl. Stats.* **2008,** *35* (9), 985-995.

116. Peyre, G.; Cohen, L. In *Surface segmentation using geodesic centroidal tesselation*, 3D
      Data Processing, Visualization and Transmission, 2004. 3DPVT 2004. Proceedings. 2nd
      International Symposium on, 6-9 Sept. 2004; 2004; pp 995-1002.

117. Yang, N.; Boselli, J.; Sinclair, I., *Journal of Microscopy* **2001,** *201* (2), 189-200.

118. Du, Q.; Faber, V.; Gunzburger, M., *SIAM Review* **1999,** *41* (4), 637-676.

119. Watson, D. F., *The Computer Journal* **1981,** *24* (2), 167-172.

120. Leggoe, J. W., *Scripta Mater.* **2005,** *53* (11), 1263-1268.

121. Leggoe, J., *J, Mater. Sci.* **2006,** *41* (17), 5718-5722.

122. Hodeau, J. L.; Guinebretiere, R., *Appl. Phys. A* **2007,** *89* (4), 813-823.

123. Blake, A. J.; Clegg, W.; Cole, J. M.; Evans, J. S. O.; Main, P.; Parsons, S.; Watkin, D. J.,
      Crystal structure analysis: principles and practice. 2nd ed.; Oxford University Press:
      2009; Vol. 13, p 387.

124. Hummel, R. E., *Understanding Materials Science: History, Properties, Applications,
      Second Edition*. Springer: 2004.

125. *International Tables for Crystallography, Space-Group Symmetry*. 5th ed.; Springer:
      2005; Vol. A, p 932.

126. Kittel, C., *Introduction to Solid State Physics*. Wiley: 1971; p 766.

127. Ewald, P. P., *Fifty years of X-ray diffraction*. Published for the International Union of
      Crystallography by A. Oosthoek's Uitgeversmij.: 1962; p 720.

128. Taylor, G., *Acta Crystallogr. Sect. D* **2003,** *59* (11), 1881-1890.

129. Grünbaum, F. A., *Proceedings of the National Academy of Sciences of the United States
      of America* **1975,** *72* (5), 1699-1701.

130. Sheldrick, G., *Acta Crystallogr. Sect. A* **2008,** *64* (1), 112-122.

131. Pawley, G., *J. Appl. Crystallogr.* **1981,** *14* (6), 357-361.

132. Bish, D. L.; Post, J. E., *Modern powder diffraction*. Mineralogical Society of America:
      1989.

133. Kaduk, J. A., *Powder Diffr.* **2007,** *22* (01), 74-82.

134. Tang, C. C., Synchrotron X-ray Powder Diffraction (SXPD) - Diamond Summer School
      Presentation 2012.

135. David, W. I. F.; Shankland, K.; van de Streek, J.; Pidcock, E.; Motherwell, W. D. S.;
      Cole, J. C., *J. Appl. Crystallogr.* **2006,** *39* (6), 910-915.

136. Lehmann, O., *Molecularphysik*. Engelmann: Leipzig, 1888.

137. Stieger, N.; Aucamp, M.; Zhang, S.-W.; de Villiers, M. M. Hot-stage Optical Microscopy
       as an Analytical Tool to Understand Solid-state Changes in Pharmaceutical Materials.
       http://www.americanpharmaceuticalreview.com/Featured-Articles/39283-Hot-stage-
       Optical-Microscopy-as-an-Analytical-Tool-to-Understand-Solid-state-Changes-in-
       Pharmaceutical-Materials/ (accessed 03/10/2012).

138. Robinson, D.; Threlfall, T., Understanding Polymorphism & Crystallisation Issues in the
       Pharmaceutical Industry. 2009.

139. de Buhr, J.; Schwarz, E., Collected Applications, Thermal Analysis, Pharmaceutical.
       Mettler Toledo: p 100.

140. Brown, M. E., *Introduction to Thermal Analysis: Techniques and Applications*. Chapman
       and Hall Ltd: New York, 1988; p 211.

CHAPTER 2

Experimental

2.1   INTRODUCTION

The aim of this chapter is to give an overview of the techniques used for the synthesis and characterisation of pyrotechnic materials (mixtures, co-crystals, metal-organic frameworks (MOFs)) which are presented throughout this thesis. The most widely used characterisation techniques were X-ray based as this type of analysis is non-destructive which is important in this work given the dangers associated with handling pyrotechnic materials.

X-ray Computed Tomography (CT) was used to investigate particle distributions within pyrotechnic compositions. The information derived from this analysis was used to correlate performance with homogeneity of the pyrotechnic mixtures. *Powder X-ray Diffraction (PXRD)* was used to ascertain whether a new material had formed, and if it did, whether it was isolatable as a pure phase from both co-crystallisation and MOF synthesis experiments. When single crystals were available they were analysed using *single-crystal X-ray diffraction (SXRD) in* order to determine their crystal structures.

Differential Scanning Calorimetry (DSC) was used to determine the thermal behaviour of the new products (investigating desolvation and decomposition). These results indicated whether these new materials had the potential to act as a pyrotechnic. *Thermo-gravimetric analysis TGA (combined with DSC)* was used to investigate MOFs which incorporated the tetrafluoroterephthalic acid linker. These were compared to pyrotechnic mixtures. Burn tests were also carried out to visualise the pyrotechnic effect associated with the new materials.

Full descriptions of the methods used during this study are detailed in this chapter. The results can be found in subsequent chapters.

2.2   COMPUTED X-RAY TOMOGRAPHY (CT)

Computed X-ray tomography (CT) was used to assess the internal characterisation of pyrotechnic mixtures. It allowed the observation of particle distribution and particle size distribution within the mixtures.

A selection of metal nitrate oxidisers, dyes, and α-lactose monohydrate were obtained from Wallop Defence Systems Limited. Sodium nitrate, β-cyclodextrin, and terephthalic acid were purchased from Sigma Aldrich. The other reagents used in the following experiments were of analytical grade or better unless otherwise stated.

Preliminary scans were carried out to assess the appropriateness of this technique for characterisation of pyrotechnic compositions. Dr. Ranko Vrcelj provided five pyrotechnic samples for CT analysis. Each of the samples, composed of sodium nitrate and α-lactose, were sieve mixed between 3 and 7 times. α-lactose and sodium nitrate were dried prior to mixing in an oven at 100°C. Each material was individually hot sieved through a 100 micron sieve. They were sieved together using a 200 micron sieve. A record was kept of the number of times the samples were sieve mixed.

The samples were placed in 2 cm lengths of carbon fibre tubes with an internal diameter of 4 mm. Each sample was separated using a 1 cm length of a wooden dowel. The samples were scanned using the X-Tek HMX CT equipment and Inspect-X software.[1]

Figure 2.2.1 - Pyrotechnic Sample Set-up and X-Tek-HMX CT equipment[2]

Due to the sensitive nature of the pyrotechnic mixtures extra precautionary measures were taken to protect the equipment: A 2 mm thin Perspex sheet with the same dimensions as the detector was purchased to protect the detector should the mixture ignite. All other parts of the instrument were covered in clingfilm to prevent the pyrotechnic powder from becoming lodged in the instrument. A blanket was also attached to the top of the instrument to protect the cabling. Each sample was scanned individually for marginally less than an hour. Two samples (mix 1 and 3) were run overnight to observe any effects of increasing duration of scan. The settings for the scans are included in the following table:

Type	Short Scans	Overnight Scans
Exposure Time (ms)	1000	4000
Voltage (kV)	70	40
Current (µA)	100	155
No. of Projections	3142	1901
No. of Frame/Projections	1	Mix 1 - 2 Mix 3 – 1
Filter	1 mm copper	1 mm copper
Total Duration (hours)	4.5	8.5

Table 2.2.1 - CT Settings for Pyrotechnic Mixtures

The settings enabled a spatial resolution of 3.4 microns. Once the scans were complete the data was reconstructed using CT Pro 3D (Nikon Metrology, Tring, UK). This programme allowed the transformation of a parameter file in addition to all the images that were collected during a scan to become a volumetric model file. At this point the data could be visualised in imaging software such as Avizo,[3] ImageJ/Fiji,[4, 5] and VG Studio.[6] The original CT scan was collected in a 32 bit format which was converted into an 8 bit format to allow for faster processing using ImageJ.[4, 5] The container, the bottom 5% and top 5% of slices were cropped out of the 3D volume using VG Studio.[6] This step further improved the data processing speed by cutting down the file size. The top

and bottom 5% of slices were cut out as they are seen to be of less value due to the angle at which the X-ray beam hits the sample, meaning that they are not penetrated as well as the central slices.
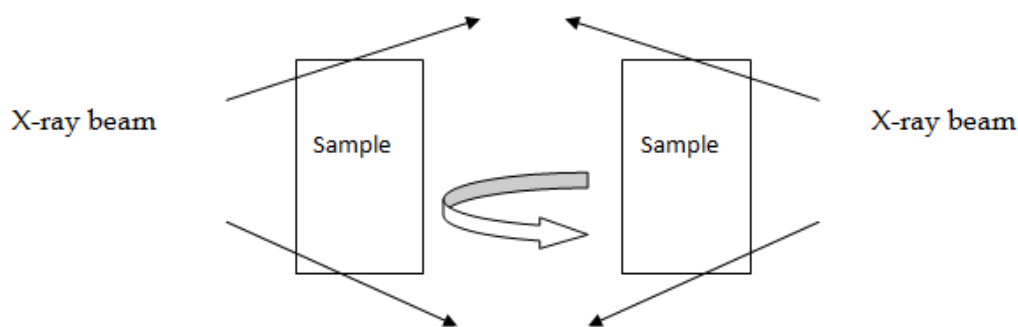
Figure 2.2.2 - X-ray beam penetration example

ImageJ[4, 5] was used to apply a median filter to all the images. The median filter replaces each pixel with the median value of the neighbouring pixel values around it thereby minimising the noise. They are useful filters as they help to reduce the appearance of ring artefacts (circles that can appear in images). There are different levels that can be used. The median filters applied to the scans were between 1.00 and 2.00. Increasing the level of median filter applied can result in a reduction in clarity of each image.

The next step was to threshold out each of the components of the mix in order to create a binarised image for each material. A binarised file is a binary image where each pixel is set to either 0 or 1 based on a selected range of values. Mathematical tools, such as tessellation tools, can be applied to binary images to describe the relationship between one particle and its neighbouring particles, thus enabling the mixture to be described based on how homogeneous it is.

As the performances of pyrotechnic compositions are influenced by numerous factors including oxidiser type, ratio of fuel to oxidiser, particle size, and number of mixing cycles further scanning was required to study these factors. The compositions manufactured to assess the variation in pyrotechnic performance due to these factors are detailed in Table 2.2.2.

Each of the oxidisers, α-lactose and terephthalic acid were dried prior to mixing in an oven at 80°C. Each material was individually hot sieved through the appropriate sieve depending on the particle size required (200, 125, 90, 75, and 38 micron sieves). They were then placed back in the oven until they were to be transported to WDSL where oxidisers and fuels would be combined. They were sieved together using a 250 micron sieve and then allowed to dry in an oven 80°C before they were ready to be pressed.

The samples were pressed using a load of 770 lbs/inch into 23 mm cardboard tubes with an internal diameter of 11 mm and 12 mm external diameter. Three increments of 0.3 g were added to the cardboard tubes. The compositions were pressed between each increment; an additional scoop (0.1 g) of SFG20 (sulfurless gunpowder) was added as a primer. Callipers were used to provide the dimensions of the cardboard tubes, and the length of compositions, this was to be used to calculate the burn rate (composition depth over burn time).
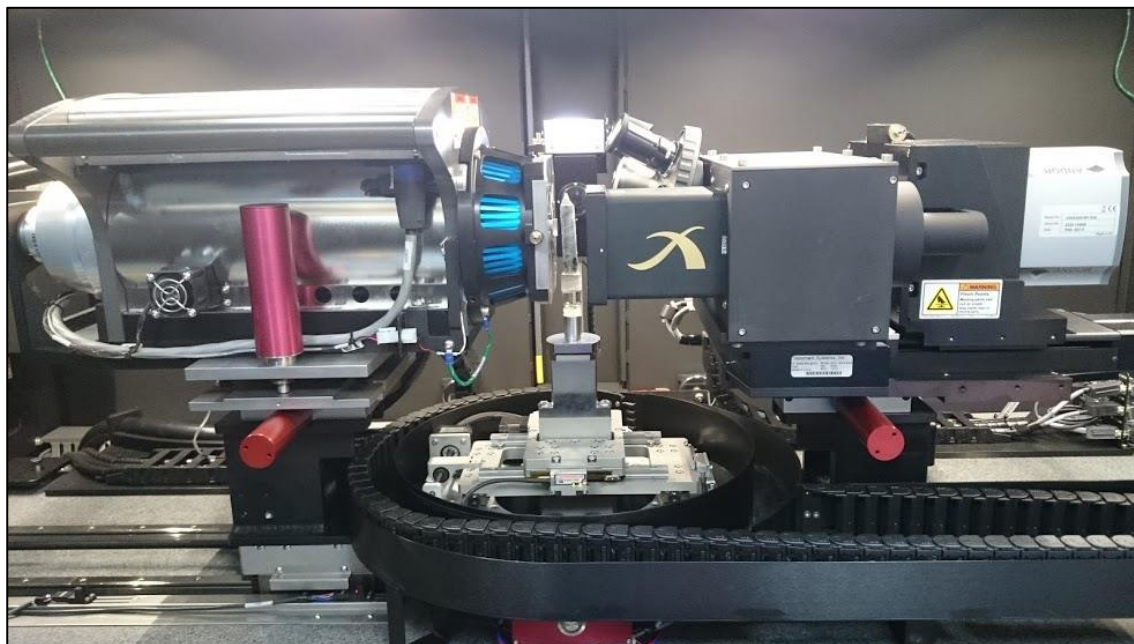
Figure 2.2.3 - Pyrotechnic Sample Set-up and VERSA 510 CT equipment

Each cardboard tube was stacked one on top of the other with a maximum of three cardboard tubes being mounted at any one time. The tubes are held within velostat wrapping which was cut down to size as an additional means to protect the instrument as well as minimise the movement of the samples whilst the scanning was taking place. The base of the tube was covered with parafilm and attached onto a glass vial using double sided sticky tape. The glass vial was attached onto one of the instrument mounts as can be seen in Figure 2.2.3 - Pyrotechnic Sample Set-up and VERSA 510 CT equipment. The samples were scanned using the Xradia VERSA 510 CT equipment and Zeiss Scan and Scout software (Carl Zeiss XRadia, Cambridge, UK).

Oxidiser	Ratio	Particle Size	Composition	Oxidiser %	Weight of Oxidiser (g)	Fuel %	Weight of Fuel (g)**
Potassium Nitrate (KNO₃)	1st ratio	38μm	AA	50	7.5	50	7.5 L
		75μm	AB	50	7.5	50	7.5 L
		90μm	AC	50	7.5	50	7.5 L
		125μm	AD	50	7.5	50	7.5 L
		200μm	AE	50	7.5	50	7.5 L
	2nd ratio	38μm	AF	64.1	9.615	35.9	5.385 L
		75μm	AG	64.1	9.615	35.9	5.385 L
		90μm	AH	64.1	9.615	35.9	5.385 L
		125μm	AI	64.1	9.615	35.9	5.385 L
		200μm	AJ	64.1	9.615	35.9	5.385 L
	3rd ratio	38μm	AK	78.1	11.715	21.9	3.285 L
		75μm	AL	78.1	11.715	21.9	3.285 L
		90μm	AM	78.1	11.715	21.9	3.285 L
		125μm	AN	78.1	11.715	21.9	3.285 L
		200μm	AO	78.1	11.715	21.9	3.285 L
	Bad Mix *	125μm	AP	50	7.5	50	7.5 L
Rubidium Nitrate (RbNO₃)	1st ratio	125μm	BA	59.3	8.895	40.7	6.105 L
	2nd ratio	125μm	BB	72.2	10.83	27.8	4.17 L
	3rd ratio	125μm	BC	83.9	12.585	16.1	2.415 L
	Bad Mix *	125μm	BD	59.3	8.895	40.7	6.105 L
Cesium Nitrate (CsNO₃)	1st ratio	38μm	CA	65.8	9.87	34.2	5.13 L
		75μm	CB	65.8	9.87	34.2	5.13 L
		90μm	CC	65.8	9.87	34.2	5.13 L
		125μm	CD	65.8	9.87	34.2	5.13 L
		200μm	CE	65.8	9.87	34.2	5.13 L
	2nd ratio	38μm	CF	77.5	11.625	22.5	3.375 L
		75μm	CG	77.5	11.625	22.5	3.375 L
		90μm	CH	77.5	11.625	22.5	3.375 L
		125μm	CI	77.5	11.625	22.5	3.375 L
		200μm	CJ	77.5	11.625	22.5	3.375 L
	3rd ratio	38μm	CK	87.3	13.095	12.7	1.905 L
		75μm	CL	87.3	13.095	12.7	1.905 L
		90μm	CM	87.3	13.095	12.7	1.905 L
		125μm	CN	87.3	13.095	12.7	1.905 L
		200μm	CO	87.3	13.095	12.7	1.905 L
	Bad Mix *	125μm	CP	65.8	9.87	34.2	5.13 L
Barium Nitrate (Ba(NO₃)₂)	Good Mix	125μm	DA	50	7.5	50	7.5 T
	Bad Mix *	125μm	DB	50	7.5	50	7.5 T

*Bad Mix = 1 Sieve cycle rather than 7
**Fuel = Lactose (L) or Terephthalic acid (T)

Table 2.2.2 – Wallop Defence Systems Limited Pyrotechnic Compositions

The source and detector distance were placed at -19.94 mm and 24.06 mm, respectively for all samples to ensure that the resolution, 3.045 microns, was the same for each sample. The number of projections used for each sample was 1601. A one hour warm up scan was carried out for each batch of samples scanned prior to the main scans. A secondary filter was used to remove residual noise and detector artefacts.

Oxidiser	KNO_3	$RbNO_3$	$CsNO_3/Ba(NO_3)_2$
Exposure Time (ms)	5500	7000	7000
Voltage (kV)	80	140	140
Current (µA)	87.8	71.7	71.7
Power (W)	7	10	10
Filter	Silicon Dioxide 1.0 mm	Calcium Fluoride 5.0mm	Calcium Fluoride 5.0mm
Secondary Filter	Silicon Dioxide 2.1 mm	Copper plate 1.0 mm	Copper plate 1.0 mm
Scan Duration (hours)	3.2	4.0	4.0

Table 2.2.3 - VERSA 510 CT Settings for Pyrotechnic Mixtures

Once the scans were completed the data were reconstructed using XM Reconstructer and XM Controller 10.7.2936 (Carl Zeiss XRadia, Cambridge, UK). These programs were used to create a txrm file which was viewable in XM 3D Viewer 1.2.6 (Carl Zeiss XRadia, Cambridge, UK) to check the initial quality of the data. The XM Controller converted the txrm file into raw tiff files. These images were visualised in Avizo,[3] ImageJ/Fiji,[4, 5] and VG Studio.[6] VG Studio[6] was used to extract regions of interest within each dataset. ImageJ/Fiji [4, 5] allowed the average grayscales values to be calculated for each slice and for certain areas within each slice. These grayscale values were used to assess the concentration of oxidiser or fuel within a given area/volume within a dataset. Additionally this program was utilised to create binary files for each volume. It was used to separate connected particles. This program was also used to determine the number of particles per slice for each dataset. Avizo[3] was used to gather information on the number of particles within a given volume. Full details of the tools utilised and how they were applied can be found in Appendix A1.

2.3   TESSELLATION & STATISTICAL TOOLS

A tessellation tool was developed for specific use on powder mixtures. The project entitled, 'Online powder mixing technology and mixture characterisation' involved applying CT to various powder mixtures to encompass materials which had the same shape but different densities, different shapes and same density, and different shapes and different densities.[7] Focus quickly gathered on the most ideal set of materials, same shape + different density. The particles for both materials were spherical and therefore they were more ideal to work with. A full description of this work can be found in Appendix A1.

A Matlab code was developed, with help from a project student, Jordan Chant, and Dr. Richard Boardman, and Dr. Anna Scott from the Muvis Team at the University of Southampton, which created a list of particles, their positions (based on their centroids) in 2D and 3D space, and calculated the distances between near neighbours.[7] It outputs values associated with particle area, cell area, local area fraction, number of near-neighbours, nearest neighbour distance and the mean near-neighbour distance. These values are output in a csv (comma separated values) file, whilst additional data is also provided in graphs and slice images. The values in the csv file are defined as follows:

- Particle area – number of pixels making up one particle
- Cell area – number of pixels making up the cell assigned to one particle
- Local Area Fraction – the particle area divided by the cell area
- Number of near neighbours – the number of nearest neighbours calculated from the Delaunay triangulation
- Nearest neighbour – the shortest near neighbour distance*
- Mean near neighbour – the average near neighbour distance*

*measured in pixels - values are arbitrary as they vary depending on the image resolution

The statistical tool applied to the powder mixtures was the co-efficient of variance (CoV). This tool was used in order to assess the homogeneity of the mixtures.

2.4   CO-CRYSTALLISATIONS

In contrast to explosives, pyrotechnics are traditionally mixtures of various materials namely a fuel, an oxidiser, and optionally a binder, colouring agent, and propellant *etc*. The design of energetic co-crystals up until now has been defined by a very narrow range of functional groups, such as the weakly interacting nitro groups. These are much less robust in terms of crystal engineering when compared to their hydrogen bonded counterparts in the pharmaceutical industry.[8,9] This work focuses on creating pyrotechnic co-crystals by incorporating both fuel and oxidiser components within a single crystalline lattice. [10]

2.4.1   STARTING MATERIALS

The first fuel candidate material selected was β-cyclodextrin. This compound was ideal as a first choice; there was little need to consider molecular complimentarity owing to the configuration of its void spaces. The configuration indicated that the compound would demonstrate shape complimentarity with sodium nitrate (the oxidiser), although in an atypical manner – one would normally consider that molecules of similar shape would co-crystallise more readily.[11] In contrast, cyclodextrins work by encapsulating materials. This represents a complete change in design philosophy as normal co-crystallisation rules would not necessarily be followed. The intention was for the compound to encapsulate sodium nitrate, however the experiments attempted yielded starting material.

Our strategy changed to look at other fuels already used by the pyrotechnic industry which could couple with other oxidisers. In searching for a fuel, a potential oxidiser was found, a fluorinated terephthalic acid. Fluorine is the main oxidiser in the well-known MTV pyrotechnic reaction and therefore this material was put forward for further investigation.[12] The fuels (bases) selected were N-containing heterocycles as it is well known that fuels with higher nitrogen content are more beneficial. N-rich materials possess high heats of formation, high propulsive power, high specific impulse, high flame temperatures, and also result in only or mostly gaseous products (smokeless

combustion). [13] The crystal structures for the starting materials can be obtained from the Cambridge Structural Database (CSD)[14] where available.

2.4.1.1   ACIDS
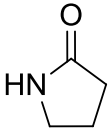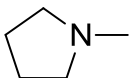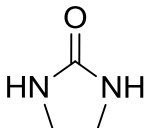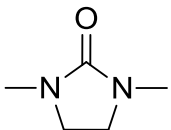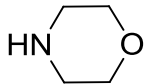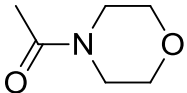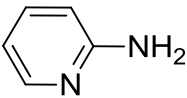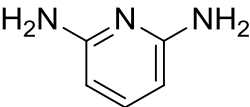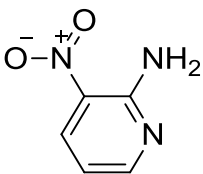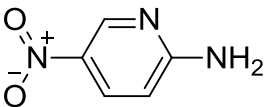
Tetrafluoroterephthalic acid (H$_2$fBDC) was chosen as a potential oxidiser as it was analogous to a fuel already used by the pyrotechnic industry, terephthalic acid (H$_2$BDC). Wang *et al.* have utilised this material in combination with various aza compounds to see whether this compound could be as useful as a supramolecular construct as its non-fluorinated equivalent. Their work focused on coupling this material with various N-heterocycles, known for their energetic properties.[15, 16] A similar approach has been followed here, using other N-heterocycles (fuels) with the various forms of this fluorinated diacid (oxidiser); tetrafluoroterephthalic acid, tetrafluoroisophthalic acid, and tetrafluorophthalic acid.
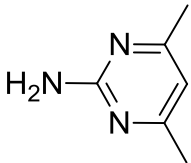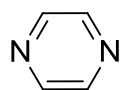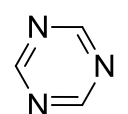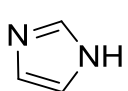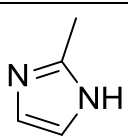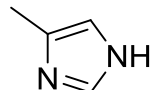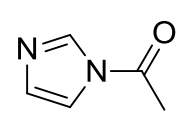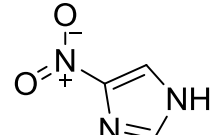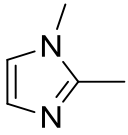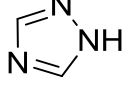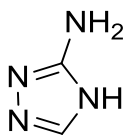
2.4.1.2   BASES

A range of structures were selected which can be broadly split into four groups: nitrogen containing saturated heterocycles, nitrogen-containing heterocycles (six-membered rings), N-heterocyclic azoles, and dye materials. All of the compounds chosen are detailed along with some of their properties in Table 2.4.1.

These materials were selected to see the effect of increasing the nitrogen content within various N-containing heterocycles. Nitrogen was incorporated into the compounds in either of two ways: 1) it was already included once or several times within a 5 or a 6-membered ring, 2) nitrogen was substituted onto the rings using both amine groups and nitro groups.

The inclusion of various functional groups on different positions on the rings was a particular point of interest because it was believed to contribute to the formation of binary compounds.

N-Heterocycle	Abbre-viation	Molecular Structure	MW	Melting Point/°C	pKa1	pKa2
2-Pyrrolidone	Pyr		85.11	25	16.62	0.06
N-Methylpyrrolidine	MPyri		85.15	-	10.55	-
2-Imidazolidone	Idn		86.09	129-132	18.39	14.58
1,3-Dimethyl-2-imidazolidone	DMIdn		114.15	7.5	-0.65	-2.84
Morpholine	Mo		87.12	-7-(-5)	8.97	-
N-Acetylmorpholine	AMo		129.16	14	-0.72	-
2-Aminopyridine	NPy		94.11	54-58	6.67	-7.60
2,6-Diaminopyridine	DNPy		109.13	117-122	6.13	0.96
3-Nitro-2-pyridinamine	3NONPy		139.11	163-165	2.40	-12.42
5-Nitro-2-pyridinamine	5NONPy		139.11	186-188	2.82	-11.94

The first group (rows 1–6) is labeled **N- containing saturated heterocycles**. The second group (rows 7–10) is labeled **N-containing heterocycles (6 membered rings)**.

	4,6-Dimethyl-2-pyrimidinamine	DMNPym		123.16	151-153	5.03	-
	Pyrazine	Az		80.09	50-56	1.22	-5.90
	s-triazine	Tri		81.08	77-83	2.07	-
N-heterocyclic azoles	Imidazole	Im		68.08	88-91	13.89	7.18
	2-Methylimidazole	2MI		82.10	142-143	14.44	8.15
	4-Methylimidazole	4MI		82.10	44-47	14.83	7.68
	1-Acetylimidazole	1AI		110.11	99-105	3.60	-
	4-Nitroimidazole	NOI		113.07	303	8.31	0.49
	1,2-Dimethylimidazole	DMI		96.13	37-39	7.76	-
	1,2,4-triazole	Tro		69.07	119-121	10.49	2.70
	3Amino-1,2,4-triazole	3NTro		84.08	150-153	11.14	4.43
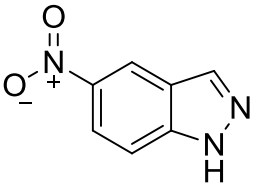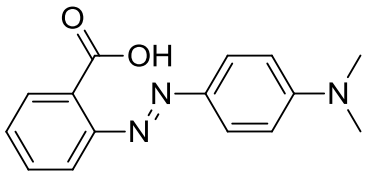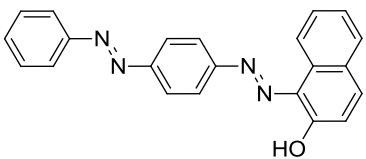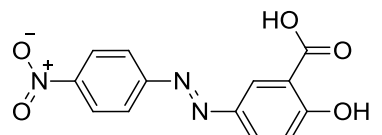
5-Nitroindazole	5NOIn		163.13	204-208	11.71	-0.81
Methyl Red	MR		269.30	179-182	3.66	3.28
Sudan III	S3		352.39	199	13.45	-
Mordant Orange 1	MO1		287.23	>300	11.89	2.85

(Left margin label spanning Dyes rows: **Dyes**)

Table 2.4.1– List of N-heterocycles and their properties(pKa values from ACD/I-Lab[17])

2.4.1.3   BINARY COMPOUNDS OF ACID-BASE COMBINATIONS FROM CSD

The CSD[14] was searched using Conquest version no. 1.16 to find binary compounds containing both the diacid and base starting materials used in this study. The search did not allow the inclusion of any metals. The important features of these structures will be discussed in the subsequent results sections; the CSD reference code is given for each of the structures obtained from the literature.

2.4.1.4   POSSIBLE HYDROGEN BONDING SYNTHONS

Etter developed general rules which predicted hydrogen bond formation; *1) all good donors and acceptors are used in hydrogen bonding, 2) six-membered ring intramolecular bonds usually form in preference to intermolecular hydrogen bonds, and 3) the best proton donors and acceptors remaining after hydrogen bond formation form intermolecular hydrogen bonds to one another.*[18, 19] Leiserowitz and Nader extensively discussed the packing arrangements of primary amides and dicarboxylic acids. They noted that there were three main hydrogen bonding motifs observed.[20] They found that the formation of homosynthons only resulted when the size of R was small *e.g.*

formamide:oxalic acid co-crystal. As the R group is increased in size heterosynthons form. They appear to have no shape or size restriction and as such the acid-amide synthon tends to be favoured over the acid-acid and the amide-amide synthons.[21] Co-crystallisations combining both acid and amide components are therefore more likely to result in co-crystals rather than pure substances.
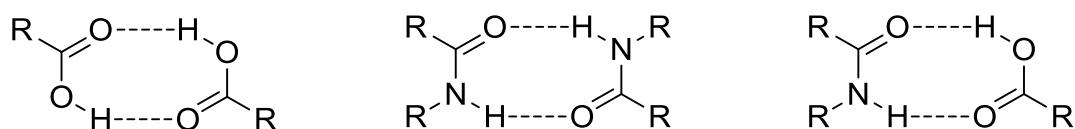
Figure 2.4.1 - Various acid and amide homo-and heterosynthons

Various hydrogen bonding synthons which form as a result of combining numerous N-containing heterocycles with perfluorinated diacids will be discussed within Chapter 4. The main hydrogen bonds which arose included; O-H⋯O, N-H⋯O, O-H⋯N, and N-H⋯N. Diacid starting materials most commonly form catameric chains. These chains were observed within the numerous products which resulted from co-crystallisations.

2.4.2   CO-CRYSTALLISATION METHODS

A number of co-crystallisation techniques were investigated which included co-crystallisation from solution and hot-stage microscopy. The latter was dismissed as the diacids are known to sublime where the N-heterocycles melt.

2.4.2.1   CO-CRYSTALLISATION FROM SOLUTION

2.4.2.1.1   Solvent Method 1 – Aqueous Solutions (1:1)

Solutions of each acid and base were prepared by adding 0.10 mmol equivalents to 5ml measures of distilled water. Each solution was then stirred for 30 mins. In cases where starting material was still present after 30 mins, gentle heating was applied to the solution in effort to dissolve the remaining starting material. Each of the acid solutions were combined with each of the base solutions and then stirred together for 10 mins before setting them aside in 50 ml beakers covered with pierced parafilm. The solutions were left to slowly evaporate and periodically inspected to check for any crystal formation.

2.4.2.1.2   Solvent Method 2 – Methanol Solutions

The same procedure for the aqueous solutions was used, however, distilled water was replaced by methanol as the solvent of choice. Instead of being combined in a 50 ml beaker each single component solution was combined in a plastic petri dish and swirled for a few seconds and then left to evaporate.

2.5   MOF/COORDINATION POLYMER SYNTHESIS

An alternative approach to co-crystallisation to incorporate multiple components within a single crystalline lattice is by synthesising MOFs. By incorporating a fuel and an oxidiser into a framework the variables within the mixture are reduced allowing for more consistency in terms of the pyrotechnics performance. The structural reinforcement provided by these frameworks additionally can help stabilise energetic materials. At present, this has been the main focus of a number of energetic material groups. [22-25] Our research uses materials already utilised by the pyrotechnic industry to make MOFireworks. Numerous linkers and metal centres were investigated to build up a structural family to correlate structure with pyrotechnic function (*e.g.* changing burn colour; Sr = red, Ba = green).

2.5.1   STARTING MATERIALS

2.5.1.1   METAL NODES (OXIDISERS)
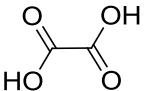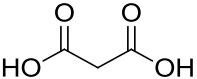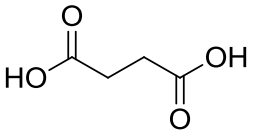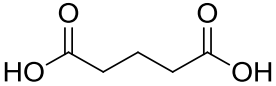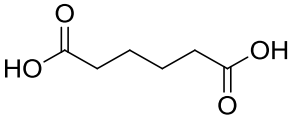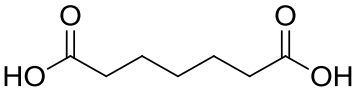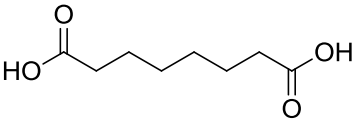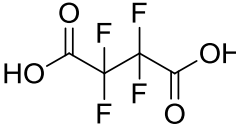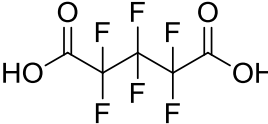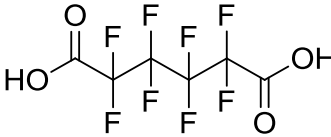
Alkali metal nitrates (Na, K, Rb, and Cs) and alkaline earth metals nitrates (Ca, Sr, and Ba) were chosen for the following reasons: 1) nitrates are less sensitive to ignition compared to chlorates/perchlorates, 2) their burn colour changes on going down both groups (group 1: yellow to purple, group 2: red to green).

2.5.1.2   ORGANIC LINKERS (FUELS)

The diacids chosen were selected initially as they are known to act as bridges between metal nodes. The acids chosen are listed in Table 2.5.1 together with some of their properties; diacids were chosen in order to assess the effect they had on MOF formation and the MOF dimensionality (1D, 2D, 3D).

The addition of a carbon atom to each acid increases the hydrophobicity [26, 27] and flexibility of the compound enabling the effects of these properties on the formation of MOFs and their crystal structures to be noted. The inclusion of the fluorinated alkane diacids, hydroxyl acid, alkene acids, aromatic acids, and fluorinated aromatic acids further extends the spectrum of compounds assessed and allows further interactions to

occur between the molecules. The importance of these interactions will be highlighted by the different crystal structures that form.

	Diacid	Abbre-viation	Molecular Structure	MW	Melting Point/°C	pKa1	pKa2
Alkane Diacids	Oxalic Acid. (dihydrate)	OxA		90.03	189	1.38	4.28
	Malonic Acid	MnA		104.06	132-135	2.92	5.61
	Succinic Acid	ScA		118.09	184-186	4.24	5.52
	Glutaric Acid	GlA		132.11	95-98	4.33	5.27
	Adipic Acid	AdA		146.16	151-154	4.39	5.13
	Pimelic Acid	PmA		160.17	103-105	4.43	5.07
	Suberic Acid	SbA		174.19	140-144	4.46	5.08
Fluorinated Alkane Diacids	Tetrafluoro-succinic Acid	fScA		190.05	115	-1.03	0.25
	Hexafluoro-glutaric Acid	fGlA		240.06	92-97	0.23	0.96
	Octafluoro-adipic Acid	fAdA		290.06	132-134	0.22	0.87
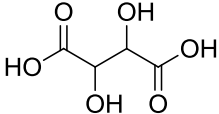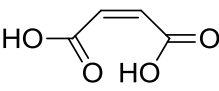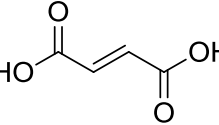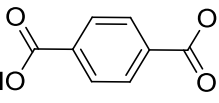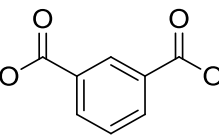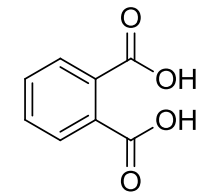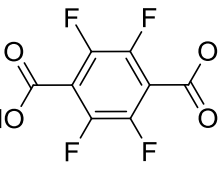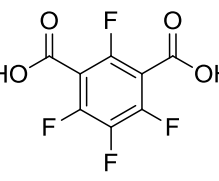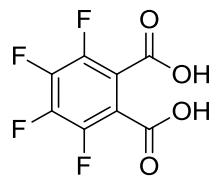
Hydroxy Diacids	L-Tartaric Acid	LTA		150.09	170-172	3.07	4.35
Alkene Diacids	Maleic Acid	MeA		116.07	137-140	2.39	5.34
	Fumaric Acid	FmA		116.07	298-300	3.15	5.34
Aromatic Diacids	Terephthalic Acid	BDC		166.13	300	3.49	4.50
	Isophthalic Acid	isoBDC		166.13	344-348	3.53	4.60
	Phthalic Acid	altBDC		166.13	210-211	2.95	5.40
Fluoroniated Diacids	Tetrafluoroterephthalic Acid	fBDC		238.09	275-277	0.95	1.96
	Tetrafluoroisophthalic Acid	isofBDC		238.09	212-214	1.27	2.34
	Tetrafluorophthalic Acid	altfBDC		238.09	149-156	1.28	3.73

Table 2.5.1 – List of diacids and their properties(pKa values from ACD/I-Lab[17])

As can been seen from Table 2.5.1, the melting point of the alkane diacids alternates with even and odd carbon chain length. Thalladi *et al.*[28] shed light on the reasons behind this noted variation. They noticed that the densities for the odd diacids with 5 carbons or more are relatively higher than that of the even acids. They attributed the melting point behaviour to 'geometry allowed or geometry forbidden of an offset packing with a non-twist molecular conformation'. Even diacids chains have offset chains within the stacks which help to reduce the repulsion between the carboxyl dimers of the adjacent chains. They position themselves in an energetically favourable, non-twisted conformation with the carboxyl groups in the molecular plane whereas odd diacids position themselves in an energetically favourable twisted confirmation. The melting points are further reduced due to the repulsion between the carboxyl groups which destabilises the structures.

On changing the aromatic acids to fluorinated aromatic acids there is a clear decrease in melting point. As the positions of the carboxylates change from positions 1,4 to 1,2 in the fluorinated structures there is a constant decrease as the carboxylates get closer to one another. This trend is not followed by their non-fluorinated equivalents instead there is an increase on moving the carboxylates from the 1,4 positions to the 1,3 positions. This may be due to the corrugated chains creating further stabilisation of the structure.

Each of the diacids has the potential to bind to the metals in a monodentate and/or bidentate fashion. This specific type of binding will be discussed for each combination with relation to how it affects the properties of the resultant MOFs.

2.5.1.3   MOFs PREVIOUSLY KNOWN

Searches were performed using the CSD[14] using Conquest version no. 1.16 to find any MOFs which have already been identified and synthesised which incorporate the starting materials used in this study. The significant features of these structures will be discussed in the results sections; the CSD reference code is given for each of the structures obtained from the literature.

2.5.2   MOF SYNTHESIS METHODS

A number of MOF synthesis techniques were used which included precipitation from solution and liquid assisted grinding (LAG).

2.5.2.1   MOF SYNTHESIS SOLUTION BASED

A thorough search of the MOF literature allowed the identification of several methods to produce the well-known MOF-5[29] which utilises terephthalic acid as the main linker in the framework. Room temperature synthesis approaches were chosen instead of a solvothermal approach given that the products were intended to be pyrotechnic. [29, 30]

2.5.2.1.1   Solvent Method 1 – DMF/TEA

A MOF-5 synthesis method used by Saha *et al.*[29] was imitated. However, instead of zinc (II) nitrate hexahydrate, calcium (II) nitrate/strontium (II) nitrate/barium (II) nitrate was used. There were several combinations trialled using 16 diacid materials (oxalic acid, malonic acid, succinic acid, glutaric acid, adipic acid, pimelic acid, suberic acid, tetrafluorosuccinic acid, hexafluoroglutaric acid, octafluoroadipic acid, L-tartartic acid, maleic acid, fumaric acid, terephthalic acid, isophthalic acid, phthalic acid, tetrafluoroterephthalic acid, tetrafluoroisophthalic acid, and tetrafluorophthalic acid).

4 mmol metal nitrate and 2 mmol of diacid were added to a round bottomed flask which contained 40 ml DMF. The solution was stirred until the starting materials had dissolved entirely in DMF then 2.2 ml TEA (deprotonating agent) was added dropwise. After stirring for 30-45 mins a white product was filtered off using a sinter funnel and washed with 5-10 ml DMF. Filtrated material was immersed in chloroform for 24 hours to exchange the DMF solution and then allowed to evaporate. Group 1 metal nitrate synthesis were added in a 1:1 ratio using 1mmols of each starting material.

2.5.2.1.2   Solvent Method 2 – Methanol/Pyridine

The same starting materials mentioned in solution method 1 were also used here. In addition, group 1 nitrates (sodium, potassium, rubidium, and cesium) were utilised.

0.5 mmol metal nitrate was added to a conical flask containing methanol (Na, Ca nitrates = 10 ml; K, Ru, Sr nitrates = 20 ml; Cs, Ba = 30 ml). The solutions were allowed to stir for 2 hours before the addition of 0.5 mmol diacid. After stirring for an additional 1 hour, 1 ml of pyridine (deprotonating agent) was added dropwise and allowed to stir for 3 hours before being distributed into both glass vials and petri dishes.

2.5.2.2   MOF SYNTHESIS USING LAG

A LAG experiment based on MOF synthesis work carried out by Friscic *et al.* was followed to assess its potential on creating pyrotechnic MOFs.[31] Initial tests involved coupling barium (II) nitrate with either terephthalic acid or tetrafluoroterephthalic acid. Additional trials included combining calcium (II) nitrate with L-tartaric acid, fumaric acid, terephthalic acid, isophthalic acid, tetrafluoroterephthalic acid, and tetrafluorophthalic acid.

Using an Ultra Turrax Tube Drive Control, 1 mmol metal nitrate and 0.5 mmol of diacid were placed into a tube along with two stainless steel balls and 120 µl DMF and set stirring for 1 hour at a rate of 2500 rpm. Calcium (II) nitrate experiments used glass beads instead of stainless steel balls. Chloroform was added to each tube to allow DMF exchange.

2.6   INITIAL PRODUCT ASSESSMENT

The crystallinity of each material was first assessed using optical microscopy. An ideal crystal should be crystalline, single, spherical, free from defects, free from strain and be of the correct size range; 10 - 500 microns. Isotropic crystals always appear black whereas anisotropic crystals show false colours. An anisotropic crystalline sample will extinguish when rotated under polarised light every 90°. Suitable crystals were set aside to be analysed using SXRD.[32]

2.7   SXRD INSTRUMENTATION AND DATA COLLECTION

The SXRD technique was used in order to obtain the molecular and crystal structure of each individual component, co-crystal, and MOF thereby allowing an understanding of each material in terms of the properties they possess.

2.7.1   *CRYSTAL SELECTION AND MOUNTING*

Using an optical microscope an appropriate single crystal/co-crystal was selected. The crystal or co-crystal chosen must not be cracked or twinned. The crystal must be within the correct size range in order for the X-ray beam to bathe the whole crystal in X-rays. If these criteria are not met then systematic errors would arise in the diffraction pattern. The crystal was mounted onto a Mitegen pip using an appropriate medium. The medium was selected based on the needs of the experiment. Crystals run at room temperature were mounted using silicon grease as it was more viscous and minimised any movement attributed to the thermal conditions. Crystals run at cryogenic temperatures were mounted using paraffin or silicon oil as these were less viscous mediums. The minimum amount of medium was used. Once the crystal was mounted the Mitegen pip was transferred to the goniometer head. This secured the pip in place so that it could be adjusted as was needed to ensure the crystal was in the correct position on each rotation axis (ϕ, κ, ω) as the crystal was rotated throughout the diffraction experiment.[32]

2.7.2   *THE DIFFRACTOMETER*

Single-crystal X-ray diffraction data was collected on a Rigaku AFC12 goniometer equipped with an enhanced sensitivity (HG) Saturn 724+18bit CCD detector mounted at the window of an FR−E + Superbright Mo Kα rotating anode generator with optics (HF Varimax 100 μm focus (right-hand port – aka KAT) and VHF Varimax 70 μm focus (left-hand port – aka ROS)).[33] (Figure 2.7.1).
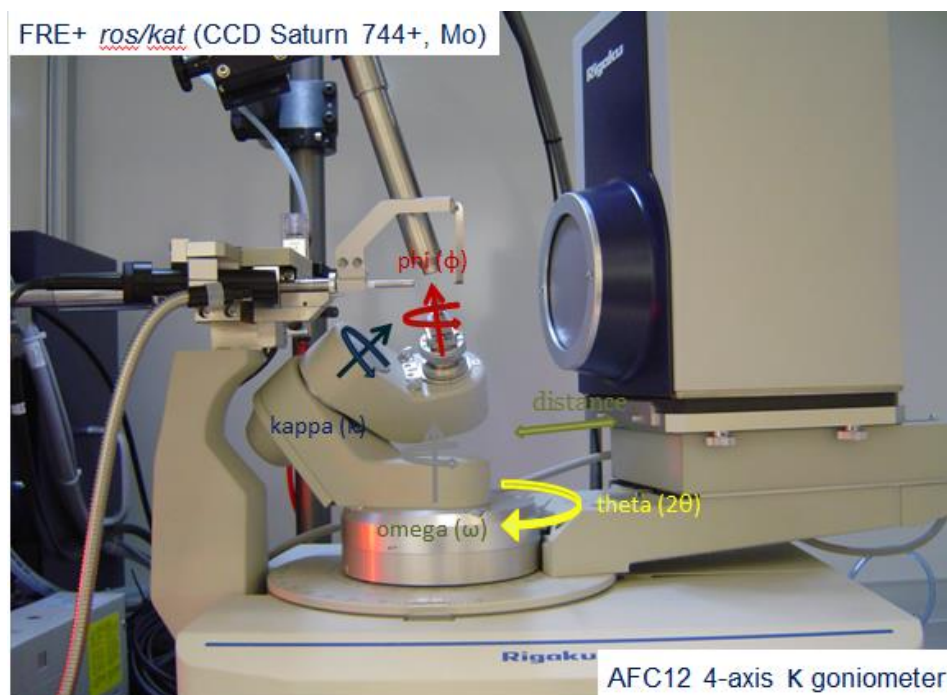
Figure 2.7.1 The diffractometer[32]

KAT/ROS generates molybdenum radiation (wavelength = 0.71073 Å). DOT generates copper radiation (wavelength = 1.54015 Å). An Oxford Cryosystems Cobra cooler uses liquid nitrogen to cool the crystal to 100K to prevent the decomposition of the crystals and to minimise molecular motion. Most crystals tend to be analysed under these conditions. During variable temperature studies of a material these conditions can be altered.

The CCD detector, an area detector, is able to collect various diffracted X-rays simultaneously as it is collecting them over a large area. This helps to reduce the collection time radically from days to hours. X-rays are not directly recorded by the CCD. A phosphor faceplate creates phosphorescence when hit by X-rays. These resultant images are transmitted to a CCD chip via fibre optic cables. The CCD chip is cooled to minimise the intrinsic electronic noise level due to the thermal excitation of electrons. The CCD chip is read by the computer to create the digital image.[34]

2.7.3   DATA COLLECTION

The software package CrystalClear-SM Expert 3.1 b27 was used for cell determination, data collection, data reduction and cell refinement, and for the application of absorption corrections.

Each crystal was first centred to make sure when it was rotated that it would remain in the beam throughout the experiment. Once centred the crystal was measured using the RAX video measuring tool. A short scan of the crystal is carried out to indicate whether the crystal is of sufficient quality based on the diffraction data it produced. This scan only collects a few frames and so it only takes a few minutes to run. If the diffraction data collected were good then the data were indexed to obtain the parameters and orientation of the unit cell. A collection strategy was calculated based on the data associated with the initial images. The scan type and width, exposure time and detector distance could be varied at this point. A typical data collection took one to two hours, however if there were weak reflections or the crystal was extremely small then it would take longer.

Once the scan was complete the reflections were integrated. These were scaled and averaged then the absorption corrections were applied.[35]

The structures were solved using various methods which included the direct methods or Patterson methods approach in SHELXS97[36] or Superflip[37] (charge flipping) program within either the WinGX[38] or Olex2[39] graphical user interface. The initial step involved assembling the residue to see if a sensible structure was output. Slight changes were made when atoms were incorrectly labelled. This would happen in the case of nitrogen atoms or oxygen atoms being mislabelled as carbon atoms. These changes were found by looking at the residual electron density around the location of an incorrectly labelled atom. Bond lengths were ascertained to check that each atom had been correctly labelled. The structures were refined in SHELXL2013.[40] Once the structure had been solved and refined the CIF (crystallographic information framework file) was updated to contain all the necessary information. This included the experimental conditions, atom locations, symmetry operations to name but a few.

2.8   STRUCTURAL ANALYSIS

The molecular assemblies of each of the crystals were viewed using Mercury.[41] This was used to observe the crystal packing structure of each material and to look more closely at the hydrogen bonding motifs of the structure. Isostar, [42] a web application used to assess the probability of the occurrence of interactions between specific functional groups, was used to assess the likelihood of hydrogen bonding between carboxylic acids and various other functional groups within the various N-heterocycles utilised in the co-crystallisation experiments. Mogul[43] was used to provide and validate a list of bond lengths, angles, torsion angle associated with each of the co-crystals and MOFs. It allowed the identification of unusual features when comparing co-crystal and MOF products to similar structures which are present on the CSD. [14]

TOPOS[44] is a crystallographic program used for geometrical and topological analysis of crystal structures. It calculates Voronoi-Dirichlet Polyhedra (VDP) for atoms and molecules in crystal structure. It provides a list of the coordination numbers for each of the atoms within the structures. It also lists the type of interaction *e.g.* covalent, non-covalent. This program was specifically used to look at the MOF structures and their packing. It was used to assess the metal coordination and to calculate the void volumes within the MOF structures when present.

2.9   PXRD INSTRUMENTATION AND DATA COLLECTION

PXRD was used in order to examine the bulk composition of the individual components, co-crystals, MOFs and mixtures of the individual components. It was used as a complimentary technique to SXRD. PXRD can be used to identify the unit cell associated with a sample and this can be compared with SXRD results. SXRD results can be used to simulate powder patterns and these can be compared to actual powder patterns collected from a sample. PXRD will assist in showing when a single crystal is selected if it is representative of the bulk composition. It was also used in cases where SXRD analysis was not possible for a crystalline sample where a suitable single crystal had not formed in order to attempt to identify the product.

The Bruker C2 diffractometer (which combines a 1.6 kW (40 kV, 40 mA) Cu sealed tube D8 generator equipped with a single Goebel mirror (0.5 mm collimator), a xyz stage, and a 2D Hi-Star multiwire detector) was used to observe the powder diffraction patterns created by a number of materials including alpha lactose and a selection of dye materials. These samples were analysed prior to being recrystallized. Each sample was crushed on a glass slide to create a relatively even and flat surface so that better results would be obtained. The diffraction pattern was collected over a 2theta range of 5-41° and recorded over 10 minutes for each sample using the GADDS software.[45]

The Rigaku Miniflex benchtop XRD system (which uses a 600W (40 kV, 15 mA) Cu (Kα1/Kα2) X-ray source and a Ni Kβ filter (detector side) with a NaI scintillator and a high speed silicon strip detector) was used to analyse numerous MOF products. The basic glass sample holders were used to mount samples. The scans were collected over a 2theta range of 5-60° at 1°/min. Each collection took 55 mins using the MiniFlex Guidance, PDXL2 Version 2.1.3.4.

The Bruker D2 Phaser benchtop XRD system (which uses a (30 kV, 10 mA) Cu (Kα1/Kα2) radiation source and a Ni Kβ filter (detector side), additional beam optics and settings: primary and secondary axial Soller slits (2.5°), fixed 0.6 mm divergence slit, 1 mm anti-scatter-screen, detector: 1D LYNXEYE with a 5° window) was used to analyse numerous co-crystal and MOF products. The samples were collected using a Si low background sample holder (20 mm x 0.5 mm sample cavity) to minimise background noise. The scans were collected over a 2theta range of 5-60° at 1sec/step with 1097 steps in total. Each scan took 20 mins using DIFFRAC.SUITE COMMANDER software.[46]

The Rigaku SmartLab 5-Axis X-ray diffractometer (equipped with an in-plane arm and a 9 kW (45 kV, 200 mA) Cu rotating anode generator, HR optics, an X-ray mirror, a secondary monochromator and a 1D detector) was used to analyse the group 2 fluorinated diacid MOFs. Two modes were trialled for collection of the powder patterns. Capillary mode, used to minimise the effects of preferred orientation, was used however this mode was only acceptable for calcium and strontium structures as barium was too strongly absorbing in transmission mode. Reflection mode was trialled next where the

samples were mounted in the default sample holder (the same sample holder used for the Miniflex). The Bragg-Brentano method in reflection mode was used as this provided the cleanest powder diffraction patterns for these samples. The Bragg-Brentano (BB) CBO optics was used in place of the parallel beam (PB) optics. A 0.5 degree in-plane parallel slit analyser (PSA) and a 0.5 degree in-plane parallel slit collimator (PSC) were used (C=incident, A=receiving). A Kβ filter was applied. The scans were collected over 5-60° 2theta range at a rate of 0.2 °/min using the SmartLab Guidance software. [47]

The data analyses were performed using the computer program EVA 16.0 (Copyright © Bruker-AXS 1996-2010).[48] The pattern matches were performed using this software linked to the ICDD (International Centre for Diffraction Data) PDF (Powder Diffraction File)[14 49] database 2001. These powder patterns were from both measured materials and calculated powder patterns derived from SXRD data. Each of the patterns were saved and then compared to search for a possible match. The co-crystal and MOF patterns were also compared to the patterns of the individual starting materials which had been previously collected. The PXRD data was also compared to the SXRD data collected for both co-crystal and MOF products.

2.10   THERMAL ANALYSIS METHODS

Differential Scanning Calorimetry (DSC) was used to study the thermal profiles of each individual component, co-crystal, MOF, and mixture of individual components in order to assess their melting behaviour, purity, and kinetics of decomposition *etc*. [50-53]

Each sample was analysed using a Mettler-Toledo instrument, model DSC821e, equipped with a liquid nitrogen low temperature attachment and a TSO801RO Universal sample robot. 2 – 14 mg of each sample were placed in 40 µl aluminium dishes. Lids were secured onto the dishes to enclose each sample. These dishes were then transferred to the rotating disk on the DSC equipment so that the robot could collect each sample from an allocated position when it was required. The heating program set up using STARe software covered a temperature range from 5˚C to 600˚C scanning at a rate of 10˚C/min. Further scans were carried out for a few of the materials

in order to confirm the original DSC results. A smaller range of temperatures were also scanned to look more closely at particular areas of interest.

DSC curves associated with possible co-crystals (A...B) and MOFs (A-B) were compared to DSC curves of the individual components (A, B) and mixtures of the components (A + B) to see how they differed.

The burn rate behaviour of the co-crystals and MOF products were carried out in a fume cupboard. Small amounts (few mgs) of product were placed within 40µl aluminium pans. The pans were transferred onto a metal mesh which was positioned on top of a tripod stand to allow heating to be applied from underneath using a blowtorch. If a composition failed to ignite from heat alone it was briefly set alight from above. Photographs of these burn tests were taken by Sharif Ahmed using a Canon EOS 7D camera with an exposure time of 1/400 sec and an ISO speed of ISO-640.

Burn rate and burn behaviour assessments were carried out on site at Wallop Defence Systems Limited with the help of Simon East (Production Technician), Les Gibbons (Senior Pyrotechnic Chemist), Ali Batchem (Radiometry) and Robin Hughes (Photography) using the following instrumentation:

- Photron Fastcam APX-RS 250K High Speed Video Serial No.141722286 (1000 fps)
- Video camera Panasonic HC-V100EBK Serial No.J2TYHO1324 (25 fps),
- Visible (eye response) Photometer L970 and Trans-impedance Amplifier L2098 manufactured by WDS calibrated using an NPL Tungsten filament lamp (specific range covered 460-660 nm),
- 4 channel radiometer L2042 manufactured by DSTL calibrated using a blackbody furnace L1012 (temperature checked using a calibrated optical thermometer) LAND Systems L2003.(Ch 1: 3.8-4.7 µm (CO_2), Ch 2: 1.9-2.3 µm (H_2O), Ch 3: 3.33-4.73 µm (MTV), Ch 4: 3.95-5.11 µm (CO_2))
- Metax IR spectroradiometer (1.8 - 14 µm) (SR5000 made by CI Systems)

These burn test results were compared to the small scale laboratory burn tests to see how physically mixed pyrotechnics compositions compared to chemically bound pyrotechnic ingredients.

Reference

1.   NikonMetrologyNV Nikon Metrology - X-ray and CT Inspection. http://www.nikonmetrology.com/en_EU/Products/X-ray-and-CT-Inspection/ (accessed 02/08/2012).

2.   http://muvis.soton.ac.uk/wiki/index.php5/About_the_CT_scanners.

3.   VisualizationSciencesGroup Avizo® Fire. http://www.vsg3d.com/avizo/fire (accessed 04/09/2012).

4.   Schneider, C. A.; Rasband, W. S.; Eliceiri, K. W., *Nat. Meth.* **2012,** *9* (7), 671-675.

5.   Schindelin, J.; Arganda-Carreras, I.; Frise, E.; Kaynig, V.; Longair, M.; Pietzsch, T.; Preibisch, S.; Rueden, C.; Saalfeld, S.; Schmid, B.; Tinevez, J.-Y.; White, D. J.; Hartenstein, V.; Eliceiri, K.; Tomancak, P.; Cardona, A., *Nat. Meth.* **2012,** *9* (7), 676-682.

6.   VolumeGraphicsGmbH VG Studio Max. http://www.volumegraphics.com/en/products/vgstudio-max.html (accessed 04/09/2012).

7.   Chant, J.; Blair, L. H.; Li, Z.; Yang, S.; Coles, S. J.; Sinclair, I., Online Mixing Technology and Mixture Characterisation - Summer Internship Project. 2012.

8.   Millar, D. I. A.; Maynard-Casely, H. E.; Allan, D. R.; Cumming, A. S.; Lennie, A. R.; Mackay, A. J.; Oswald, I. D. H.; Tang, C. C.; Pulham, C. R., *CrystEngComm* **2012,** *14* (10), 3742-3749.

9.   Landenberger, K. B.; Bolton, O.; Matzger, A. J., *Angew. Chem. Int. Ed.* **2013,** *52* (25), 6468-6471.

10.   Leggoe, J. W., *Scripta Mater.* **2005,** *53* (11), 1263-1268.

11.   Fabian. L, *Cryst. Growth Des.* **2009,** *9* (3), 1436-1443.

12.   Koch, E.-C., *Propellants Explos. Pyrotech.* **2002,** *27* (5), 262-266.

13.   Steinhauser, G.; Klapötke, T. M., *Angew. Chem. Int. Ed.* **2008,** *47* (18), 3330-3347.

14.   Allen, F. H., *Acta Crystallogr.* **2002,** *B58*, 380-388.

15.   Wang, L.; Zhao, L.; Hu, Y.; Wang, W.; Chen, R.; Yang, Y., *CrystEngComm* **2013,** *15* (15), 2835-2852.

16.   Wang, L.; Hu, Y.; Wang, W.; Liu, F.; Huang, K., *CrystEngComm* **2014**.

17.   *ACD/I-Lab*, Advanced Chemistry Development, Inc.: Toronto, ON, Canada, 2014.

18.   Etter, M. C., *Acc. Chem. Res.* **1990,** *23* (4), 120-126.

19.   Etter, M. C.; MacDonald, J. C.; Bernstein, J., *Acta Crystallogr. Sect. B* **1990,** *46* (2), 256-262.

20.   Leiserowitz, L.; Nader, F., *Acta Crystallogr. Sect. B* **1977,** *33* (9), 2719-2733.

21.   Moragues-Bartolome, A. M.; Jones, W.; Cruz-Cabeza, A. J., *CrystEngComm* **2012,** *14* (7), 2552-2559.

22.   Bushuyev, O. S.; Arguelles, F. A.; Brown, P.; Weeks, B. L.; Hope-Weeks, L. J., *Eur. J. Inorg. Chem.* **2011,** *2011* (29), 4622-4625.

23.   Bushuyev, O. S.; Brown, P.; Maiti, A.; Gee, R. H.; Peterson, G. R.; Weeks, B. L.; Hope-Weeks, L. J., *J. Am. Chem. Soc.* **2011,** *134* (3), 1422-1425.

24.   Bushuyev, O. S.; Peterson, G. R.; Brown, P.; Maiti, A.; Gee, R. H.; Weeks, B. L.; Hope-Weeks, L. J., *Chem. Eur. J.* **2013,** *19* (5), 1706-1711.

25.   Li, S.; Wang, Y.; Qi, C.; Zhao, X.; Zhang, J.; Zhang, S.; Pang, S., *Angew. Chem. Int. Ed.* **2013,** *52* (52), 14031-14035.

26.   Smith, R.; Tanford, C., *Proceedings of the National Academy of Sciences* **1973,** *70* (2), 289-293.

27.   Zhang, G.; Tao, L.; Zhang, G., *Chin. J. Chem. Eng.* **2008,** *16* (4), 631-634.

28.   Thalladi, V. R.; Nüsse, M.; Boese, R., *J. Am. Chem. Soc.* **2000,** *122* (38), 9227-9236.

29.   Saha, D.; Deng, S.; Yang, Z., *J. Porous Mater.* **2009,** *16* (2), 141-149.

30.   Clegg, W.; Russo, L., *Cryst. Growth Des.* **2009,** *9* (2), 1158-1163.

31.   Friščić, T.; Reid, D. G.; Halasz, I.; Stein, R. S.; Dinnebier, R. E.; Duer, M. J., *Angew. Chem. Int. Ed.* **2010,** *49* (4), 712-715.

32.   Light, M., CHEM6024 - Theory & Practice of Single Crystal X-ray Structure Determination. University of Southampton: 2011.

33.   NCS UK National Crystallography Service - Diffractometers. http://www.ncs.ac.uk/equipment/diffractometers/ (accessed 15/10/2012).

34.   Blake, A. J.; Clegg, W.; Cole, J. M.; Evans, J. S. O.; Main, P.; Parsons, S.; Watkin, D. J., *Crystal structure analysis: principles and practice*. 2nd ed.; Oxford University Press: 2009; Vol. 13, p 387.

35.   Rigaku, CrystalClear - Software User's Guide for the Rigaku R-AXIS, and Mercury and Jupiter CCD Automated X-ray Imaging Systems. 1.3 ed.; Rigaku MSC/ SSI: 2001.

36.   Sheldrick, G. M., SHELX97. Programs for crystal structure analysis. 1997.

37.   Palatinus, L.; Chapuis, G., *J. Appl. Crystallogr.* **2007,** *40* (4), 786-790.

38.   Farrugia, L. J., *J. Appl. Cryst.* **1999,** *32*, 837-838.

39.   Dolomanov, O. V.; Bourhis, L. J.; Gildea, R. J.; Howard, J. A. K.; Puschmann, H., *J. Appl. Crystallogr.* **2009,** *42* (2), 339-341.

40.   Sheldrick, G., *Acta Crystallogr. Sect. A* **2008,** *64* (1), 112-122.

41.   Macrae, C. F.; Edgington, P. R.; McCabe, P.; Pidcock, E.; Shields, G. P.; Taylor, R.; Towler, M.; van de Streek, J., *J. Appl. Crystallogr.* **2006,** *39*, 453-457.

42.   Bruno, I. J.; Cole, J. C.; Lommerse, J. P. M.; Rowland, R. S.; Taylor, R.; Verdonk, M. L., *J. Comput. Aided Mol. Des.* **1997,** *11*, 525-537.

43.   Bruno, I. J.; Cole, J. C.; Kessler, M.; Luo, J.; Motherwell, W. D. S.; Purkis, L. H.; Smith, B. R.; Taylor, R.; Cooper, R. I.; Harris, S. E.; Orpen, A. G., *J. Chem. Inf. Comput. Sci.* **2004,** *44* (6), 2133-2144.

44.   Blatov, V. A.; Shevchenko, A. P.; Serezhkin, V. N., *J. Appl. Crystallogr.* **1999,** *32* (2), 377.

45.   *GADDS: General Area Detector Diffraction System* 4.1.13; Bruker: 2002.

46.   *DIFFRAC.SUITE.COMMANDER*, Bruker-AXS©: 2010-2012.

47.   *SmartLab Guidance* 2.0.2.5; Rigaku Corporation 2005-2013.

48.   Bruker-AXS© *EVA 16.0*, 1996-2010.

49.   Fawcett, T. G.; Kabbekodu, S. N.; Faber, J.; Needham, F.; McClune, F., *Powder Diffr.* **2004,** *19* (1), 20-25.

50.   Lee, J. S.; Hsu, C. K., *Thermochim. Acta* **2001,** *367*, 367-370.

51.   Tuukkanen, I. M.; Brown, S. D.; Charsley, E. L.; Goodall, S. J.; Laye, P. G.; Rooney, J. J.; Griffiths, T. T.; Lemmetyinen, H., *Thermochim. Acta* **2005,** *426* (1-2), 115-121.

52.   Kwon, Y. S.; Gromov, A. A.; Ilyin, A. P.; Popenko, E. M.; Rim, G. H., *Combust. Flame* **2003,** *133* (4), 385-391.

53.   Hill, V. L.; Craig, D. Q. M.; Feely, L. C., *Int. J. Pharm.* **1998,** *161* (1), 95-107.

CHAPTER 3

Results and Discussion (Macroscopic Characterisation)

3.1   INTRODUCTION

Pyrotechnic performance is monitored in several ways; photography, high speed videography, radiography, spectrophotometry *etc*. Specific pyrotechnic properties which are investigated include burn rate (m/s), heat generated, and smoke/light output. Problems arise as pyrotechnic compositions frequently fail to meet their set criteria and it is not understood why. There are possible reasons, *e.g.* too many fines, too much moisture, but in many instances an explanation cannot be found. [1-5] Several factors known to contribute to pyrotechnic performance (for example particle size and oxidiser:fuel ratio) have been investigated to rationalise particular trends. Pourmortazavi *et al.* [6] investigated the influence of the particle size of potassium chlorate in pyrotechnic compositions. The authors discovered that as the particle size decreased the heat of reaction increased whilst the temperature of ignition decreased. Similar work has been done to investigate the effects for other oxidisers (ammonium perchlorate)[3] and fuels (Al, W, and Zr *etc*).[7]

The 'required effect' of a pyrotechnic is also influenced by how well the pyrotechnic ingredients are mixed. The question pertains as to what makes a good mixture. Theoretical work has been carried out to estimate the effect mixing has on the end performance of several binary pyrotechnic systems. Brown *et al.*[8] estimated the number of contact points between oxidiser and fuel particles and related that to performance. Their work demonstrated that increased number of contact points increased the burning rate of the pyrotechnic. However, this was a compound effect as it was tied in with an increase in percentage of fuel used in the composition. Beyond the optimum ratio the contact points fall, along with the burning rate. The optimum fuel to oxidiser ratio was shown to vary between each binary mixture assessed. The model implemented assumed that both oxidiser and fuel particles were uniform and spherical, however, in the real situation that is far from the case, as shall be shown below.

Our strategy was to visualise particle distributions within pyrotechnic compositions and apply basic tessellation and statistical tools with the intention of being able to mathematically and objectively describe a mix, and then correlate these results with pyrotechnic performance. Based on the position of each particle in relation to each other we should be able to assess their homogeneities. Analysing compositions in this way may also allow for impurity identification, if present at the length relevant scales. In addition to assessing mixture homogeneity, we wish to shed more light on other known contributing factors to performance, *e.g.* particle size, oxidiser selection, and oxidiser to fuel ratio.   In this chapter we discuss the results associated with macroscopic characterisation of various pyrotechnic compositions listed in Table 3.4.1. The results describing the homogeneity of the compositions will be correlated against other known factors which contribute to pyrotechnic performance. Additionally the statistical results derived from the application of tessellation tools to various pyrotechnic composition CT datasets will be presented and discussed throughout this chapter.

This chapter is divided into eight parts:

3.2 Preliminary Scans.

3.3 Mixture Characterisation

3.4 X-Ray Tomography results for each pyrotechnic composition.

3.5 Pyrotechnic Scan Analysis.

3.6 Results from Tessellation Tool and Statistical Tool Application.

3.7 Burn Results of Compositions.

3.8 Summary of Factors Influencing Pyrotechnic Performance

3.9 Conclusion

3.2   PRELIMINARY SCANS

Initial scans were carried out to assess the potential of using CT with pyrotechnic compositions. The first scan carried out was on a 'dummy mix' as it contained only fuel components (lactose/potato starch, chalk, and methyl red).
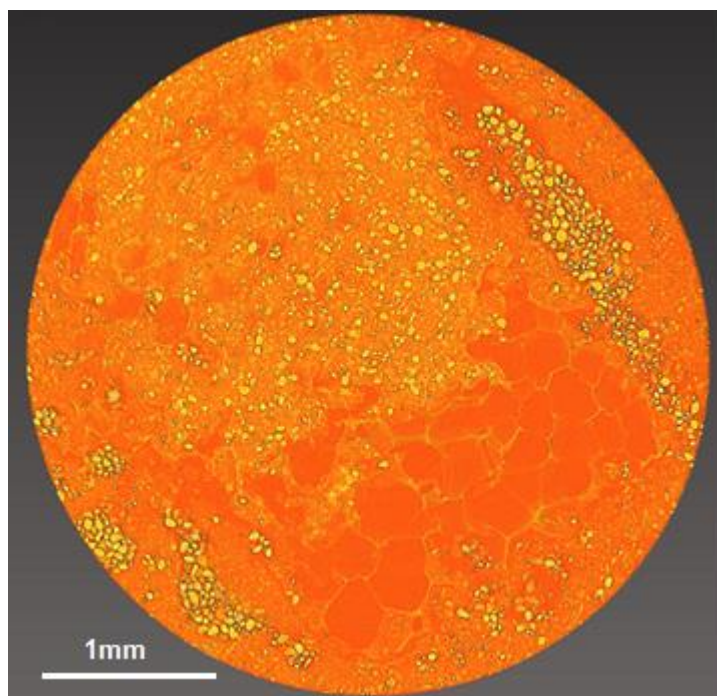
Figure 3.2.1 - Example CT image of 'dummy' mixture

False colour has been used, with lighter colours indicating materials with higher attenuation coefficients. The 'dummy' mixture scans looked relatively similar: There was little obvious change even when an extra component (methyl red) was added. Methyl red and lactose/potato starch could not be differentiated, consistent with their similar densities/expected attenuation coefficients (methyl red = 0.79 g/cm^3, lactose = 1.53 g/cm^3, potato starch = 1.55 g/cm^3). Chalk particles were very clear in comparison (2.50 g/cm^3). The foam used to separate each sample was also observed. To thoroughly assess the CT route of analysis, data for an actual pyrotechnic composition was of course necessary. As such, $NaNO_3$ and lactose was sieve mixed and CT scanned. These results showed good contrast between the fuel and oxidiser ingredients.
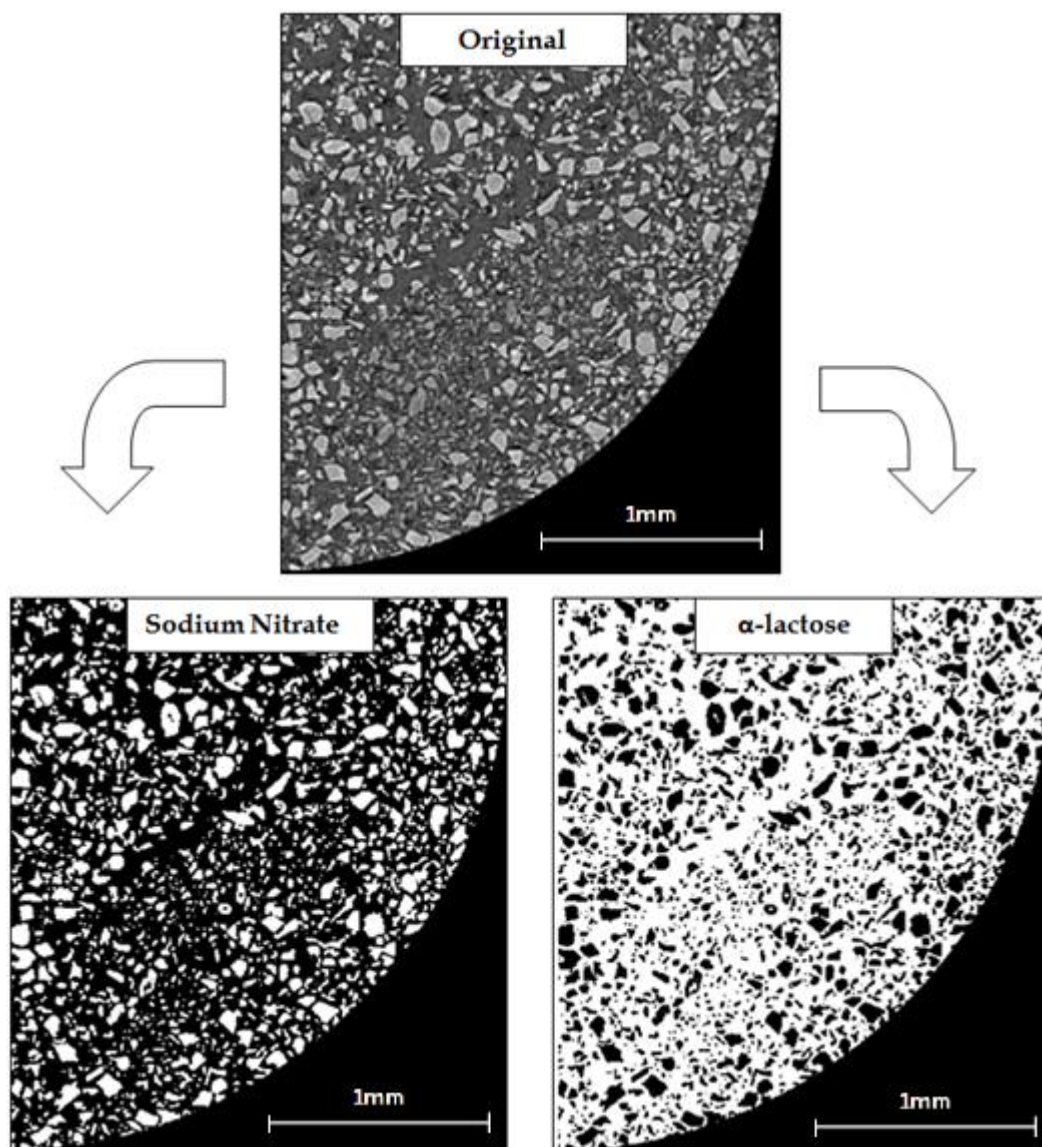
Figure 3.2.2 - Example slice of original CT reconstruction of NaNO₃ and lactose mixture (top) sodium nitrate only (bottom left) lactose only (bottom right)

Figure 3.2.2 highlights the irregularity of $NaNO_3$ particles. It has already been shown from the 'dummy' mixture results that α-lactose monohydrate agglomerates. This image helps to highlight the point as it is difficult to observe individual particles associated with this component given the extent of agglomeration/clumping. A batch scan was set up to investigate the impact of mixing cycles on the homogeneity of a mixture using the same composition ($NaNO_3$ and lactose). The results are highlighted in Figure 3.2.3.
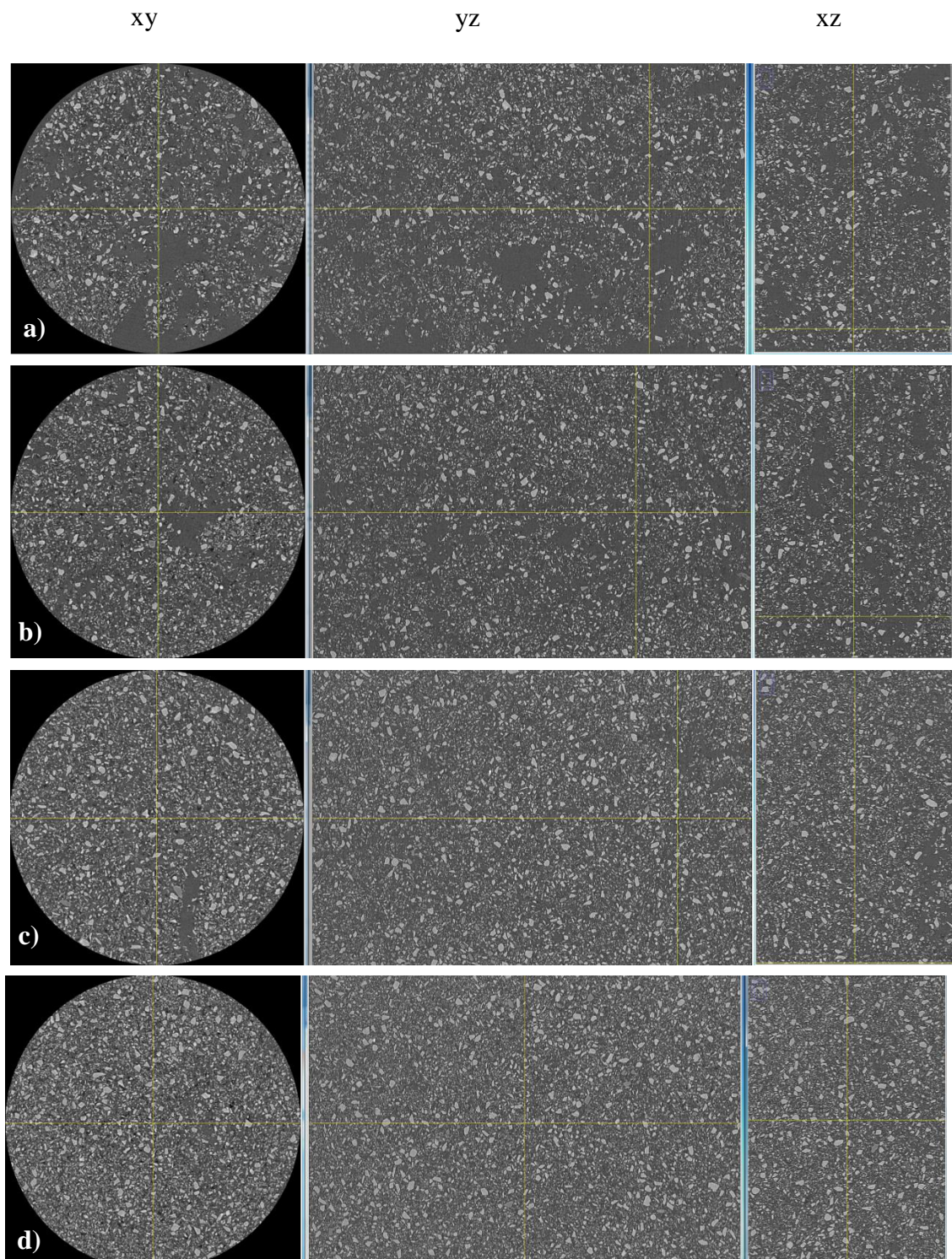
Figure 3.2.3 - NaNO$_3$ and lactose compositions, number of sieve mixing cycles: a) 4, b) 5, c) 6 d) 7

By visual inspection, the degree of homogeneity appears to improve with increasing number of mixing cycles, see Figure 3.2.3. Four mixing cycles would appear

insufficient to ensure uniform mixing as there are still fuel agglomerates present within the composition. The same can be said for five mixing cycles but to a lesser degree. Moving onto the composition resulting from the use of six or seven mixing cycles these samples appear to be much more homogeneous, however quantification is clearly of value. To that end the next section describes a means to characterise the mixing quality of mixtures of granular media.

3.3   MIXTURE CHARACTERISATION

The following results are associated with a project entitled, 'Online mixing technology and mixture characterisation' which involved applying CT to various powder mixtures to encompass materials which had the same shape but different densities, different shapes and same density, and different shapes and different densities. Focus was made on the most ideal set of materials, for the same shape and different density (both spheres).[9] Figure 3.3.1 displays the positions of particles in arbitrary space in both 2D and 3D in the form of a Delaunay triangulation. Figure 3.3.2 shows a typical slice image of a powder mixture highlighting the particles of one material (poloxamer) and each cell associated with an individual particle.
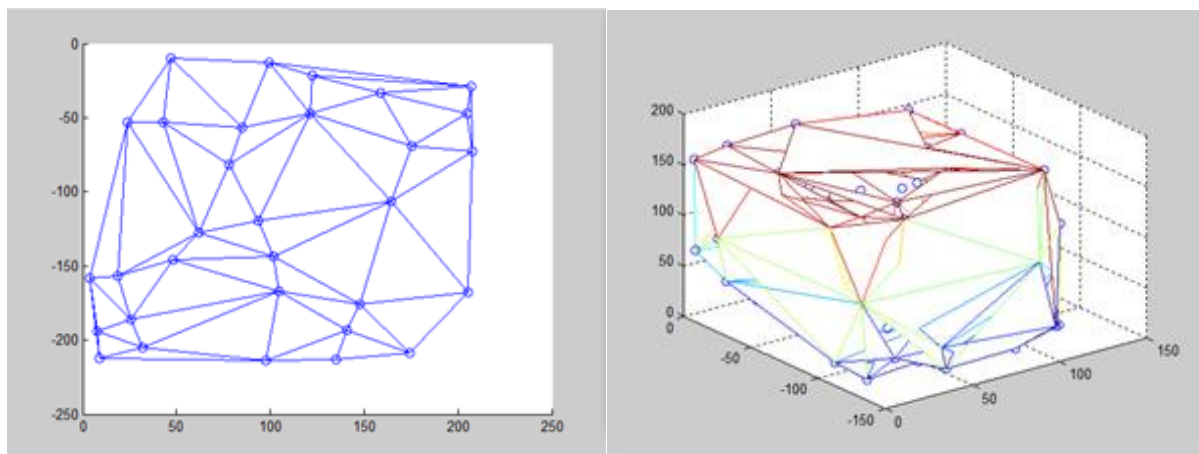
Figure 3.3.1- Poloxamer Dataset Delaunay Triangulation of 2D (left) and 3D data set (right)
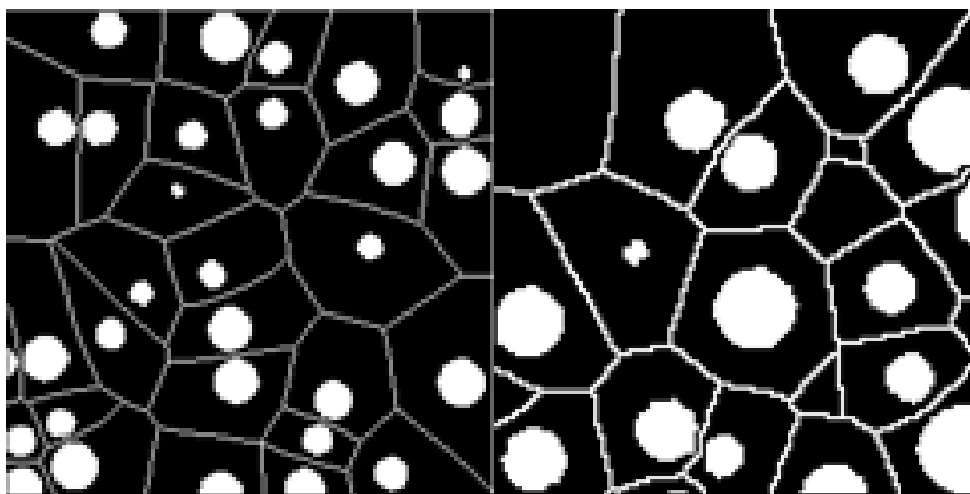
Figure 3.3.2 - Poloxamer Dataset Combination of Particles and Cells for 2D (left) and 3D data set (right)

Figure 3.3.2 also shows local tessellation of the distribution with Table 3.3.1 tabulating the variety of first order parameters in terms of coefficient of variance (CoV) values. CoV is a normalized measure of the variation (standard deviation divided by the mean). Data are associated with various 2D slices of a data set for binary images of poloxamer with dimensions of 2.89 mm x 2.89 mm x 2.74 mm (3D volume dataset trialled = 1.73 mm x1.73 mm x 2.18 mm). Each voxel measured 13.2 μm.

	CoV				
Slice no.	Cell area	Local area fraction	Number of near-neighbours	Nearest-neighbour distance	Mean near-neighbour distance
1	0.442	0.498	0.207	0.316	0.247
52	0.447	0.400	0.181	0.313	0.242
104	0.492	0.467	0.223	0.291	0.224
154	0.345	0.394	0.156	0.233	0.239
208	0.370	0.487	0.181	0.406	0.384

Table 3.3.1- Coefficient of Variance Results for Poloxamer
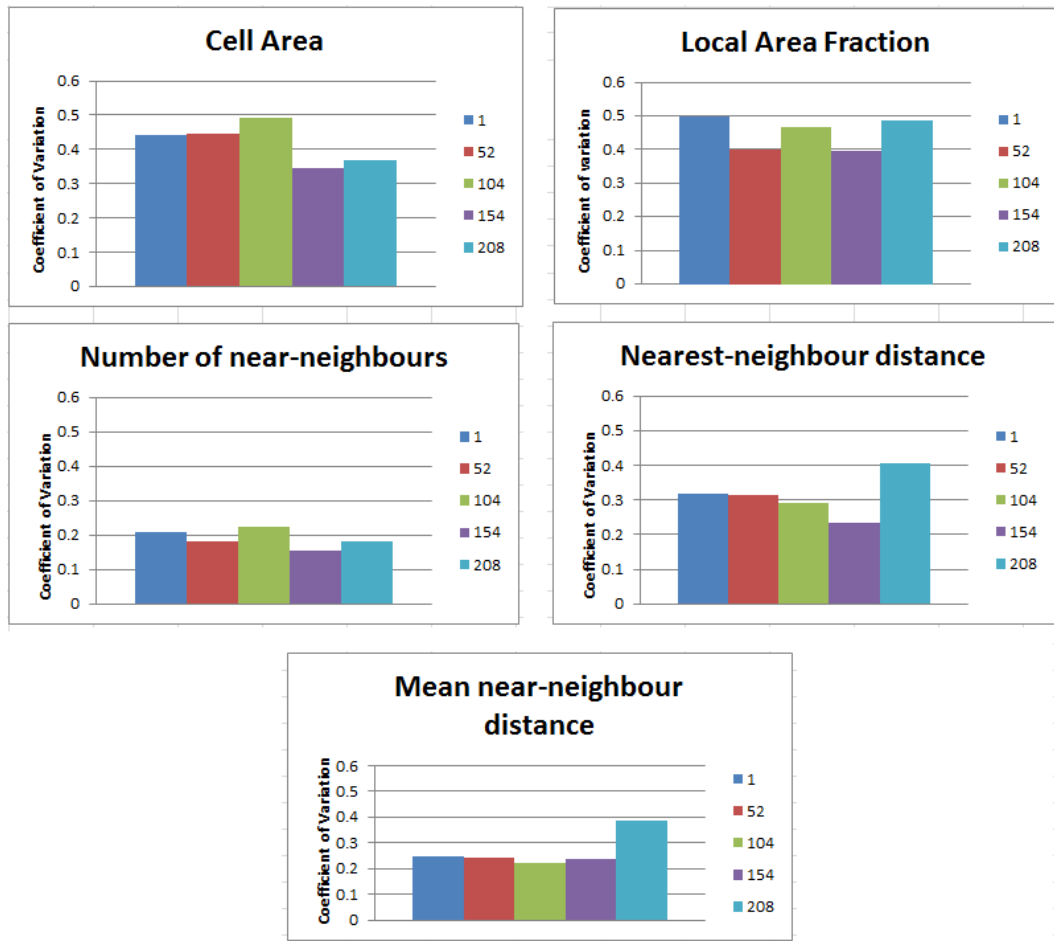
Figure 3.3.3 - Coefficient of Variance Results for Poloxamer

Based on an extensive distribution simulation exercise carried out by Yang *et al.*[10] the CoV of the mean-near neighbours distance was found to be a powerful tool to identify homogeneity. Homogenous particle distributions in their study were characterised by a CoV mean-near neighbour distance value of 0.36 (± 0.02). Truly regular distributions would have a CoV of 0 (*i.e.* a grid has no variation in separation distances), a heavily clustered distribution will have some very high and some very low separation distances (high CoV), a random distribution falls somewhere between the two. The CoV value for the poloxamer dataset was 0.27 (±0.07). As such, the CoV value was lower than the characteristic stochastic distribution value. This was to be expected as these images were from a mixture of particles rather than from an individual material. Particles of the different phases may be expected to force each other apart, imposing a degree of regularity (reducing the CoV). Slices 1(bottom slice), 52, 104 (middle slice), 154 CoV

values were relatively similar, however slice 208 (top slice) showed a noticeable increase and acted to offset the mean near neighbour CoV value. This difference was likely to be due to possible movement which occurred during sample transportation: if the sample was vibrated in anyway the particles at the top of the sample would move first.
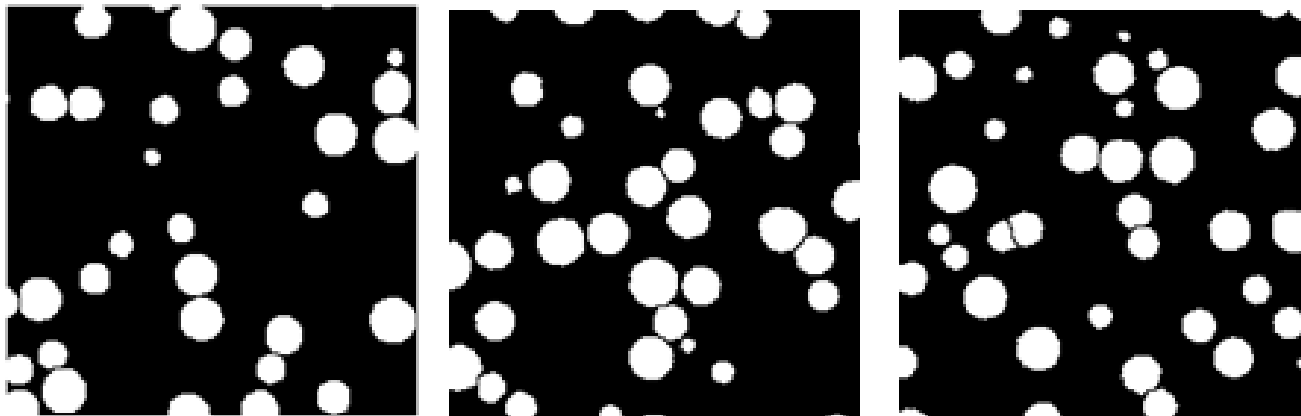
Figure 3.3.4 - Slices 001, 052, 104 of poloxamer volume dataset
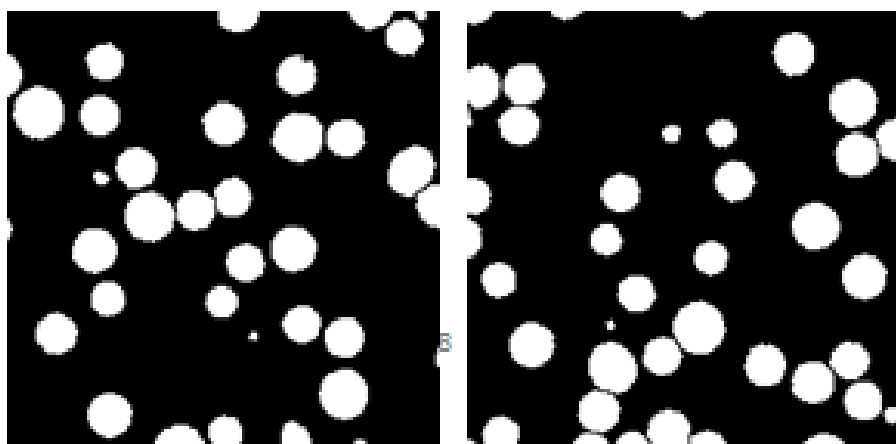
Figure 3.3.5 – Slices 154 and 208(top slice) of poloxamer volume dataset

Slice 208 (top slice) does appear to show a greater degree of clustering in the bottom half of the image in comparison to the other images. These were from only a small section of the data collected and so it is not a true representation of the whole dataset. This tool was used on several of the pyrotechnic compositions. These results shall follow in Section 3.6.

3.4   PYROTECHNIC SCANS

Initial burn tests were carried out to assess the suitability of various compositions which contained lactose and alkali metal nitrates for pyrotechnic applications. The results from these tests were positive.

Figure 3.4.1 - Initial Burn Test Results a) Safety Test $NaNO_3$, b) Safety Test $CsNO_3$, c) Pressed Burn Test $CsNO_3$ and Pressed Burn Test KNO_3

All compositions ignited and burned for a short duration with the exception of $NaNO_3$ containing compositions. They ignited easily when in loose powder form but as soon as they were compressed they would not ignite. It is possible that the burn could not carry through to the rest of the composition due to the lack of air pockets. $NaNO_3$ is also more hygroscopic than the other alkali metal nitrates and it is possible that this was a contributing factor in effect dampening the effect of the pyrotechnic composition. As a loose powder, all compositions burned rapidly as was to be expected given that there was greater surface area exposed for burning. Each gram of composition mimicked that of a mini signal flare burning a bright red colour when in a pressed state. The candela output appeared to be less for the pressed compositions compared to their loose powder forms. The compositions generated a lot of smoke, especially when the oxidiser:fuel ratio was 50:50. Higher ratios generated more heat and less smoke. With these results in mind further compositions which included KNO_3, $RbNO_3$, and $CsNO_3$ were manufactured so they could be CT scanned and quantitatively analysed. These compositions are detailed in Table 3.4.1.

Oxidiser	Ratio	Particle Size	Composition	Oxidiser %	Weight of Oxidiser (g)	Fuel %	Weight of Fuel (g)**
Potassium Nitrate (KNO₃)	1st ratio	38μm	AA	50	7.5	50	7.5 L
		75μm	AB	50	7.5	50	7.5 L
		90μm	AC	50	7.5	50	7.5 L
		125μm	AD	50	7.5	50	7.5 L
		200μm	AE	50	7.5	50	7.5 L
	2nd ratio	38μm	AF	64.1	9.615	35.9	5.385 L
		75μm	AG	64.1	9.615	35.9	5.385 L
		90μm	AH	64.1	9.615	35.9	5.385 L
		125μm	AI	64.1	9.615	35.9	5.385 L
		200μm	AJ	64.1	9.615	35.9	5.385 L
	3rd ratio	38μm	AK	78.1	11.715	21.9	3.285 L
		75μm	AL	78.1	11.715	21.9	3.285 L
		90μm	AM	78.1	11.715	21.9	3.285 L
		125μm	AN	78.1	11.715	21.9	3.285 L
		200μm	AO	78.1	11.715	21.9	3.285 L
	Bad Mix *	125μm	AP	50	7.5	50	7.5 L
Rubidium Nitrate (RbNO₃)	1st ratio	125μm	BA	59.3	8.895	40.7	6.105 L
	2nd ratio	125μm	BB	72.2	10.83	27.8	4.17 L
	3rd ratio	125μm	BC	83.9	12.585	16.1	2.415 L
	Bad Mix *	125μm	BD	59.3	8.895	40.7	6.105 L
Cesium Nitrate (CsNO₃)	1st ratio	38μm	CA	65.8	9.87	34.2	5.13 L
		75μm	CB	65.8	9.87	34.2	5.13 L
		90μm	CC	65.8	9.87	34.2	5.13 L
		125μm	CD	65.8	9.87	34.2	5.13 L
		200μm	CE	65.8	9.87	34.2	5.13 L
	2nd ratio	38μm	CF	77.5	11.625	22.5	3.375 L
		75μm	CG	77.5	11.625	22.5	3.375 L
		90μm	CH	77.5	11.625	22.5	3.375 L
		125μm	CI	77.5	11.625	22.5	3.375 L
		200μm	CJ	77.5	11.625	22.5	3.375 L
	3rd ratio	38μm	CK	87.3	13.095	12.7	1.905 L
		75μm	CL	87.3	13.095	12.7	1.905 L
		90μm	CM	87.3	13.095	12.7	1.905 L
		125μm	CN	87.3	13.095	12.7	1.905 L
		200μm	CO	87.3	13.095	12.7	1.905 L
	Bad Mix *	125μm	CP	65.8	9.87	34.2	5.13 L
Barium Nitrate (Ba(NO₃)₂)	Good Mix	125μm	DA	50	7.5	50	7.5 T
	Bad Mix *	125μm	DB	50	7.5	50	7.5 T

*Bad Mix = 1 Sieve cycle rather than 7
**Fuel = Lactose (L) or Terephthalic acid (T)

Table 3.4.1 - Wallop Defence Systems Limited Pyrotechnic Compositions

The following section describes each of the compositions (AA-DB) based on specific particle features which include: 1) Size Distribution (38-200 μm), 2) Shape Distribution (particles with sharper edges or smoother edges attributed to surface roughness) and 3) Degree of Local Clustering. Examples of each are presented below in Figure 3.4.2. It's significant to note that some systems present greater signal-to-noise and spatial resolution challenges. A reality of laboratory microCT analysis is that X-ray flux is always limited, and scanning campaigns can become unfeasibly long where high signal-to-noise ratios are sought. In this work, a compromise was necessary between scan quality and scan durations, particularly given the numbers of samples involved.
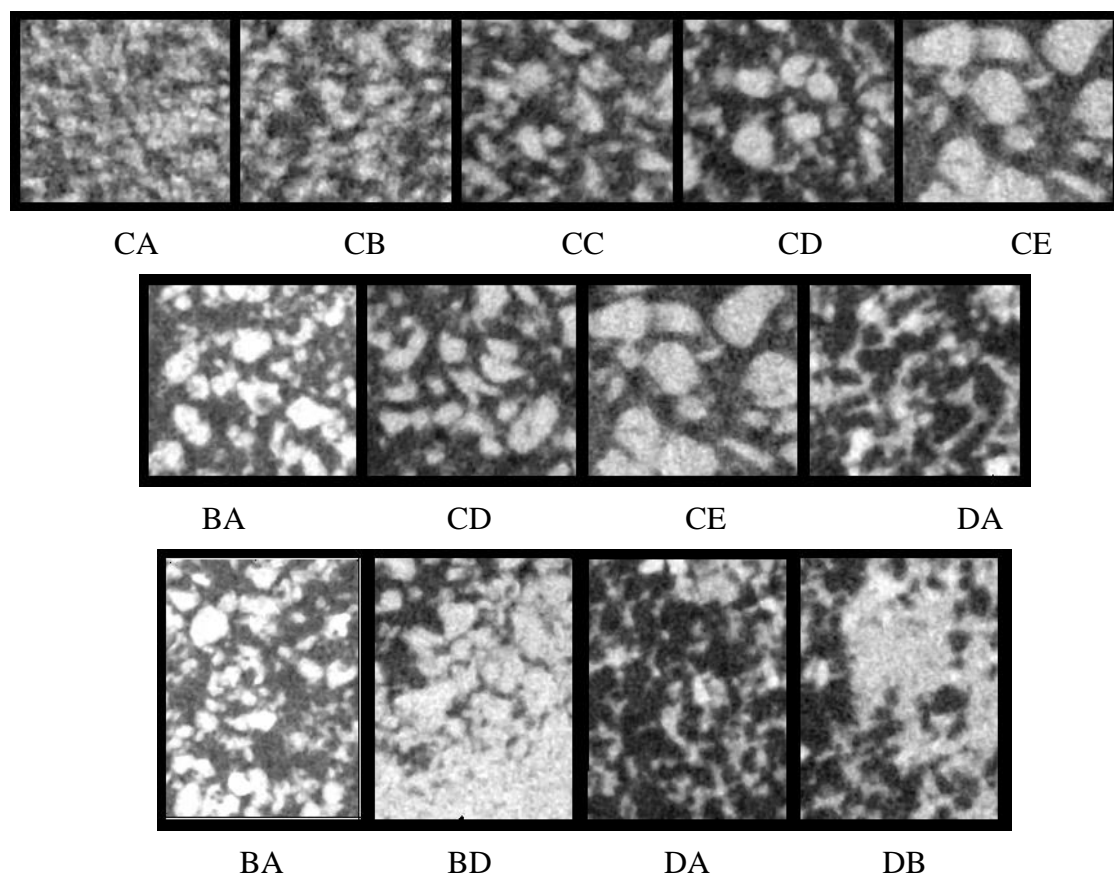
Figure 3.4.2 - CT Scan Characteristic Features for Pyrotechnic Compositions

Figure 3.4.3 - CT Scan Volumes of AA-AE (KNO$_3$ 1st ratio varying particle size)

Figure 3.4.3 shows the variation in particle size from 38 µm - 200 µm for the 1st oxidiser:fuel ratio for compositions containing KNO$_3$. It is clear from these images that the primer positioned at the top of each composition is of similar density which is not surprising as the primer also contains KNO$_3$. Distinct particle shapes start to emerge at ~90 µm and above. By visual inspection, these samples appear to be relatively homogeneous.

Figure 3.4.4 - CT Scan Volumes of AF-AJ (KNO$_3$ 2nd ratio varying particle size)

Figure 3.4.4 shows the variation in particle size from 38 μm - 200 μm for the 2nd oxidiser:fuel ratio for compositions containing KNO$_3$. For the compositions containing particles at the lower end of the particle size range, 38μm and 75μm, it is apparent that there is a loss in contrast. This is expected to have arisen due to the materials in effect plasticising, becoming one material. The density (and hence attenuation) difference is not sufficient to allow the visualisation of distinct particles within the compositions especially for those containing the greatest KNO$_3$ content. The same can be said for the lower ratio and especially for the highest ratio of oxidiser to fuel.
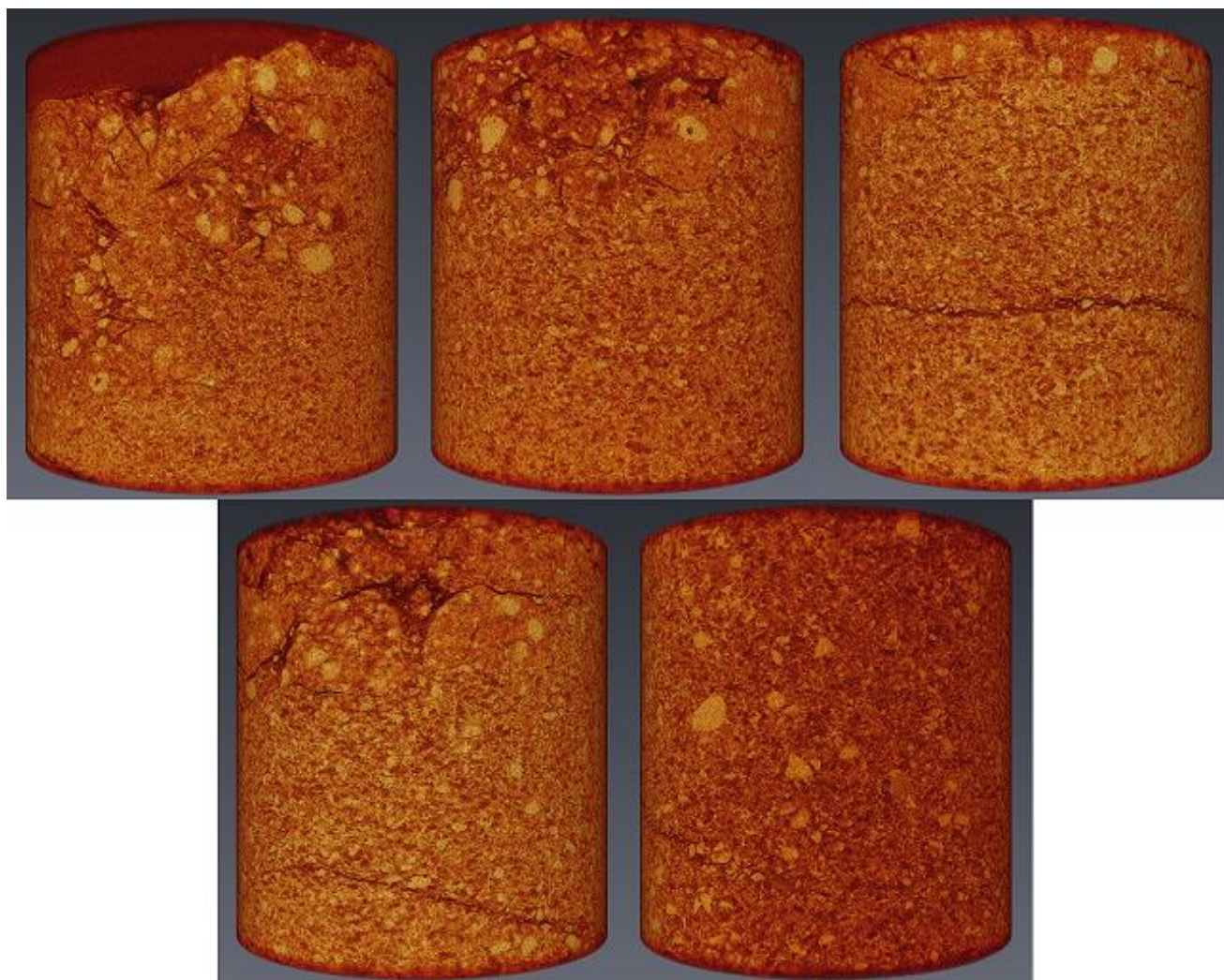
Figure 3.4.5 - CT Scan Volumes of AK-AO (KNO_3 3rd ratio varying particle size)

Figure 3.4.5 shows the variation in particle size from 38 µm - 200 µm for the 3rd oxidiser:fuel ratio for compositions containing KNO_3. It became more difficult to see distinct particles as the oxidiser content was increased. It was possible to the see the compression points left by the die used to press these compositions which was not so apparent in the compositions with a lower oxidiser:fuel ratio. The specific particle shapes are not particularly clear within this series for the reasons previously stated for the compositions composed of lower oxidiser:fuel ratios. Particle edges tend to be obscured when two particles belonging to the same component (*e.g.* oxidiser) are touching. CT (at the chosen resolution) cannot easily visualise the small spaces around touching particles. There are other types of scans which can be carried out, *e.g.* using the University's Zeiss VERSA 510 to attempt to reveal these connections with 'phase contrast' enhancement:

scan times are especially long however and beyond the expectations for this work for this number of materials. There are also post image-processing tools which can be used to separate touching particles. This would be an intensive process for AK-AO compositions as there were so many touching particles.
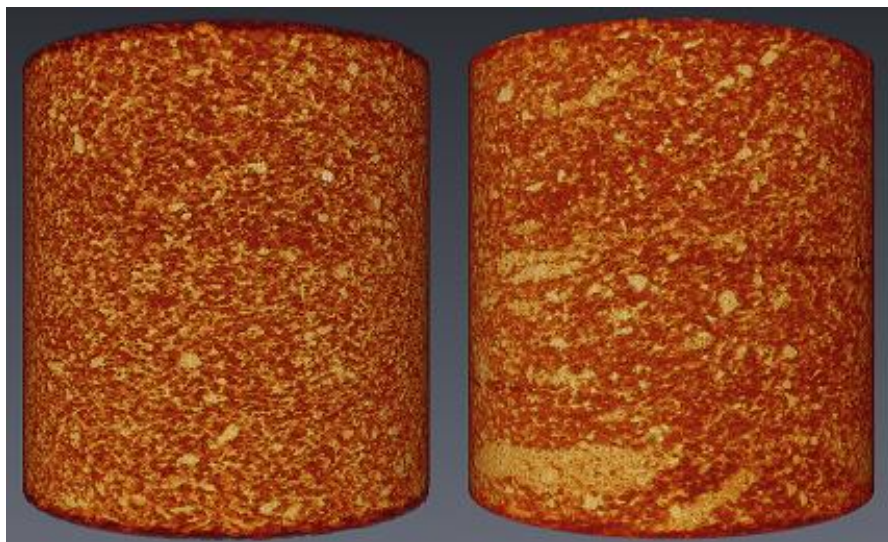
Figure 3.4.6 - CT Scan Volumes of AD vs AP (KNO_3 Good vs Bad Mix (7 vs 1 sieve cycle))

It is clear from the figure above that one sieve cycle is not sufficient to produce a homogeneous composition. Clusters of oxidiser particles can be seen throughout the length of composition AP.
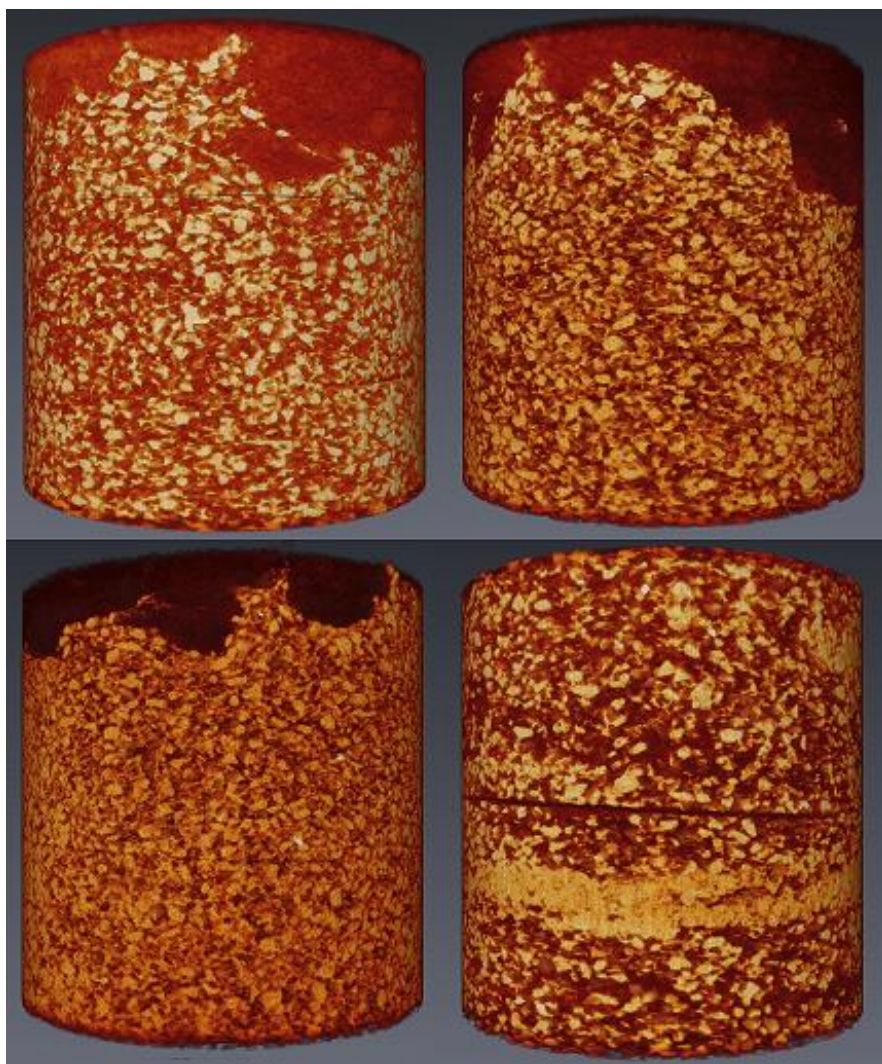
Figure 3.4.7 - CT Scan Volumes of BA-BD (RbNO$_3$ varying ratio (BA-BC), BD Bad Mix (1 sieve cycle))

The density difference is greater for the RbNO$_3$ containing compositions, (RbNO$_3$ = 3.11 g/cm^3). A much better contrast was achieved for these compositions. Similar observations were made for these compositions as were made for the KNO$_3$ compositions: the greater the oxidiser content the more difficult it becomes to see oxidiser particle edges or the lactose channels. It is evident that using one mixing cycle is again not enough to produce a homogeneous mixture. Here we can see a layer of oxidiser particles within BD. A relatively high accelerating voltage and power settings (140 kV, 10 W) were required to penetrate through each composition. The same settings were used for the CsNO$_3$ compositions.
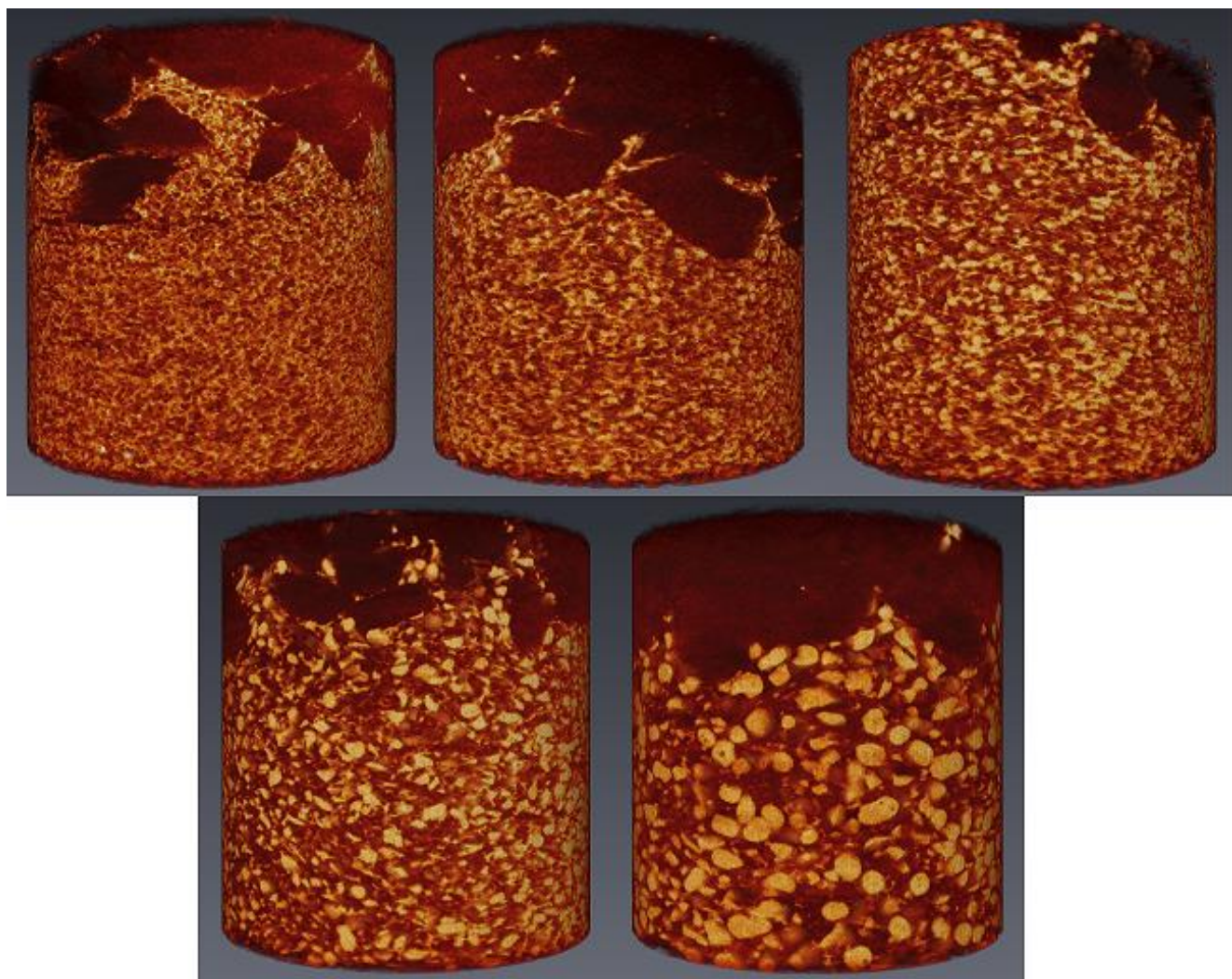
Figure 3.4.8 - CT Scan Volumes of CA-CE (CsNO$_3$ 1st ratio varying particle size)

Figure 3.4.8 shows the variation in particle size from 38 μm - 200 μm for the 1st oxidiser:fuel ratio for compositions containing CsNO$_3$. In comparison to the KNO$_3$ containing compositions, the oxidiser particle shapes and sizes are much clearer. CsNO$_3$ is relatively dense, 3.68 g/cm^3. Larger particles have smoother edges and are more spherical compared to those at lower particle sizes which have been pushed through a smaller sieve, consequently creating ellipsoid shaped particles with sharper edges as they have been broken down.

103
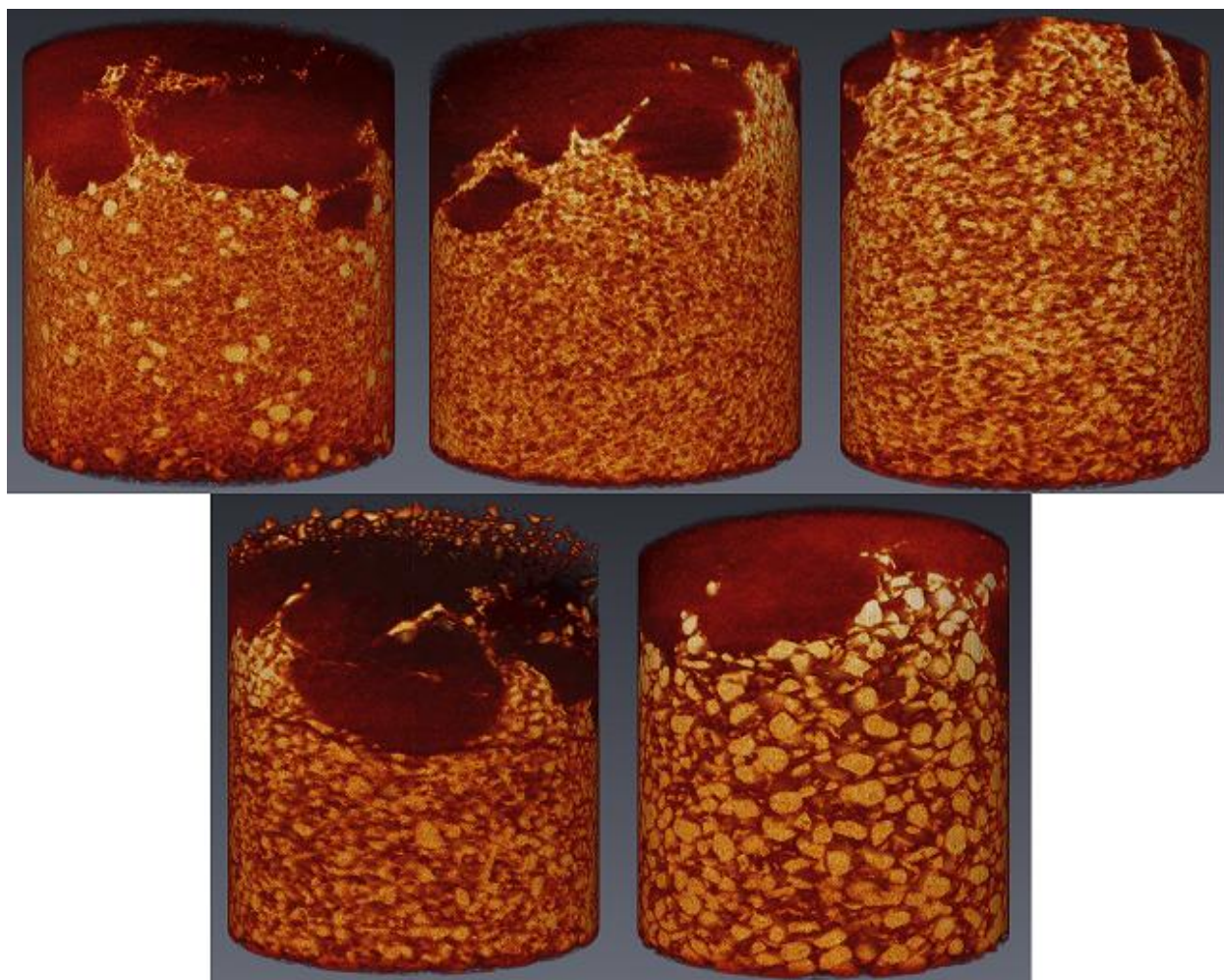
Figure 3.4.9 - CT Scan Volumes of CF-CJ (CsNO$_3$ 2nd ratio varying particle size)

Figure 3.4.9 shows the variation in particle size from 38 μm - 200 μm for the 2nd oxidiser:fuel ratio for compositions containing CsNO$_3$. CF appears to contain much larger particles than the intended 38 μm potentially caused by the removal of compressed residual composition which was scraped off the end of the press die to minimise composition loss during manufacture. The same observations made for CA-CE (CsNO$_3$ 1st ratio) apply to CF-CJ (CsNO$_3$ 2nd ratio).
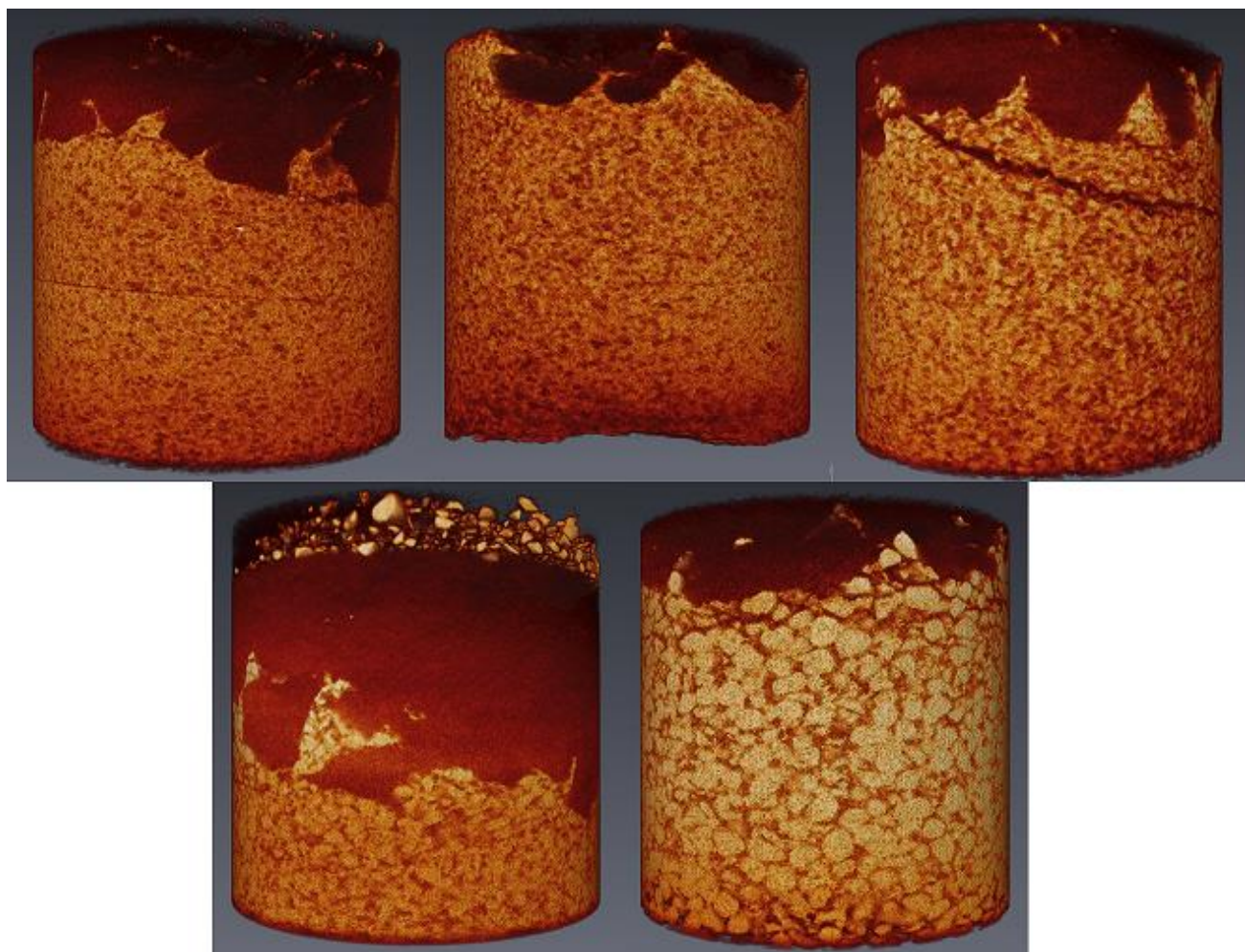
Figure 3.4.10 - CT Scan Volumes of CK-CO (CsNO$_3$ 3rd ratio varying particle size)

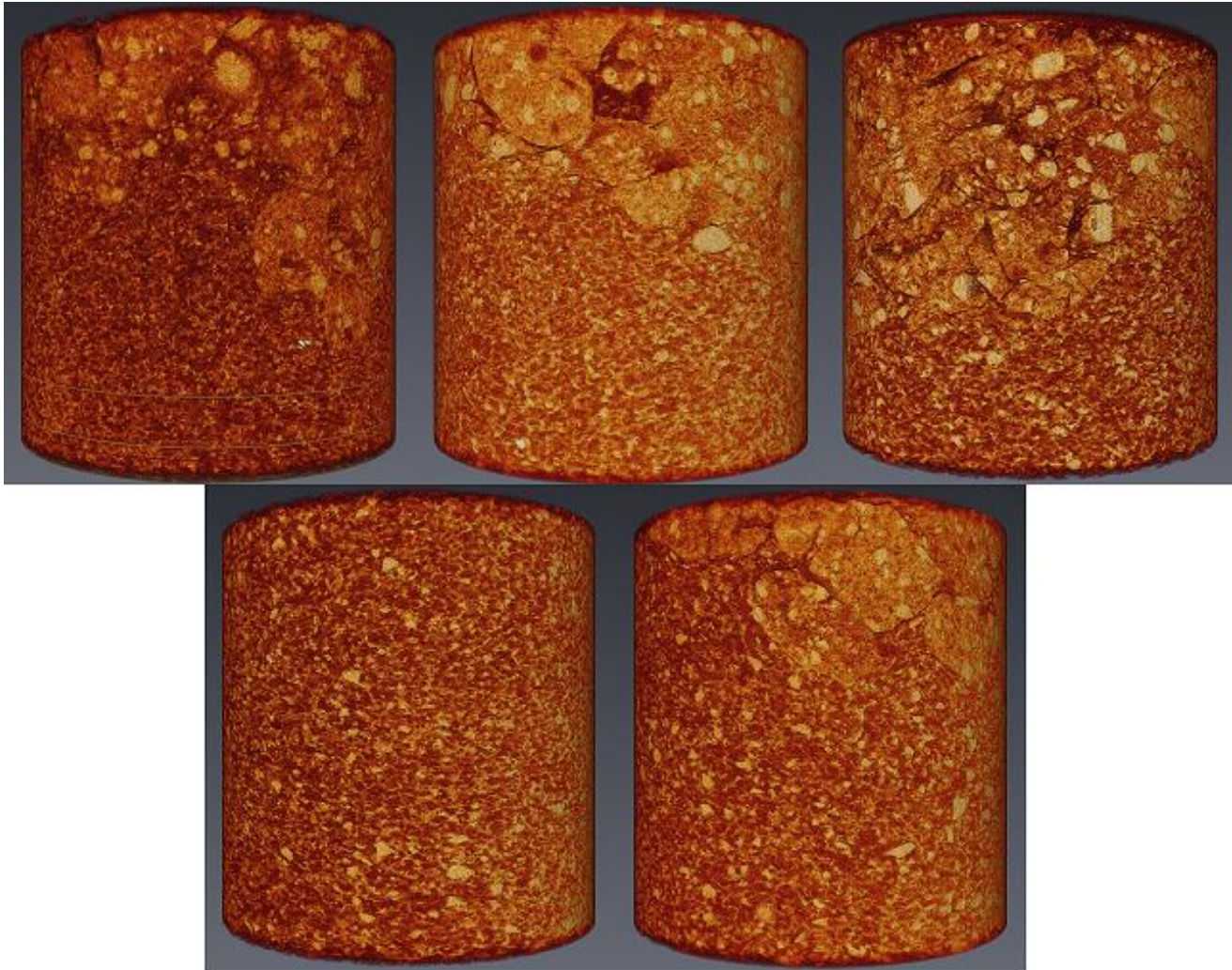Figure 3.4.10 shows the variation in particle size from 38 µm - 200 µm for the 3rd oxidiser:fuel ratio for compositions containing CsNO$_3$. As suggested for both of the other alkaline metal nitrate compositions it is clear that as the oxidiser content is increased, the oxidiser particle edges become harder to detect, especially at the lower end of the particle size range used in this study.
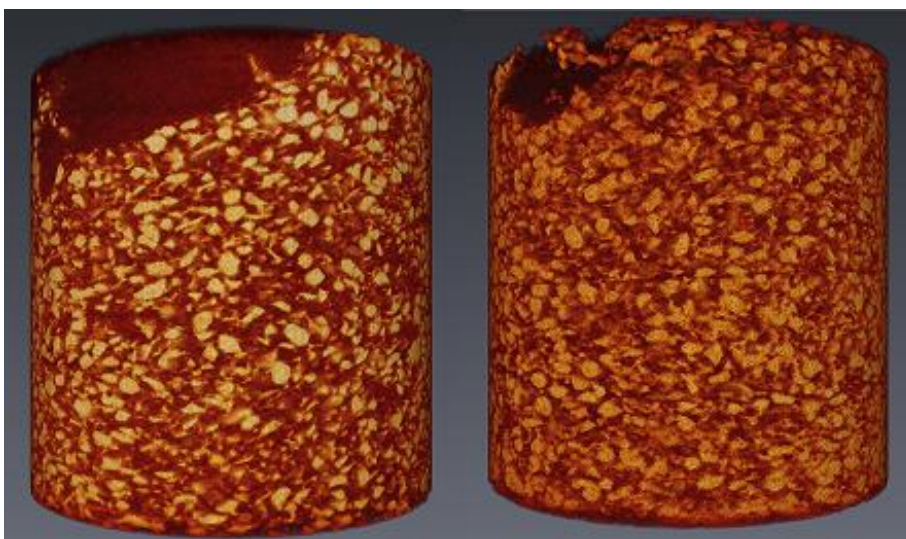
Figure 3.4.11 - CT Scan Volumes of CD vs CP (CsNO$_3$ Good vs Bad Mix (7 vs 1 sieve cycle))

It is not so easy to see from Figure 3.4.11 the vast difference between these CsNO$_3$ compositions as both appear to be well mixed.
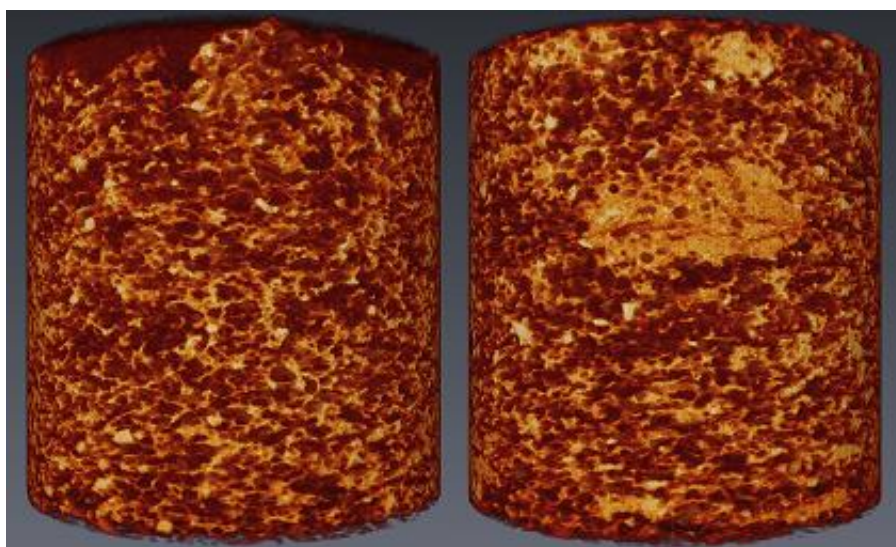
Figure 3.4.12 - CT Scan Volumes of DA-DB(Ba(NO$_3$)$_2$ Good vs Bad Mix (7 vs 1 sieve cycle))

Ba(NO$_3$)$_2$ appears to behave more like the lactose in the other compositions. It is difficult to see discrete particles. The opposite is true for the terephthalic acid particles as they appear as small ellipsoid like particles. These compositions appear to be the inverse of all of the lactose containing compositions. Clustering/inhomogeneity is evident in both mixtures but more so for the 'bad mix'.

In summary, the primer (SFG20) was clearly visible in all compositions except those containing KNO_3. A simple reason for this is that the primer itself is comprised of KNO_3. KNO_3 compositions (AA-AP) were also more difficult to assess because the difference in density/attenuation attributed to each of the components (KNO_3 (2.11 g/cm^3) and lactose (1.53 g/cm^3)) was small making it difficult to isolate each component. As the oxidiser was substituted for a material of higher density ($RbNO_3$ (3.11 g/cm^3) $CsNO_3$ (3.68 g/cm^3)) it became a lot easier to separate out each definitively.

As the oxidiser particle size was reduced, the distinct particle shapes became more difficult to observe and this issue was exacerbated by increasing oxidiser content. Poorly mixed compositions, *i.e.* compositions manufactured using only one sieve cycle, were evident in all cases except one (CP) where local clustering of each component was clearly visible. CP ($CsNO_3$, one sieve cycle) appeared to be homogeneous but this may be due to $CsNO_3$ compositions mixing more readily than the others.

3.5   PYROTECHNIC COMPOSITION ANALYSIS

Having highlighted the CT reconstructed volumes within the previous section it was decided that for simplification we would focus on $RbNO_3$, $CsNO_3$ and $Ba(NO_3)_2$ compositions as here we achieved better contrast between the fuel and oxidisers, as noted above.

Initial assessment of the homogeneity of the compositions can be estimated using grayscale values. For well-defined systems where there is no overlap between the grayscale values associated with each component this can be a fairly simple process. There was a degree of overlap observed between the components here but not severe, so this method was used to better understand the contribution of each ingredient within the composition.

Using a single average grayscale as an area average of attenuation in a given slice/area, in a way that is analogous to the partial volume effect, allows for an efficient estimate of phase distributions within local regions, where normalisation of grayscales has been made for the component phases. The total grayscale range for each dataset was between 0 and 255 as all files were 8 bit. The range of values associated with the fuel component ranged from 10 - 150 and for the oxidiser 151 - 246.
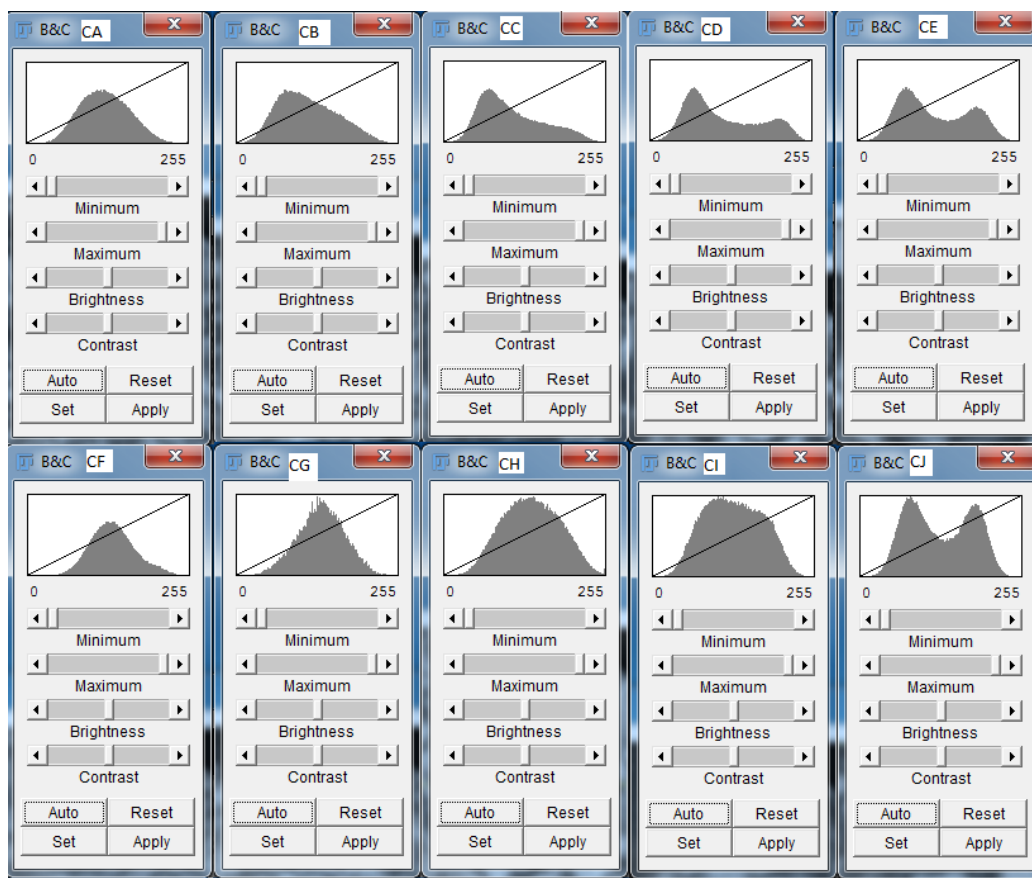
Figure 3.5.1 - Grayscale Range Values for CA-CJ (CsNO$_3$ 1st and 2nd ratio datasets)

For each composition dataset, a region of interest (ROI)(Oval, Left_Central, Right_Central, Top_Central, Bottom_Central, Central, and Large_Central, see Figure 3.5.2) was selected for each slice within the volume, and average grayscale values then calculated. The smaller boxes were 250 x 220 pixels which equated to 0.76 x 0.67 mm. These were the length scales used to assess the inhomogeneity based on grayscale values. Inhomogeneity at various sorts of length scales may of course be of interest ultimately. Within the scope of this thesis, we have considered the current length scales as it is clear that inhomogeneities do exist at this scale, and it is therefore important to assess for correlation with pyrotechnic performance.
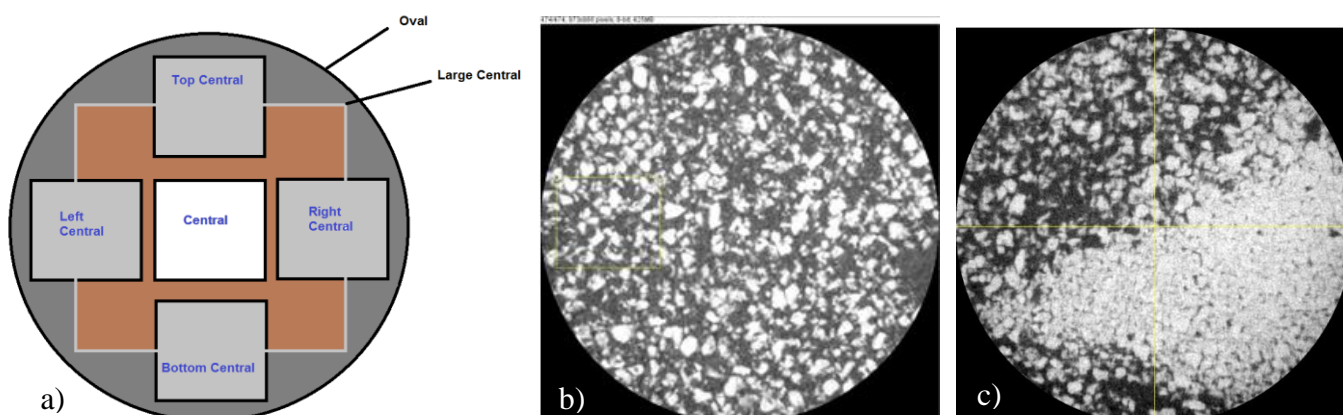
Figure 3.5.2 - a) Schematic of Grayscale Measurement Approach, b) Example of application on Top Slice of BA (RbNO$_3$, 1st ratio, 7 sieve cycles) and c) 25% Slice BD (RbNO$_3$, 1st ratio,1 sieve cycle)
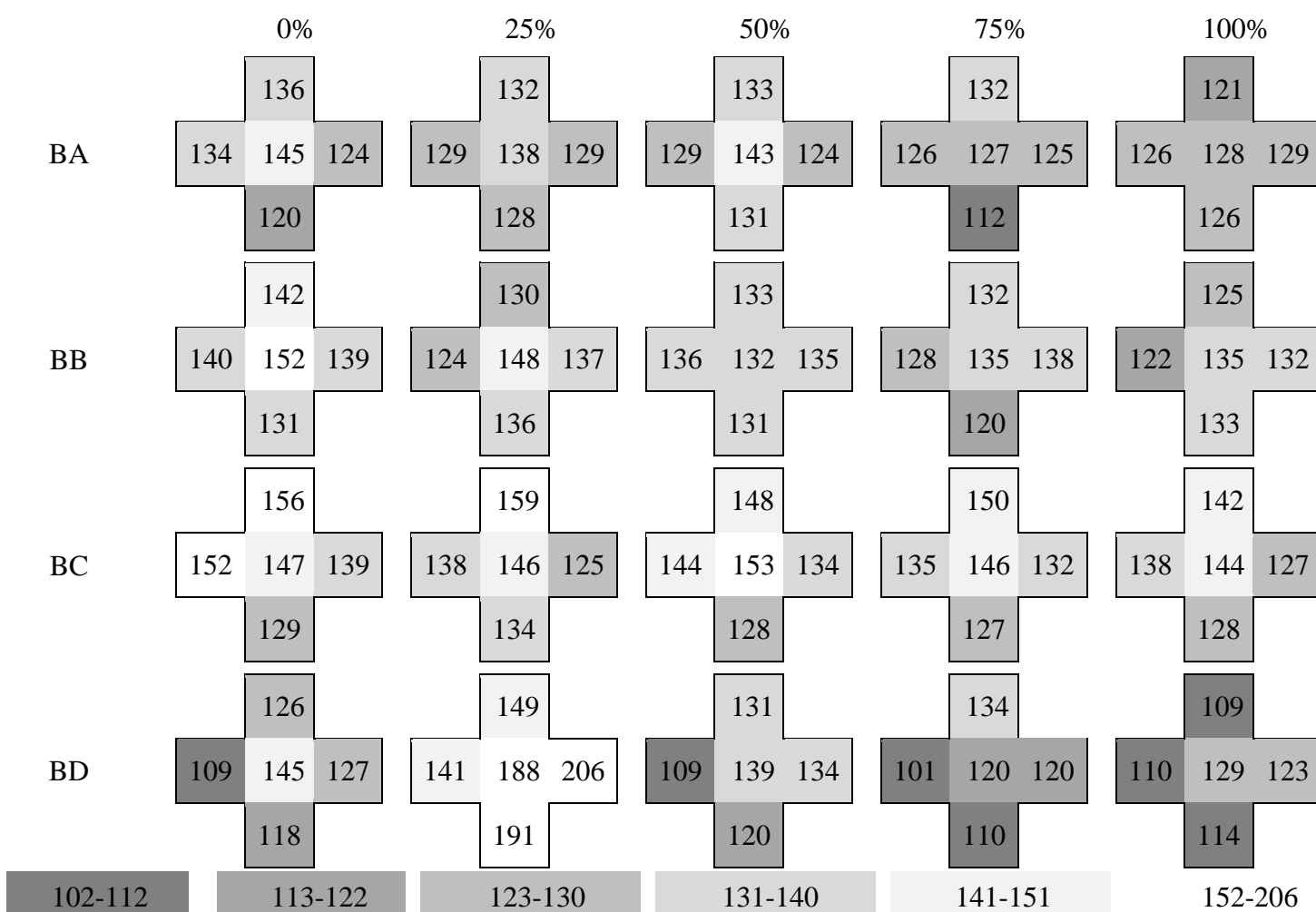
Figure 3.5.3 - Grayscale Averages within RbNO$_3$ compositions (BA-BD) (0 - 100% height within sample dataset, fuel rich; darker grey and oxidiser rich: lighter grey to white)

By visual assessment the composition which showed the greatest variation was sample BD (Bad Mix - the lower row of Figure 3.5.3). Figure 3.5.3 shows the sample viewed on a slice by slice basis. It highlights the general increase in average grayscale value on moving from BA-BC which was anticipated because of the increased oxidiser content. Slight variations are observed between each sub-volume within BA to BC, more so for BC ($RbNO_3$, 3rd ratio) indicating areas which are less homogeneous than others. The larger spread of values attributed to the various sub-volumes within BD clearly indicates that this was a poor mix.
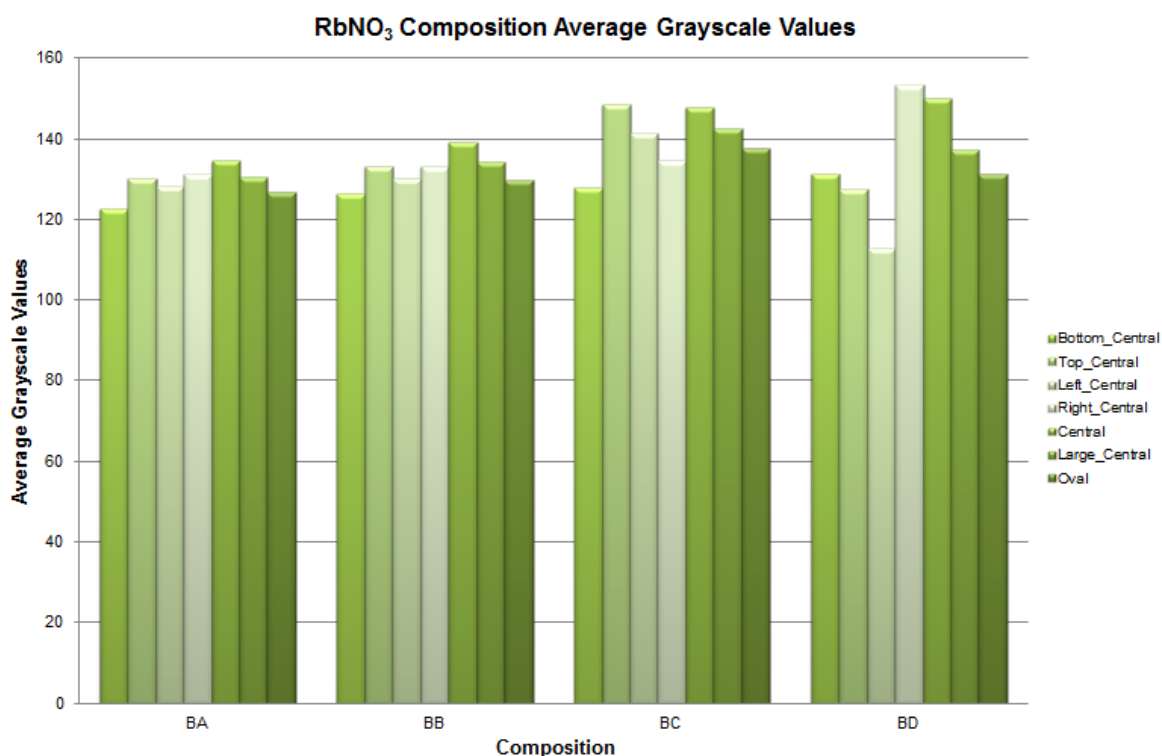
Figure 3.5.4 - 3D Volume Average Grayscale Values for $RbNO_3$ compositions

Another observation to note was the general trend on moving from Oval, Large_Central, to Central grid size values for each dataset. There was a general decrease in average grayscale values attributed to focussing on smaller sample sections. The slight incremental reduction in the average grayscale values noted between the larger regions of interest and the smaller sections was believed to have been caused by the use of a beam hardening correction which was applied during image reconstruction. It is believed that the correction applied may have been slightly higher than necessary. The same observations were made for $CsNO_3$ containing compositions as can be seen in

Figure 3.5.5. The large scale grayscale variation was minimal for these mixtures as can be seen on comparing Large_Central and Oval volumes (~950 x 950 x 450 voxels). Greater variation is seen between the different sections within each volume (Bottom_Central, Top_Central, Left_Central, Right_Central and Central covering a volume of 250 x 250 x 200 voxels). It is interesting to note that CP (Bad Mix), based on these results and visual inspection, appeared to be well mixed. Only small variations between the sections of the compositions were found but these were equivalent to those seen for a similar mix, CD (125 μm, 1st ratio, 7 sieve cycles). This was believed to be an exception to the general rule as each of the other oxidiser 'bad mixes' (KNO_3 (AP) $RbNO_3$ (BD) and $Ba(NO_3)_2$ (DB)) made in this work were shown to be poorly mixed by visual inspection of the CT reconstructions based on the amount of consolidated oxidiser particle layers identified within each sample (Figure 3.4.11 and Figure 3.4.12).
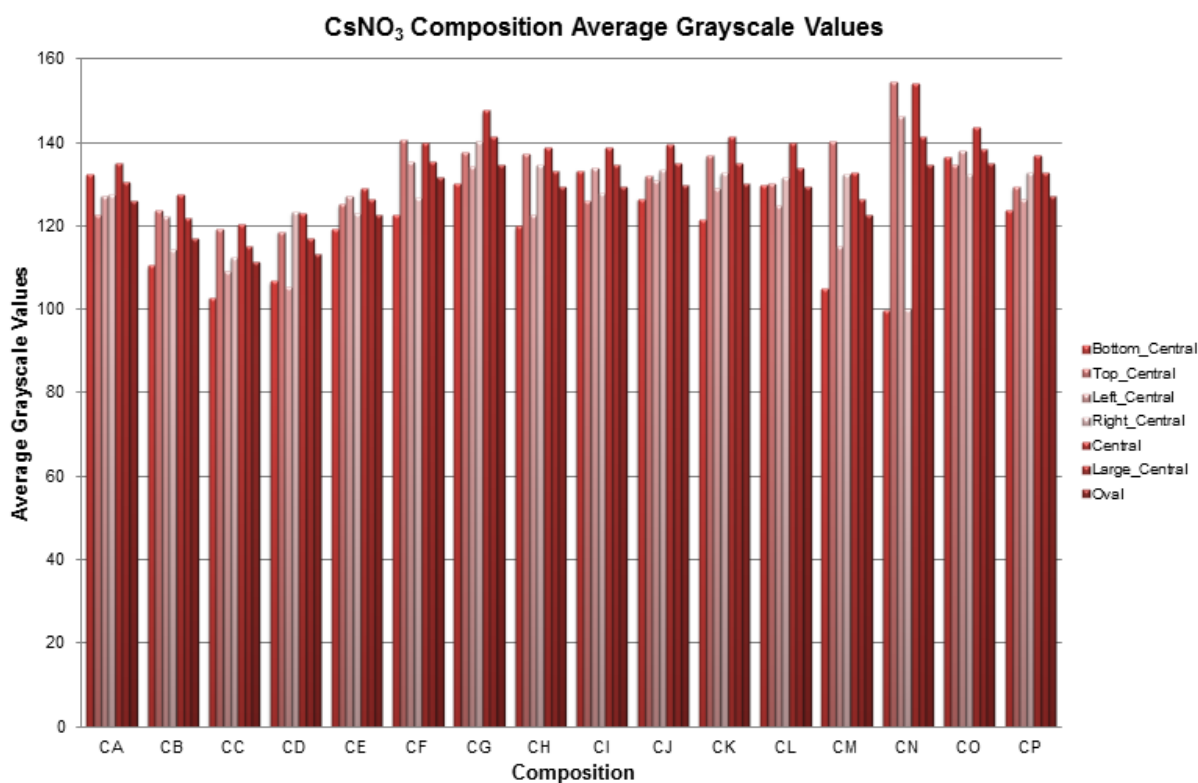
Figure 3.5.5 - 3D Volume Average Grayscale Values for $CsNO_3$ compositions

The objective behind using grayscale averages within this work was to provide an indication of the variations in concentration of each component within the mixtures. Higher grayscale values were attributed to higher oxidiser concentration whereas lower

values indicated that fuel was more prevalent. The level of variation in grayscale values for each sub-volume helped to identify poorly mixed sections of the composition. The $RbNO_3$ composition results confirmed the expected result that BD was a poor quality mix. However, the 'bad mix' manufactured from the $CsNO_3$ compositions, CP, could not be confirmed as there was little variation observed within the grayscale values. These results suggest that CP, the poorly mixed material, actually resulted in a homogeneous system as greater variation was more noticeable within the sub-volumes for the rest of the $CsNO_3$ compositions (CA-CO).

In order to further assess the quality of mixing and given that one of the main parameters being altered was particle size, each composition was evaluated to ascertain the number of particles and the particle size distribution within each sample volume. Two pieces of software were used to achieve this; ImageJ/Fiji (Analyze Particles Plugin) and Avizo.[11-13] The methodology of how these numbers were calculated is provided in Appendix A-1. The number of particles within a small 3D sub-volume was assessed initially which had dimensions of roughly 0.76 mm x 0.76 mm x 0.61 mm. Each voxel measured 3.045 microns. Automatic particle analysis within ImageJ/Fiji[11, 12] required a binary file input therefore the first step was to threshold the image and then apply a watershed (separated apparent touching particles). In the majority of cases this tool worked well although in some cases particles were separated when they should have been connected and vice versa. We accepted that this tool would not work with 100% accuracy but it worked well enough for our needs and correctly separated at least ~90% of the individual particles from each other. Once particles were separated edge particles were removed so as to only account for complete particles. In addition to a collection of images which depicted the labelled particles within a slice there was also an assortment of measurements provided which included particle number, location, size, feret diameter, circularity, solidity *etc.*
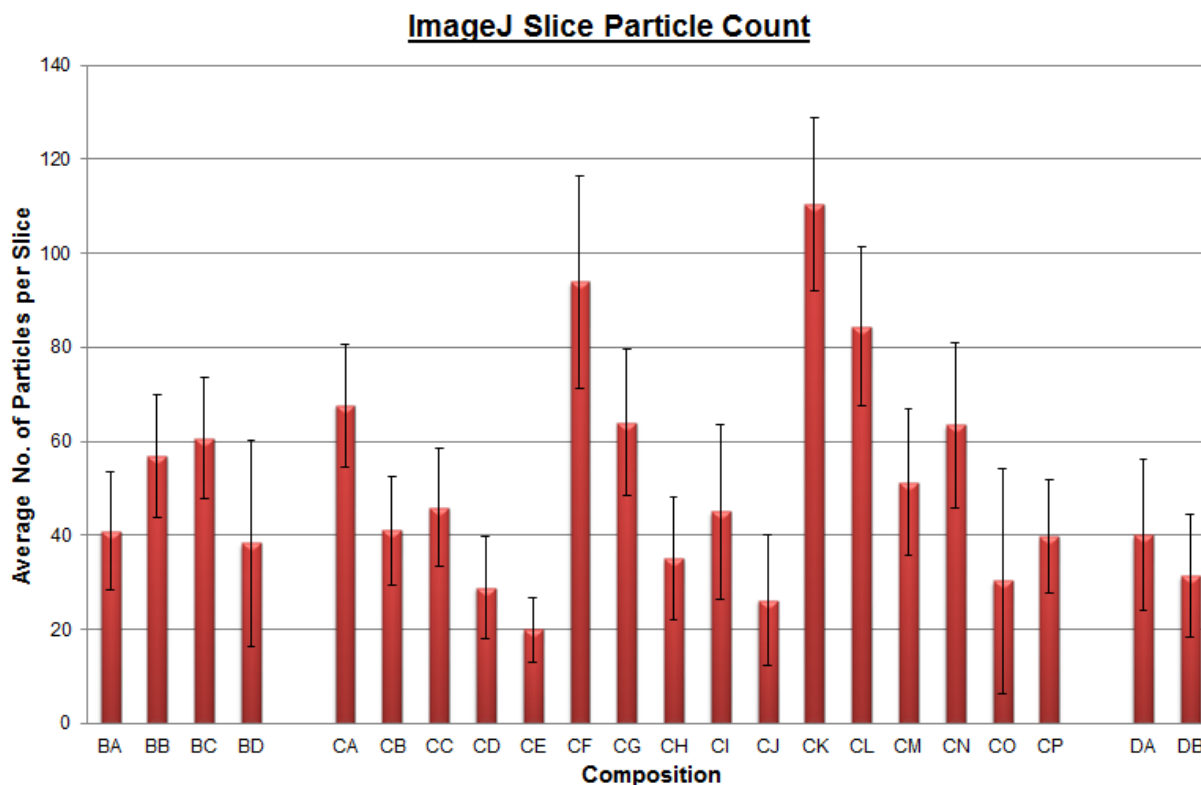
Figure 3.5.6- ImageJ/Fiji 2D Slice Particle Count

As was to be expected there was a general trend of the number of oxidiser particles increasing as the ratio of the oxidiser to fuel increased for compositions including either $RbNO_3$ (BA-BD) or $CsNO_3$ (CA-CP). The particle count generally decreased as the particle size was increased which was also to be expected for a given total phase content. As much as the 'Analyze Particle' plugin within Fiji/ImageJ was useful for calculating the number of particles on a slice to slice basis, however, it was unable to ascertain the number of particles within a volume.[11, 12] The program treated each slice separately and couldn't combine the information attributed to one slice and associate it with the preceding slice and as such it was over counting the number of particles within a given volume. Avizo was therefore used to assess the number of particles within a volume.[13]
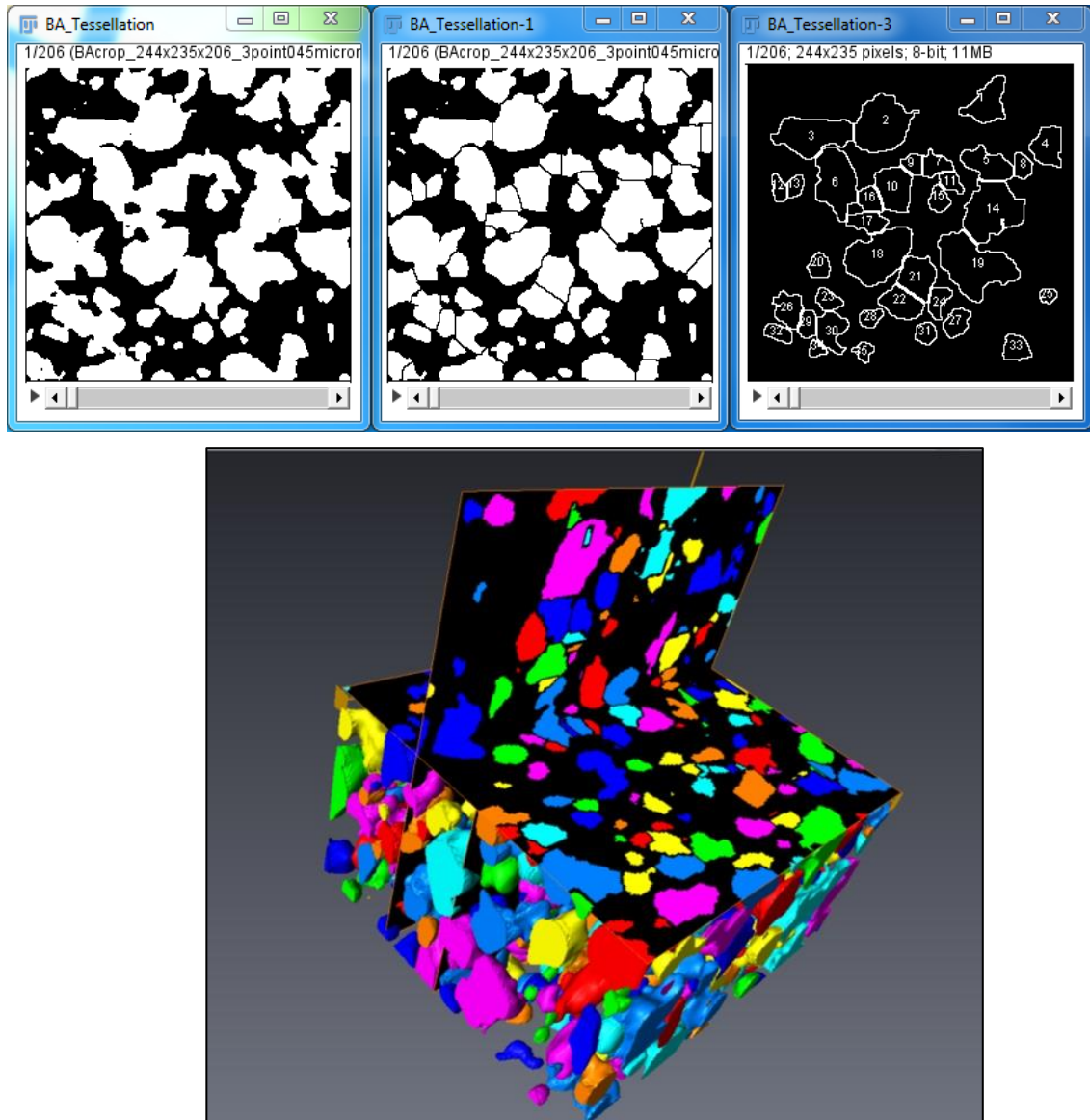
Figure 3.5.7 - a) - c) ImageJ/Fiji Output from Analyse Particles Plugin, a) Thresholding, b) Application of Watershed (Particle Separation) c) Analyse Particles (Particle Counting) d) Example of Avizo Output using Quantification Tools (Surface Generation of Oxidiser Particles)

The input read by Fiji/ImageJ [11, 12] is formed of successive slices, at a spatial resolution of 3.045 μm. One particle may be labelled multiple times and therefore an accurate determination of the number of particles within a 3D volume could not be obtained using this approach. Avizo[13] provided better results. These are detailed in Figure 3.5.7 and Figure 3.5.8. Once the grayscale original images are converted to binary images a distance transform was applied. Centroids of each particle are then searched for and

labelled. A watershed correction was given by coupling the inverse distance transform and the particle centroids. Lines are effectively drawn between the channels observed within the distance transform to allow for particle separation. The watershed step treated the whole volume rather than each individual slice and therefore a more accurate determination of particle count, positions, and volumes was provided.
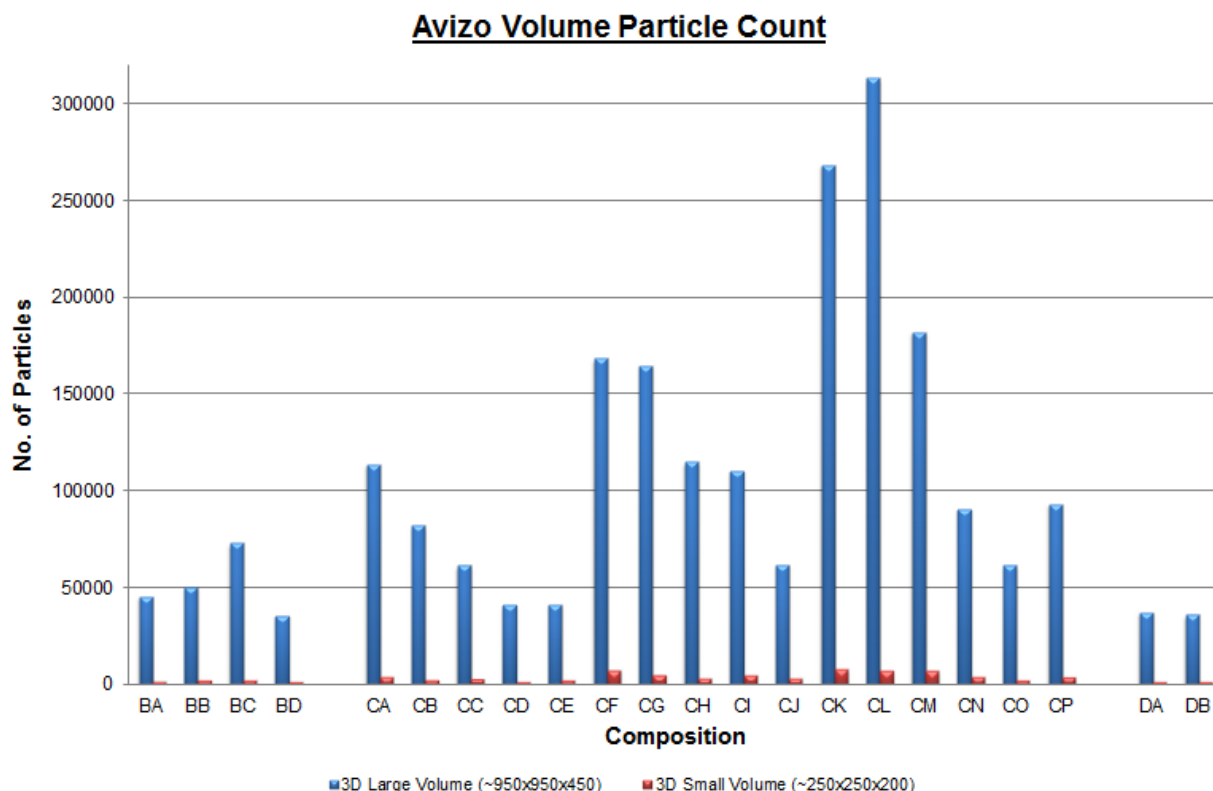
Figure 3.5.8 - Avizo 3D Volume Particle Count

The particle count patterns typically follow the same trend as was discussed for the output from Fiji/ImageJ. Figure 3.5.8 shows the particle count within both a small volume (250 x 250 x 200 voxels) and the complete volume (~950 x 950 x 450 voxels). The smaller dataset was used as the input for both Fiji/ImageJ and Avizo. [11-13] Whilst the small dataset was a central region of interest within the larger dataset they did produce slightly different results. A key caveat to mention regarding the use of these measurement algorithms is that in some cases a cluster of particles were seen as one particle and conversely larger particles were deemed to be a collection of smaller particles.

To summarise, it is clear that using only one imaging analysis approach is insufficient as has been highlighted by the use of two pieces of software designed to yield the same information *i.e.* particle numbers. The way in which the watershed is calculated differs. ImageJ/Fiji separates particles on a slice by slice basis whereas the watershed applied within Avizo are based on the whole volume therefore the inconsistencies caused by the former approach is overcome. Although the slice-wise method (ImageJ/Fiji) lacks in some ways it excels in others as other measurements can be extracted such as particle number, location, size, feret diameter, circularity, solidity *etc*. This can be combined with the information gained from the volume-wise approach within Avizo (particle location and volume) to achieve a more complete assessment of each dataset and its contents. The summation of the areas/volumes within the dataset allows a more accurate estimate of oxidiser concentration on a slice/volume basis and by extension the concentration of the other component(s) within the sample. Work has previously been carried out by Brown *et al*. to assess the relationship between pyrotechnic burning performance to the number of contact points between fuel and oxidiser.[8] They used Hao-Tanaka formula to determine the number of binary contacts.[14] Their work assumed that the components are spherical which of course as has been shown is far from the truth. However, information gained from the volume-wise and slice-wise approach obtained through the use of Avizo and ImageJ/Fiji could expand upon the insights made within their work and provide a more accurate assessment of the number of contact points within a mixture because particle geometries, number of particles, and component concentrations can be ascertained.

3.6   TESSELLATION AND STATISTICAL TOOL APPLICATION

Figure 3.6.1 and Figure 3.6.2 highlights results associated with applying the tessellation tool to the $NaNO_3$ component of the initial trial pyrotechnic mixture. The Delaunay tessellation tool was not optimised for irregular particles such as those found within the pyrotechnic samples studied, however, along with the Finite Body Tessellation (Figure 3.6.2) they do provide a clear indication of the oxidiser distribution within each composition.
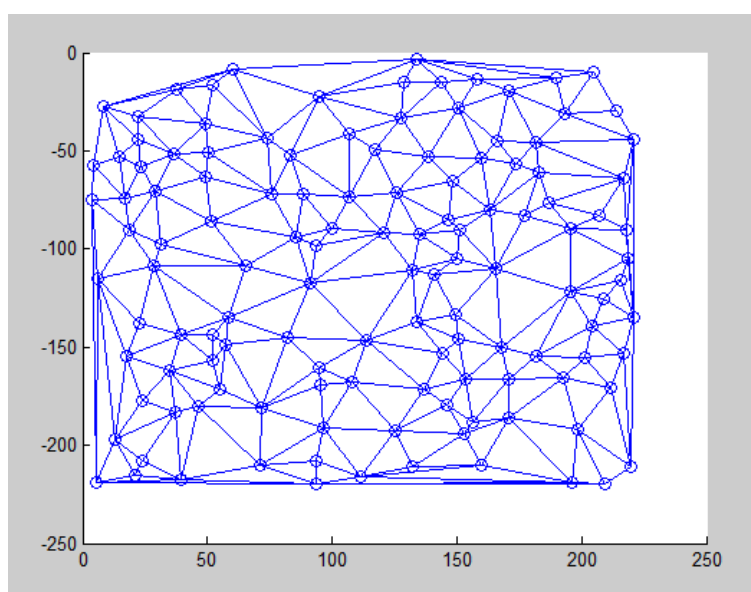
Figure 3.6.1 - Delaunay Triangulation of Initial Pyrotechnic mix ($NaNO_3$ + lactose (2D))
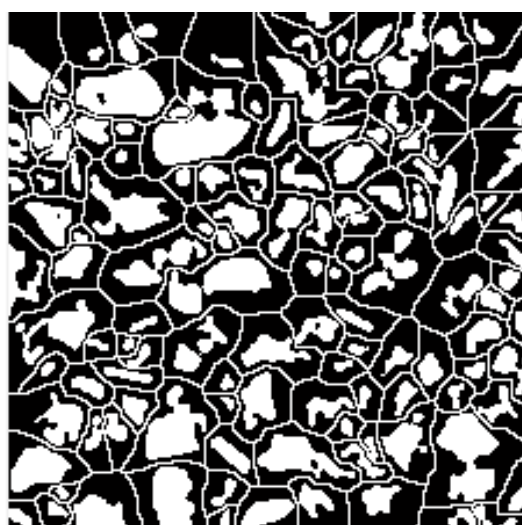
Figure 3.6.2 - Tessellation Results for Initial Pyrotechnic mix ($NaNO_3$ + lactose (2D))

The following results show the CoV values associated with the 2D data sets for binary images of the sodium nitrate component of the pyrotechnic mixture. 2D slices with dimensions of 0.76 mm x 0.76 mm were assessed. Each pixel measured 3.40 microns.
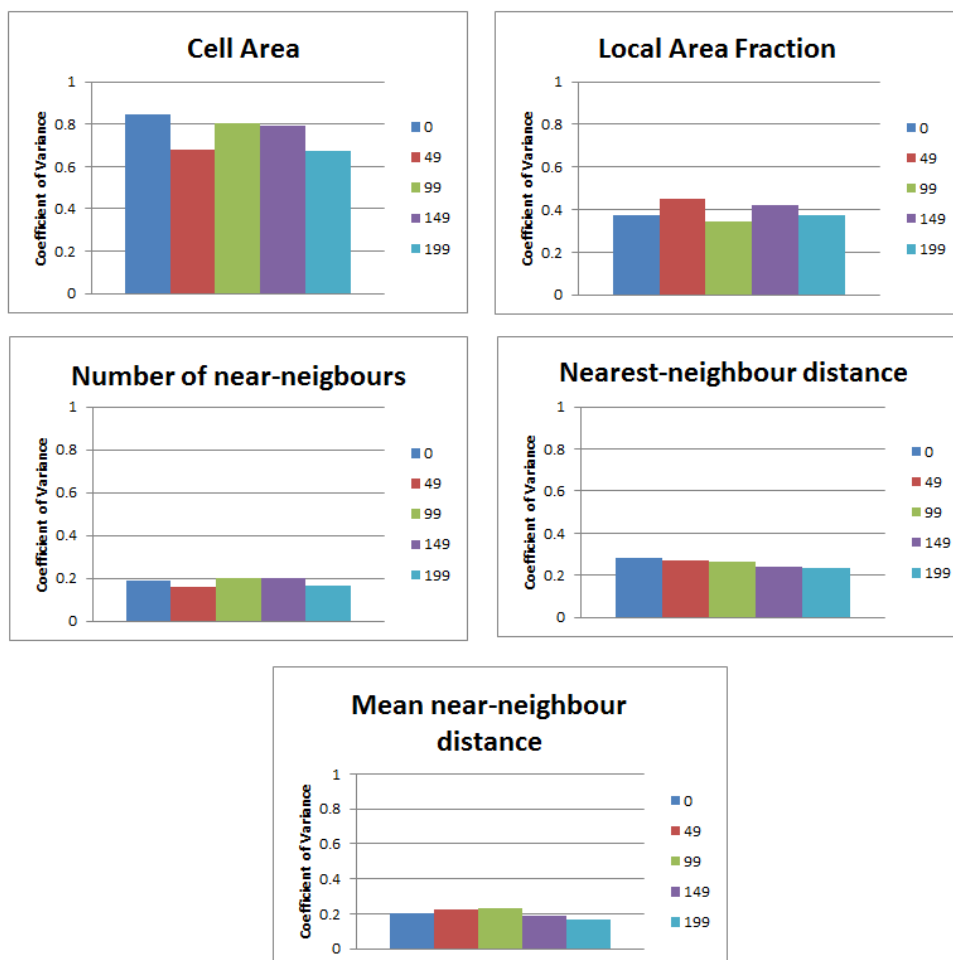
Figure 3.6.3 - Coefficient of Variance Results for NaNO$_3$

The CoV values associated with the mean near-neighbour distances suggests a degree of ordering (*i.e.* less than 0.36) and as such the distribution of NaNO$_3$ was considered to be homogenous throughout the sample, with only marginal changes noticeable between slices.

Figure 3.6.4 – Slices 000, 049, and 099 for Initial Pyrotechnic Mixture (NaNO$_3$ + lactose)
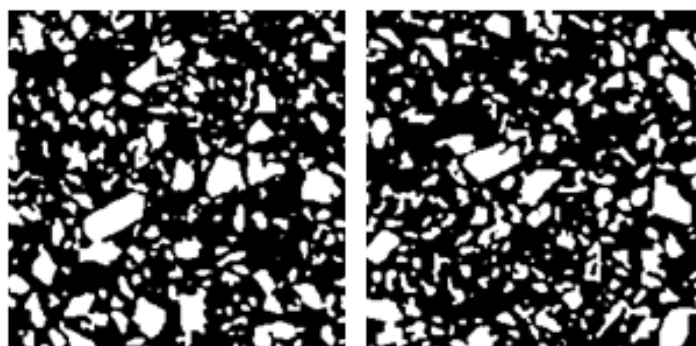
Figure 3.6.5 – Slices 149 and 199 for Initial Pyrotechnic Mixture (NaNO$_3$ + lactose)

The tessellation tool was applied to each of the compositions formed in this study. Figures 3.6.6 - 3.6.9 details results obtained for RbNO$_3$ and CsNO$_3$ compositions. Each RbNO$_3$ composition was made with the same oxidiser particle size, 125 micron, with no real variation in the average number of near neighbours being recorded. The number of near neighbours for a given particle will be affected by the relative particle geometries as well as the particle size range of the sample under investigation (*e.g.* individual large particles may be anticipated to have large numbers of near neighbours if surrounded by small particles). The number of near neighbours was seen to range from 3-12 with 6 being the average for RbNO$_3$ compositions (BA-BD). The main CoV parameters which may indicate a non-homogeneous mixture are particle area, nearest-neighbour distance, and mean near-neighbour distance as can be seen from the following graphs (Figure 3.6.6 and Figure 3.6.8). When particles of similar density are close together it is difficult to identify their edges which mean the clusters of particles tend to be treated as larger particles than they actually are. At 25% height there was a large cluster of

oxidiser particles within BD which explains why there is a significant increase in the CoV value for particle area compared to the other $RbNO_3$ compositions (BA-BC).
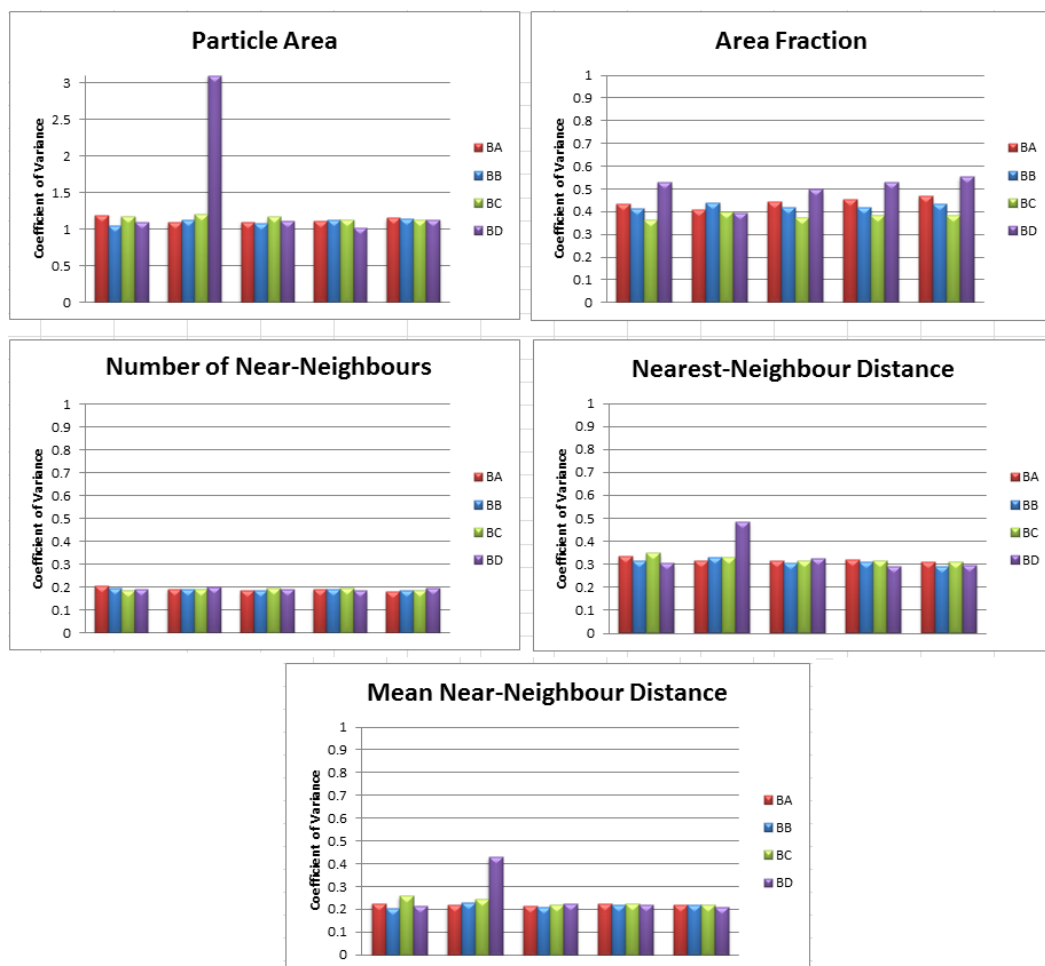
Figure 3.6.6 - BA-BD Tessellation CoV Results (Five columns represent 0%, 25%, 50%, 75% and 100% height within each of the composition datasets (BA-BD))
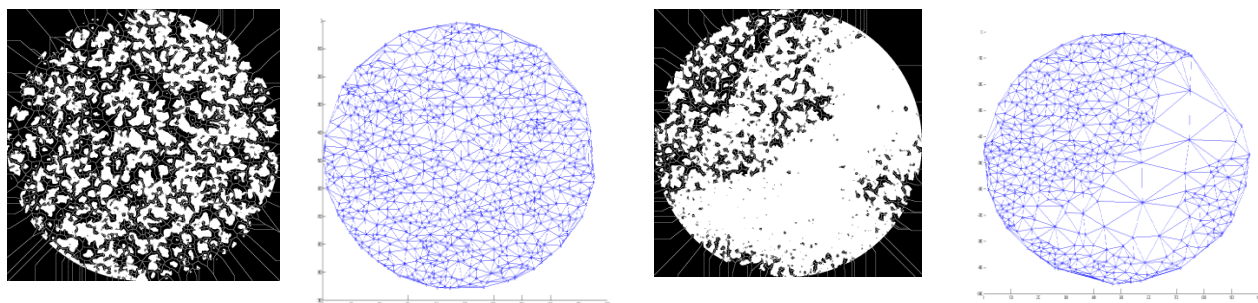
Figure 3.6.7 - Homogeneous vs Non-homogenous (BD 50%, BD 25%)

Whilst some tessellation assessments showed errors, those where the tool was able to provide an output for each slice throughout the volume dataset (0%, 25%, 50%, 75%, 100% volume) were collected and are highlighted here. The resolution was insufficient for particle sizes; 38, 75, 90 microns. CP ($CsNO_3$, bad mix) was expected to give higher CoV values for a number of the parameters assessed compared to CD, its well mixed equivalent. The CoV values for particle area, nearest-neighbour distance and mean neighbour distance all have slightly higher CoV values in relation to CD highlighting that CD is, on this local, particle to particle basis, more homogenous than CP. The oxidiser clustering within the 'bad' mixes for the other oxidiser compositions (KNO_3 (AP) and $RbNO_3$ (BD) were fairly clear by eye compared to the $CsNO_3$ 'bad' mix (CP). Only by closer inspection, slice by slice, was it possible to notice clusters of oxidiser particles within sections of the composition CP.
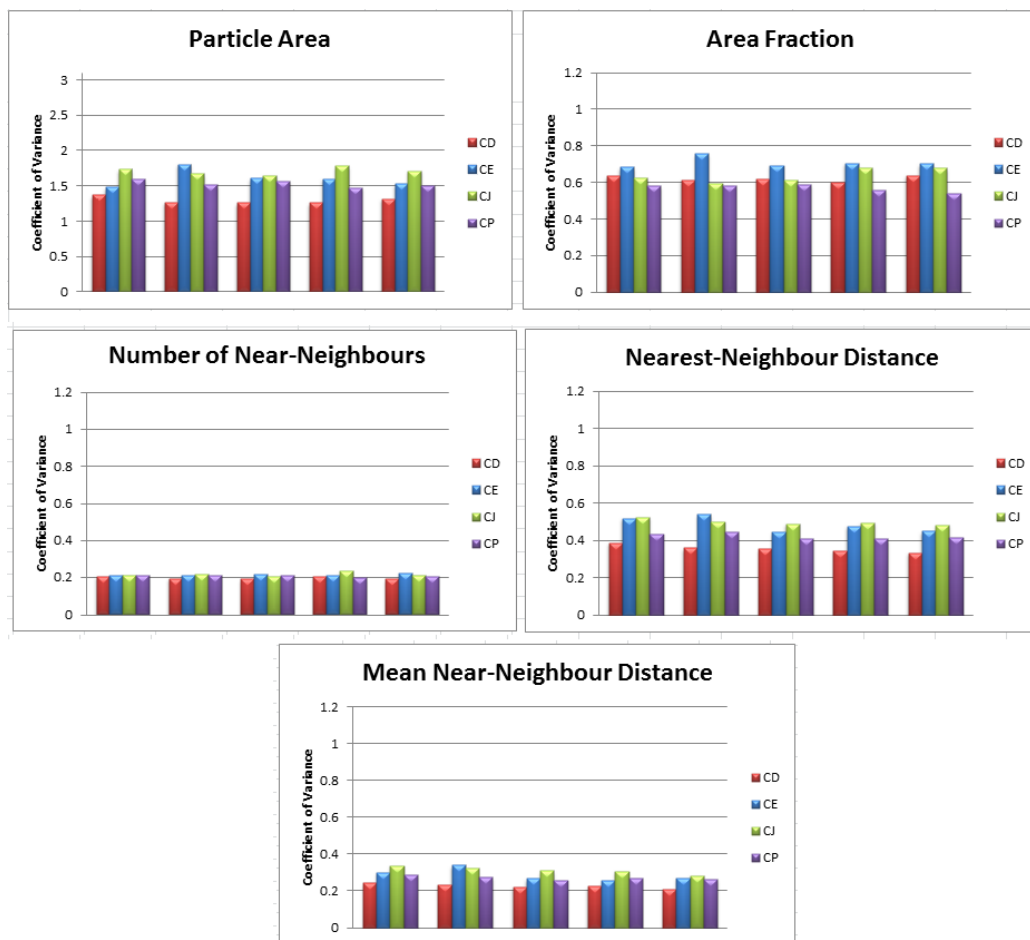
Figure 3.6.8 - CD, CE, CJ, CP Tessellation CoV Results
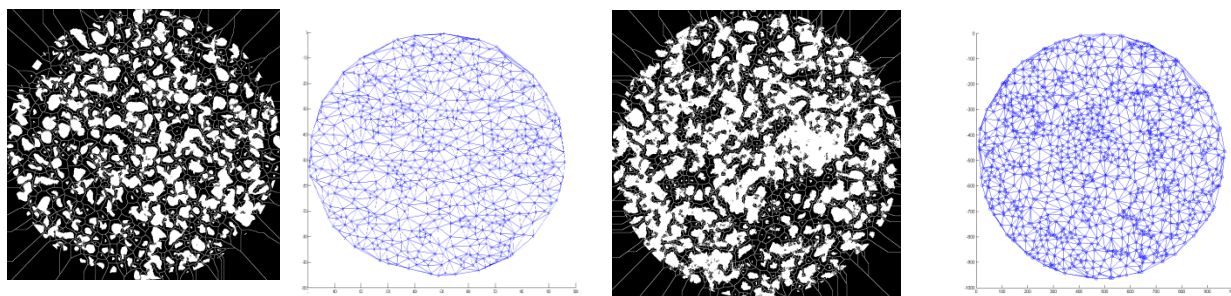
Figure 3.6.9 - Homogeneous vs Non-homogenous (CD 75%, CP 25%)

An important aspect of this form of analysis is that aggregated/agglomerated particles will be treated as one particle in the tessellation (the gray level averaging approach of Figure 3.5.3for example avoids this issue). The CoV approach will not detect this issue as such as it is particle size insensitive. It may therefore be useful to trial this tool on sub-volumes and compare across smaller material regions to gain a better indication and measure of mixture quality.

No one image analysis approach will easily cover all of the possible ways that phases and particles behave and as such it is useful to trial various tools and extract the information provided by each to obtain a better understanding of granular media. Tessellation tools combined with diagnostic tools, such as CoV, provide great value in the assessment of powder mixtures as they are able to quantify the mixture quality based on the distribution of a single component within a mixture. Truly regular distributions would have a CoV of 0 (*i.e.* a grid has no variation in separation distances), a heavily clustered distribution will have some very high and some very low separation distances (high CoV), a random distribution falls somewhere between the two.

In the first instance it may be expected that those compositions containing smaller particle sizes would burn fastest. Burn rate values will differ depending on the oxidiser used as will the heat of reaction which is dependent on oxidiser type, quantity of oxidiser and oxidiser particle size. Based on the image analysis results, as there were two burn assessments carried out for each composition, it would be further expected that those attributed to 'bad mixes' (AP, BD, CP, DB) may show a greater variation in burn response as they have generally been shown to be poorly mixed (apart from CD vs. CP).

3.7   BURN RESULTS

The burn results associated with each of the compositions are discussed throughout this section. A few examples for KNO_3 tests are shown in Figure 3.7.1. It is clear to see that a substantial amount of smoke was generated from the compositions. Compared to the initial tests carried out to assess the pyrotechnic effect, these results were somewhat different. The initial tests indicated that the compositions behaved as a mini-signal flare with a strong coloured flame presence, whereas in the final burn tests they behaved as smoke compositions. This change in behaviour is consistent with ageing of the product, as the burn tests were carried out several months after manufacture. It is therefore anticipated that moisture will have had a dampening effect on the pyrotechnic compositions.
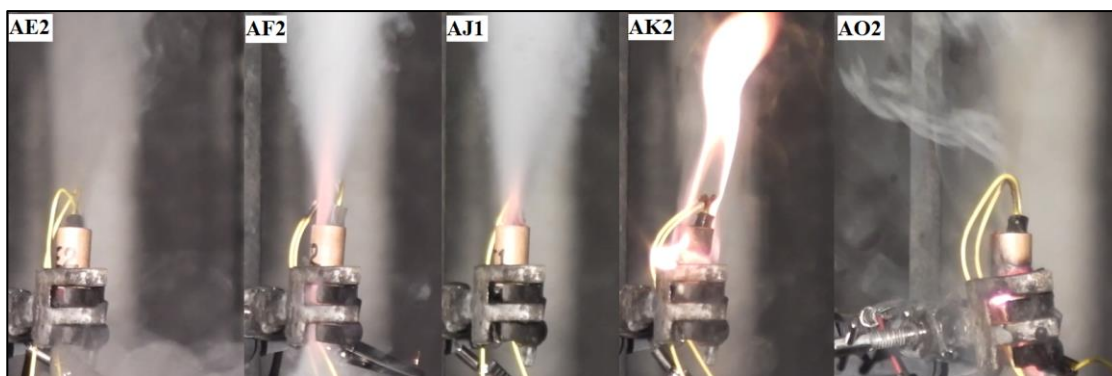
Figure 3.7.1 - KNO_3 composition normal video snapshot(Examples: AE2, AF2, AJ1, AK2, and AO2)

Although pyrotechnics in Figure 3.7.1 did not perform as initially expected there were still useful results obtained from analysis of their burn characteristics. Two of the compositions, AA and AK, both comprised the smallest size of oxidiser particles. It is believed that the burn could not carry forward due to lack of sufficient void space within the sample, see Figure 3.7.2. The second oxidiser:fuel ratio produced the fastest burn rate as can also be seen from Figure 3.7.2. The burn lengths, times and rate can be found in Table 3.7.1.

	Ratio	Particle Size (µm)	Burn Length (mm)	Burn Time (secs)	Burn Rate (mm/sec)	Burn Length (mm)	Burn Time (secs)	Burn Rate (mm/sec)
AA	1st ratio	38	5.83	0	0	5.82	0	0
AB		75	5.58	7.5	0.744	5.68	10	0.568
AC		90	5.8	9	0.644	5.77	9	0.641
AD		125	5.53	10	0.553	5.84	7	0.834
AE		200	5.79	7	0.827	6.11	8	0.764
AF	2nd ratio	38	5.97	2	2.985	5.81	2	2.905
AG		75	5.46	2	2.730	5.69	2	2.845
AH		90	5.56	1.7	3.271	5.55	1.7	3.265
AI		125	5.88	2	2.940	5.56	1.8	3.089
AJ		200	5.47	1.8	3.039	5.89	1.8	3.272
AK	3rd ratio	38	5.33	0	0	6.03	30	0.201
AL		75	6.02	20	0.301	5.74	50	0.115
AM		90	5.58	28	0.199	5.93	28	0.212
AN		125	5.64	40	0.141	5.69	80	0.071
AO		200	5.71	35	0.163	5.41	33	0.164
AP	Bad Mix	125	5.96	11	0.542	6.26	12	0.522

Table 3.7.1- KNO_3 Composition Burn Results
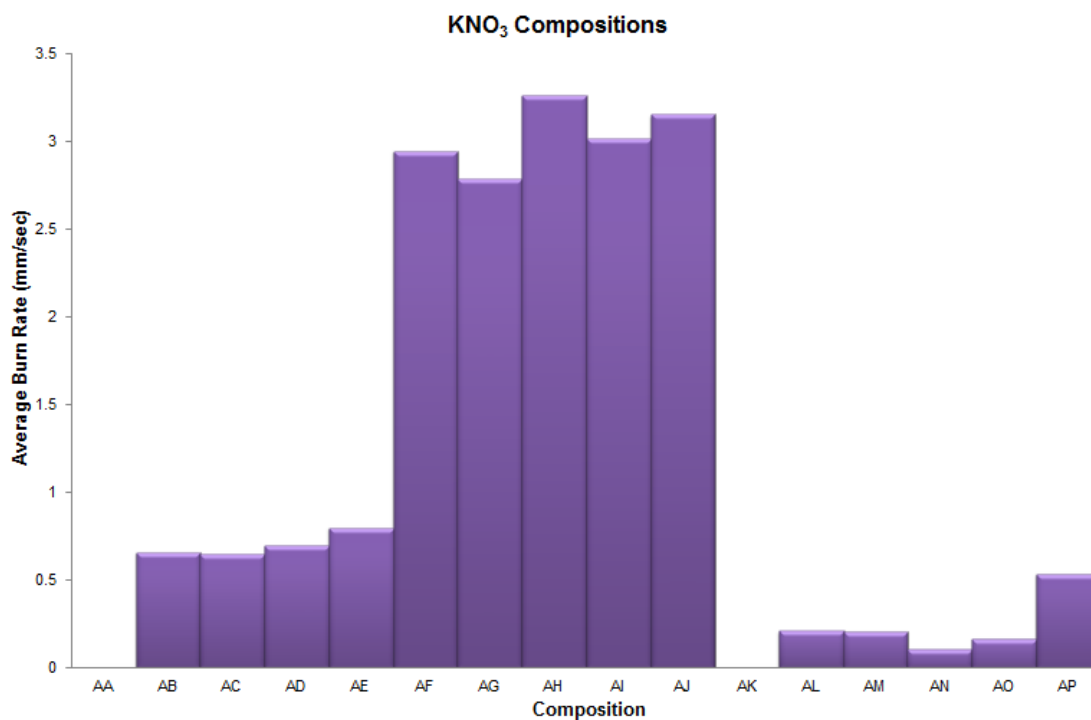
Figure 3.7.2 - KNO_3 Composition Average Burn Results (AA-AE (1st ratio), AF-AJ (2nd ratio), AK-AO (3rd ratio), AP ('bad mix')

As oxidiser content increased there was a marked increase in heat of reaction observed by the destruction of the cardboard tube which is shown in Figure 3.7.3. The burn test results for the third oxidiser:fuel ratio was a compound effect of the compositions and the convoluted cardboard tubes burning. Further tests with longer lengths of composition would be desirable to see the small difference attributed to the changes in particle size as these were not clearly identified from this work.

In a cylindrical container comprising pyrotechnic composition, the composition volume generating heat is proportional to the square of the diameter, and the heat loss through the surface is proportionate to the diameter. As the diameter decreases the ratio of the rate of heat loss to heat generation increases therefore it is expected if the column diameter is too small that a combustion reaction may fail to propagate.[5] Therefore it would be advised that further scanning would encompass compositions of longer lengths but similar diameters. The results identified from this work indicate that it would be advisable to use the same material thickness as has been used in this work as this is a limiting factor for CT analysis. In order to maximise information it would be required to stitch multiple scans of a composition together which is relatively easy to do, it just requires more CT scanning time.
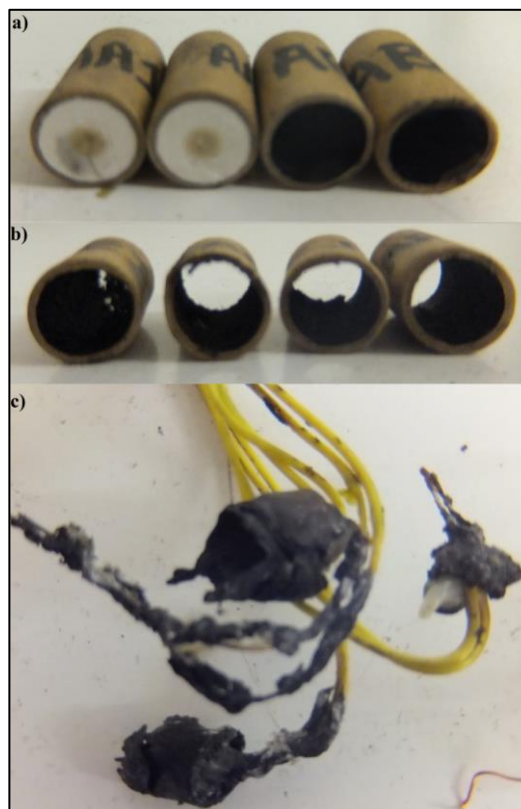
Figure 3.7.3 - KNO$_3$ Composition Burn Test Residues a) AA1, AA2, AB1, AB2, b) AE1, AE2, AF1, AF2, c) Highest KNO$_3$ concentration (convoluted cardboard tubes disintegrate)

Radiometry and photometry measurements for the KNO$_3$ compositions only picked up the initial ignition rather than the entirety of the burn and so these are not highlighted here. The RbNO$_3$ composition burn results were fairly similar. Normal and high-speed images are shown in Figure 3.7.4 and Figure 3.7.5 respectively.

Figure 3.7.4 - RbNO$_3$ composition (BB2) normal video snapshot
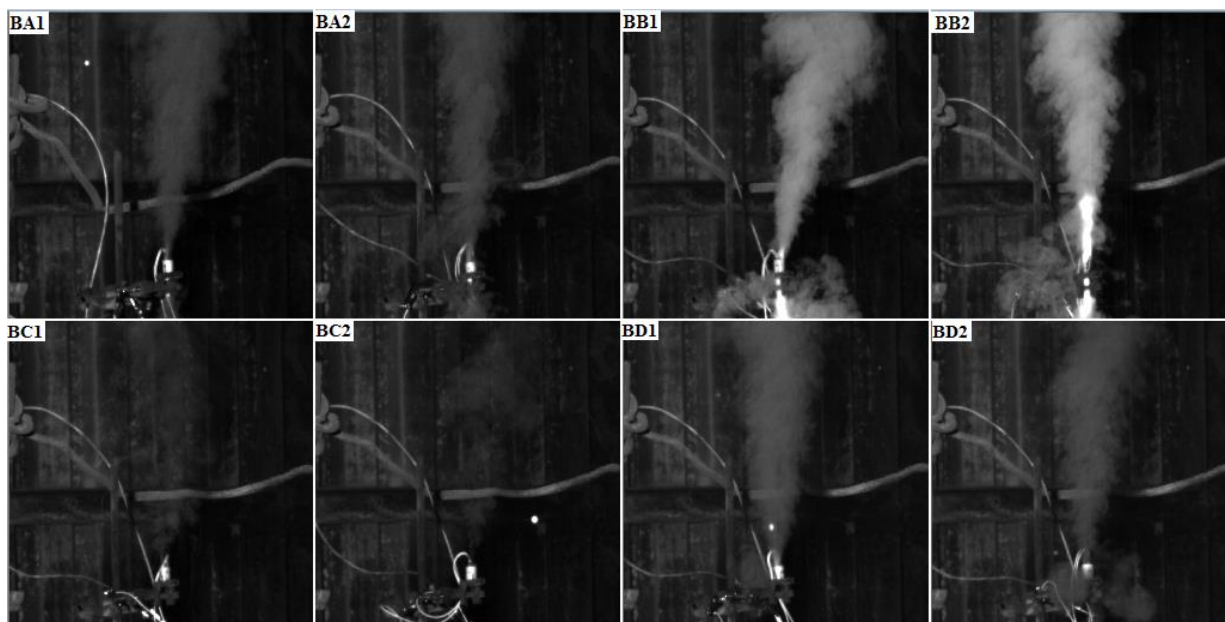
Figure 3.7.5 - High-Speed Camera Images, BA1-BD2

The photometry output generated across the visible channel was consistent with the high speed camera images. These photometry results are shown in Figure 3.7.6. The specific range covered is between 460-660 nm. The initial peak is attributed to the primer ignition and the other peaks are associated with each of the compositions burning. Larger peaks are attributed to the presence of a more intense flame. A small quantity of smoke was seen generated for the BA composition ($RbNO_3$, 1st ratio). The smoke intensity within both BB compositions ($RbNO_3$, 2nd ratio) was significantly higher and a flame was seen in both cases. On moving up to the highest oxidiser concentration, BC compositions, the quantity of smoke is at its lowest. The poor mixes appeared to show inconsistencies in performance expected due to poor mixing as can be seen in the bottom right of Figure 3.7.5 and bottom of Figure 3.7.6.
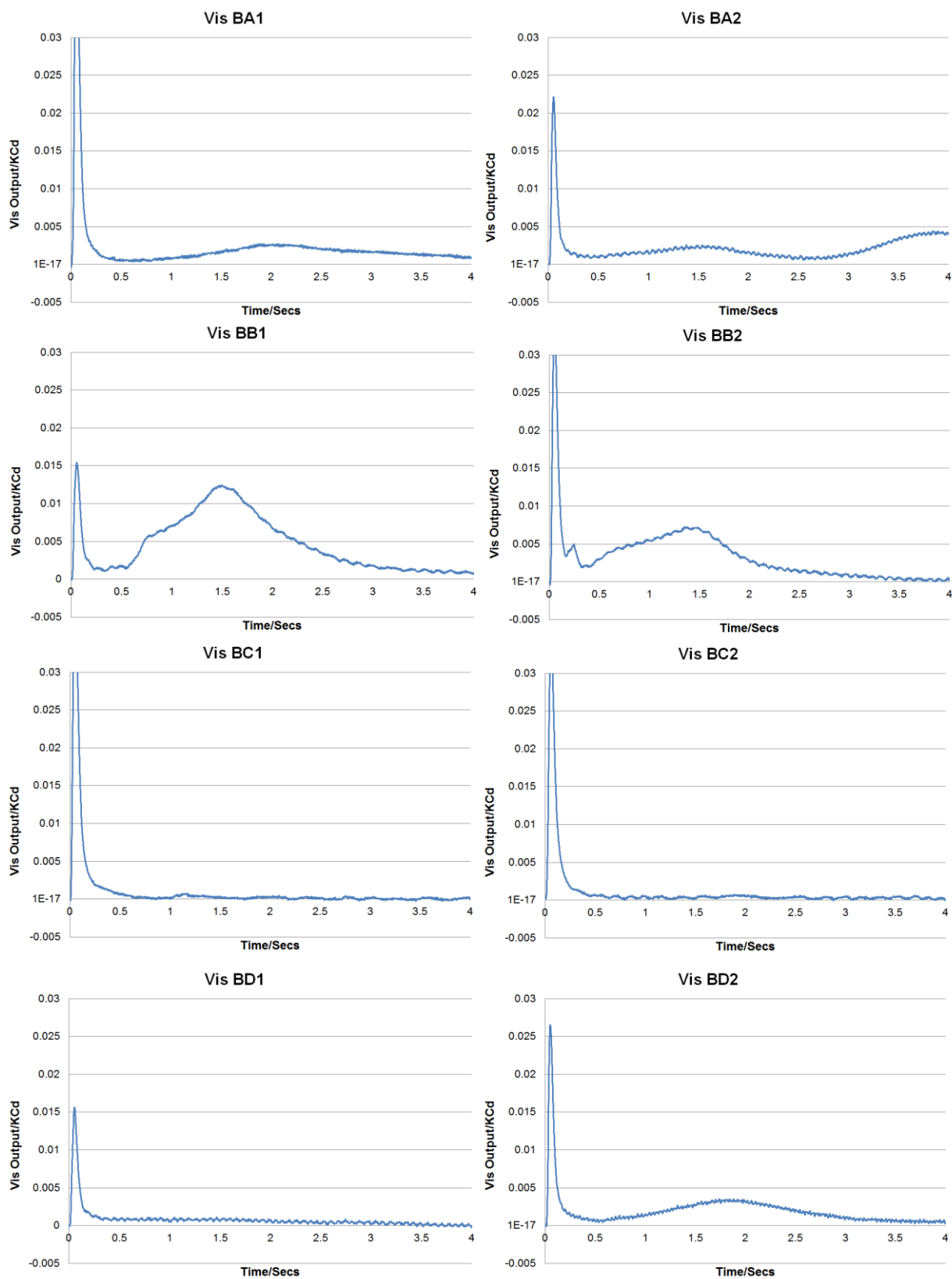
Figure 3.7.6 - Vis Output Photometry Data for BA-BD

The second oxidiser:fuel ratio appears to be the optimum for this binary set as can be seen by the enhanced signature within the photometry data for both of the BB composition samples and from the average burn rates shown in Figure 3.7.7. The photometry results also highlight the major consequence of not achieving a homogeneous mix. The two samples taken from the 'bad mixture' produce entirely different burn profiles. One produced a response similar to BC and the other behaved most like BA. The burn lengths, time, and rate are detailed in Table 3.7.2.

	Ratio	Particle Size (µm)	Burn Length (mm)	Burn Time (secs)	Burn Rate (mm/sec)	Burn Length (mm)	Burn Time (secs)	Burn Rate (mm/sec)
BA	1st ratio	125	4.23	2	2.115	4.93	2	2.465
BB	2nd ratio	125	4.32	1.5	2.880	4.38	1.5	2.920
BC	3rd ratio	125	4.11	4	1.028	4.04	7	0.577
BD	Bad Mix	125	4.89	4	1.223	4.69	7	0.670

Table 3.7.2 - $RbNO_3$ Composition Burn Results
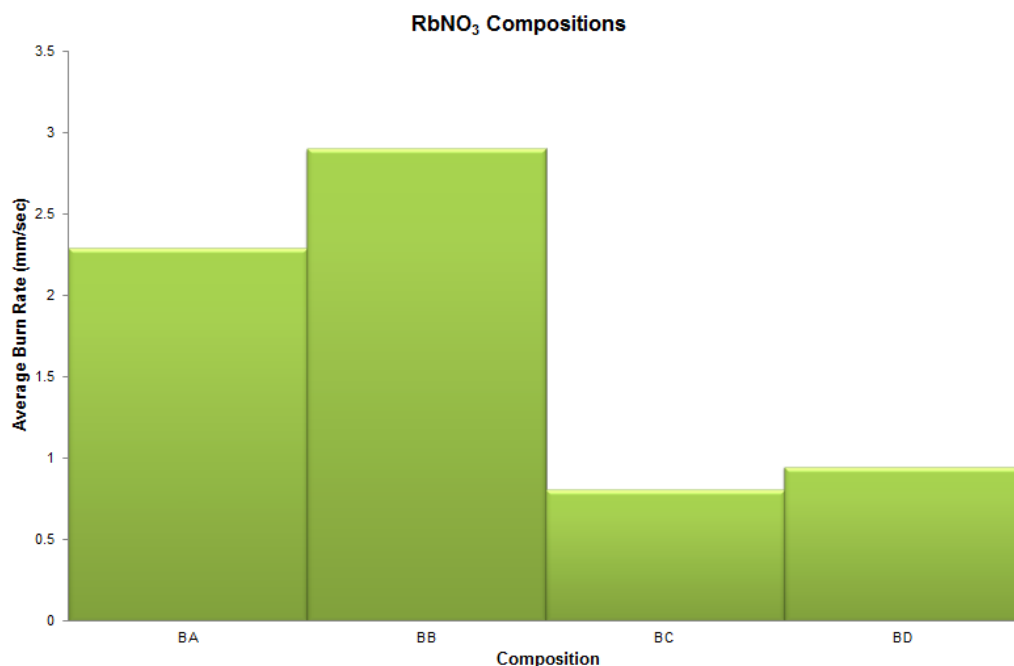
Figure 3.7.7 - $RbNO_3$ Composition Burn Results

The heat generated from the burning of this composition did not cause the cardboard container to burn (*i.e.* it remained intact).

CsNO$_3$ compositions showed a similar progression to the KNO$_3$ series although in this case the first ratio resulted in a relatively quick burn. The second ratio produced the highest burning rates although on moving onto the third ratio once again the cardboard tube started to degrade and act as an additional fuel.
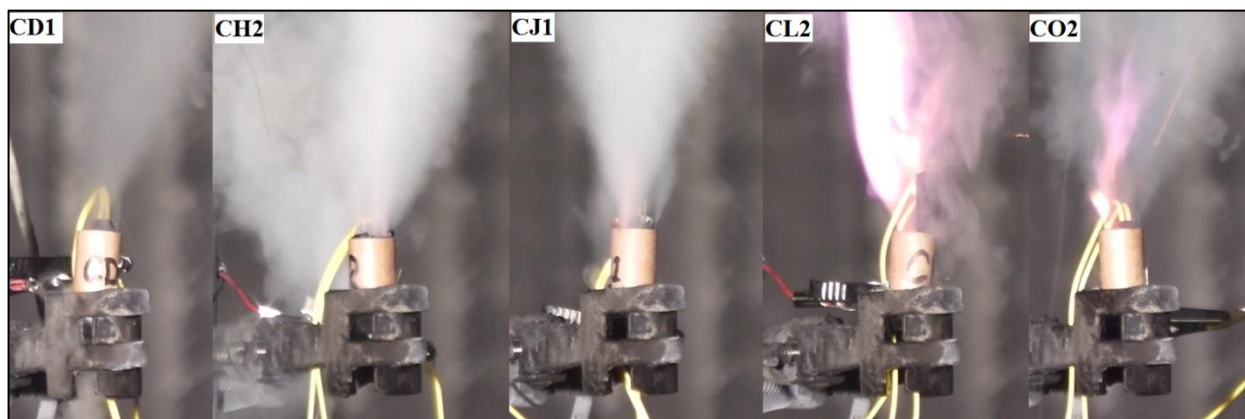
Figure 3.7.8 - CsNO$_3$ composition normal video snapshot (Examples: CD1, CH2, CJ1, CL2, and CO2)

The measurements taken for each CsNO$_3$ composition are detailed in Table 3.7.3 and average burn rates shown in Figure 3.7.9.

	Ratio	Particle Size (µm)	Burn Length (mm)	Burn Time (secs)	Burn Rate (mm/sec)	Burn Length (mm)	Burn Time (secs)	Burn Rate (mm/sec)
CA	1st ratio	38	4.08	2	2.04	4.54	2	2.270
CB		75	4.94	2.5	1.976	4.52	2	2.260
CC		90	3.88	2	1.940	4.44	2.5	1.776
CD		125	3.86	2	1.930	4.5	2	2.250
CE		200	4.39	2	2.195	4.05	2	2.025
CF	2nd ratio	38	3.15	1.2	2.625	4.16	1.2	3.467
CG		75	4.1	1.4	2.929	3.85	1.4	2.750
CH		90	3.84	1.5	2.560	4.15	1.5	2.767
CI		125	3.88	1.5	2.587	3.96	1.5	2.640
CJ		200	4	1.5	2.667	4.05	1.5	2.700
CK	3rd ratio	38	3.77	3	1.257	4.05	3	1.350
CL		75	4.02	5	0.804	3.68	4	0.920
CM		90	3.65	2	1.825	3.79	3	1.263
CN		125	3.73	8	0.466	3.57	4	0.893
CO		200	3.96	10	0.396	3.67	10	0.367
CP	Bad Mix	125	5.36	2	2.680	4.04	2	2.020

Table 3.7.3 - CsNO$_3$ Composition Burn Results
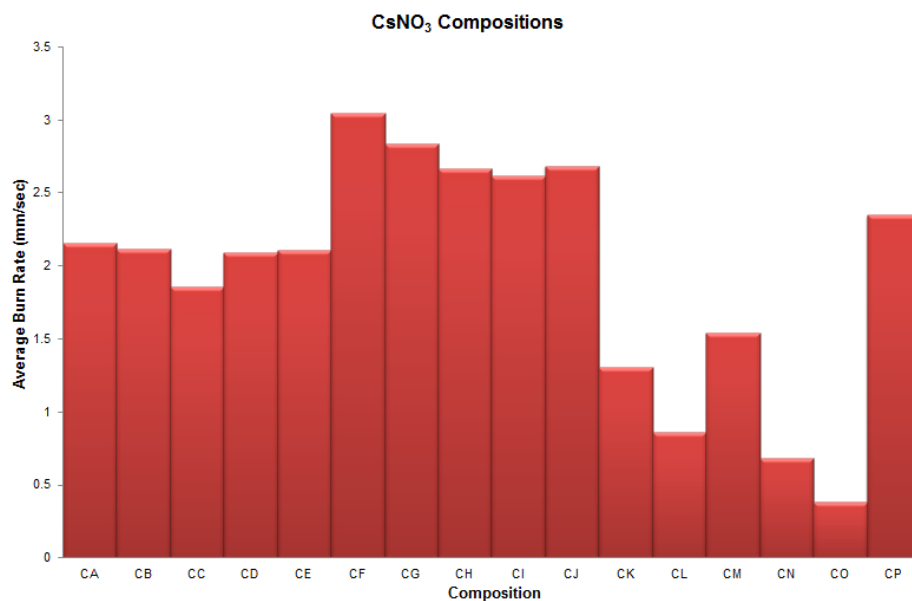
Figure 3.7.9 - CsNO$_3$ Composition Burn Results
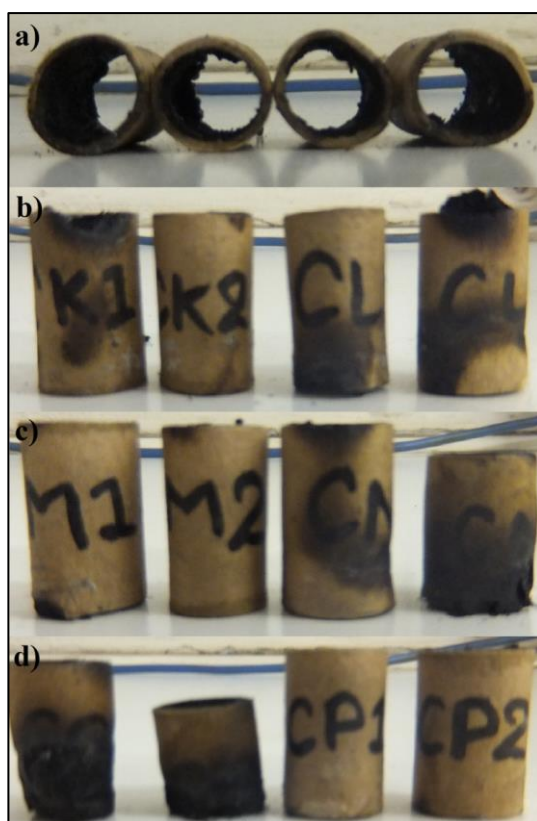
Figure 3.7.10 - CsNO$_3$ Composition Burn Test Residues a) CI1, CI2, CJ1, CJ2, b) CK1, CK2, CL1, CL2, c) CM1, CM2, CN1, CN2, d) CO1, CO2, CP1, CP2

Ba(NO$_3$)$_2$ compositions did not burn due to the lack of void spaces within the samples.

3.8   DISCUSSION OF FACTORS INFLUENCING PERFORMANCE

There are a number of factors which influence the way in which a pyrotechnic performs; homogeneity of a composition, particle size, choice of oxidiser, and oxidiser to fuel ratio. These factors are discussed here based on the results of this study.

3.8.1   OXIDISER SELECTION

On moving down Group 1, the quality of the pyrotechnic effect tended to increase. The intensity of the colour produced from the $CsNO_3$ compositions was much greater than either of the other two main oxidisers studied in this work. This is likely to be due to the pyrotechnic mixture being less fuel rich than the others and therefore it requires less atmospheric oxygen to sustain burning. Table 3.8.1 details the results from analysing the metal nitrate mixtures using the Pyro Valency Method.[15] This method is based on the concept of oxidation numbers. It utilises the concentration of the oxidation numbers associated with each element and assumes that the products which result are their most stable form. A more positive value indicates a mixture is fuel rich whereas a negative value is oxygen rich. A value of zero indicates equilibrium between both.

	Fuel	*Oxidiser*		
	Lactose ($C_{12}H_{22}O_{11}.H_2O$)	**KNO_3**	**$RbNO_3$**	**$CsNO_3$**
Weight (g)	*7.5(K), 6.1(Rb), 5.1(Cs)*	*7.5*	*8.9*	*9.9*
Formula Weight (g/mol)	*360.3*	*101.1*	*147.5*	*195.0*
No. of Moles	*0.021, 0.017, 0.014*	*0.074*	*0.060*	*0.051*
Valence/Mole	*+48*	*-8*	*-8*	*-8*
Valence/Formula	*+1.008, +0.816, +0.672*	*-0.592*	*-0.480*	*-0.408*
		+0.416	***+0.336***	***+0.264***
		Fuel Rich		

Table 3.8.1 - Pyro Valence Method for Metal Nitrate Compositions coupled with Lactose

The greatest heat generated, though not quantitatively analysed, was attributed to KNO_3 compositions. It was apparent that on moving up the group, metal nitrates tend to be more hygroscopic which is not desirable for pyrotechnic compositions.[15]

3.8.2   ALTERNATING OXIDANT/FUEL RATIO

As the oxidant:fuel ratio was increased there was a general increase in heat of reaction especially for KNO_3 containing compositions. The cardboard tubes containing the powders disintegrated (due to burning) as the compositions burned. Each of the metal nitrate series tended to burn faster with the increase in oxidiser content with the exception of the last ratio. This decrease in burn rate was consistent with the cardboard tube also burning and the inability to distinguish the end burn time of the actual compositions. Another observation made on increasing the oxidant:fuel ratio was the change of colour of the smoke and the amount of smoke generated. Black smoke was generated by the compositions containing lower levels of oxidiser signifying that the materials were fuel rich. As they became more fuel lean the smoke became whiter.

	Fuel	*KNO_3 Ratio*		
	Lactose ($C_{12}H_{22}O_{11}.H_2O$)	**1st**	**2nd**	**3rd**
Weight (g)	*7.5(1), 5.4(2), 3.3(3)*	*7.5*	*9.6*	*11.7*
Formula Weight (g/mol)	*360.3*	*101.1*		
No. of Moles	*0.021, 0.015, 0.009*	*0.074*	*0.095*	*0.116*
Valence/Mole	*+48*	*-8*		
Valence/Formula	*+1.008, +0.720, +0.432*	*-0.592*	*-0.760*	*-0.928*
		+0.416	***-0.040***	***-0.496***

Table 3.8.2 - Pyro Valence Method for KNO_3 Compositions of varying ratios

The pyro valency values found in Table 3.8.3 and Table 3.8.4 indicate that for each oxidiser the second ratio is the closest to oxygen balance equilibrium.

	Fuel	*RbNO$_3$ Ratio*		
	Lactose (C$_{12}$H$_{22}$O$_{11}$.H$_2$O)	**1st**	**2nd**	**3rd**
Weight (g)	*6.1(1), 4.2(2), 2.4(3)*	*8.9*	*10.8*	*12.6*
Formula Weight (g/mol)	*360.3*	*147.5*		
No. of Moles	*0.017, 0.012, 0.007*	*0.060*	*0.073*	*0.085*
Valence/Mole	*+48*	*-8*		
Valence/Formula	*+0.816, +0.576, +0.336*	*-0.480*	*-0.584*	*-0.680*
		+0.336	***-0.008***	***-0.344***

Table 3.8.3 - Pyro Valence Method for RbNO$_3$ Compositions of varying ratios

	Fuel	*CsNO$_3$ Ratio*		
	Lactose (C$_{12}$H$_{22}$O$_{11}$.H$_2$O)	**1st**	**2nd**	**3rd**
Weight (g)	*5.1(1), 3.4(2), 1.9(3)*	*9.9*	*11.6*	*13.1*
Formula Weight (g/mol)	*360.3*	*195.0*		
No. of Moles	*0.014, 0.009, 0.005*	*0.051*	*0.059*	*0.067*
Valence/Mole	*+48*	*-8*		
Valence/Formula	*+0.672, +0.432, +0.240*	*-0.408*	*-0.472*	*-0.536*
		+0.264	***-0.040***	***-0.296***

Table 3.8.4 - Pyro Valence Method for CsNO$_3$ Compositions of varying ratios

3.8.3   PARTICLE SIZE INFLUENCE

For lighter molecular weight oxidisers such as NaNO$_3$ and KNO$_3$ the incorrect particle size could play a part in the prevention of ignition. There were two cases where KNO$_3$ did not ignite and both were at the smallest particle size. It was possible that the void volumes present within the samples were decreased to such a point that the flame front could not carry through the composition. It was unfortunately not possible to fully establish the change in pyrotechnic effect based solely on the particle size measurements. At smaller particle sizes, 38-90 μm, it was more difficult to assess the whole samples using CT. In terms of improving this study to gain more information

about these materials, longer scan times would be required at a higher resolution. In order to obtain a better understanding of the burn behaviours longer lengths of compositions would be required. 1g of material was insufficient to provide a measure for comparisons of particle sizes given the small deviations in burn time noticed between each particle size for each composition. The error margins between the average burn rates for each composition was greater than the differences noticed between each particle size. It would be advisable to burn a greater amount of material as well as burn several more of the same composition to assess its effect on performance.

3.8.4   MIXING EFFICIENCY/HOMOGENEITY

The mixing efficiency was best demonstrated by the comparisons made within the $RbNO_3$ series. Both the CT results, photography and photometry data all provided a consistent story and highlighted the disadvantages to poor quality mixing of materials. BD (Bad Mix) produced two distinct results compared to the others which produced reasonably consistent results. Whilst CP was notionally a bad mix, the actual imaging showed that the sample was relatively homogenous, however, based on burn test data (radiometry and videography) there were noticeable differences in burn behaviour. One of the CP samples was homogeneous and burned in a consistent manner (steady burn) whilst the other CP sample spluttered. A poor mixture will cause many problems as each sample removed from a single batch of composition may differ in terms of oxidiser/fuel ratio and consequently so will the density. The density of pyrotechnic mixture is important as slight variations in this property can have drastic effects on its behaviour. Well-mixed materials tend to be able to burn smoothly and at a specific rate. The dangers of using a poorly mixed composition are that a cluster of either fuel or oxidiser could cause an uneven burn. At one end of the scale we could see the material stop burning if say for example a large amount of fuel was burning rather than a mixture of fuel and oxidiser where there would not be enough oxygen generated to keep the material burning. At the opposite end of the scale if there was a pocket of oxidiser particles this may cause a substantial increase in pressure and cause the pyrotechnic to explode rather than burn. Neither of these cases is desirable for a pyrotechnic product, especially given that the majority of pyrotechnics are used to initiate another reaction.

This investigative approach allows for diagnostic assessment of the mixing quality of pyrotechnic compositions as has been shown by the comparisons of each dataset. In the majority of cases it was clear to see by eye when a mixture was poorly mixed, however, a more quantitative approach was necessary to establish the homogeneity of a mix. The initial quantitative approach was to determine the average grayscale values associated with regions of interest and assess their variation. This not only allowed for an estimate of the quality of a mixture but it also provided a rough indication of the concentration of fuel and oxidiser within the areas/volumes investigated. Next, the number of particles within a given area/volume were assessed, providing a means to identify their locations, accurately estimate their areas/volumes and sphericity value. A more accurate determination of the concentration of each component can be estimated using this approach and consequently their densities. This would also provide a means to assess particle size distribution if one were dealing with a bimodal or trimodal mixture. The final approach was to use tessellation coupled with CoV to allow the direct assessment between samples as CoV was particle size independent but it also gave specific values associated with separation distances between particles; near neighbours.

At an atomic scale it is all 'inhomogeneous' of necessity (*i.e.* different elements need to react) but at what 'larger' length scale is 'homogeneity' critical. This is entirely dependent on the system under investigation and its purpose. In pyrotechnics it is necessary from nanoscale and upwards to manufacture homogeneous mixtures in order to ensure the components are in intimate contact. It is important because these materials are typically governed by solid state reactions *i.e.* mass transport rates between reactants whereas explosives release their energy much faster because they are ruled by chemical kinetics-control.[1] The methods discussed previously show it is possible to assess the degree of mixing homogeneity whilst also extracting other information such as particle size distribution, bulk densities, amongst others.

3.9   CONCLUSION

Using CT analysis as a route to investigate pyrotechnic compositions is particularly useful especially for cases where there is a sufficient difference in attenuation between fuel and oxidiser components. As the oxidiser particle size was reduced, the distinct particle shapes became more difficult to observe and this issue was enhanced by increasing oxidiser content. However, it would be possible to carry out longer scans with a smaller field of view to obtain a clearer picture of the particle outlines for compositions containing smaller particle sizes. By visual assessment of the CT datasets it was clearly evident when the number of mixing cycles was insufficient to allow the manufacture of a homogeneous mixture in all cases except one, CP. It is assumed that $CsNO_3$ compositions were more readily mixed.

As has already been stated no one image analysis approach will easily cover all of the conceivable ways that both phases and particles behave and as such it is useful to trial various tools and extract the information provided by each to obtain a better understanding of granular media. Numerous tools were used in this study to investigate mixing efficiency, these included grayscale averaging which provided an indication of the contribution of each pyrotechnic ingredient. The concentration of each component was estimated by using these average grayscale values to assess whether sections within the volume, or the entire volume, are oxidiser rich or fuel rich although these values would not be conclusive. Extending on this approach we used 2D and 3D algorithms to ascertain the particle count. Along with the number of particles, their locations, areas/volumes and sphericity values were also provided allowing a more accurate determination of the concentration of each component. Tessellation tools combined with diagnostic tools, such as CoV, provide great value in the assessment of powder mixtures as they were able to quantify the mixture quality based on the distribution of a single component within a mixture.

Although KNO_3 compositions could not be fully assessed by CT analysis because of the small difference in attenuation values between the fuel and oxidiser, their burn test results were interesting as these showed the greatest variation in burn rate moving from one ratio to the next (1st ratio 0.50 mm/secs, 2nd ratio 2.00 mm/secs, 3rd ratio 0.20

mm/secs). The main observation which can be concluded from this is the rapid increase in burn rate on moving from the 1st ratio to the 2nd ratio as the last ratio's burn rate suggests it burns more slowly however, this was a compound effect of the container burning in addition to the composition. $RbNO_3$ compositions showed only small variations in burn rate moving from one ratio to the next (1st ratio 2.25 mm/secs, 2nd ratio 3.00 mm/secs, 3rd ratio 1.00 mm/secs). $CsNO_3$ compositions showed only small variations in burn rate moving from one ratio to the next (1st ratio 2.00 mm/secs, 2nd ratio 3.00 mm/secs, 3rd ratio 1.50 mm/secs). Moving towards oxygen balance (2nd ratio) for each composition provides the fastest burn. Moving past this point (3rd ratio) there was a noticeable decrease in burn rate for all oxidiser compositions possibly attributed to smaller generation of hot gases attributed to there being less fuel to evolve CO_2 from the compositions as they burned.

In hindsight it may have been better to have larger volumes of compositions investigated in order to effectively evaluate the impact of particle size, change of oxidiser and oxidiser to fuel ratio *etc.* This would have required longer lengths of convoluted cardboard tubes rather than ones with a greater diameter as the path length that the X-rays pass through must be reasonably low as the oxidisers themselves are very dense. If the path length/quantity of oxidiser was increased, laboratory μCT facilities will be of necessity to require a reduction in resolution as tube energy/power is increased, increasing the X-ray spot size. Longer composition lengths would have allowed for longer burning times which may have been useful to have a proper indication of how the burn rates differed. 1g of composition was insufficient to definitively ascertain the impact of changes in particle size, oxidiser, oxidiser to fuel ratio and quality of mixing.

This approach to characterising a powder mixture would be particularly useful to allow the comparison of different mixing mechanisms *e.g.* tumbling powders or sieve mixing. This could be used to compare the efficiency of various pieces of mixing equipment from one another to allow the selection of the most appropriate mixer for a specified product. It also could be useful to compare resultant mixtures on moving from a small scale laboratory mixing system to a large scale industrial setup to assess if there are any differences which arise as a consequence of scaling up the mixing process.

This chapter has shown a means to characterise compositions to assess their homogeneity and briefly highlighted the problems of physically mixing pyrotechnic ingredients. Moving away from traditional manufacturing approaches, the next chapter suggests a different means to make pyrotechnic products by using crystal engineering tools to ensure that both fuel and oxidiser ingredients are in intimate contact. Instead of physically mixing pyrotechnic ingredients we propose chemically binding them.

References

1.   Teipel, U., *Energetic Materials - Particle Processing and Characterization*. WILEY-VCH: 2005; p 621.

2.   Berger, B., *Propellants Explos. Pyrotech.* **2005,** *30* (1), 27-35.

3.   Steinz, J. A.; Stang, P. L.; Summerfield, M. *Effects of Oxidizer Particle Size on Composite Solid Propellant Burning: Normal Burning, Plateau Burning and Intermediate Pressure Extinction*; Princeton University Princeton University 1967; p 18.

4.   Wild, A. M. *The measurement and control of particle size in pyrotechnic ingredients*; Royal Armiment Research and Development Establishment: 2008; p 17.

5.   Davies, N., *Pyrotechnics Handbook*. Cranfield University; Defence College of Management and Technology; Department of Applied Science, Security and Resilience: 2009.

6.   Fathollahi, M.; Pourmortazavi, S. M.; Hosseini, S. G., *Combust. Flame* **2004,** *138* (3), 304-306.

7.   Ivanov, Y. F.; Osmonoliev, M. N.; Sedoi, V. S.; Arkhipov, V. A.; Bondarchuk, S. S.; Vorozhtsov, A. B.; Korotkikh, A. G.; Kuznetsov, V. T., *Propellants Explos. Pyrotech.* **2003,** *28* (6), 319-333.

8.   Brown, M. E.; Taylor, S. J.; Tribelhorn, M. J., *Propellants Explos. Pyrotech.* **1998,** *23* (6), 320-327.

9.   Chant, J.; Blair, L. H.; Li, Z.; Yang, S.; Coles, S. J.; Sinclair, I., Online Mixing Technology and Mixture Characterisation - Summer Internship Project. 2012.

10. Yang, N.; Boselli, J.; Sinclair, I., *Journal of Microscopy* **2001,** *201* (2), 189-200.

11. Schneider, C. A.; Rasband, W. S.; Eliceiri, K. W., *Nat. Meth.* **2012,** *9* (7), 671-675.

12. Schindelin, J.; Arganda-Carreras, I.; Frise, E.; Kaynig, V.; Longair, M.; Pietzsch, T.; Preibisch, S.; Rueden, C.; Saalfeld, S.; Schmid, B.; Tinevez, J.-Y.; White, D. J.; Hartenstein, V.; Eliceiri, K.; Tomancak, P.; Cardona, A., *Nat. Meth.* **2012,** *9* (7), 676-682.

13. VisualizationSciencesGroup Avizo® Fire. http://www.vsg3d.com/avizo/fire (accessed 04/09/2012).

14. Hao, Y.-J.; Tanaka, T., *Can. J. Chem. Eng.* **1988,** *66*, 761-766.

15. Conkling, J. A., *Chemistry of pyrotechnics: basic priniciples and theory*. 10th ed.; M. Dekker: New York, 1985; p 190.

CHAPTER 4

Results and Discussion (Molecular Control – Binary Systems)

4.1   INTRODUCTION

Co-crystals, defined as a system where two or more components exist within the same crystalline lattice, offer great potential to change physicochemical properties of known materials. Thus far the pharmaceutical industry has been the main contributor to research in this area of crystal engineering. Through the use of co-crystals, improvements in dissolution rate, thermal stability, and bioavailability of Active Pharmaceutical Ingredients (APIs) have been recognised. More recently, the energetic materials industry has become active in this area of research with the aim of improving properties of existing compounds in terms of their stability/sensitivity and performance. The design of energetic co-crystals up until now has been defined by a very narrow range of functional groups, such as the weakly interacting nitro groups. These are much less robust in terms of crystal engineering when compared to their hydrogen bonded counterparts in the pharmaceutical industry.[1] [2]

Matzger and Bolter were one of the first to create a set of energetic co-crystals. They made an energetic-energetic co-crystal containing CL-20 (2,4,6,8,12-hexanitro-2,4,6,8,10,12-hexaazaisowurtzitane) and TNT (trinitrotoluene). It provided the economy and stability of TNT whilst retaining the density and power of CL-20. One of the other interesting findings they made was that if an energetic and a non-energetic component are combined the non-energetic component has the effect of diluting the energetic material. This was beneficial in some ways as the thermal stability was improved and the density was increased but the explosive power was reduced.[3] Numerous energetic co-crystals have been discovered since this work. [1, 2, 4]

Much of the research in the energetic materials field has focused on explosives. This work focuses on creating pyrotechnic co-crystals by incorporating both fuel and oxidiser components within a single crystalline lattice. Tetrafluoroterephthalic acid

(H$_2$fBDC) was chosen as a potential oxidiser as it was analogous to a fuel already used by the pyrotechnic industry, terephthalic acid (H$_2$BDC). Wang *et al.* have utilised this material in combination with various N-heterocyclic aza compounds known for their energetic properties in order to distinguish its versatility as a supramolecular construct relative to its non-fluorinated equivalent.[5, 6] A similar approach has been utilised here, using other N-heterocycles (fuels) with fluorinated diacids (oxidiser).

In this chapter, the formation of co-crystals, salts, and hydrates containing N-heterocycles and H$_2$fBDC are discussed. Single crystal structure determinations of co-crystals based on combinations of oxidiser and fuel ingredients shall be presented throughout this chapter. Their bulk characterisation as well as their thermal properties will also be discussed.

These structures will be discussed in terms of the intermolecular interactions which govern their final molecular assembly. Strongest interactions will be highlighted along with common packing arrangements. Thermal observations will also be summarised after the structural discussion to pull out any connections to stability of each of the binary systems with the final DSC trace and burn test results.

This chapter is divided into four parts:

4.2 N-containing Heterocyclic Structures

4.3 Crystal Packing Arrangements

4.4 Thermal Analysis of Binary Systems

4.5 Conclusion

Where a CSD reference code is given in Table 4.1.1 the crystallographic data for the compound was obtained from the CSD.[7] Any further information about the compound was gathered from the literature. Microcrystalline products were assessed using PXRD to ascertain whether the products were either of the two starting materials or a new product.

Unless stated, the transferrable hydrogen atom positions were found in the electron difference density map, and their correct assignment was confirmed not only by the difference between the C-O and C=O bond lengths, but also by moving the hydrogen atom to the other possible position and seeing where it refined to. All other hydrogen positions were added at calculated positions and refined using a riding model. Transfer of one or more hydrogen atoms from a diacid to a base meant that a salt had formed.

X-ray crystal structure figures for each structure display the molecules present in the asymmetric unit and the numbering scheme. Thermal ellipsoids are drawn at 50% probability; hydrogen atoms are shown as spheres. The cell dimensions for each of the products are listed in the Appendix, Table A6. The crystal structure CIFs, PXRD and DSC data are available on the Appendix CD.

	Tetrafluoroterephthalic acid (fBDC)	Tetrafluoroisophthalic acid (isofBDC)	Tetrafluorophthalic acid (altfBDC)
Pyr	Blocks SXRD	-	Blocks SXRD
MPyri	Blocks SXRD	-	Chips SXRD (high angle)
Idn	Blocks SXRD	Chips SXRD	Needles SXRD
DMIdn	Chunks SXRD	-	Microcrystalline
Mo	Plates SXRD	Blocks SXRD	Chips SXRD
AMo	Blocks SXRD	-	-
NPy	Blocks SXRD	Microcrystalline	Plates SXRD
DNPy	Chips SXRD	Prisms SXRD	Blocks SXRD
3NONPy	Chips SXRD	Starting Material Mixture	Blocks SXRD
5NONPy	Plates SXRD	Plates SXRD	Needles SXRD
DMNPym	Blocks and Plates SXRD	Plates SXRD	Chips SXRD
Az	Starting Material Mixture	Starting Material Mixture	Starting Material Mixture
Tri	Starting Material Mixture	Starting Material Mixture	Starting Material Mixture
Im	KURBUV[8]	Fine Hairs	Chips SXRD
2MI	Chips SXRD	Microcrystalline	Plates SXRD
4MI	Blocks SXRD	Chips SXRD	Chips SXRD
1AI	KURBUV	Microcrystalline	Chips SXRD
4NOI	Starting Materials Reacted	Starting Materials Reacted	Starting Materials Reacted
DMI	Chips SXRD	Microcrystalline	Chips SXRD
Tro	Chips SXRD	Plates SXRD	Chips SXRD
3NTro	Blocks SXRD	Fine Hairs	Fine Hairs
5NOIn	Starting Materials Reacted	Starting Materials Reacted	Starting Materials Reacted
MR	Starting Material Mixture	Starting Material Mixture	Starting Material Mixture
S3	Starting Material Mixture	Starting Material Mixture	Starting Material Mixture
MY3/MO1	Starting Material Mixture	Starting Material Mixture	Starting Material Mixture

Table 4.1.1 - Observations from co-crystallisation experiments and their relative method of analysis utilised.

The majority of the identified products (salts, salt hydrates, co-crystals) result from combinations with fBDC and altfBDC, whilst isofBDC remained in solution or resulted in microcrystalline material in the majority of cases. When combining each of the substituted fluorinated acids with either 4NOI (4-nitroimidazole) or 5NOIn (5-nitroindazole) it was found that the components reacted to form a white powder. All co-crystallisations using 1AI (1-acetylimidazole) were found to result in decomposition products whereby the acetyl group was removed from imidazole. Similar findings were discovered for the co-crystallisation of fBDC and 3NTro (3-aminotriazole) where an amino group had been displaced. Combinations involving Az (pyrazine), Tri (triazine), and each of the dye materials MR (methyl red), S3 (sudan III), and MO1 (mordant orange 1) were found to result in a mixture of starting materials. Although neither a salt nor co-crystal formed in combination with Az an interesting observation was made; a clear to strong pink colour change was noted as the carboxylates moved from positions 1, 4 to 1, 2 whereby the colour intensity increased as the carboxylates were in closer proximity to one another. It is suspected that there are various charge transfer interactions between the aromatic pyrazine molecules and the various substituted fluorinated diacids which cause this colour change. As the carboxylates changes from positions 1, 4 to 1, 2 the carboxylates twist in relation to one another. Within 1,4 fBDC the carboxylates lie along the same plane at 20° to the benzene ring (BITCEM)[9] whereas for 1,3 fBDC (ODUSEM)[10] the carboxylates are ~40° in relation to one another. The carboxylates of 1,2 fBDC (BOLNAR)[11] each differ with respect to the benzene ring one being ~10° and the other being ~80°. This noted change was not evaluated for this work however, the use of UV-Vis analysis, chromatography and NMR ((nuclear magnetic resonance) based on shifts noted within the solutions) would be able to provide a qualitative and quantitative measure of how the change in carboxylate positions affects the colour intensity.

The following section describes each crystal structure and highlights the intermolecular interactions which govern their molecular assembly.

4.2   N-CONTAINING HETEROCYCLIC STRUCTURES

4.2.1   AZOLES HETEROCYCLES
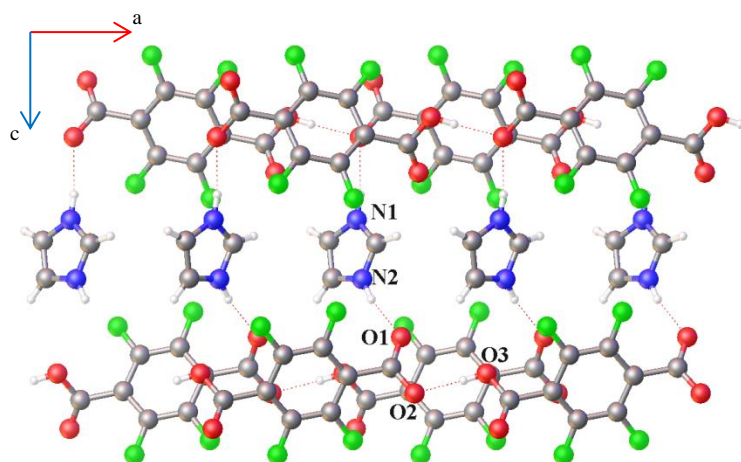
fBDC_Im = fBDC_1AI = KURBUV

Orthorhombic	*Pna2₁*
a = 9.716(3) Å	α = 90°
b = 7.229(3) Å	β = 90°
c = 17.406(6) Å	γ = 90°
V = 1222.54 Å³	Z′ = 1.000

fBDC_Im crystallised in a 1:1 ratio as a salt. The asymmetric unit contains a fBDC molecule and one Im molecule. Monoanion chains are observed which form along crystallographic axis a (O2-H1···O3 = 1.724Å). Further hydrogen bonding between monoanion chains and protonated Im molecules leads to the formation of 2D sheets (N1-H2···O2 = 2.034Å, N2-H3···O1 = 1.885Å)
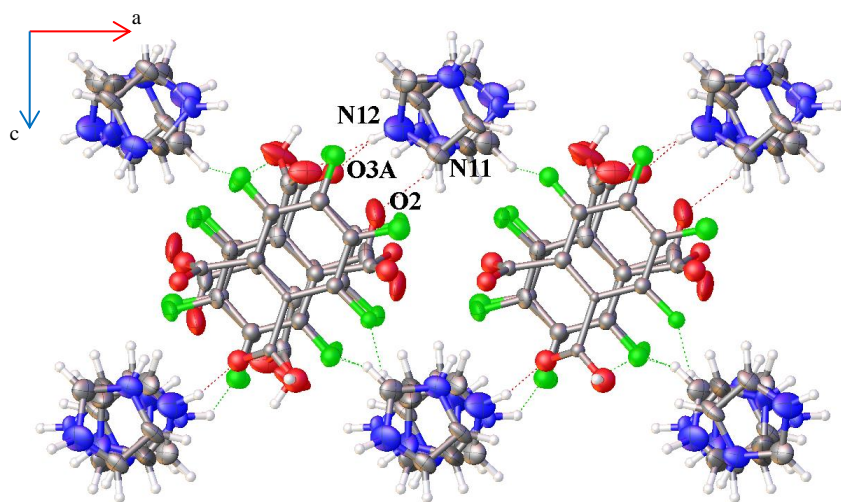
altfBDC_Im = (altfBDC_1AI)

Monoclinic	*C2/c*
a = 17.0193(15)Å	α = 90°
b = 7.7530(5) Å	β = 92.472(10)°
c = 17.1572(11) Å	γ = 90°
V = 2261.8(3) Å³	Z′ = 1.000

altfBDC_Im crystallised in a 1:1 ratio as a salt. The asymmetric unit contains an altfBDC molecule and one Im molecule all of which are disordered over two sites. Base molecules connect monoanion chains in two directions creating a 3D supramolecular structure (O2-H2···O1 = 1.718Å, O4-H4···O4 = 1.721Å, N11-H11···O2 = 1.931Å, N12-H12···O3 = 1.622Å). One of the hydrogen bonds associated with the diacids is bifurcated.

148
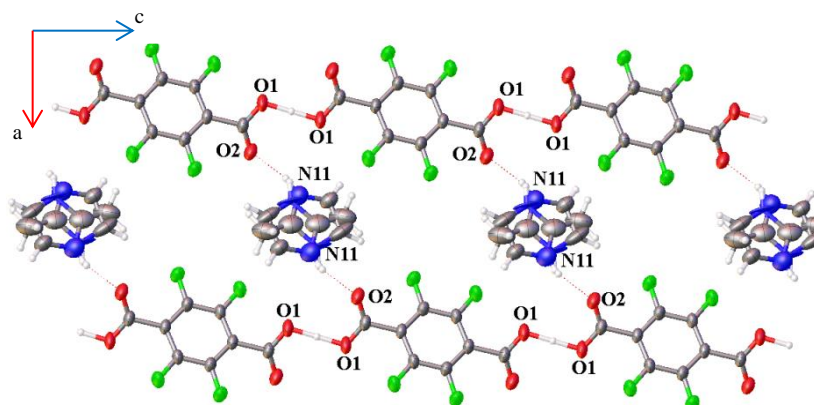
fBDC_2MI

Monoclinic $P2_1/c$

a = 9.2084(5) Å   a = 90°

b = 7.3851(5) Å   b = 97.547(2)°

c = 9.6353(7) Å   c = 90°

V = 649.57(7) Å^3 Z′ = 0.500

fBDC_2MI crystallised in a 0.5:1 ratio as a salt. Monoanion chains(O1-H1···O1 = 1.238Å) form along crystallographic axis c. 2MI is disordered over two positions as can be seen in the figure above. The chains are connected by 2MI molecules creating a 2D supramolecular structure mediated by hydrogen bonding (N11-H11···O2 = 1.819Å).
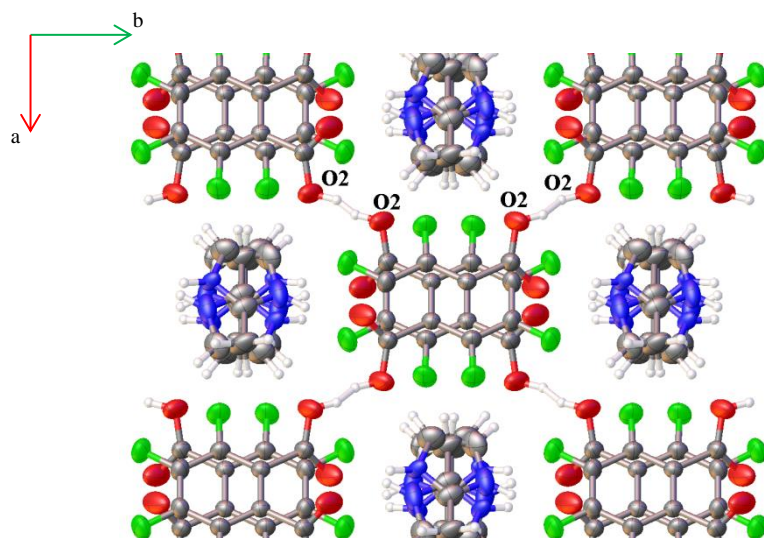
altfBDC_2MI

Monoclinic $C2/c$

a = 12.1886(11) Å   a = 90°

b = 12.3727(11) Å   b = 112.570(11

c = 9.4275(7) Å   c = 90°

V = 1312.8(2) Å^3 Z′ = 0.500

altfBDC_2MI crystallised in a 1:1 ratio as a salt. The asymmetric unit contains half an altfBDC molecule and one half occupied 2MI molecule. Structures which incorporate 2MI have shown to be consistently disordered in the same manner. Base molecules connect each chain to another two chains creating a 3D supramolecular structure mediated by hydrogen bonding (O2-H2···O2 = 1.668Å, 1.721Å, N11-H11···O1 = 1.804Å, N12-H12···O1 = 1.916Å).
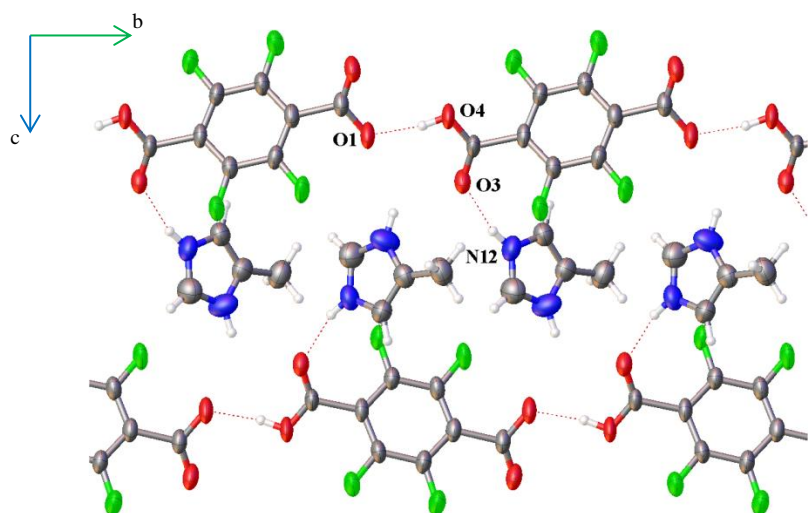
fBDC_4MI

Orthorhombic $P2_12_12_1$

a = 7.2233(5) Å   a = 90°

b = 9.6951(7) Å   b = 90°

c = 18.3487(13) Å   c = 90°

V = 1284.97(16) Å³   Z′ = 1.000

fBDC_4MI crystallised in a 1:1 ratio as a salt. Monoanion chains(O4-H4···O1 = 1.693Å) form along crystallographic axis b. Two chains are hydrogen bonded through base molecules to form a wider chain (N11-H11···O3 = 2.020Å, N12-H12···O3 = 1.945Å).
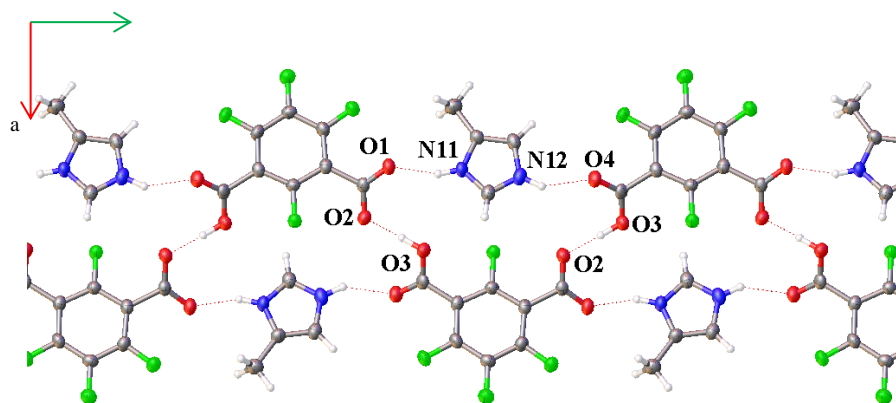
isofBDC_4MI

Monoclinic $P2_1/c$

a = 12.4952(9) Å   a = 90°

b = 14.5165(10) Å   b = 98.090(3)°

c = 7.0035(5) Å   c = 90°

V = 1257.70(15) Å³   Z′ = 1.000

isofBDC_4MI crystallised in a 1:1 ratio as a salt. Monoanion chains(O3-H3···O2 = 1.556Å) form along crystallographic axis b. Base molecules accommodate themselves within the diacid chains and are stabilised by hydrogen bonding (N11-H11···O1 = 1.823Å, N12-H12···O4 = 1.962Å).
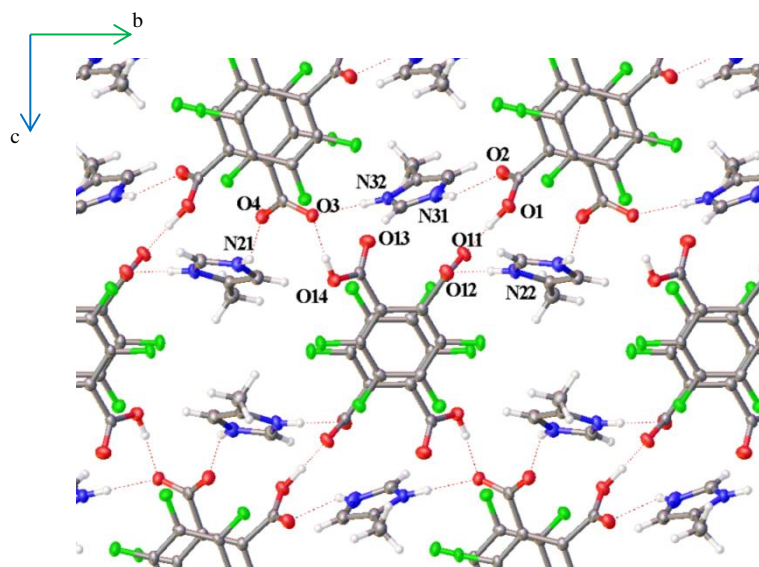
altfBDC_4MI

Triclinic   *P-1*

a = 7.5331(5) Å   α = 80.509(6)°

b = 11.0533(8) Å   β = 79.044(5)°

c = 15.5493(11) Å   γ = 80.805(6)°

V = 1242.64(15) Å^3 Z′ = 2.000

altfBDC_4MI crystallised in a 1:1 ratio as a salt. The asymmetric unit contains two altfBDC molecules and two 4MI molecules. Monoanion chains(O1-H1···O11 = 1.489Å, O14-H14···O3 = 1.708Å) form along crystallographic axis b and extend into 2D via hydrogen bonding links by 4MI between chains along the a axis(N21-H21···O4 = 1.966Å, N22-H22···O12 = 1.930Å, N31-H31···O2 = 2.060Å, N32-H32···O3 = 1.980Å).
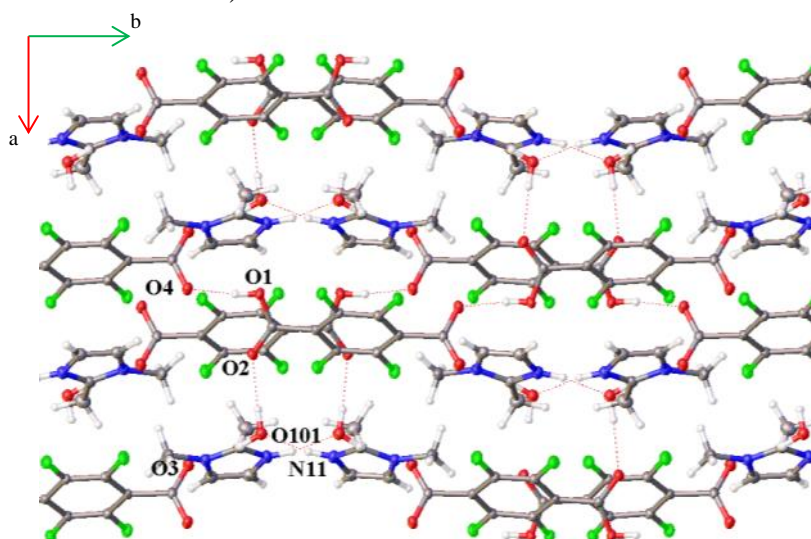
fBDC_DMI

Monoclinic   *P2$_1$/c*

a = 8.0471(5) Å   a = 90°

b = 18.6519(13) Å   b = 91.257(2)°

c = 9.5052(7) Å   c = 90°

V = 1426.33(17) Å^3 Z′ = 1.000

fBDC_DMI crystallised in a 1:1 ratio as a salt hydrate. Monoanion diacid chains form (O1-H1···O4 = 1.665Å) along crystallographic axis b. The chains are linked via water molecules to create 2D supramolecular sheets along crystallographic axis a (0101-H10a···O2 = 1.954Å, 0101-H10b···O3 = 1.982Å). Base molecules do not contribute to extending the dimensionality of the structure, they are hydrogen bonded to water molecules (N11-H11···O101 = 1.846Å).
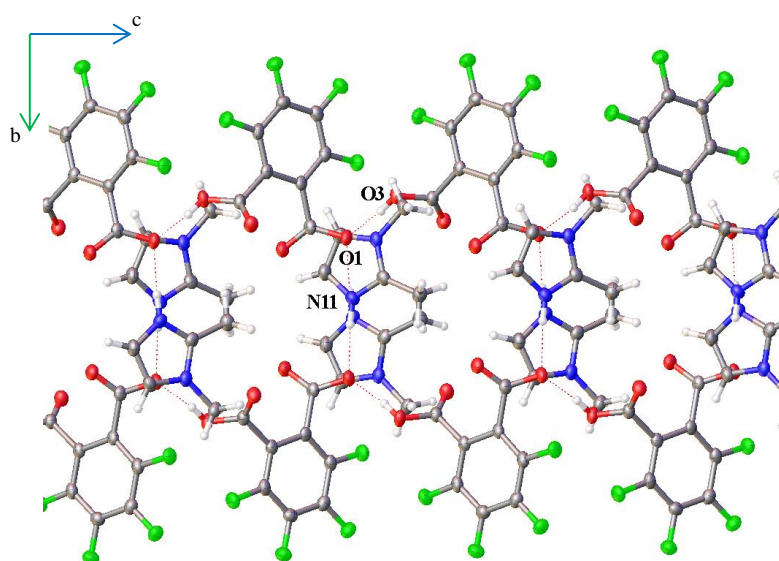
altfBDC_DMI

Orthorhombic $Pca2_1$

a = 7.6757(5) Å   a = 90°

b = 13.4117(9) Å   b = 90°

c = 13.0049(9) Å   c = 90°

V = 1338.78(16) Å^3 Z′ = 1.000

altfBDC_DMI crystallised in a 1:1 ratio as a salt. Chains form (O3-H3···O1 = 1.694Å) along the crystallographic axis c. (N11-H11···O1 = 1.824Å). One side of the chain is composed of the diacids whilst the other is occupied by the base molecules. The base molecules from one chain sit within the pockets created by the zigzag monoanion chain from another diacid base chain forming a bilayer motif like a lipid.
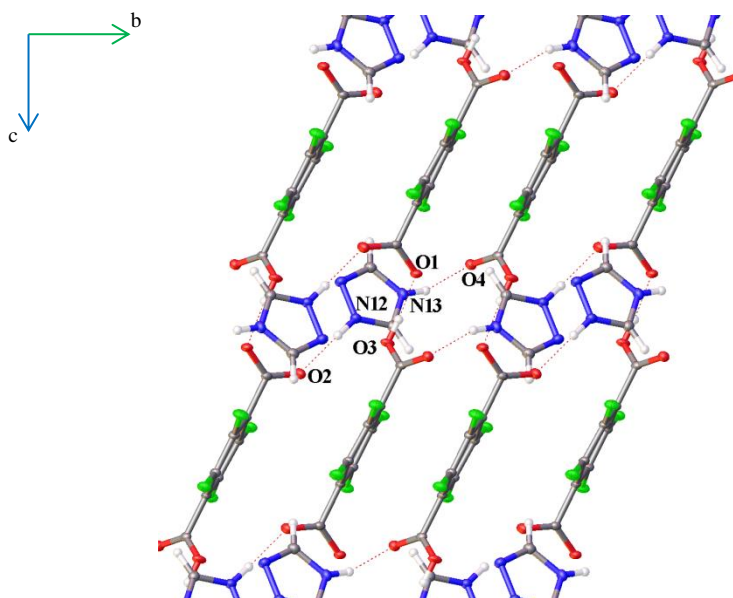
fBDC_Tro

Triclinic P-1

a = 7.6932(5) Å   α = 73.924(8)°

b = 8.1306(5) Å   β = 84.624(9)°

c = 9.5538(7) Å   γ = 70.797(8)°

V = 542.27(7) Å^3 Z′ = 1.000

fBDC_Tro crystallised in a 1:1 ratio as a salt. Monoanion diacid chains form (O3-H3···O1 = 1.632Å) along crystallographic axis c. Base molecules connect the chains to form a 2D network along crystallographic axis b (N12-H12···O2 = 1.818Å, N13-H13···O4 = 1.909Å).
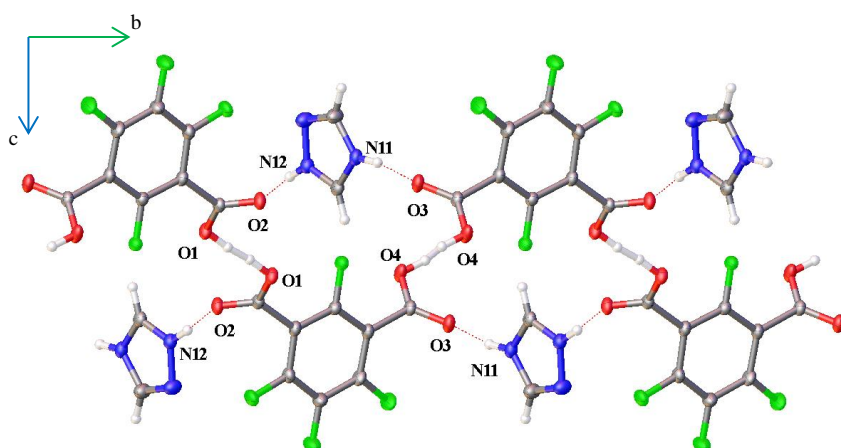
isofBDC_Tro

Triclinic   *P-1*

a = 4.6416(2) Å   α = 72.150(5)°

b = 11.3274(8) Å   β = 89.610(6)°

c = 11.3941(8) Å   γ = 84.359(6)°

V = 567.30(6) Å^3 Z′ = 1.000

isofBDC_Tro crystallised in a 1:1 ratio as a salt. Hydrogen atoms from the diacid chains are bifurcated (O1-H1···O1 = 1.644Å, O4-H4···O4 = 1.613Å). Base molecules connect the chains to create a 2D network (N11-H11···O3 = 1.852Å, N12-H12···O2 = 1.771Å).
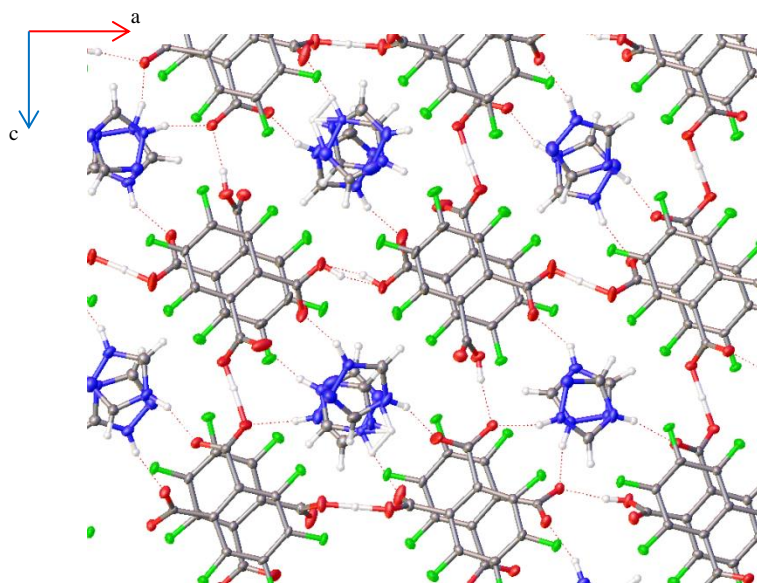
altfBDC_Tro

Monoclinic   *P2/c*

a = 26.6344(19) Å a = 90°

b = 7.7400(5) Å   b = 106.651(1)°

c = 33.874(2) Å   c = 90°

V = 6690.3(8) Å^3 Z′ = 6.000

altfBDC_Tro crystallised in a 1:1 ratio as a salt. The asymmetric unit comprises six altfBDC molecules and six Tro molecules. One of the six base molecules is disordered over two positions. The average hydrogen bond lengths for the diacid chains are O-H···O = 1.600Å. Base molecules connect chains in two directions with an average N-H···O = 1.830Å hydrogen bond length creating a 3D supramolecular structure. Some of the hydrogen bonds associated with the diacids are also bifurcated as observed in isofBDC_Tro.
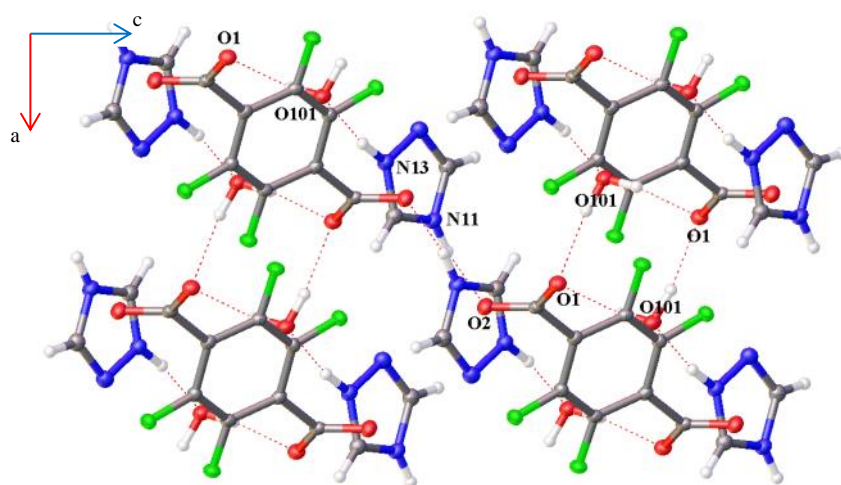
fBDC_3NTro

Triclinic	*P-1*
a = 5.6137(4) Å	α = 77.613(7)°
b = 8.0917(5) Å	β = 78.978(7)°
c = 8.9568(7) Å	γ = 82.252(7)°
V = 388.18(5) Å³	Z′ = 0.500

fBDC_3NTro crystallised in a 0.5:1 ratio as a salt hydrate. The product is a decomposition product as the amino group was removed from the system. Although the system was made up of the same components as another previously discussed structure, fBDC_Tro, a different crystal structure formed. This system incorporated water molecules. The inclusion of the water molecules provided additional hydrogen bond donors and acceptors allowing the system to develop into a 3D supramolecular arrangement. Typical monoanion diacid chains did not form within the system. The 3D arrangement arises from several hydrogen bonds which link each of the components to one another (N11-H11···O2 = 1.776Å, N13-H13···O101 = 1.732Å, O101-H10a···O1 = 1.868Å, O101-H10b···O1 = 1.904Å).

4.2.2   6-MEMBERED RING HETEROCYCLES
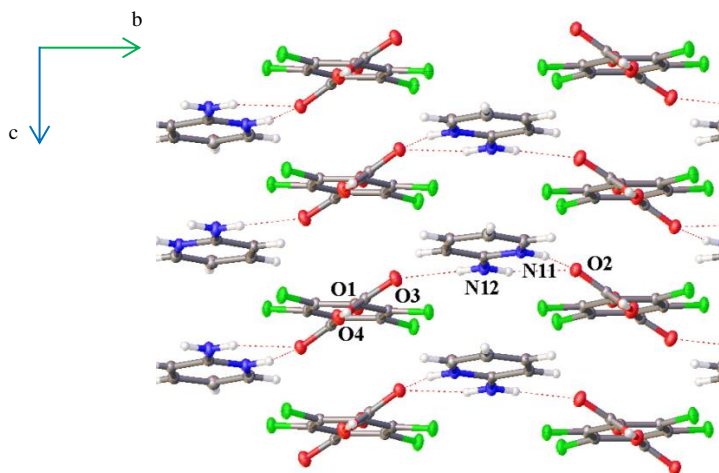
fBDC_NPy

Monoclinic $P2_1/c$

a = 9.7001(7) Å   a = 90°

b = 17.4712(11) Å   b = 112.681(1)°

c = 8.2971(5) Å   c = 90°

V = 1297.39(15) Å^3 Z′ = 1.000

fBDC_NPy crystallised in a 1:1 ratio as a salt, both fBDC molecules are monodeprotonated. It possesses a bifurcated hydrogen in which 66.7% of the time the hydrogen is placed on one side of the acid (O4) where the other 33.3% it's positioned on the other (O1). The components form a hydrogen bonded sheet structure. fBDC molecules form typical monoanion chains along crystallographic axis a (O4-H4···O1 = 1.581Å). The chains are crosslinked by NPy molecules through further hydrogen bonding (N11-H11···O2 = 1.903Å, N12-H12a···O2 = 2.169Å, N12-H12b···O3 = 2.074Å) to form corrugated 2D sheets.
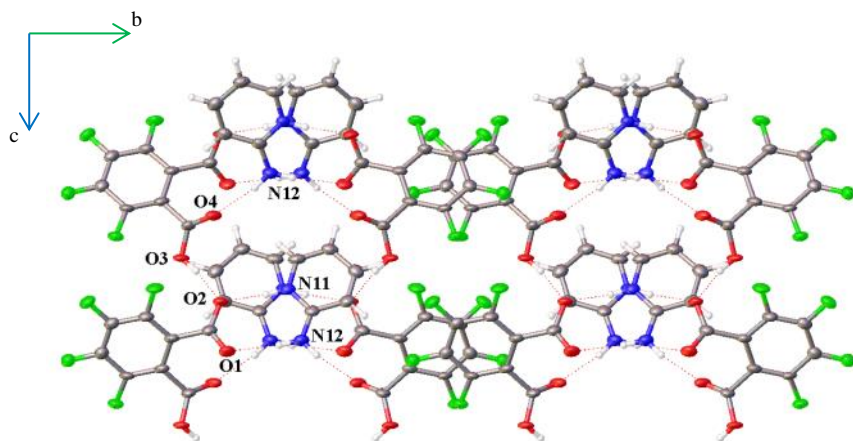
altfBDC_NPy

Orthorhombic $Pca2_1$

a = 7.5087(6) Å   α = 90°

b = 13.3571(10) Å   β = 90°

c = 12.9653(9) Å   γ = 90°

V = 1300.35(17) Å^3 Z′ = 1.000

altfBDC_NPy crystallised in a 1:1 ratio as a salt forming the same type of monoacid chains as were observed within altfBDC_DMI. (O3-H3···O2 = 1.693Å). Further hydrogen bonding between the monoanion chains and the NPy molecules leads to the formation of 2D sheets along crystallographic axis a (N11-H11···O2 = 1.793Å, N12-H12a···O1 = 2.032Å, N12-H12b···O4 = 2.091Å).

155
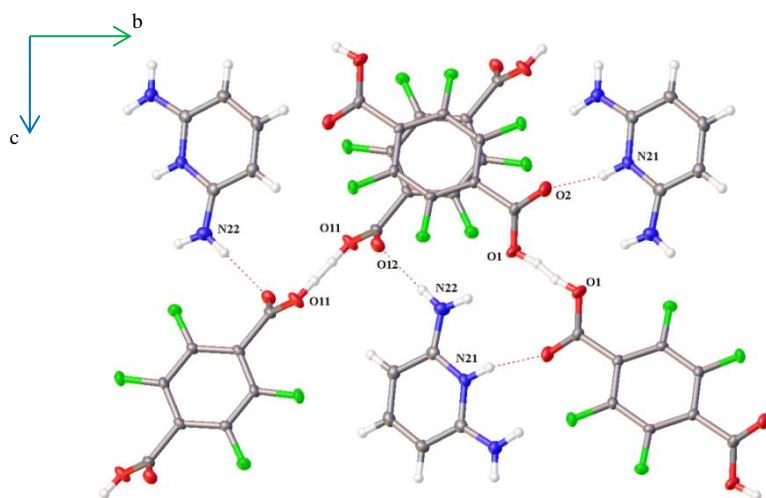
fBDC_DNPy

Triclinic   *P*-1

a = 7.5134(5) Å   α = 87.589(5)°

b = 9.6553(7) Å   β = 78.010(5)°

c = 9.6897(7) Å   γ = 88.793(6)°

V = 686.93(9) Å³   Z′ = 1.000

fBDC_DNPy crystallised in a 1:1 ratio as a salt. The asymmetric unit includes two halves of different fBDC molecules, which both lie across inversion centres, and one DNPy molecule. Hydrogens positioned on either side of the acids are half occupied. fBDC molecules form two distinct monoanion chains along crystallographic axis b and c (O11-H11···O11 = 1.622Å, O1-H1···O1 = 1.622Å). Chains are cross-linked by DNPy molecules by further hydrogen bonding leading to a supramolecular 3D architecture (N21-H21···O2 = 1.871Å, N22-H22b···O12 = 2.008Å)
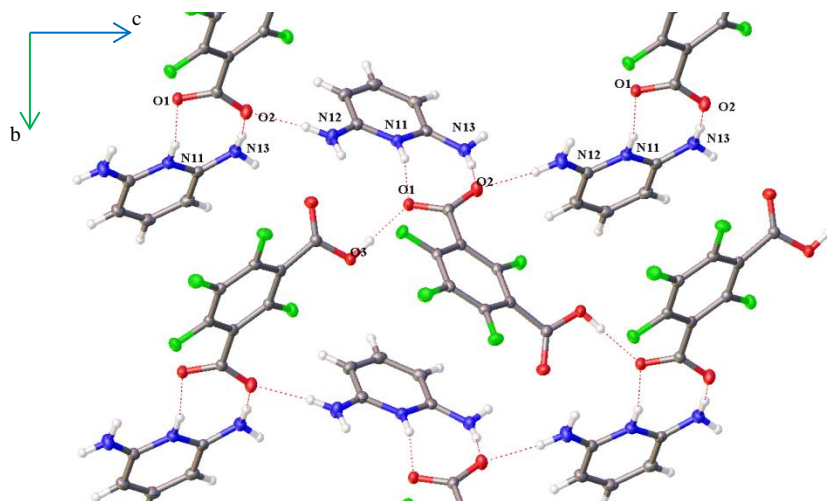
isofBDC_DNPy

Monoclinic   *Pc*

a = 5.4774(4) Å   α = 90°

b = 8.6080(5) Å   β = 95.254(2)°

c = 14.5149(10) Å   γ = 90°

V = 681.49(8) Å³   Z′ = 1.000

isofBDC_DNPy crystallised in a 1:1 ratio as a salt. The asymmetric unit contains an isofBDC molecule and one DNPy molecule. Monoanion chains are observed which form along crystallographic axis c (O3-H3···O1 = 1.722Å). Further hydrogen bonding between the monoanion chains and the DNPy molecules leads to the formation of 2D sheets (N11-H11···O1 = 2.011Å, N12-H12b···O2 = 1.940Å, N13-H13a···O2 = 1.929Å).
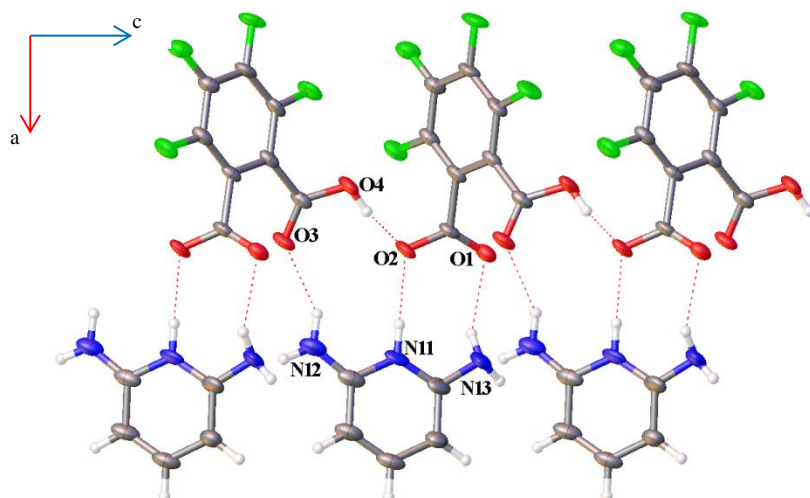
altfBDC_DNPy

Monoclinic   *P*2$_1$/*c*

a = 13.4821(9) Å   a = 90°

b = 8.9965(5) Å   b = 95.930(8)°

c = 11.6354(8) Å   c = 90°

V = 1403.73(16) Å^3 Z′ = 1.000

altfBDC_DNPy crystallised in a 1:1 ratio as a salt. Monoanion chains, seen previously in altfBDC_DMI are observed (O4-H4⋯O2 = 1.771Å) where one side of the chain is composed of diacids whilst the other is composed of base molecules. (N11-H11⋯O2 = 1.981Å, N12-H12a⋯O3 = 2.142Å, N13-H13b⋯O1 = 2.169Å).
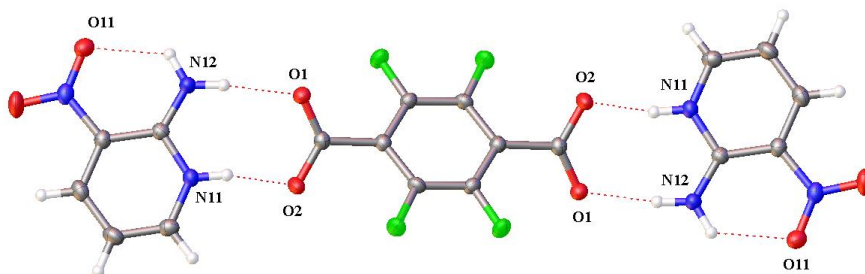
fBDC_3NONPy

Monoclinic   *P*2$_1$/n

a = 11.9143(8) Å   a = 90°

b = 5.7314(4) Å   b = 98.179(3)°

c = 14.2611(10) Å   c = 90°

V = 963.92(12) Å^3 Z′ = 0.5

fBDC_3NONPy crystallised in a 0.5:1 ratio. The acid hydrogens transferred to the base molecules resulting in a salt. The asymmetric unit contains one half fBDC molecule, which lies across an inversion centre, and one 3NONPy molecule. Two hydrogen bonded chains of alternate acid and base molecules develop along the ac plane and crystallographic axis b (N11-H11⋯O2 = 1.739Å, N12-H12a⋯O1 = 1.976Å, N12-H12b⋯O11 = 2.144Å).
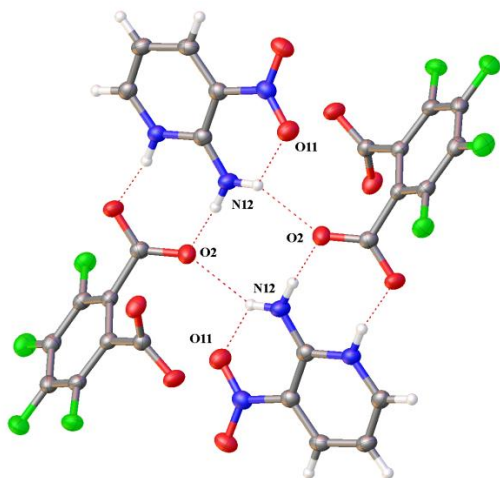
altfBDC_3NONPy

Orthorhombic   *Pbcn*

a = 18.9915(13) Å   a = 90°

b = 14.7926(10) Å   b = 90°

c = 6.9717(5) Å   c = 90°

V = 1958.6(2) Å^3 Z′ = 0.500

altfBDC_3NONPy crystallised in a 0.5:1 ratio. Acidic hydrogens were transferred to base molecules resulting in the formation of a salt. The asymmetric unit is composed of one half alt fBDC molecule, which lies across an inversion centre, and one 3NONPy molecule. Each carboxylate from the altfBDC molecules hydrogen bonds two 3NONPy molecules (N12-H12a···O2 = 1.915Å, N12-H12b···O2 = 2.113Å) resulting in the formation of 1D chains.
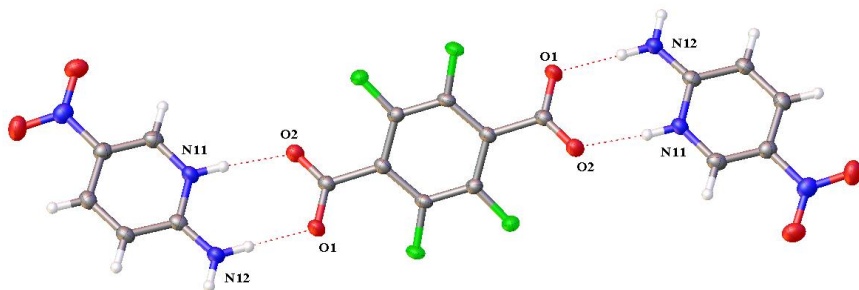
fBDC_5NONPy

Monoclinic   *P2$_1$/n*

a = 11.0144(8) Å   a = 90°

b = 5.7306(4) Å   b = 99.253(4)°

c = 15.0766(11) Å   c = 90°

V = 939.24(12) Å^3 Z′ = 0.500

fBDC_5NONPy crystallised in a 0.5:1 ratio. The asymmetric unit contains one half fBDC molecule, which lies across an inversion centre, and one 5NONPy molecule. Diacid hydrogens were transferred to base molecules resulting in a salt. Similarly to the pairing with 3NONPy two hydrogen bonded tapes of alternate acid and base molecules form which hydrogen bond to create 2D sheets (N11-H11···O2 = 1.897Å, N12-H12a···O1 = 1.821Å, N12-H12b···O1 = 1.998Å).
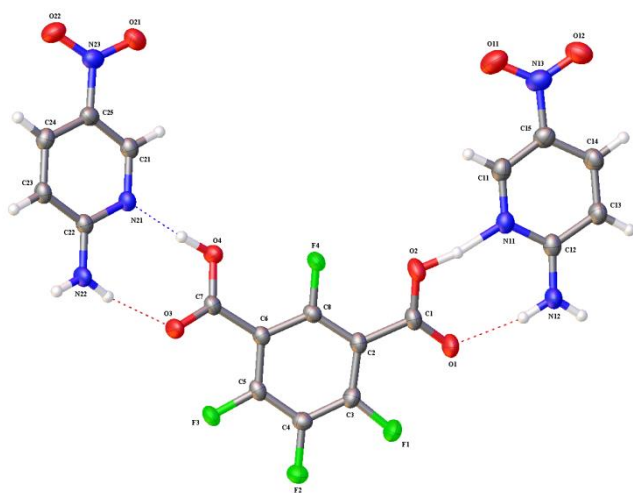
isofBDC_5NONPy

Monoclinic   *C*2/*c*

a = 40.957(3) Å   a = 90°

b = 5.5165(4) Å   b = 94.334(2)°

c = 17.5477(11) Å   c = 90°

V = 3953.4(5) Å^3 Z′ = 1.000

isofBDC_5NONPy crystallised in a 1:2 ratio. From SXRD data alone it was not possible to accurately assign this binary system as either a co-crystal or a salt as one of the hydrogen atoms from the carboxylates appears to be bifurcated, split between isofBDC and 5NONPy. Based on solely the hydrogen bond distances it would appear that this system forms a co-crystal. Similarly to the pairing with 3NONPy, two hydrogen bonded tapes of alternate acid and base molecules form (O2-H2···N11 = 1.458Å, N12-H12a···O1 = 1.971Å, O4-H4···N21 = 1.720Å, N22-H22a···O3 = 1.949Å, N22-H22b···O3 = 2.095Å). 2D sheets arise as tapes hydrogen bond to each other.
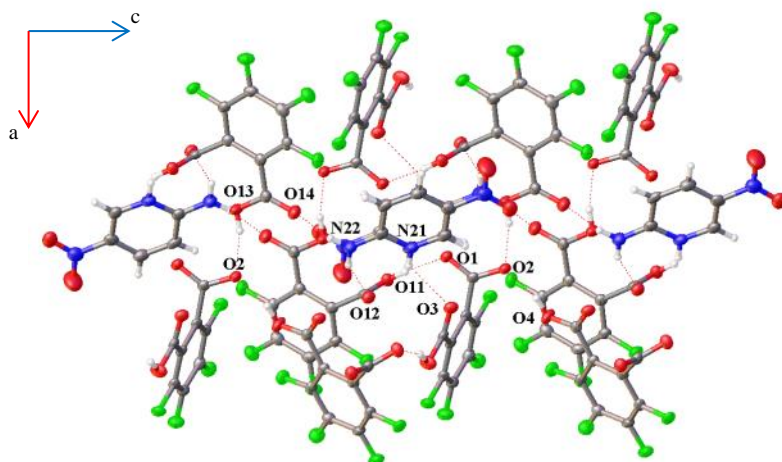
altfBDC_5NONPy

Orthorhombic   *Pbca*

a = 27.7330(19) Å   a = 90°

b = 15.5833(11) Å   b = 90°

c = 10.5778(7) Å   c = 90°

V = 4571.4(5) Å^3 Z′ = 1.000

altfBDC_5NONPy crystallised in a 2:1 ratio. The asymmetric unit contains two fBDC molecules and one 5NONPy molecule. Acid hydrogens were transferred to base molecules resulting in a salt. Two monoanion altfBDC chains form within this structure (O11-H11···O1 = 1.692Å, O4-H4···O2 = 1.701Å). These chains hydrogen bond to one another through O13-H13···O2 (1.777Å).   Chains are further stabilised by 5NONPy molecules which hydrogen bond between the two chains (N21-H21···O3 = 2.253Å, N22-H22a···O12 = 2.085Å, N22-H22b···O14 =1.969Å) resulting in 2D sheets.

fBDC_DMNPym_1

Monoclinic $P2_1/n$

a = 10.7556(8) Å   a = 90°

b = 6.7291(5) Å   b = 102.236(2)°

c = 15.6457(11) Å   c = 90°

V = 939.24(12) Å^3 Z′ = 0.500
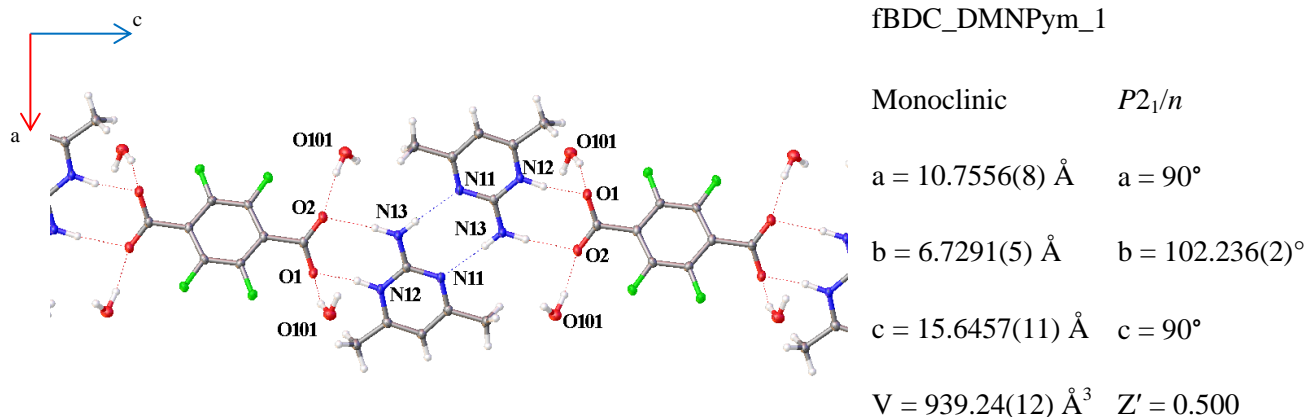
fBDC_DMNPym_1 crystallised in a 0.5:1 ratio as a salt hydrate. A chain composed of diacid base base repeating units formed (N12-H12···O1 = 1.704Å, N13-H13a···O2, = 2.020Å, N13-H13b···N11 = 2.145Å).These chains are stacked creating 2D sheets via hydrogen bonding to water molecules (O101-H10a···O1 = 2.080Å, O101-H10b···O2 = 1.960Å).

fBDC_DMNPym_2

Orthorhombic   *Pnma*

a = 14.5325(11) Å   a = 90°

b = 25.4428(19) Å   b = 90°

c = 3.8068(2) Å   c = 90°

V = 1407.55(17) Å^3 Z′ = 0.500
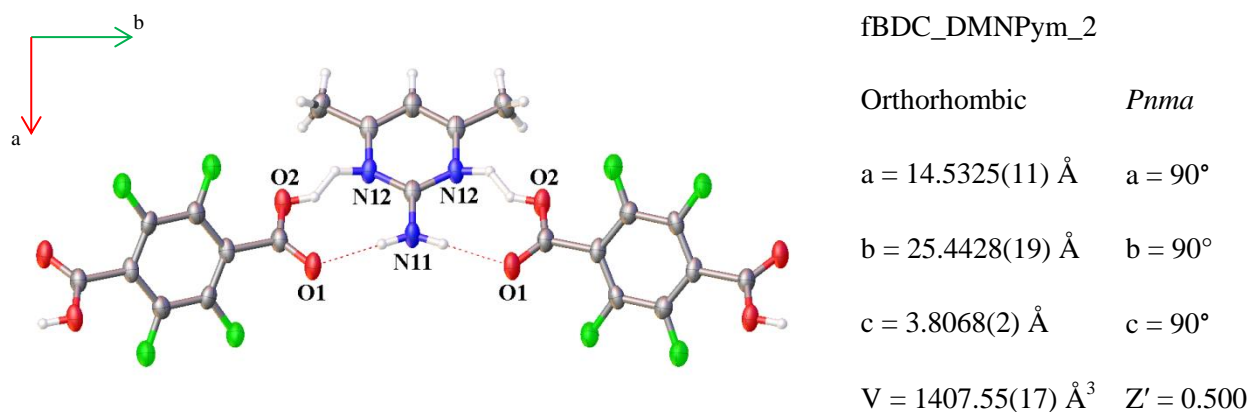
fBDC_DMNPym_2 crystallised in a 1:1 ratio as a salt. The asymmetric unit contains one half fBDC molecule, which lies across an inversion centre, and one half DMNPym molecule, which lies across a mirror plane. The hydrogen bonded chain is constructed of alternating diacid base molecules (N11-H11···O1 = 2.073Å, N12-H12···O2 = 1.702Å). One of the hydrogen atoms is split across the diacid and the base molecule.
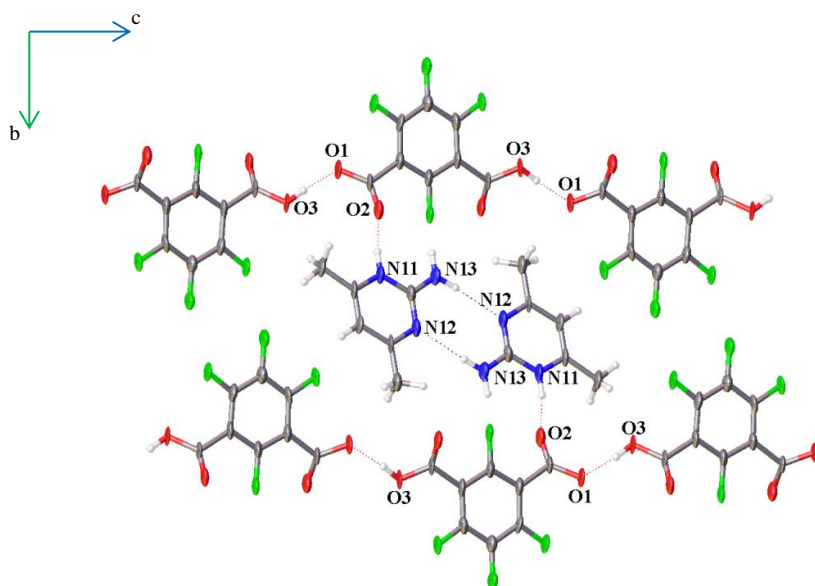
isofBDC_DMNPym

Monoclinic $P2_1/c$

a = 4.1071(2) Å   a = 90°

b = 20.2136(14) Å   b = 95.393(5)°

c = 17.2161(11) Å   c = 90°

V = 1422.94(15) Å^3 Z′ = 1.000

isofBDC_DMNPym crystallised in a 1:1 ratio as a salt. Monoanion chains are observed which form along crystallographic axis c (O3-H3···O1 = 1.675Å). Further hydrogen bonding between the monoanion chains and pairs of DMNPym molecules (N13-H13b···N12 = 2.188Å) leads to the formation of 2D sheets (N11-H11···O2 = 1.822Å).
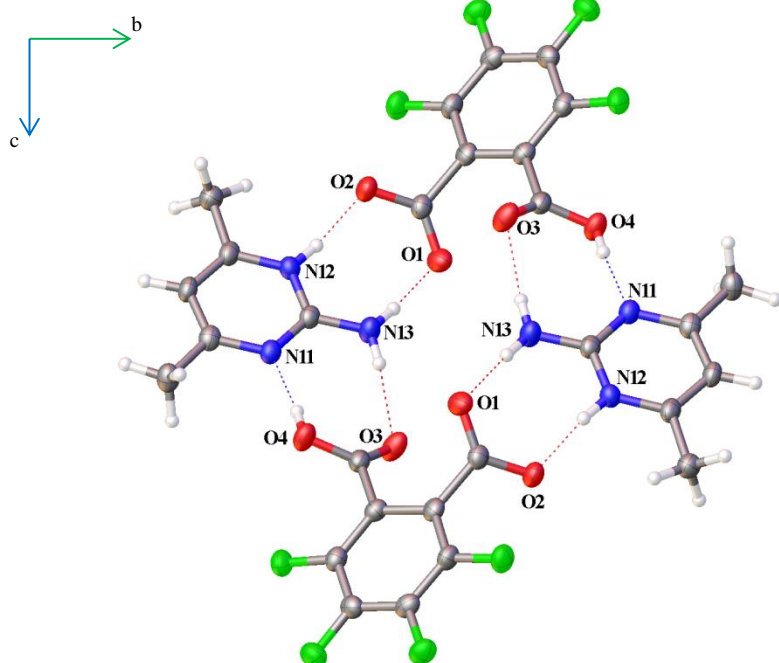
altfBDC_DMNPym

Triclinic P-1

a = 8.7030(5) Å   α = 81.583(11)°

b = 9.0169(5) Å   β = 73.347(1)°

c = 10.7766(8) Å   γ = 66.528(9)°

V = 742.67(10) Å^3 Z′ = 1.000

altfBDC_DMNPym crystallised in a 1:1 ratio as a salt. A tetramer arises composed of two of each component (N12-H12···O2 = 1.698Å, N13-H13b···O1 = 2.058Å, N13-H13a···O3 = 2.062Å, O4-H4···N11 = 1.819Å).

4.2.3   SATURATED HETEROCYCLES
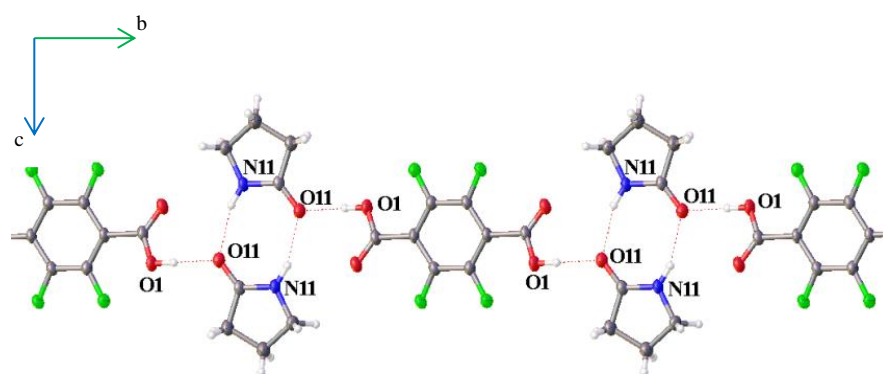
fBDC_Pyr

Triclinic   *P-1*

a = 6.9399(5) Å α = 69.472(13)°

b = 6.9624(5) Å β = 70.986(13)°

c = 9.8741(7) Å γ = 85.597(15)°

V = 422.05(7) Å^3 Z′ = 0.500

fBDC_Pyr crystallised in a 0.5:1 ratio as a co-crystal. A chain composed of diacid base base repeating units formed (O1-H1···O11 = 1.738Å, N11-H11···O11, = 2.034Å)
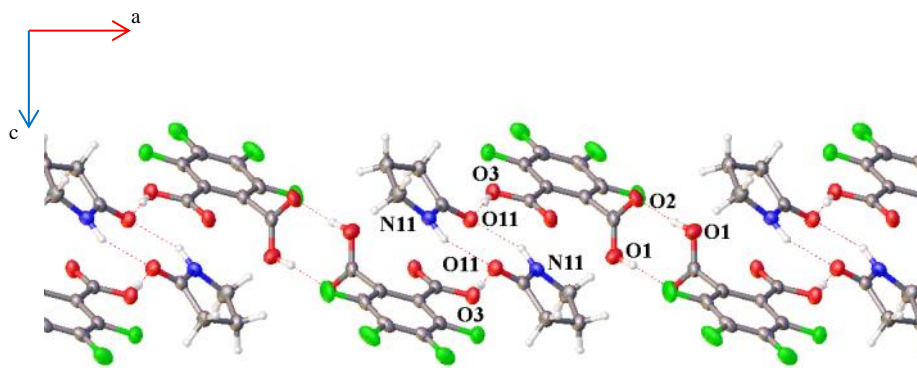
altfBDC_Pyr

Monoclinic   *P2$_1$/n*

a = 11.6267(8) Å α = 90°

b = 6.9266(5) Å β = 104.992(2)°

c = 16.4226(11) Å γ = 90°

V = 1277.55(15) Å^3 Z′ = 1.000

altfBDC_Pyr crystallised in a 1:1 ratio as a co-crystal. A chain composed of diacid diacid base base repeating units formed (O1-H1···O2 = 1.838Å, O3-H3···O11 = 1.700Å, N11-H11···O11, = 2.239Å)

fBDC_MPyri

Triclinic   *P-1*

a = 8.4868(5) Å   a = 96.033(7)°

b = 8.5397(5) Å   b = 104.841(8)°

c = 9.7164(7) Å   c = 95.630(7)°

V = 671.18(8) Å^3 Z′ = 1.000
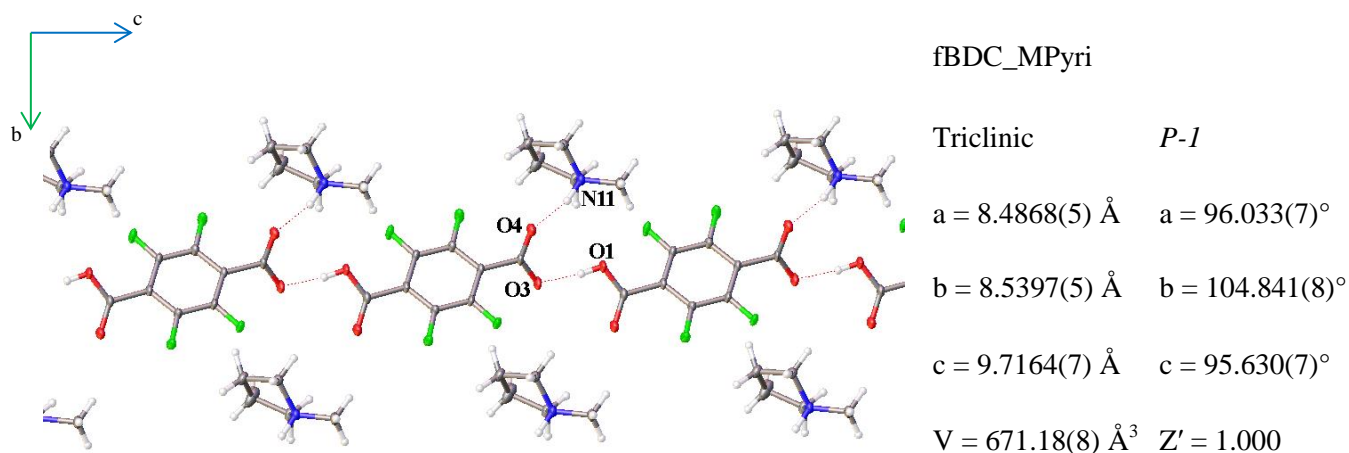
fBDC_MPyri crystallised in a 1:1 ratio as a salt. This structure is composed of numerous monoanion diacid chains (O1-H1···O3 = 1.661Å). Base molecules terminally link to the chains (N11-H11···O4, = 1.750Å)
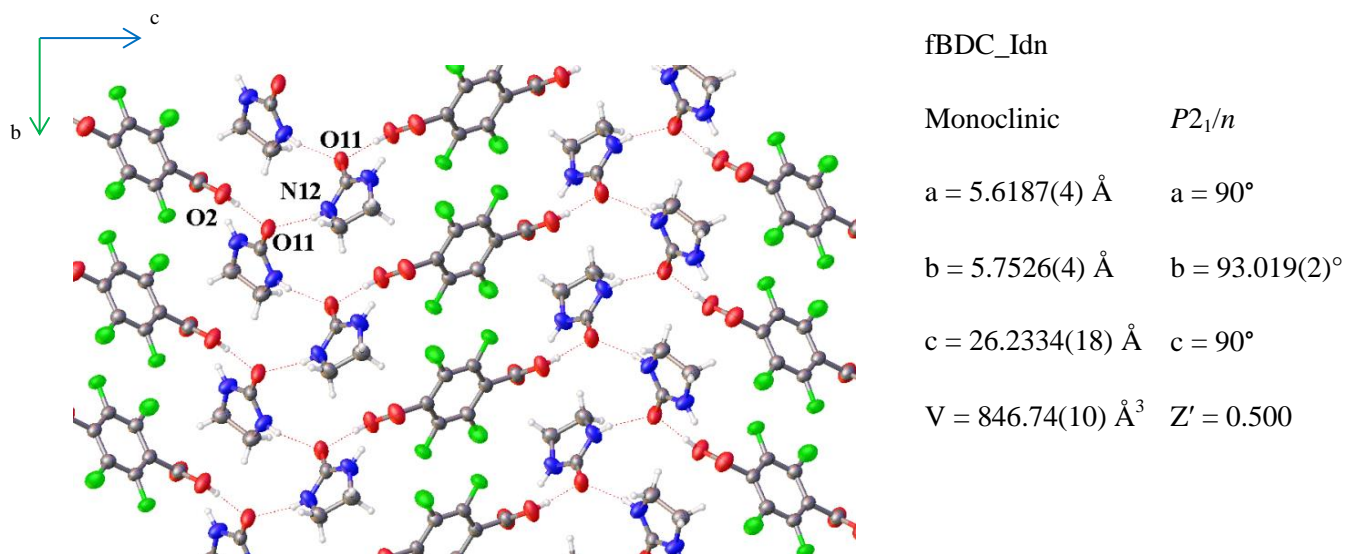
fBDC_Idn

Monoclinic   *P2$_1$/n*

a = 5.6187(4) Å   a = 90°

b = 5.7526(4) Å   b = 93.019(2)°

c = 26.2334(18) Å   c = 90°

V = 846.74(10) Å^3 Z′ = 0.500

fBDC_Idn crystallised in a 0.5:1 ratio as a co-crystal. The asymmetric unit includes half an fBDC molecule, which lies across an inversion centre, and one Idn molecule. The components form a hydrogen bonded sheet structure along crystallographic axis b where two base molecules are hydrogen bonded (N12-H12···O11 = 2.074Å). These units are then additionally linked via hydrogen bonding to either side of the acid molecule (O2-H2···O11 = 1.737Å).

isofBDC_Idn

Monoclinic $P2_1$

a = 5.5381(4) Å   a = 90°

b = 9.4554(7) Å   b = 90.558(4)°

c = 11.7661(8) Å   c = 90°

V = 616.10(8) Å³   Z′ = 1.000
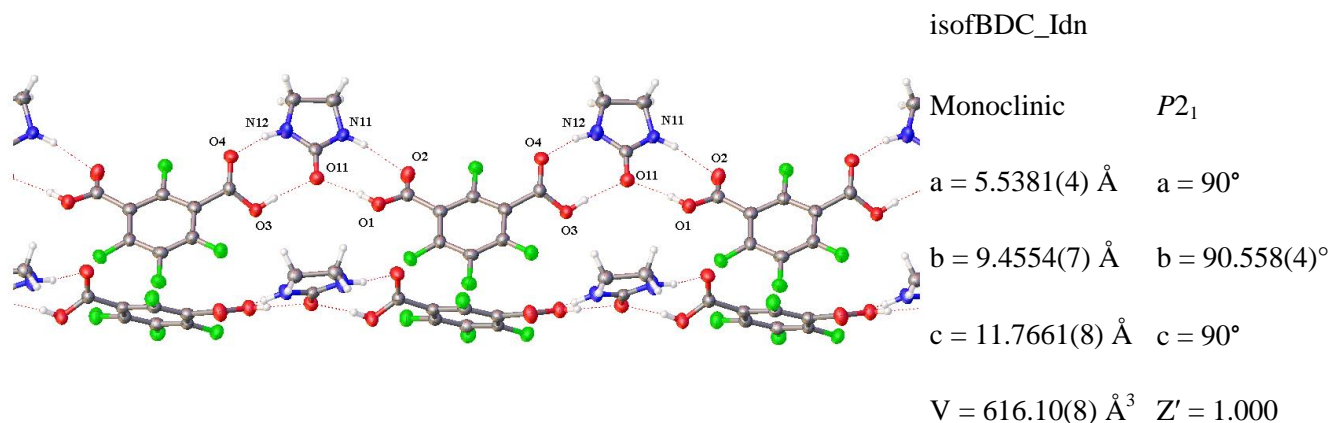
isofBDC_Idn crystallised in a 1:1 ratio as a co-crystal. The structure consists of hydrogen bonded chains of alternate acid and base molecules which develops along crystallographic axis c (O1-H1···O11 = 1.849Å, O3-H3···O11 = 1.843Å, N11-H11···O2 = 2.116Å, N12-H12···O4 = 2.078Å). The chains form in pairs resulting in a zig zag motif. Fluorine contacts are observed between these two interdigitating molecules (N12-H12···F1= 2.345Å). There are weak C-F contacts between the isofBDC molecules from parallel chains (C8-F2 = 3.134Å, C4-F4 = 3.125Å).

altfBDC_Idn

Monoclinic $P2_1/n$

a = 10.2841(7) Å   a = 90°

b = 26.8071(19) Å b = 102.211(2)°

c = 10.7871(8) Å   c = 90°

V = 2906.6(4) Å³   Z′ = 1.000
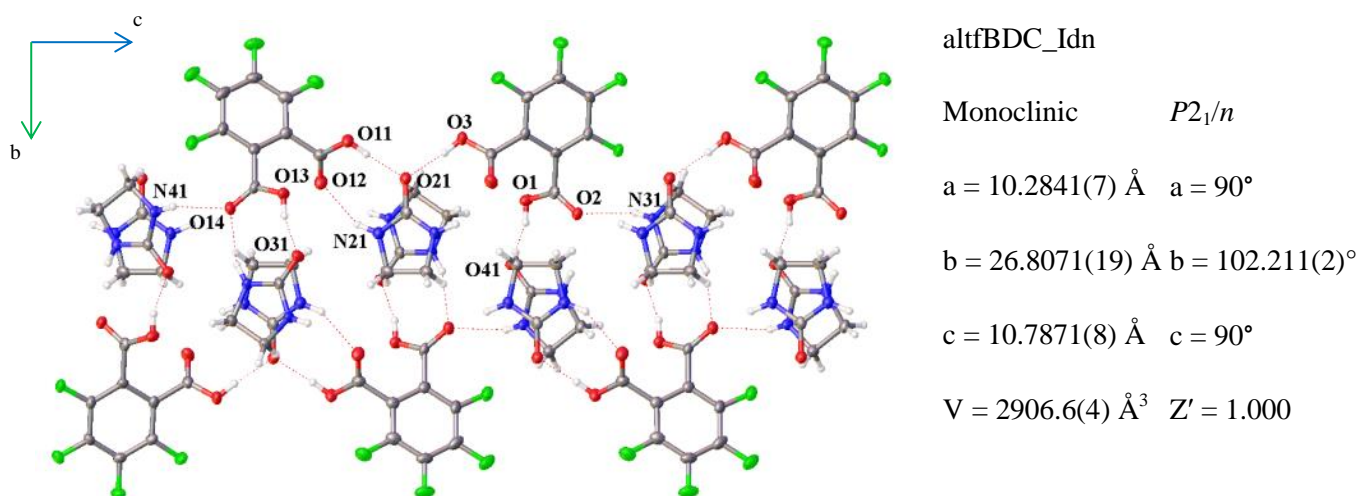
altfBDC_Idn crystallised in a 2:3 ratio as a co-crystal. The structure consists of hydrogen bonded chains of alternate acid and base molecules (O1-H1···O41 = 1.649Å O3-H3···O21 = 1.738Å, O11-H11···O21 = 1.727Å, N21-H21···O12 = 2.147Å, O13-H13···O31 = 1.635Å, N31-H31···O2 = 2.151Å, N32-H32···O14 = 2.144Å), N41-H41···O14 = 1.635Å Chains interlock along crystallographic axis b via the altfBDC terminal molecules which appear at either side of each chain. Weak C-F contacts are observed for the altfBDC molecules between chains (*e.g.* C5-F11 = 3.025Å).
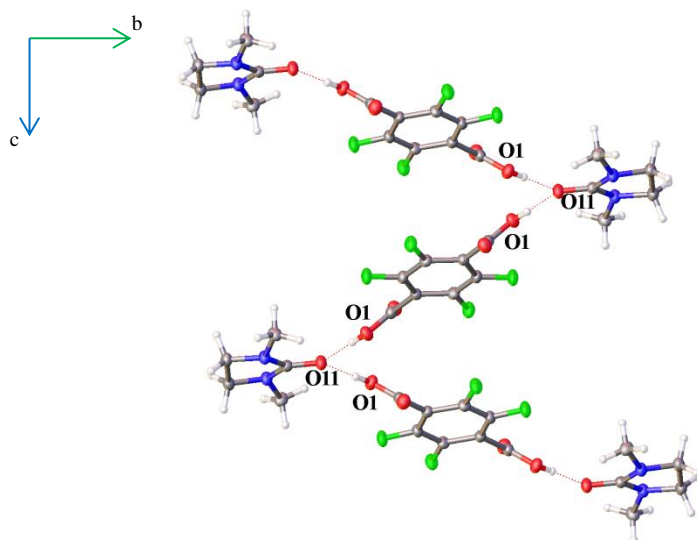
fBDC_DMIdn

Monoclinic   *C*2/*c*

a = 10.7847(8) Å   a = 90°

b = 12.0847(8) Å   b = 98.107(2)°

c = 10.8783(8) Å   c = 90°

V = 1403.60(17) Å³ Z′ = 0.500

fBDC_DMIdn crystallised in a 1:1 ratio as a co-crystal. The asymmetric unit includes half an fBDC molecule and half a DMIdn molecule, both of which lie across inversion centres. Alternate diacid base chain which forms arise because of one hydrogen bond, O1-H1···O11 = 1.797Å. The chains are corrugated.
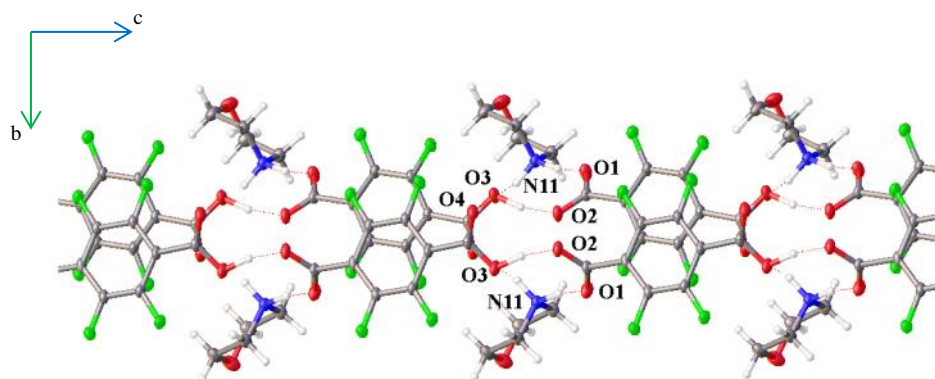
fBDC_Mo

Monoclinic   *Ia*

a = 7.6822(5) Å   α = 90°

b = 17.8120(13) Å   β = 106.992(4)°

c = 9.6799(6) Å   γ = 90°

V = 1266.73(15) Å³ Z′ = 1.000

fBDC_Mo crystallised in a 1:1 ratio as a salt. The asymmetric unit includes an fBDC molecule and one Mo molecule. Each of the fBDC molecules are mono-deprotonated thus resulting in a salt. The proton migrated to nitrogen from the Mo molecule. The components form hydrogen bonded sheets. fBDC molecules form typical monoanion chains in one direction (O3-H3···O2 = 1.481Å). These are extended into two dimensions by hydrogen bonding to the base molecules (N11-H11b···O1 = 1.868Å, N11-H11a···O4 = 1.824Å)
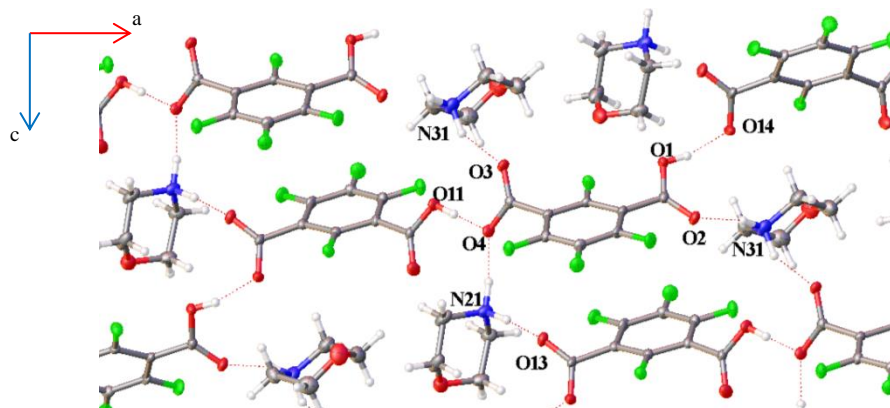
isofBDC_Mo

Monoclinic   Pc

a = 10.9814(8) Å   a = 90°

b = 5.9090(4) Å   b = 99.012(2)°

c = 20.5436(14) Å   c = 90°

V = 1316.60(16) Å^3 Z′ = 2.000

isofBDC_Mo crystallised in a 1:1 ratio as a salt. The asymmetric unit includes two of each of the components. Monoanion diacid chains form which are each linked via hydrogen bonding between two different base molecules resulting in a 3D supramolecular structure (O1-H1···O14 = 1.649Å, O11-H11···O4 = 1.701Å, N21-H21a···O4 = 1.752Å, N21-H21b···O13 = 1.813Å, N31-H31a···O3 = 1.835Å, N31-H31b···O2 = 1.905Å).
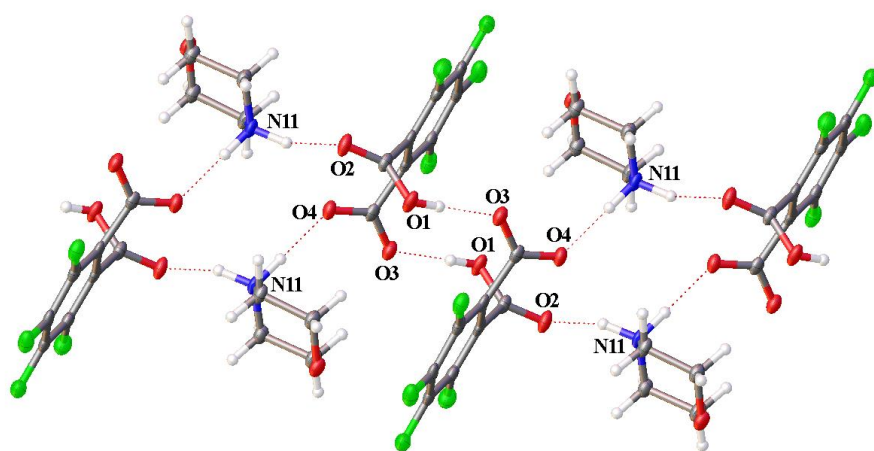
altfBDC_Mo

Triclinic   _P-1_

a = 7.8849(5) Å   α = 85.128(11)°

b = 8.9876(5) Å   β = 68.953(9)°

c = 9.5444(7) Å   γ = 78.823(11)°

V = 619.19(8) Å^3 Z′ = 1.000

altfBDC_Mo crystallised in a 1:1 ratio as a salt. The chain arising from this system is unusual compared to those previously observed. The unusual chain which comprises this structure is formed of alternating diacid base molecules with the difference being that each half of the diacid has a hydrogen bonded support (O1-H1···O3 = 1.671Å, N11-H11a···O2 = 2.017Å, N11-H11b···O4 = 1.777Å).
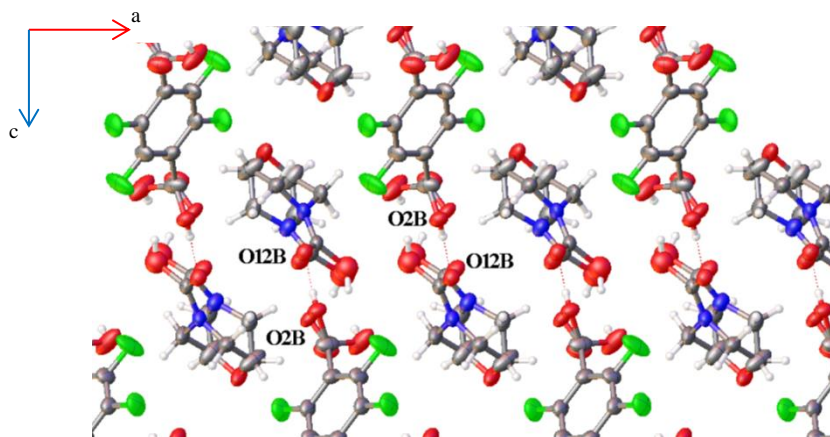
fBDC_AMo

Monoclinic   *C2/c*

a = 17.4048(11) Å   α = 90°

b = 6.3536(4) Å   β = 106.955(3)°

c = 20.4021(14) Å   γ = 90°

V = 2158.1(3) Å^3 Z' = 0.500

fBDC_AMo crystallised in a 0.5:1 ratio as a co-crystal. Both components are disordered over two sites Each end of the diacid is hydrogen bonded to the carboxylate from AMo molecules resulting in a trimer unit (O2-H2···O12 = 1.673Å).

Tying in with the huge surge in interest in crystal engineering and crystal structure prediction the necessity for analysis methods which allow the comparison of various crystal structures arises.[12] A complete understanding of crystal engineering requires the comparison of the whole crystal structure including all of its interactions which govern its molecular assembly.[13] Several methods have been developed over the years,[14-17] some of which focus on a specific subset of structures for comparison *i.e.* polymorphs of a single compound.[18] Others have looked at specific interactions such as hydrogen bonding to describe similarities within structures.[15, 19] However, crystal structures are formed by the complex combination of intermolecular interactions and therefore only choosing one interaction will only provide one part of the story. In order to gain a full understanding of the formation of crystal structures it is important that the analysis method utilised is capable of pulling out information regarding the weaker interactions and structures which are mainly formed due to close-packing. It should also be able to compare crystal structures which are composed of similar molecular species. In order to understand the potential effect caused by for example changing a functional group within a molecule and assessing its corresponding effect on the crystal packing arrangements. Given this analysis criteria XPac[16] was chosen to analyse the binary systems which formed within this work.

XPac,[16] a crystallographic program which looks for crystal packing similarities, is based on the concept of supramolecular constructs (SC). These are defined as any geometrically similar assembly of molecules arising in two or more crystal structures. SCs can be 3D (isostructural), 2D (similar sheets), 1D (similar stacks or chains), or 0D (discrete molecular assemblies *e.g.* dimers).[20] Rather than focusing on bonding and conventional intermolecular interactions, XPac works by evaluating the geometrical proximity of molecules thereby allowing the collection of implicit information associated with all interactions of the SC. Comparisons of structures and the potential identification of SCs starts out by the user selecting a corresponding series of points (COSP) which are used to define common shapes of particular molecular components of interest within a set of crystal structures.[21] For this study the diacid components were chosen as the COSP and compared. By relating structures using this approach it allows comparisons of similar fragments of non-identical molecular species to be drawn. Feasibly one could assess the effect of not only changing a functional group within a molecular species but also changing the substitution of said functional group eg meta to para, ortho to para.[22] Similar arrangements within crystal structures are highlighted based on the chosen COSP and found by XPac through the automated evaluation of large numbers of internal coordinates of representative clusters composed of a seed molecule and a 'shell' of near neighbours generated by space group symmetries of the crystal structures being assessed.

By assessing crystal packing arrangements of the fluorinated diacid series similar packing motifs can be found. The aim is to correlate these with a particular pyrotechnic effect or intensity of effect. The next section discusses the similarities found within this series.

4.3   CRYSTAL PACKING ARRANGEMENTS

Thirty-eight binary systems resulted from pairing three fluorinated diacids with various N-containing heterocycles, the majority of which were attributed to fBDC. A number of co-crystals were found on inspection of the products attributed to the saturated heterocycles. A co-crystal was discovered for all cases in syntheses involving Idn. The other materials that generated co-crystals were Pyr, DMIdn, Mo, and AMo. N-containing saturated heterocycles were the most likely materials to produce co-crystals as they had minimal, if any, possible protonation sites.

Using XPac[16] three main different structural arrangements were identified which included 2D sheets, 1D stacks and 1D catamers.
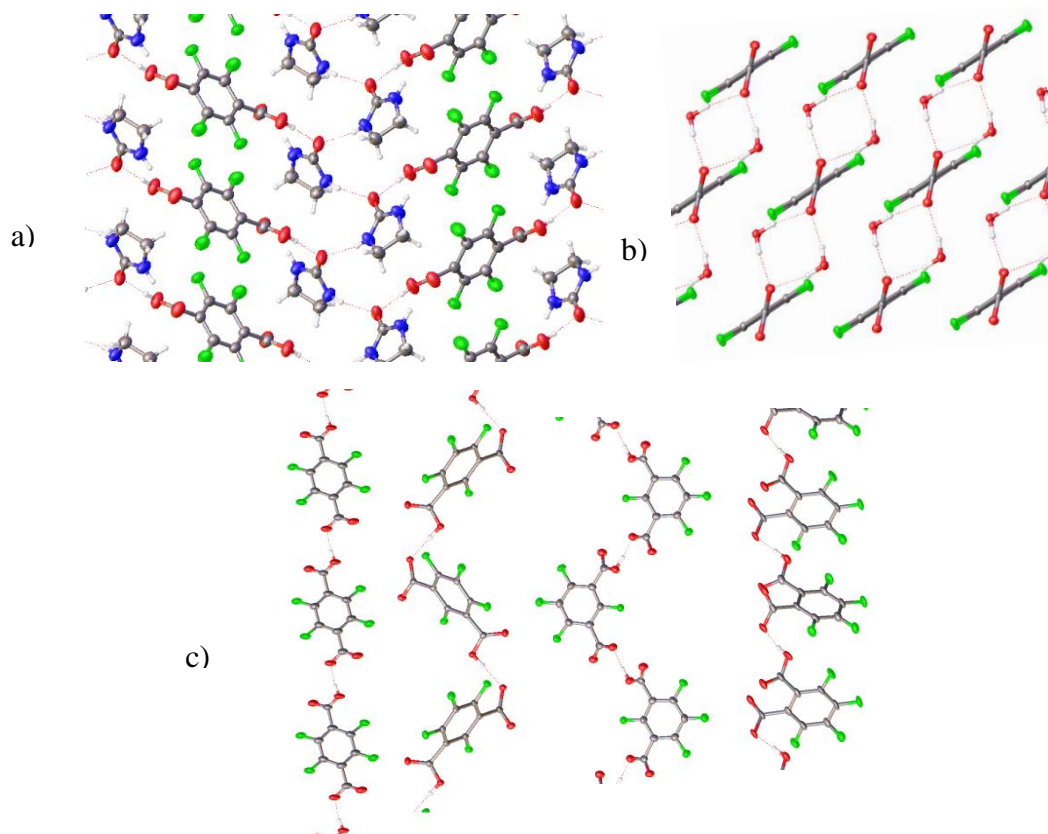
Figure 4.3.1 - a) 2D sheet, b) 1D stack, c) 1D catamer

2D sheet similarities were found within the azole series (Im, 2MI) specifically when coupled with fBDC. NPy created 2D sheets with fBDC and altfBDC. DMI only formed sheets with altfBDC. Additional structures created 2D sheets which were not identified

from the XPac search as they were unique for the structure series. A total of seventeen out of the thirty-eight binary systems discovered from this work formed 2D supramolecular networks. Only six systems were found to create structures with greater dimensionality; fBDC_3NTro, fBDC_DNPy, isofBDC_Mo, altfBDC_Im, altfBDC_2MI and altfBDC_Tro (fBDC_3NTro is a decomposition product). 0D units were found for fBDC_AMo and altfBDC_DMNPym forming trimers and tetramers respectively. The dimensionality of the supramolecular assemblies are highlighted in Table 4.3.1

	fBDC	isofBDC	altfBDC
Im	2D	-	3D
2MI	2D	-	3D
4MI	1D	1D	2D
DMI	2D	-	1D
Tro	2D	2D	3D
3NTro	3D	-	-
NPy	2D	-	2D
DNPy	3D	2D	1D
3NONPy	2D	-	1D
5NONPy	2D	2D	2D
DMNPym_1	2D	2D	0D
DMNPym_2	*1D*	-	-
Pyr	1D	-	1D
MPyri	1D	-	-
Idn	2D	1D	1D
DMIdn	1D	-	-
Mo	2D	3D	1D
AMo	0D	-	-

Table 4.3.1 - Supramolecular Dimensionality for Fluorinated Diacid Binary Systems

1D supramolecular chains were found within the fBDC series when coupled with 4MI, DMNPym_2, Pyr, MPyri and DMIdn, Within the isofBDC series: 4MI, 5NONPy and Idn. altfBDC created 1D chains when paired with DMI, DNPy, 3NONPy, Pyr and Mo. Numerous 1D stacks formed with all substituted versions of the fluorinated diacid. (fBDC = 12/18, isofBDC 6/7, and altfBDC 6/13). 1D catamers were produced in

roughly half of the structures which were found belonging to each diacid series (fBDC = 8/18, isofBDC 3/, altfBDC 5/13). No similarities were drawn between fBDC_DMI, fBDC_3NONPy, fBDC_AMo, altfBDC_Tro, altfBDC_3NONPy and altfBDC_Idn with the rest of the crystal structures. The complete results are summarized in Table 4.3.2.

	2D Sheets	1D Stacks	1D Catamers	No Similarity
Im	1	3	1, 3	-
2MI	1	1, 3	1	-
4MI	-	3	1, 2	-
DMI	3	-	3	1
Tro	-	1, 2	1, 2	3
3NTro	-	1	-	-
NPy	1,3	1	1, 3	-
DNPy	-	2	1, 2, 3	-
3NONPy	-	-	-	1, 3
5NONPy	-	1, 2	3	-
DMNPym_1	-	1, 2, 3	-	-
DMNPym_2	-	*1*	-	-
Pyr	-	1, 3	-	-
MPyri	-	1	1	-
Idn	-	1, 2	-	3
DMIdn	-	1	-	-
Mo	-	1, 2, 3	1	-
AMo	-	-		1

Table 4.3.2 - XPac Search Results (1 = fBDC, 2 = isofBDC, 3 = altfBDC)

The azole series, Im, 2MI, and Tro all form 2D arrangements when coupled with fBDC but when paired with altfBDC they generate a 3D supramolecular network. 2D sheets form as a result of the linking of the individual catameric diacid chains by base molecules. fBDC_NPy follows a similar pattern to both of the equivalent Im and 2MI structures, however within the NPy structure the diacid chains are all parallel to one another. These arrangements are highlighted in Figure 4.3.2.
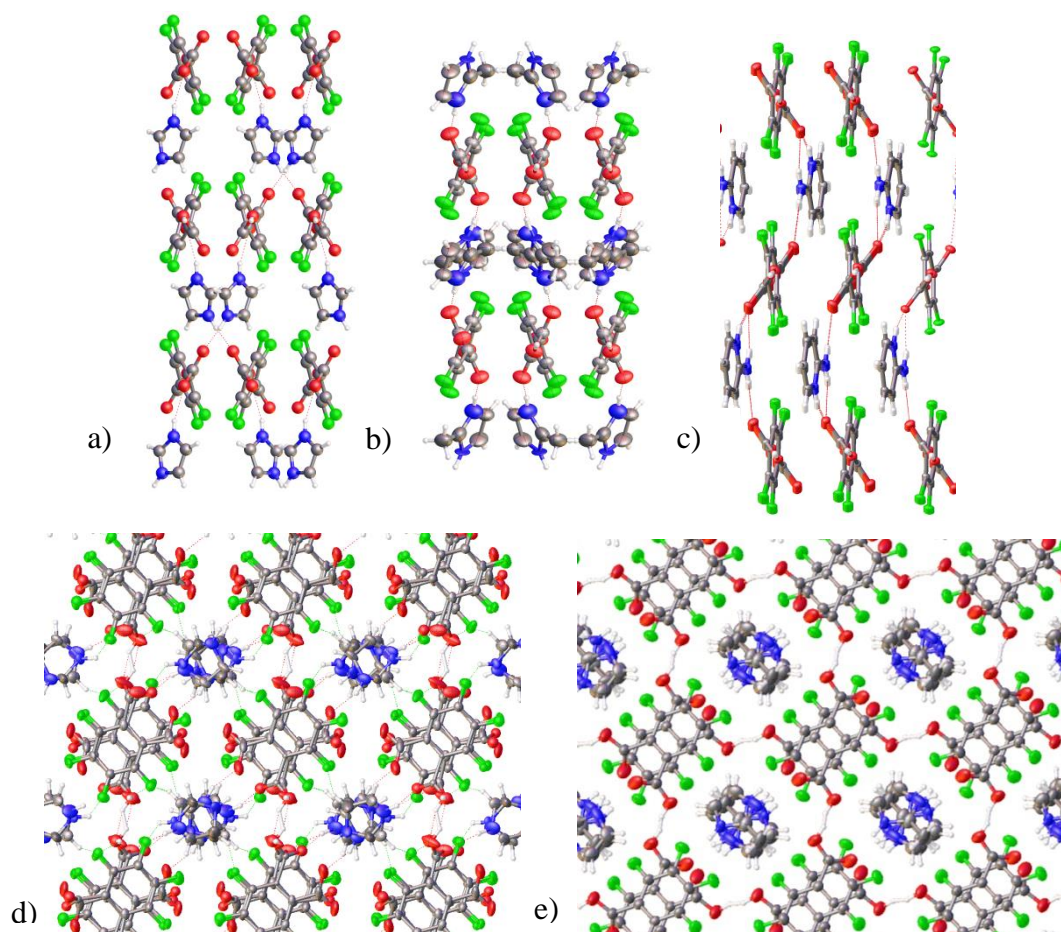
Figure 4.3.2 a) fBDC_Im, b) fBDC_2MI, c) fBDC_NPy, d) altfBDC_Im, e) altfBDC_2MI

fBDC_Tro closely resembles the assembly present within fBDC_Im where catameric chains of the diacids are seen to link via the base molecules to create a 2D network. An analogous pattern is observed for the isofBDC equivalent. altfBDC_Tro although in this case forms a 3D supramolecular framework is most like altfBDC_Im and altfBDC_2MI.
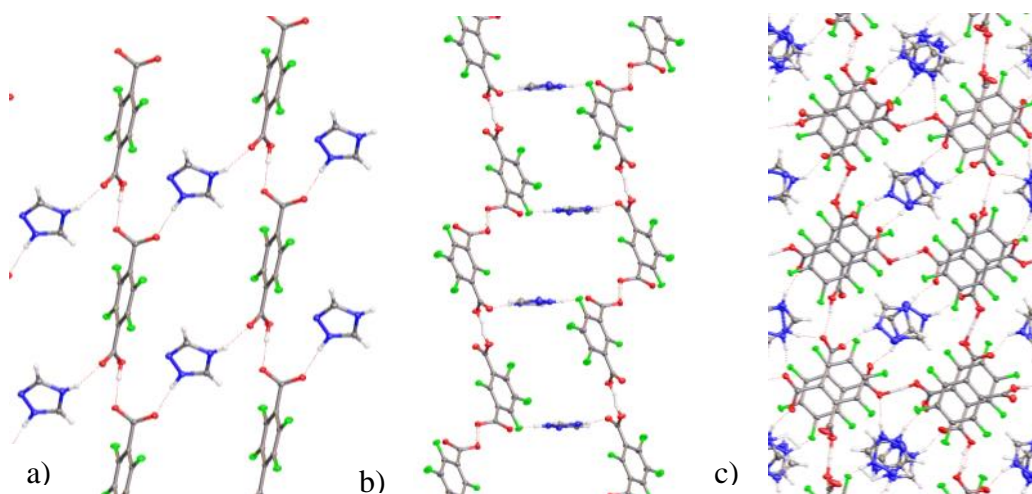
Figure 4.3.3 a) fBDC_Tro, b) isofBDC_Tro, c) altfBDC_Tro

4MI assemblies do not yield the same patterns as shown above for the other systems within the azole series. fBDC_4MI consists of catameric diacid chains which are linked by base molecules to create larger 1D chain. isofBDC_4MI also forms catameric chains but the base molecules instead reside between the diacid molecules and interact with only a single chain. altfBDC_4MI combines the features of both of the diacid products. The catameric chains which form are most similar to the chains observed in the isofBDC equivalent. Two unique catameric chains are linked by base molecules.
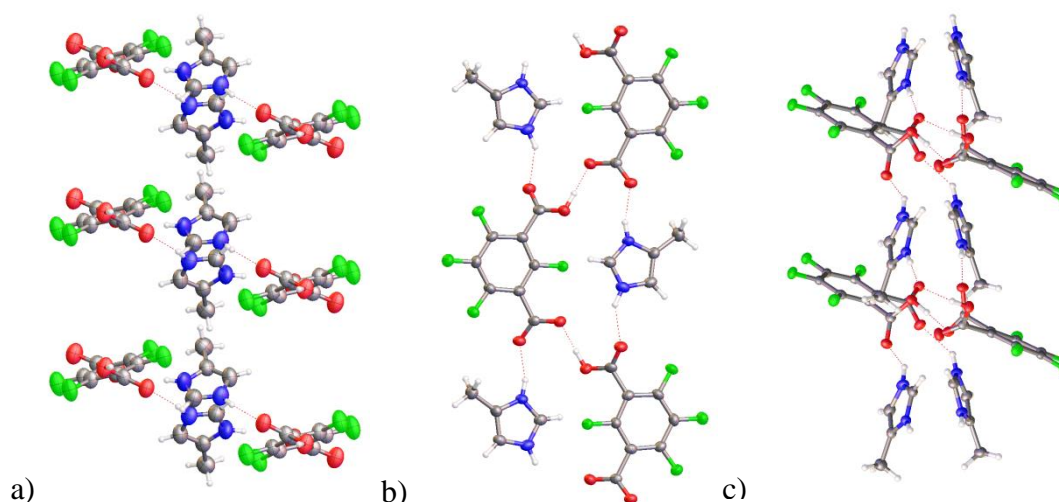
Figure 4.3.4 4MI assemblies a) fBDC (1D), b) isofBDC (1D), c) altfBDC (2D)

Pairings of fBDC and altfBDC with Pyr forms 1D chains rather than 2D networks irrespective of the use of fBDC or altfBDC. Both form alternate acid base 1D chains but they differ in their exact connectivity. fBDC_Pyr has a repeating unit of diacid:base:base, whereas altfBDC_Pyr is composed of a diacid:diacid:base:base repeating unit as is shown in Figure 4.3.5.

a)

b)
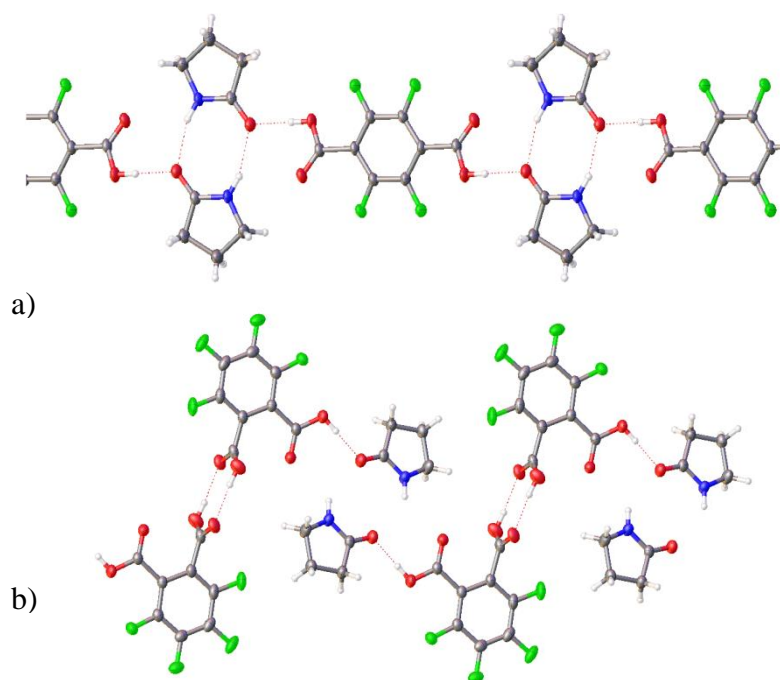
Figure 4.3.5 Pyr diacid 1D chain arrrangements

All of the crystal structures comprising NONPy molecules formed 2D networks except for altfBDC_3NONPy which formed 1D chains. Both fBDC and isofBDC arrangements for the NONPy molecules are alike.
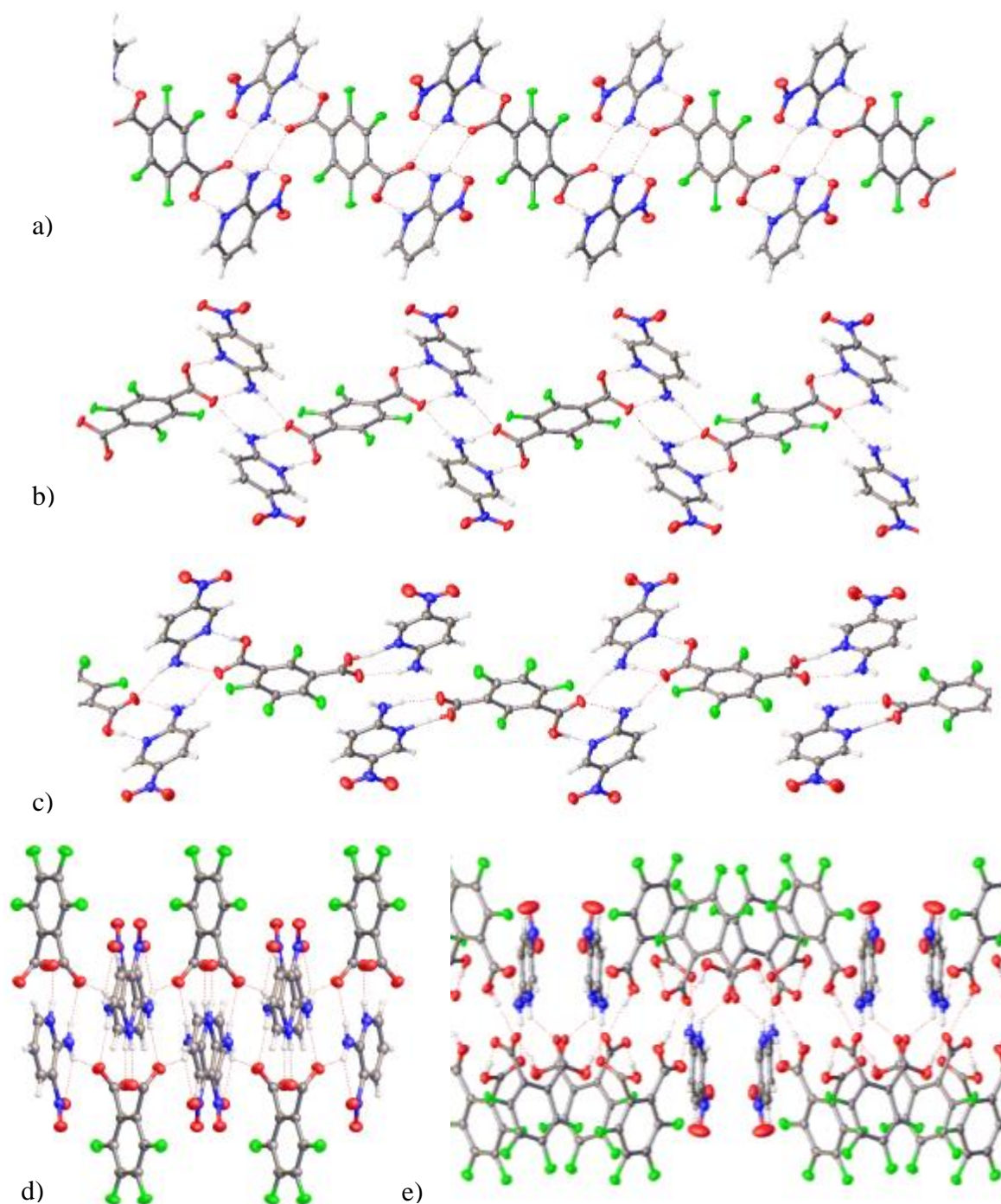
Figure 4.3.6 a) fBDC_3NONPy, b) fBDC_5NONPy, c) isofBDC_5NONPy, d)
altfBDC_3NONPy, e) altfBDC_5NONPy

A 2D network arrangement was found for all crystal structures containing 5NONPy.
However, the related substituted pyridine, DNPy, produces a different trend where the

impact of moving the carboxylates closer to one another reduces the supramolecular dimensionality of the structure systematically from 3D to 1D.
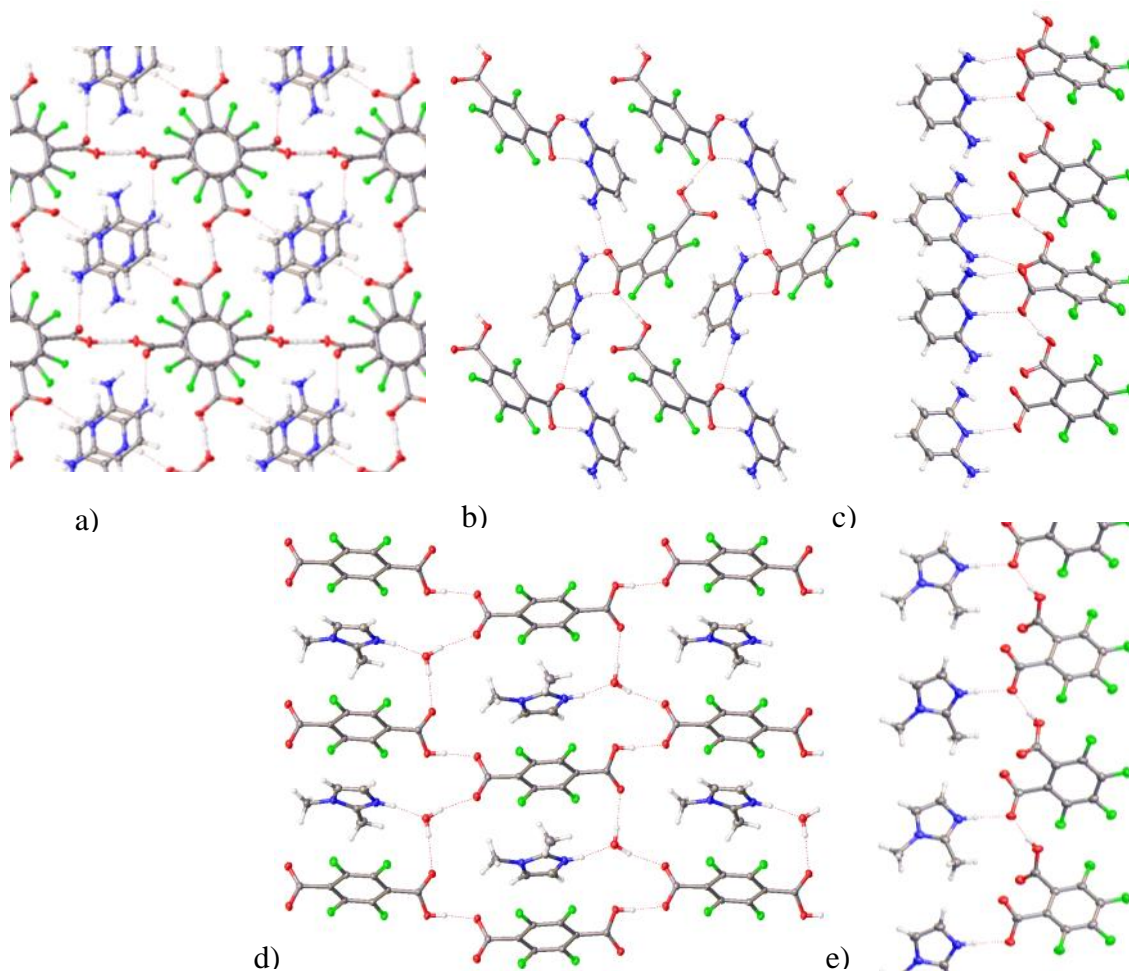
Figure 4.3.7 - a) fBDC_DNPy, b) isofBDC_DNPy, c) altfBDC_DNPy, d) fBDC_DMI, e) altfBDC_DMI

As can be seen in Figure 4.3.7 the altfBDC assemblies are the same for both DNPy and DMI such that rather than the typical catameric chain where altfBDC usually blocks either side of the 1D chains from propagating into supramolecular structures of greater dimensionality, it only blocks one side whilst the base caps the other. The presence of a water molecule within fBDC_DMI directly contributes to the 2D sheet formation as it links catameric chains of the diacid molecules and also links with the base molecules. The base does not interact directly with the diacid molecules.

Within fBDC_Idn two base molecules are hydrogen bonded which are then additionally linked via hydrogen bonding to either side of an acid molecule to form a chain. Hydrogen bonding between the base molecules along the crystallographic b axis leads to the formation of a sheet which is completed by acid molecules. The 2D sheets are corrugated. isofBDC_Idn is also a corrugated structure but rather than 2D sheets it is the hydrogen bonded chains of alternate acid and base molecules which form in pairs which result in a zig zag motif. Idn molecules belonging to one chain interdigitate with isofBDC molecules from another chain. Fluorine contacts are observed between these two interdigitating molecules (N12-H12···F1= 2.345Å). The altfBDC_Idn structure consists of a hydrogen bonded double layered chain of alternate acid and base molecules Chains interlock along crystallographic axis b via the altfBDC terminal molecules which appear at either side of each chain. Weak C-F contacts are observed for the altfBDC molecules between the chains (*e.g.* C5-F11 = 3.025Å).
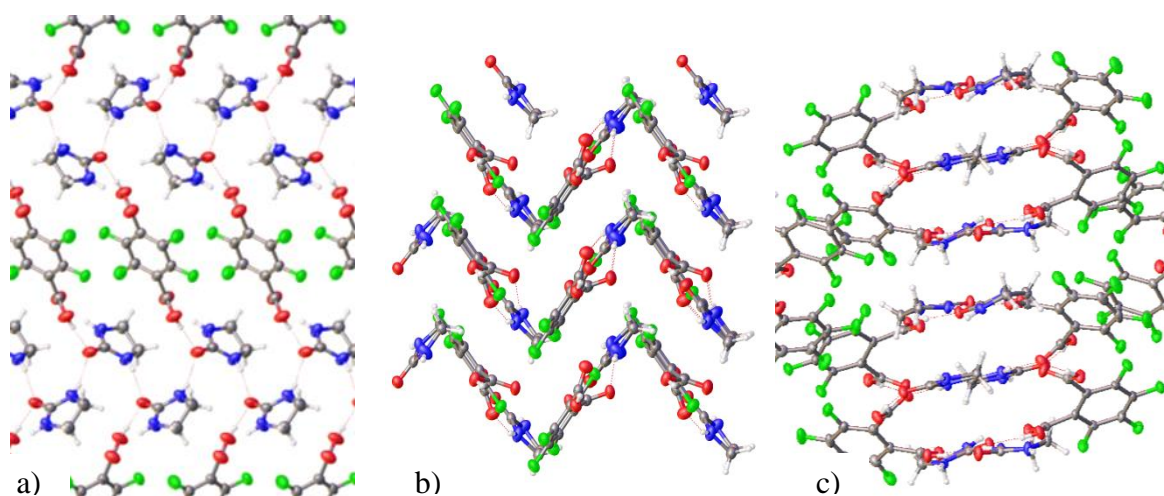
Figure 4.3.8 Idn assemblies a) fBDC (2D), b) isofBDC (1D), c) altfBDC (1D)

Unique patterns emerged for binary systems containing DMNPym (fBDC = 2D, isofBDC = 2D, altfBDC = 0D), and Mo (fBDC = 2D, isofBDC = 3D, altfBDC = 1D). Two crystal structures were uncovered for the coupling of fBDC with DMNPym. One forms a simple alternate acid base chain whereas the other forms a 2D network as a direct consequence of the additional component, water, which is present. Not only does the water affect its dimensionality but it also impacts on the chain arrangement which occurs between the acid and base molecules. Rather than forming an alternate acid base

chain a repeating unit of acid, base, base forms instead. This repeating unit pattern was also observed within fBDC_Pyr. isofBDC_DMNPym forms a 2D sheet by the linking of the catameric diacid chains by a pair of DMNPym molecules. altfBDC_DMNPym was one of only two cases which did not form a binary system which would extend into 1D, 2D, or 3D. Here a tetramer formed.

a)

b)

c)   d)
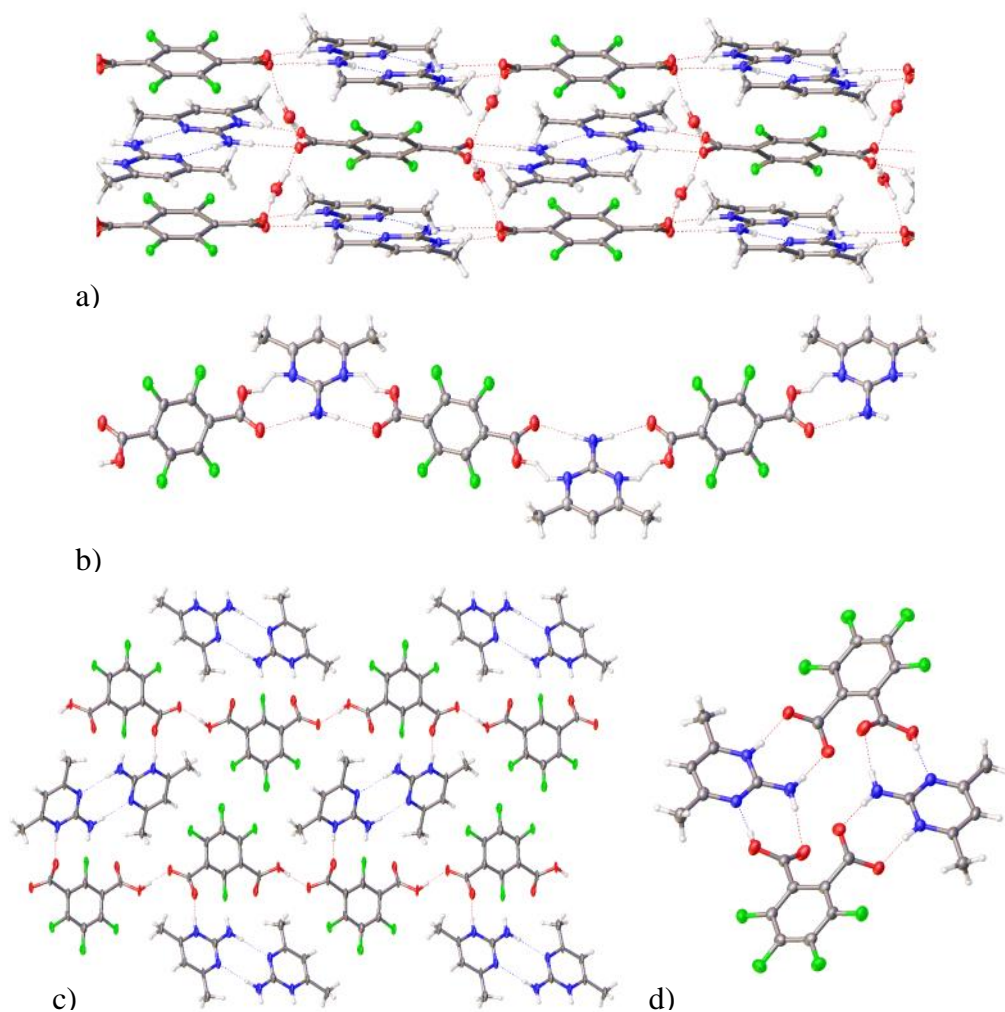
Figure 4.3.9 a) fBDC_DMNPym_1, b) fBDC_DMNPym_2, c) isofBDC_DMNPym,
d) altfBDC_DMNPym

Out of the Mo series fBDC and altfBDC are most alike although the former results in a 2D network and the latter in a 1D chain. Mo connects two different catameric chains within fBDC_Mo whereas in altfBDC there are no catameric chains, rather repeating

units of pairs altfBDC which are linked by Mo. The potential hydrogen bond acceptor within the Mo molecule is not utilised within this series.
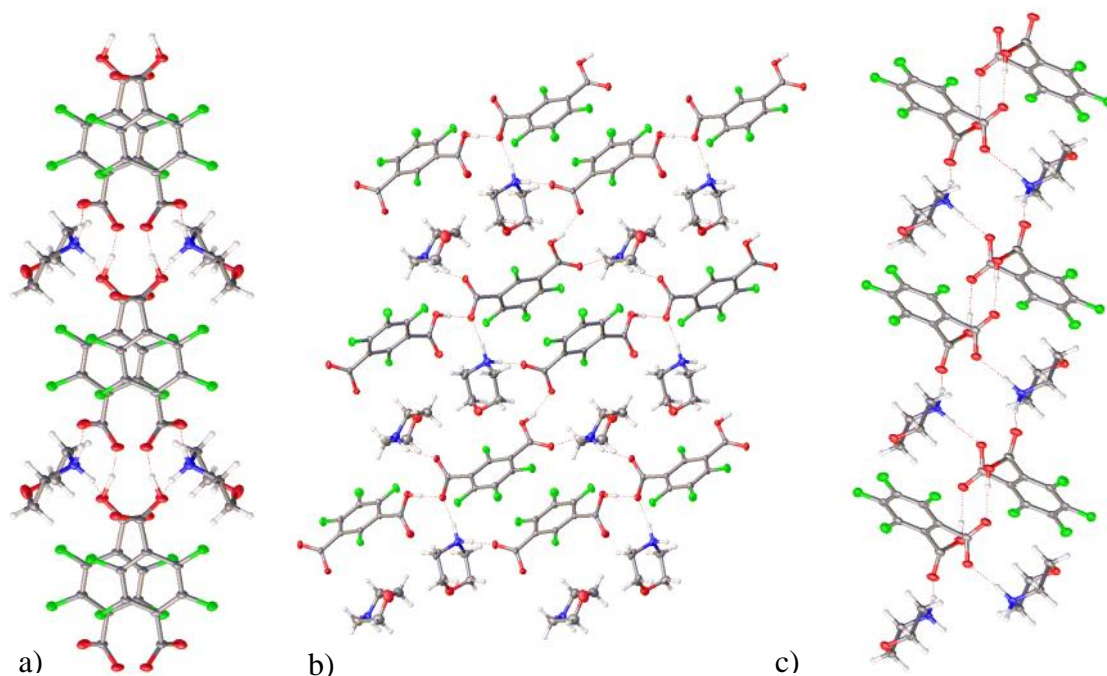
Figure 4.3.10 a) fBDC_Mo, b) isofBDC_Mo, c) altfBDC_Mo

No comparisons could be drawn for crystal structures which included 3NTro, MPyri, DMIdn, and AMo as they were unique to the fBDC series.

The next section highlights the thermal analysis results for the series of binary systems found from this work.

4.4   THERMAL ANALYSIS OF BINARY SYSTEMS

The DSC traces and burn test images for this work can be found in Appendix CD. One example of the DSC traces is highlighted here and multiple burn test examples are shown. The binary systems which resulted in an exothermic event when heated from 25-400°C were all produced with materials containing altfBDC. When paired with the majority of the azoles, Im, 2MI, 4MI, and DMI, and with NPy and DNPy a positive result was obtained. Interesting observations were made when the aluminium pans were removed from the DSC instrument. Each of the materials when heated had expanded and had become flaky. They formed what looked like ash. The material, as it had expanded broke the aluminium pan seal and burst through possibly additionally aided by the release of carbon dioxide and nitrogen gas generated by the decomposition of binary system. There looked to be a lot more material present than had initially been placed in the pan. The burn tests produced similar results but as they were in contact with the flame they essentially caramelised.
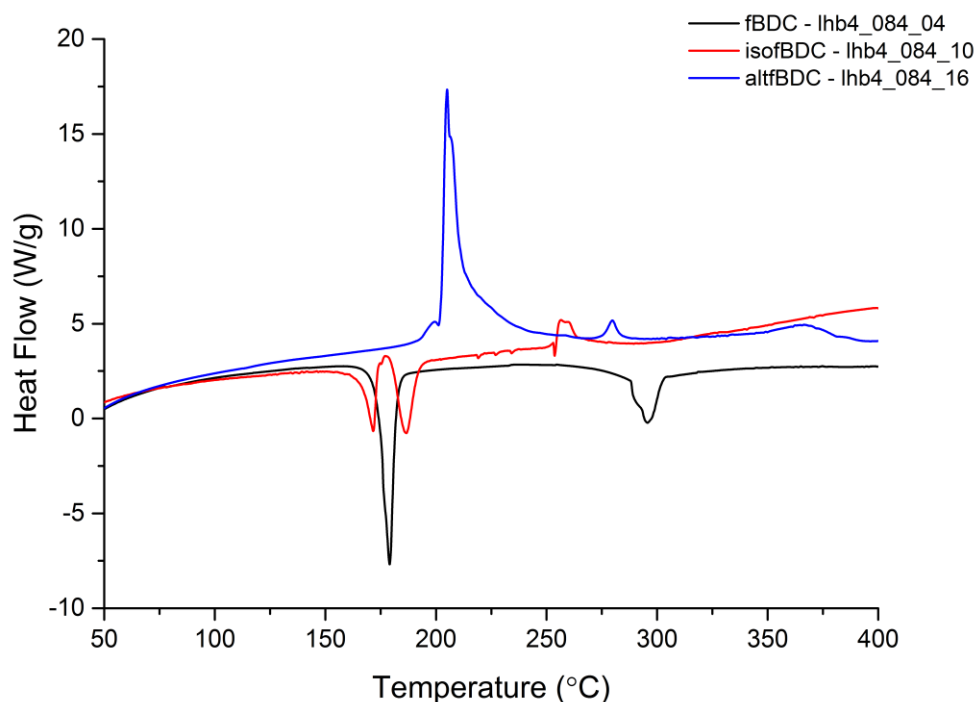
Figure 4.4.1 - Example of DSC Trace - 2MI series
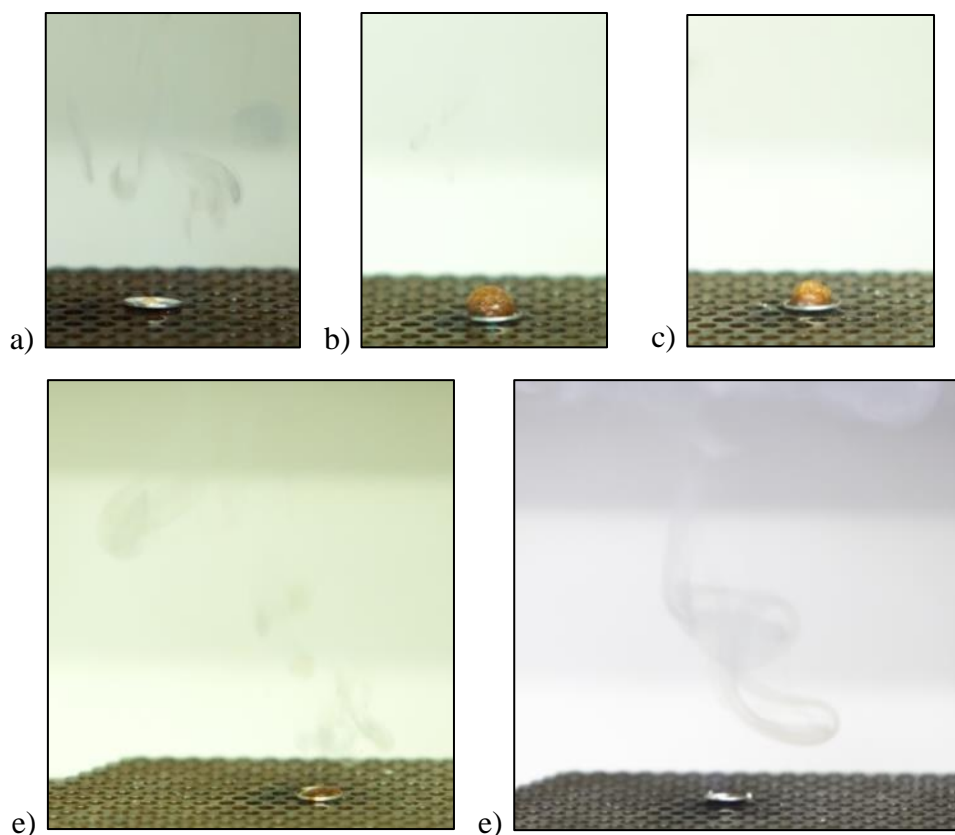
Figure 4.4.2 Burn Tests a) fBDC_2MI, b) altfBDC_2MI, c) altfBDC_4MI,
d) altfBDC_DMI, e) isofBDC_NPy

The majority of the samples appeared to create smoke. None of the materials in this work were deemed to possess significant pyrotechnic characteristics. The aforementioned altfBDC samples need to be investigated further in order to fully understand the decomposition pattern.

4.5   CONCLUSION

The main packing motifs formed within this collection of binary system crystal structures were catameric diacid chains and alternate diacid base chains. Where a 2D or 3D network was found the base units would tend to act as a link between these chains. Numerous similarities were observed across the crystal structures especially within the azole series. This series produced the most positive response to both the DSC and burn test results.

Although numerous crystal structures were identified from the devised set of combinations only a small number produced an exothermic event; the azole series, NPy and DNPy but this was mainly attributed to one of the diacids, altfBDC. The decomposition mechanism of these binary systems needs to be further investigated. The oxygen balance results, which can be found in Appendix A7, show that the azole series are closest in terms of reaching oxygen equilibrium (0). The other N-heterocycles investigated were in general more oxygen deficient (<0). The oxygen balance results associated with the azole series range from -10.06-(-2.66). The lowest value observed for the N-heterocycles was -30. 81 which was attributed to fBDC_DMNPym_1.

Although not all of the fluorinated diacids produced the same exothermic response as altfBDC it is believed that these materials could still be useful as pyrotechnic ingredients within other arrangements. The next chapter highlights their use in addition to other non-fluorinated diacids in MOFs. It is possible that in order for a significant pyrotechnic response to be generated that the fluorinated acids need to be coupled with a substance which incorporates a metal instead of another organic molecule.

References

1.   Millar, D. I. A.; Maynard-Casely, H. E.; Allan, D. R.; Cumming, A. S.; Lennie, A. R.; Mackay, A. J.; Oswald, I. D. H.; Tang, C. C.; Pulham, C. R., *CrystEngComm* **2012,** *14* (10), 3742-3749.

2.   Landenberger, K. B.; Bolton, O.; Matzger, A. J., *Angew. Chem. Int. Ed.* **2013,** *52* (25), 6468-6471.

3.   Bolton, O.; Matzger, A. J., *Angew. Chem. Int. Ed.* **2011,** *50* (38), 8960-8963.

4.   Zhang, H.; Guo, C.; Wang, X.; Xu, J.; He, X.; Liu, Y.; Liu, X.; Huang, H.; Sun, J., *Cryst. Growth Des.* **2012,** *13* (2), 679-687.

5.   Wang, L.; Zhao, L.; Hu, Y.; Wang, W.; Chen, R.; Yang, Y., *CrystEngComm* **2013,** *15* (15), 2835-2852.

6.   Wang, L.; Hu, Y.; Wang, W.; Liu, F.; Huang, K., *CrystEngComm* **2014**.

7.   Allen, F. H., *Acta Crystallogr.* **2002,** *B58*, 380-388.

8.   Yu, L.-L.; Cheng, M.-L.; Liu, Q.; Zhang, Z.-H.; Chen, Q., *Acta Crystallogr. Sect. C* **2010,** *66* (4), o179-o181.

9.   Orthaber, A.; Seidel, C.; Belaj, F.; Albering, J. H.; Pietschnig, R.; Ruschewitz, U., *Inorg. Chem.* **2010,** *49* (20), 9350-9357.

10. Wang, Z.; Kravtsov, V. C.; Walsh, R. B.; Zaworotko, M. J., *Cryst. Growth Des.* **2007,** *7* (6), 1154-1162.

11. Sake Gowda, D. S.; Rudman, R., *Acta Crystallogr. Sect. C* **1983,** *39* (2), 250-253.

12. Day, G. M., *Cryst. Revs.* **2011,** *17* (1), 3-52.

13. Desiraju, G. R., *Crystal engineering: the design of organic solids*. Elsevier: 1989.

14. Fabian. L, *Cryst. Growth Des.* **2009,** *9* (3), 1436-1443.

15. Oswald, I. D. H.; Motherwell, W. D. S.; Parsons, S.; Pidcock, E.; Pulham, C. R., *Cryst. Revs.* **2004,** *10* (1), 57-66.

16. Gelbrich, T.; Hursthouse, M. B., *CrystEngComm* **2005,** *7* (53), 324-336.

17. Price, S. L., *Acc. Chem. Res.* **2008,** *42* (1), 117-126.

18. Mukherjee, A.; Grobelny, P.; Thakur, T. S.; Desiraju, G. R., *Cryst. Growth Des.* **2011,** *11* (6), 2637-2653.

19. Wood, P. A.; Feeder, N.; Furlow, M.; Galek, P. T. A.; Groom, C. R.; Pidcock, E., *CrystEngComm* **2014**.

20. Coles, S. J.; Ellis, A. L.; Leung, K.; Sarson, J.; Threlfall, T. L.; Tizzard, G. J., *CrystEngComm* **2014,** *16* (47), 10816-10823.

184

21.   Tizzard, G. J. Characterisation and investigation of structural relationships of 4,4'-disubstituted chalcones. PhD, University of Southampton, 2008.

22.   Gelbrich, T.; Threlfall, T. L.; Hursthouse, M. B., *CrystEngComm* **2012,** *14* (17), 5454-5464.

CHAPTER 5

Results and Discussion (Molecular Control - MOFs)

5.1   INTRODUCTION

Metal Organic Frameworks (MOFs) comprise organic ligands and metal ions or clusters forming infinite 1D, 2D or 3D arrangements.[1, 2] The use of a diverse range of ligands exhibiting various functionality coupled with numerous metal ions results in a myriad of properties which can be explored.[3] Thus far, MOFs have been recognized as useful materials for applications in gas storage (CO_2, CH_4, and H_2), gas purification, catalysis, and as sensors.[4-6]

Until recently the application of MOFs in the energetic materials field extended solely to explosive chemical sensors whereby the porosity of a MOF is employed to absorb and trap explosive compounds and trigger a detectable response.[7-16] Recently it has been reported that MOFs could be used in the energetic materials industry by incorporating known explosive compounds within the framework and thereby creating structural reinforcement to stabilize unstable components. Hope-Weeks et al.[17] have reported two hydrazine-perchlorate 1D MOFs, $[Ni(NH_2NH_2)_5(ClO_4)_{2n}(NHP)]$ and $[Co(NH_2NH_2)_5(ClO_4)_2)n(CHP)]$ (NHP = nickel hydrazine perchlorate; CHP = cobalt hydrazine perchlorate), which have linear polymeric structures and are regarded as possibly the most powerful metal-based energetic materials known to date. Unfortunately, an unacceptably high level of sensitivity still remained and prevented these MOFs from being useful in a practical setting so in order to decrease its sensitivity hydrazine was replaced with a derivative (hydrazine-carboxylate). This modification enabled 2D MOFs to form and reduced the sensitivity, but the heat of detonation also decreased.[18] Pang and co-workers[19] extended this approach of increasing coordination to enhance the structural reinforcement of the framework and have successfully created $[Cu(atrz)_3(NO_3)_2]_n$ and $[Ag(atrz)_{1.5}(NO_3)]_n$ (atrz = 4,4′-azo-1,2,4-triazole) which are 3D energetic MOFs.

However, rather than stabilizing known energetic materials we propose to use traditional fuels and oxidisers already utilized by the pyrotechnic industry and incorporate them within a MOF scaffold as a means to minimise performance variation caused by inconsistencies within physically mixed compositions.

In this chapter, the structures of a family of 1D, 2D, and 3D frameworks are discussed. These MOFs were created using a combination of various diacid compounds (fuels) and group 1 and group 2 metal nitrates (Na, K, Rb, Cs and Ca, Sr, Ba) (oxidisers).

Organic linkers commonly used to construct MOFs require ligands which have at least two different functionalities *e.g.* two carboxylates, one carboxylate and one pyridine, or bipyridine in order for an infinite structure to be generated. A list of commonly used fuels was searched in order to find materials which include this functionality. Oxalic acid and terephthalic acid are presently used as fuels by the pyrotechnic industry.[20] Along with these fuels numerous other diacids were selected to assess their potential to create a so-called MOFirework.

Alkali and alkaline earth metal nitrates were selected as the oxidisers in this study for their ability to impart colour into the MOFs. Alkaline earth metal nitrates were originally chosen based on their potential ability to mimic the function of zinc nitrate in the generation of MOF-5.[21] Alkali metal nitrates were also considered because of their popular use noted within the pyrotechnic industry. The products are labelled as follows, Ba_OxA_1(oxidiser_fuel_preparation method). There are a number of groups who have synthesised various combinations of these metal nitrates and diacids previously, however their uses in pyrotechnic applications have never been exploited.

Single crystal structure determinations of MOFs based on combinations of oxidiser and fuel ingredients are presented throughout this chapter. Their bulk characterisation as well as their thermal properties will also be discussed. In order to identify trends for each diacid ligand used within this study, several parameters were measured and compared. Specific features discussed in this chapter include; cation coordination mode, carboxylate binding type, and packing arrangement.

The effect of using fluorinated analogues of the aromatic compounds is discussed both in terms of how they affect the molecular packing arrangement and how they influence potential pyrotechnic properties. Other parameters which were assessed include the aliphatic ligand carbon chain length, hydroxyl group addition, and saturation level (alkane vs alkene).

The metal nitrates (oxidisers) and the dicarboxylate ligands (fuels) used to create potential pyrotechnic MOFs are summarised in Table 5.1.1. The fluorinated dicarboxylate ligands are exceptions as these could potentially act as oxidisers rather than as fuels. Where a CSD reference code is given in Table 5.1.1, the crystallographic data for the compound were obtained from the CSD.[22] Any further information about the compound was gathered from the literature. Microcrystalline products not of sufficient quality for SXRD were analysed using PXRD to ascertain if the resulting solid was either of the starting materials. X-ray crystal structure figures for each structure display the molecules present in the asymmetric unit and the numbering scheme. Thermal ellipsoids are drawn at 50% probability; hydrogen atoms are shown as spheres. The cell dimensions for each of the products are listed in the Appendix, Table A6. The crystal structure CIFs, PXRD and DSC data are available on the Appendix CD.

This chapter is divided into four parts:

5.2 Structure discussion for those incorporating fluorinated and non-fluorinated aromatic diacids (fBDC, isofBDC, altfBDC, BDC, isoBDC and altBDC)

5.3 Structure discussion for those incorporating alkane diacids (OxA, MnA, ScA, GlA, AdA, PmA, and SbA)

5.4 Structure discussion for those incorporating alkene and hydroxy diacids (LTA, MeA, and FmA)

Error! Reference source not found. Conclusions

	Ca(NO₃)₂.4H₂O	Sr(NO₃)₂	Ba(NO₃)₂
OxA	1- CALOXM (PXRD) 2 - Microcrystalline	1 - Microcrystalline 2 - Plates (SXRD)	1 - BALMUW (PXRD) 2 - Plates (SXRD)
MnA	1 - Microcrystalline 2 - CAMALD (SXRD)	1 - SRMALO (PXRD) 2 - Prisms (SXRD)	1 - Microcrystalline 2 - Microcrystalline
ScA	1 - Microcrystalline 2 - Amorphous	1 - Microcrystalline 2 - Mixture of S.M's	1 - Microcrystalline 2 - Mixture of S.M's
GlA	1 - YUDYAX (PXRD) 2 - Amorphous	1 - Prisms (SXRD) 2 - Microcrystalline	1 - Needles (SXRD) 2 - Mixture of S.M's
AdA	1 - LEGREU (PXRD) 2 - ADIPAC (S.M)	1 - Microcrystalline 2 - No Precipitate	1 - DEKZEA (PXRD) 2 - Mixture of S.M's
PmA	1 - Microcrystalline 2 - PIMELA (S.M)	1 - Microcrystalline 2 - No Precipitate	1 - Plates (SXRD) 2 - PIMELA (S.M)
SbA	1 - Microcrystalline 2 - SUBRAC (S.M)	1 - Microcrystalline 2 - Mixture of S.M's	1 - Microcrystalline 2 - Mixture of S.M's
fScA	1 - No Precipitate 2 - No Precipitate	1 - Plates (SXRD) 2 - Plates (SXRD)	1 - No Precipitate 2 - No Precipitate
fGlA	1 - No Precipitate 2 - No Precipitate	1 - No Precipitate 2 - No Precipitate	1 - No Precipitate 2 - No Precipitate
fAdA	1 - No Precipitate 2 - No Precipitate	1 - No Precipitate 2 - No Precipitate	1 - No Precipitate 2 - No Precipitate
LTA	1- CATART03 (SXRD) 2- CATART03 (SXRD)	1 - Amorphous 2 - CUGSUT, QALNIA (SXRD)	1 - HIXZOD (PXRD) 2 - HIXZOD (PXRD)
MeA	1 - Microcrystalline 2 - Microcrystalline	1 - Plates (SXRD) 2 - Microcrystalline + S.M	1 - Microcrystalline 2 - Microcrystalline + S.M
FmA	1 - Prisms (SXRD) 2 - Microcrystalline	1 - DUCLUJ01 (PXRD) 2 - DUCLUJ01 (PXRD)	1 - Microcrystalline 2 - Mixture of S.M's
BDC	1 - Microcrystalline 2 - CATPAL (SXRD)	1 - IJOVEJ, NOCLOH (SXRD) 2 - LOCCAH (SXRD)	1 - Microcrystalline 2 - Microcrystalline + S.M
isoBDC	1 - Amorphous 2 - Microcrystalline	1 - Microcrystalline + S.M 2 - Mixture of S.M's	1 - Plates (SXRD) 2 - Microcrystalline + S.M
altBDC	1 - N/A 2 - Microcrystalline	1 - N/A 2 - Mixture of S.M's	1 - N/A 2 - Microcrystalline + S.M
fBDC	1 - Plates (SXRD) 2 - Blocks (SXRD)	1 - Plates (SXRD) 2 - Plates (SXRD)	1 - Prisms (SXRD) 2 - Prisms (SXRD)
isofBDC	1 - Microcrystalline 2 - Microcrystalline	1 - Plates (SXRD) 2 - Blocks (SXRD)	1 - Microcrystalline 2 - Microcrystalline + S.M
altfBDC	1 - Microcrystalline 2 - Needles (SXRD)	1 - Plates (SXRD) 2 - Plates (SXRD)	1 - Highly Amorphous 2 - Prisms (SXRD)

Table 5.1.1 – Group 2 List of morphologies, CSD ref codes, and method of analysis used

5.2   CRYSTAL STRUCTURES BASED ON AROMATIC LINKERS

This section describes the features of crystal structures from the aromatic systems trialled. The coordination geometries of the metal centres from the crystal structures obtained for the aromatic and fluorinated aromatic products in this study are shown in Table 5.2.1. There are a total of 6 structures previously listed in the CSD[22] and 11 novel structures. Each of the products are discussed in terms of how their pyrotechnic outputs are directly related to their packing arrangements.

The carboxylate moieties coordinate to metal cations typically by bridging, chelating, or via a combination of both as is highlighted by Scheme 5.2.1. Following a discussion of each of the products individually each will be compared to look for similar packing motifs and/or comparable DSC traces and burn tests.
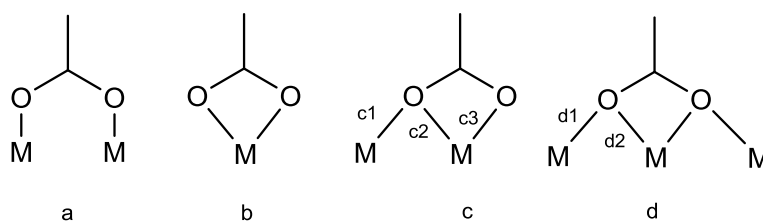
Scheme 5.2.1 - Schematic Diagram of Coordination Modes of the RCOO- Moiety a) bridging, b) chelating, c) chelating and bridging with one oxygen, d) chelating and bridging with two oxygens.

The main aim of this work is to uncover a system which possesses significant pyrotechnic potential such that it could rival common physical mixtures presently used within the pyrotechnic industry. BDC is used at present as a fuel and a gassing agent. The question that arises is, 'Will its inclusion in a MOF allow it to behave in a similar manner to it being physically mixed with an oxidiser?'. The aromatic series will be compared to the other aliphatic and hydroxyl/alkene series assessed within this work.

Ca_fBDC_2
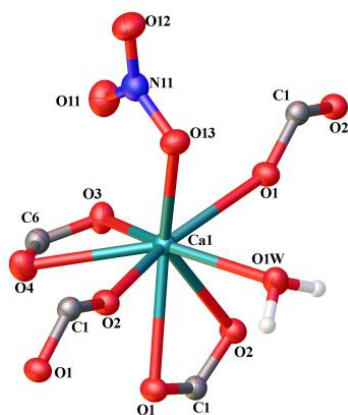
Ca1-O3(COO)b
Ca1-O4(COO)b
Ca1-O1(COO)d1
Ca1-O2(COO)d1
Ca1-O1(COO)d2
Ca1-O2(COO)d2
Ca1-O13(NO3)
Ca1-O1W(H2O)t

Sr_fBDC_2
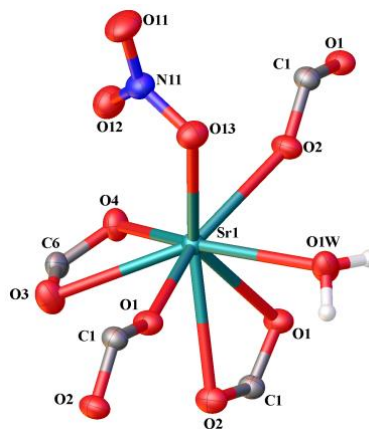
Sr1-O3(COO)b
Sr1-O4(COO)b
Sr1-O1(COO)d1
Sr1-O2(COO)d1
Sr1-O1(COO)d2
Sr1-O2(COO)d2
Sr1-O13(NO3)
Sr1-O1W(H2O)t

Ba_fBDC_1/2
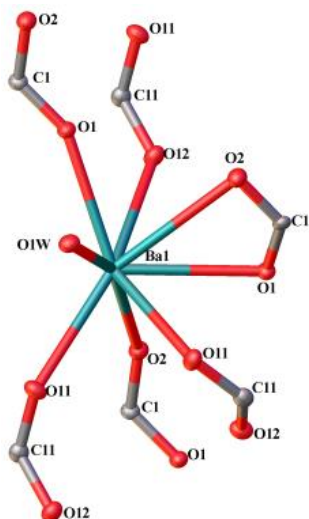
Ba1-O11(COO)a
Ba1-O11(COO)a
Ba1-O12(COO)a
Ba1-O1(COO)d1
Ba1-O1(COO)d2
Ba1-O2(COO)d1
Ba1-O2(COO)d2
Ba1-O1W(H2O)br

K_fBDC_2 - (PIPDOJ)
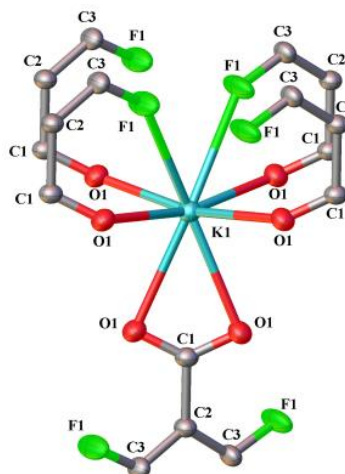
K1-O1(COO)d1
K1-O1(COO)d1
K1-O1(COO)d1
K1-O1(COO)d1
K1-O1(COO)d2
K1-O1(COO)d2
K1-F1(COO)
K1-F1(COO)

Rb_fBDC_2
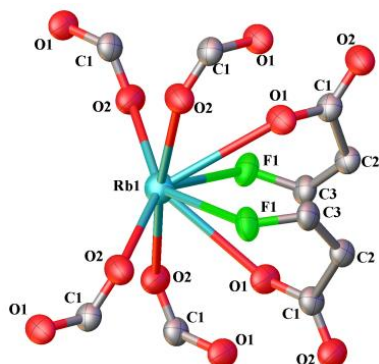
Rb1-O1(COO)a
Rb1-O1(COO)a
Rb1-O2(COO)a
Rb1-O2(COO)a
Rb1-O2(COO)a
Rb1-O2(COO)a
Rb1-F1(COO)
Rb1-F1(COO)

Cs_fBDC_2
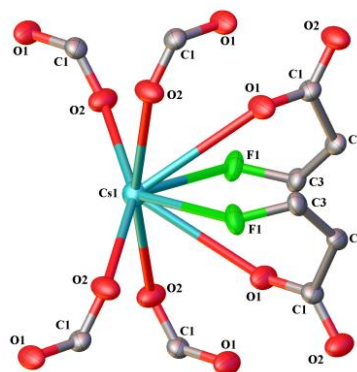
Cs1-O1(COO)a
Cs1-O1(COO)a
Cs1-O2(COO)a
Cs1-O2(COO)a
Cs1-O2(COO)a
Cs1-O2(COO)a
Cs1-F1(COO)
Cs1-F1(COO)

190
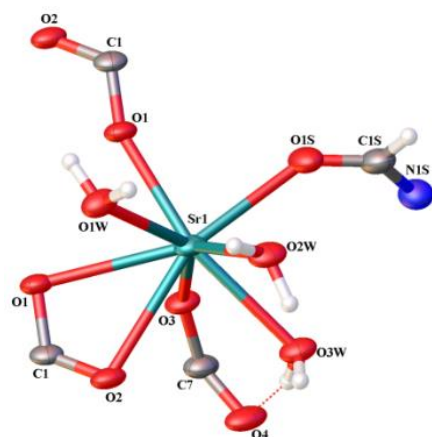
Sr_isofBDC_1

Sr1-O1(COO)c1
Sr1-O1(COO)c2
Sr1-O2(COO)c3
Sr1-O3(COO)*
Sr1-O1S(DMF)t
Sr1-O1W(H2O)t
Sr1-O2W(H2O)t
Sr1-O3W(H2O)t

Sr_isofBDC_2
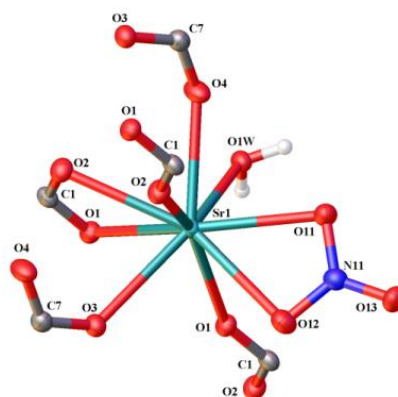
Sr1-O3(COO)a
Sr1-O4(COO)a
Sr1-O1(COO)d1
Sr1-O2(COO)d1
Sr1-O1(COO)d2
Sr1-O2(COO)d2
Sr1-O1W(H2O)t
Sr1-O11(NO3)
Sr1-O12(NO3)

Ca_altfBDC_2
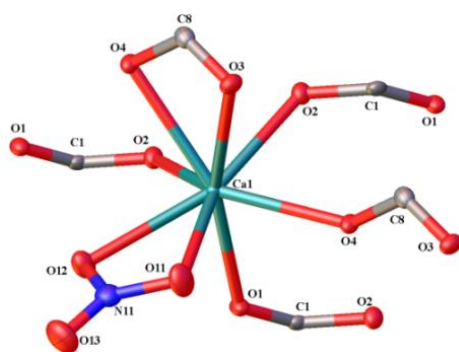
Ca1-O1(COO)a
Ca1-O2(COO)a
Ca1-O2(COO)a
Ca1-O4(COO)c1
Ca1-O4(COO)c2
Ca1-O3(COO)c3
Ca1-O11(NO3)
Ca1-O12(NO3)

Sr_altfBDC_1
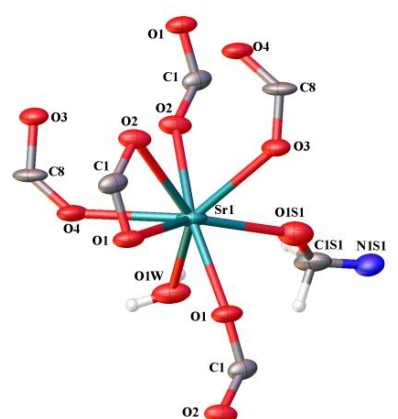
Sr1-O3(COO)a
Sr1-O4(COO)a
Sr1-O1(COO)d1
Sr1-O2(COO)d1
Sr1-O2(COO)d2
Sr1-O1(COO)d2
Sr1-O1W(H2O)t
Sr1-O1S1(DMF)t

Sr_altfBDC_2 (Sr1)
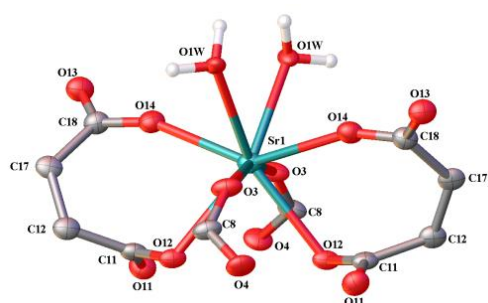
Sr1-O3(COO)a
Sr1-O3(COO)a
Sr1-O12(COO)a
Sr1-O12(COO)a
Sr1-O14(COO)c1
Sr1-O14(COO)c1
Sr1-O1W(H2O)br
Sr1-O1W(H2O)br

Sr_altfBDC_2 (Sr2)
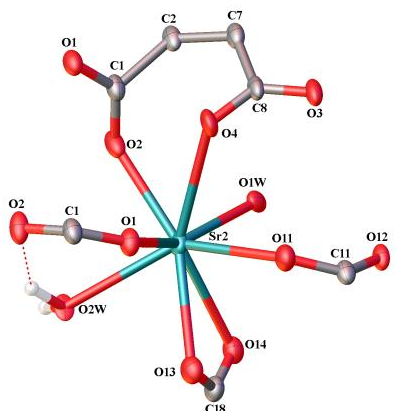
Sr2-O1(COO)a
Sr2-O2(COO)a
Sr2-O4(COO)a
Sr2-O11(COO)a
Sr2-O14(COO)c2
Sr2-O13(COO)c3
Sr2-O1W(H2O)br
Sr2-O2W(H2O)t

Ba_altfBDC_2
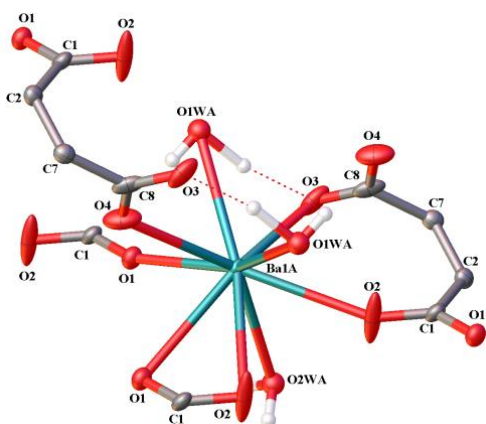
Ba1A-O3(COO)a
Ba1A-O4(COO)a
Ba1A-O1(COO)d1
Ba1A-O2(COO)d1
Ba1A-O1(COO)d2
Ba1A-O2(COO)d2
Ba1A-O1WA(H2O)br
Ba1A-O1WA(H2O)br
Ba1A-O2WA(H2O)t

Ca_BDC_2 - (CATPAL)
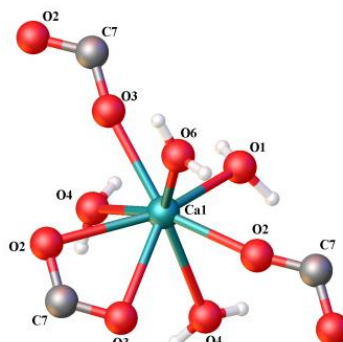
Ca1-O2(COO)d1
Ca1-O3(COO)d1
Ca1-O3(COO)d2
Ca1-O2(COO)d2
Ca1-O4(H2O)br
Ca1-O4(H2O)br
Ca1-O1(H2O)t
Ca1-O6(H2O)t

Sr_BDC_1a - (IJOVEJ)
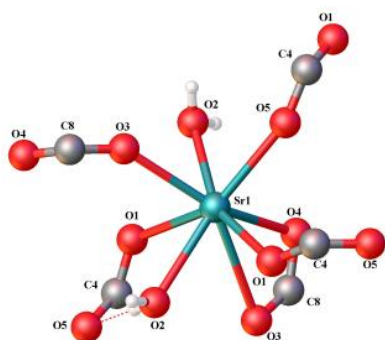
Sr1-O1(COO)a
Sr1-O1(COO)a
Sr1-O5(COO)a
Sr1-O3(COO)c1
Sr1-O3(COO)c2
Sr1-O4(COO)c3
Sr1-O2(H2O)br
Sr1-O2(H2O)br

Sr_BDC_1b - (NOCLOH)
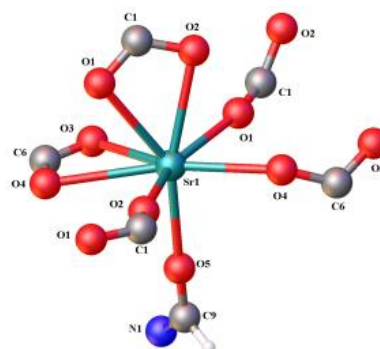
Sr1-O4(COO)c1
Sr1-O4(COO)c2
Sr1-O3(COO)c3
Sr1-O1(COO)d1
Sr1-O2(COO)d1
Sr1-O1(COO)d2
Sr1-O2(COO)d2
Sr1-O5(DMF)t

Sr_BDC_2 - (LOCCAH)
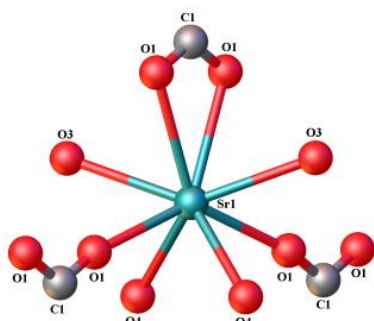
Sr1-O1(COO)d1
Sr1-O1(COO)d1
Sr1-O1(COO)d2
Sr1-O1(COO)d2
Sr1-O3(H2O)t
Sr1-O3(H2O)t
Sr1-O4(H2O)t
Sr1-O4(H2O)t

Ba_isoBDC_2 - (BAFORM)
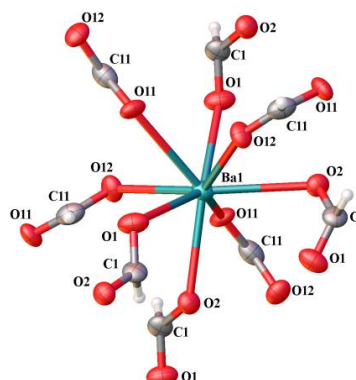
Ba1-O1(COO)a
Ba1-O1(COO)a
Ba1-O2(COO)a
Ba1-O2(COO)a
Ba1-O11(COO)a
Ba1-O11(COO)a
Ba1-O12(COO)a
Ba1-O12(COO)a

Table 5.2.1 - Coordination geometries of the metal centres in the aromatic and
fluorinated aromatic MOFs (t = terminal, br = bridging, * = non-bridging M-O bond)

The majority of the crystal structures presented in this series are 8-coordinate and have biaugmented triangular prism coordination geometry. All of the group 1 metal structures are 6-coordinate and have trigonal prism geometry.

Modes c (c1, c2, and c3) are most prevalent for the aromatic crystal structures although their presence seems to affect fluorinated and non-fluorinated structures differently. When found in fluorinated structures the dimensionality is 1D with the exception of Sr_altfBDC_2 which is 2D. However, this crystal structure possessed two unique Sr environments. The non-fluorinated structures, which include BDC ligands with connectivity mode c result in 3D frameworks. The other BDC crystal structures are 1D; these have a higher coordinated water content which occupies sites on the metal centres, preventing the formation of covalent constructs with higher dimensionality. The additional water content does not allow for a supramolecular 3D framework to form. A summary of the features of the aromatic structures is presented in Table 5.2.2. The aromatic and fluorinated aromatic structures create a variety of topologies which extend into 1D, 2D and 3D.

Product	Building Units	Coordination Geometry	Linker Connectivity	Dimensionality	Carboxylate Torsion Angles/°
Ca_fBDC_2	$Ca(OH_2)(NO_3)(COO)_4$	Biaugmented triangular prism (8)	(b, d1, d2) x2, t	3D	61.8(4), -58.5(4)
Sr_fBDC_2	$Sr(OH_2)(NO_3)(COO)_4$	Biaugmented triangular prism (8)	(b, d1, d2) x2, t	3D	62.2(6), -59.4(6)
Ba_fBDC_1/2	$Ba(OH_2)(COO)_6$	Pentagonal-triangle prismatoid (8)	(a) x3 (d1, d2) x2, br	3D	42.8(4), 34.4(4)
K_fBDC_2	$K(COO)_5$	Distorted trigonal prism (6)	(d1x2, d2) x2	3D	-33.40(12)
Rb_fBDC_2	$Rb(COO)_6$	Distorted trigonal prism (6)	(a) x6	3D	48.4(7)
Cs_fBDC_2	$Cs(COO)_6$	Distorted trigonal prism (6)	(a) x6	3D	50.7(3)
Sr_isofBDC_1	$Sr(OH_2)_3(DMF)(COO)_3$	Biaugmented triangular prism (8)	c1, c2, c3, *, (t) x4	1D	-41.5(9), 65.2(9)
Sr_isofBDC_2	$Sr(OH_2)(NO_3)(COO)_5$	Pentagonal biwedge (9)	(a, d1, d2) x2, t	2D	-61.8(5), 54.0(5)
Ca_altfBDC_2	$Ca(NO_3)(COO)_5$	Biaugmented triangular prism (8)	(a) x3, c1, c2, c3	1D	84.9(5), 38.1(5)
Sr_altfBDC_1	$Sr(OH_2)(DMF)(COO)_5$	Biaugmented triangular prism (8)	(a, d1, d2) x2, (t) x2	2D	57.6(15), 57.2(14)
Sr_altfBDC_2	$Sr(OH_2)_2(COO)_6,$ $Sr(OH_2)_2(COO)_5$	Biaugmented triangular prism (8)	(a) x4, (c1) x2, (br) x2 (a) x4, c2, c3, t, br	2D	-75(2), -15(2), 74.2(19), -42(2)
Ba_altfBDC_2	$Ba(OH_2)_3(COO)_5$	Triaugmented triangular prism (9)	(a, d1, d2) x2, t, br (x2)	2D	43.8(5), 73.1(5)
Ca_BDC_2	$Ca(OH_2)_4(COO)_3$	Biaugmented triangular prism (8)	(d1, d2, t, br) x2	1D	4.1, -5.2
Sr_BDC_1a	$Sr(OH_2)_2(COO)_5$	Biaugmented triangular prism (8)	(a) x3, c1, c2, c3, (br) x2	3D	1.6, -7.9
Sr_BDC_1b	$Sr(DMF)(COO)_5$	Biaugmented triangular prism (8)	c1, c2, c3, (d1, d2) x2, t	3D	-2.7, 12.1
Sr_BDC_2	$Sr(OH_2)_4(COO)_3$	Biaugmented triangular prism (8)	(d1, d2) x2, (t) x4	1D	0.5, -8.1
Ba_isoBDC_2	$Ba(COO)_8$	Square antiprism (8)	(a) x8	1D	-

Table 5.2.2 - Aromatic Structures: List of MOF building units, coordination geometry, linker connectivity, dimensionality and carboxylate torsional angles.

Ba_fBDC resulted in the same product irrespective of the synthesis method chosen. The DMF approach was more effective as it resulted in a pure material. Residual oxidiser starting material was present within the MeOH synthesis product.

a)   b)
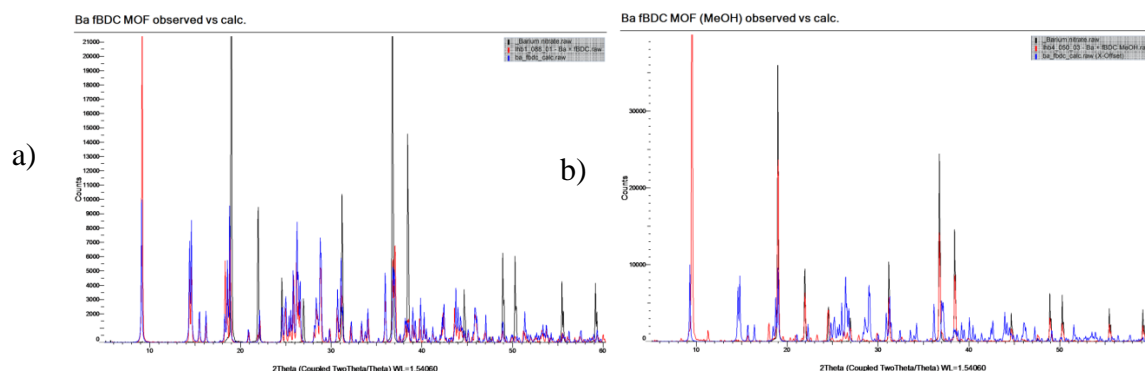
Figure 5.2.1 a) Ba_fBDC_1 PXRD data b) Ba_fBDC_2 PXRD data (Red = Observed PXRD Pattern, Blue = SXRD simulated PXRD pattern)

Crystal structures could not be found for Ca and Sr when paired with fBDC using the DMF method. It was evident from both SXRD and PXRD data that the products resulting from the MeOH approach were isostructural (Figure 5.2.2).

a)   b)
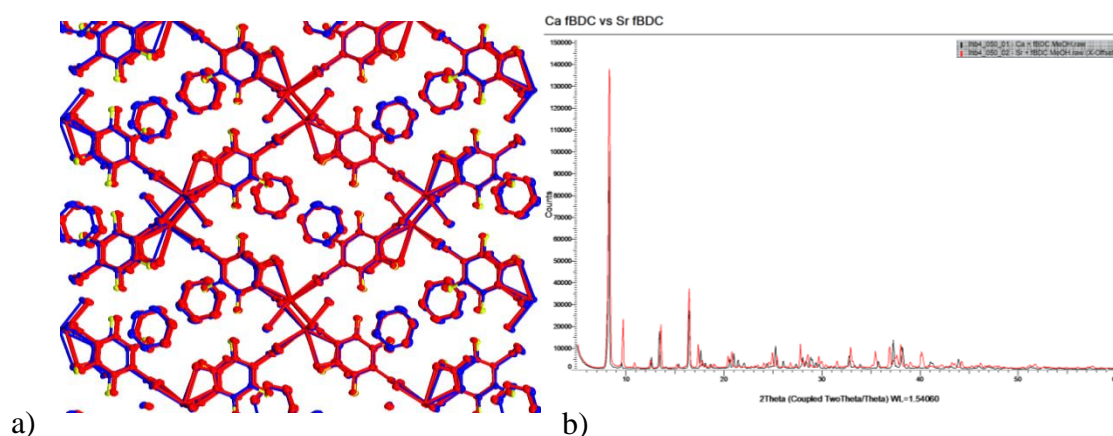
Figure 5.2.2- Ca_fBDC_2 vs Sr_fBDC_2 a) Crystal Structure Overlay (hydrogen atoms omitted for clarity, b) Observed PXRD data (Black = Ca_fBDC_2, Red = Sr_fBDC_2)

This was not the only case of isostructurality as there were similar findings made for the alkaline metals where Rb_fBDC_2 and Cs_fBDC_2 resulted in the same crystal structure (Figure 5.2.3). It is apparent from the comparison of the observed and simulated PXRD data that an unidentified isostructural component exists. A cluster of peaks are present at 2θ values of 10° and above which only appear in the observed

195

pattern and not in the calculated pattern as is highlighted in Figure 5.2.3 (b) for both Rb_ fBDC and Cs_fBDC.
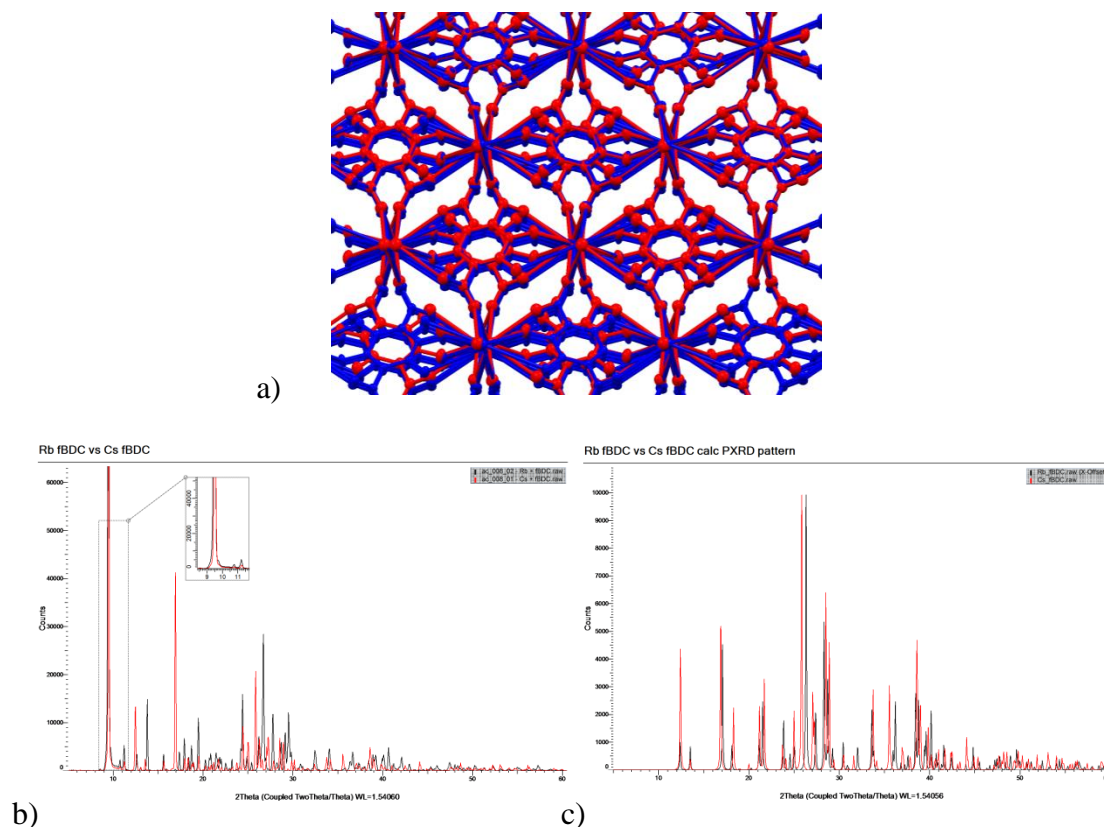
Figure 5.2.3 - Rb_fBDC_2 vs Cs_fBDC_2 a) Crystal Structure Overlay (hydrogen atoms omitted for clarity, b) Observed PXRD data c) Calculated PXRD data (Black = Rb_fBDC_2, Red = Cs_fBDC_2)

K_fBDC_2, previously reported by Werker et al.[23], is most similar to Ba_fBDC_1/2 in that the structures are composed of 2D sheets which are constructed by $M(COO)_n(OH_2)_x$ (K; n = 5, x = 0, Ba; n = 6, x = 1). These sheets are cross-linked through the fBDC linkers. These lie roughly parallel to one another, however, for Ba_fBDC_1/2 on moving from one sheet to the next the fBDC linkers rotate by 73° as can be seen in Figure 5.2.4.
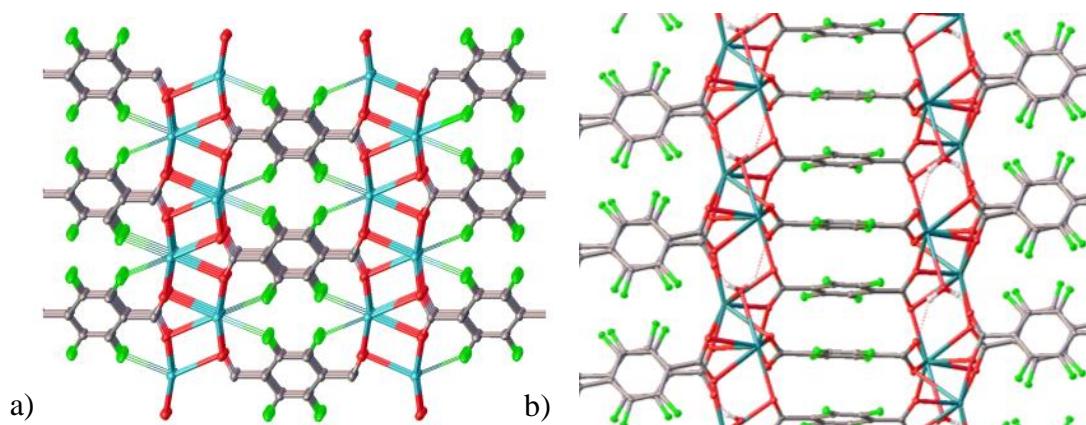
Figure 5.2.4 a) K_fBDC_2, b) Ba_fBDC_1/2

Although a product resulted from all combinations including the alternate substituted versions of fBDC (1,4), isofBDC (1,3) and altfBDC (1,2), it was not possible to identify a full set of crystal structures for these products. In the case of isofBDC a crystal structure was found for both synthetic approaches when using Sr.
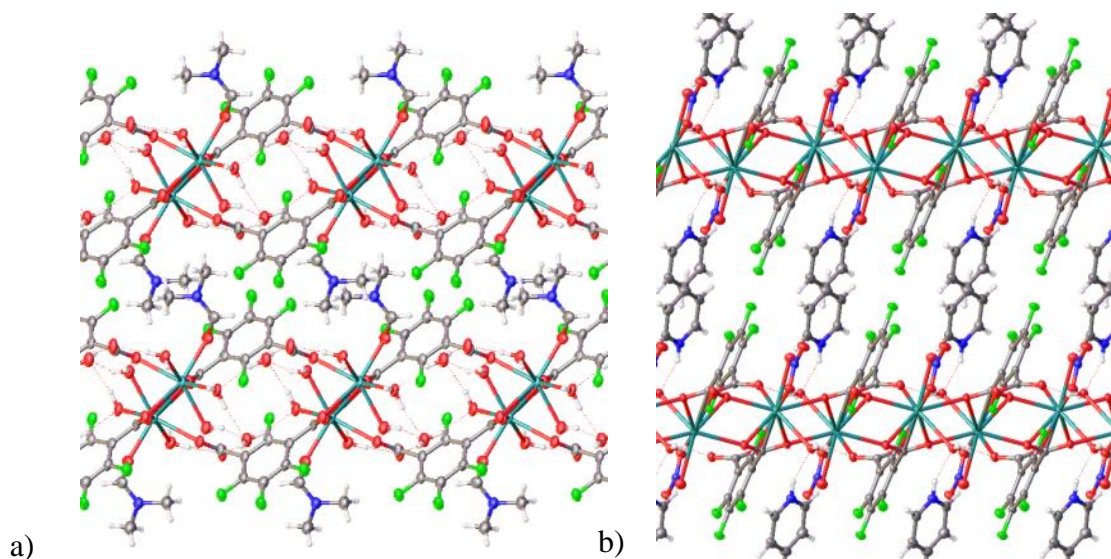
Figure 5.2.5 a) Sr_isofBDC_1, b) Sr_isofBDC_2

The first structure consists of monomeric units which possess two Sr centres which are further connected by isofBDC linkers to create a 1D chain. The second structure formed 2D sheets via the $Sr(OH_2)(NO_3)(COO)_5$ and $Sr(NO_3)(COO)_5$ units. Sr_isofBDC_1 are composed of $Sr(OH_2)_3(DMF)(COO)_3$ units. The terminal water molecules prevent the

formation of 2D covalent sheets, favouring a structure mediated by hydrogen bonding to create supramolecular 2D sheets.

When Sr was combined with altfBDC both crystal structures resulting from each synthetic approach were identified. Only products which formed via the MeOH method were identified for Ca and Ba.

a)   b)
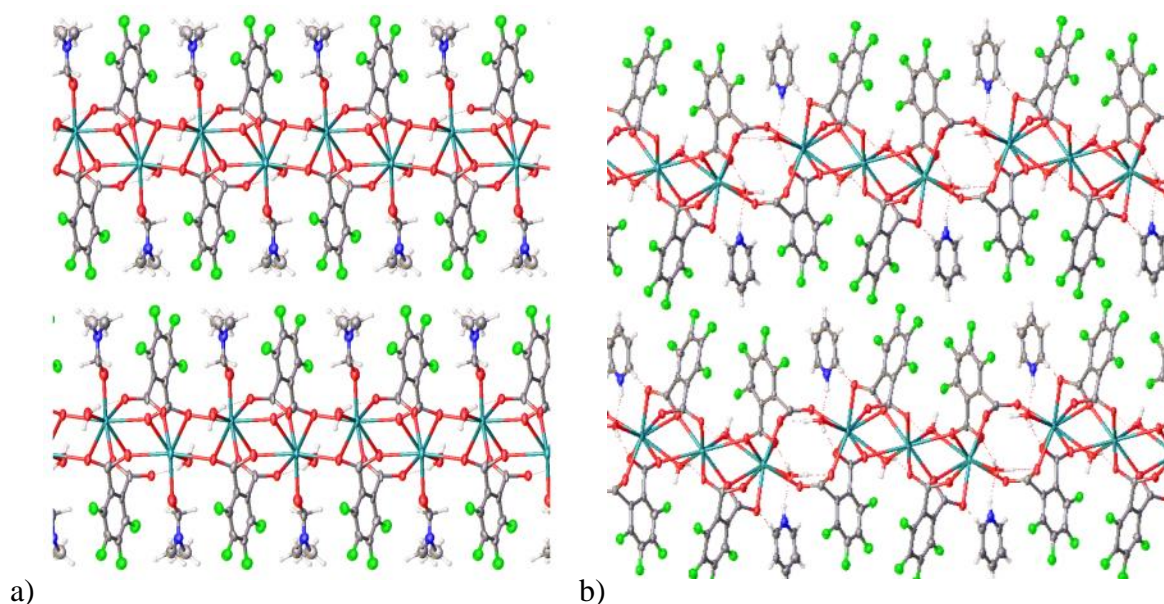
Figure 5.2.6 a) Sr_altfBDC_1 b) Sr_altfBDC_2

$Sr(OH_2)(DMF)(COO)_5$ units link together to create 2D sheets. The solvent to acid ratio in this case is 1:1 whereas for the second structure the ratio is reduced to 1:2. $Sr(OH_2)(COO)_6$ and $Sr(OH_2)(COO)_5$ units link together to create 2D sheets. The altfBDC linkers within the first structure appear to be parallel to one another. The altfBDC arrangement changes for the second structure as the second carboxylate from each of the altfBDC linkers differ with torsion values changing from -15(2)° (C6C7C8O3) to -42(2)° (C16C17C18O13).

Ca_altfBDC_2 forms 1D chains composed of monomeric units which possess two Ca centres ($Ca(NO_3)(COO)_5$ x2) which are connected by altfBDC linkers similarly to Sr_isofBDC_1. Ba_altfBDC_2 is composed of 2D sheets constructed by $Ba(OH_2)(COO)_5$ units which are cross-linked by altfBDC linkers. Ba_altfBDC_2 more closely resembles Sr_altfBDC_1 in that they both possess a solvent molecule 'spacer' between each of the diacids above and below the 2D sheets.

a)   b)
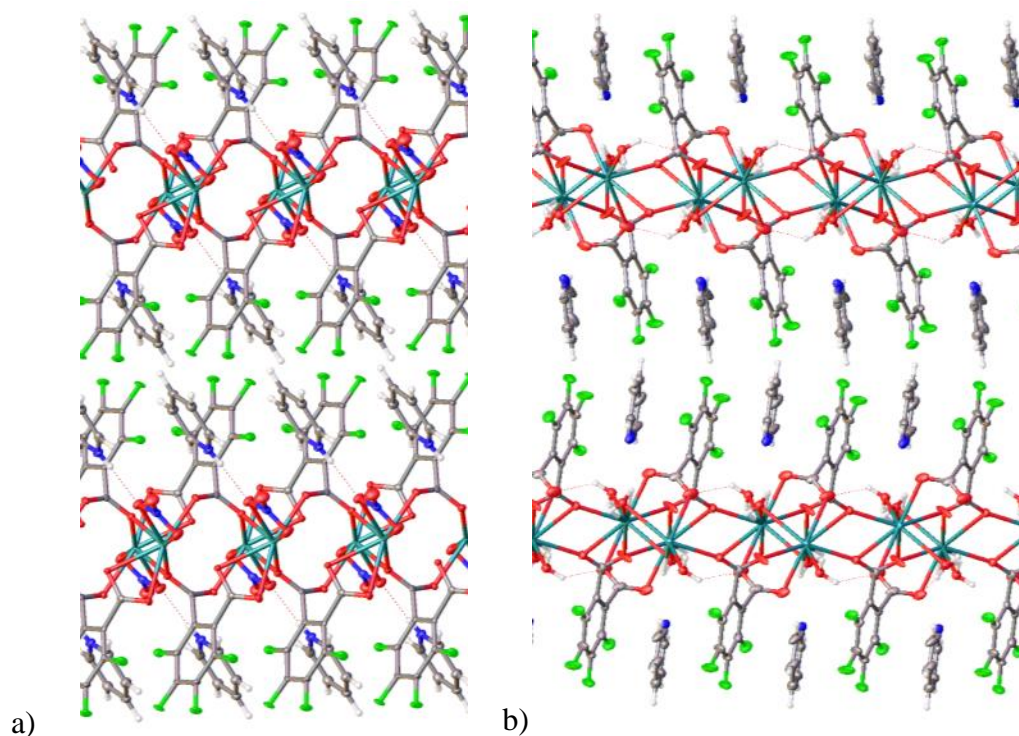
Figure 5.2.7 a) Ca_altfBDC_2 b) Ba_altfBDC_2

Initial burn tests revealed that alkaline earth metal MOFs had more pyrotechnic potential than alkali metal MOFs. K_MOF_2 appeared to only melt and give off only a few sparks compared to Rb_fBDC_2 and Cs_fBDC_2 which both behaved in a similar way. Ca_fBDC_2 and Sr_fBDC_2 also behaved similarly in that they both gave off numerous sparks. Ba_fBDC_2 burned steadily for a short period of time.
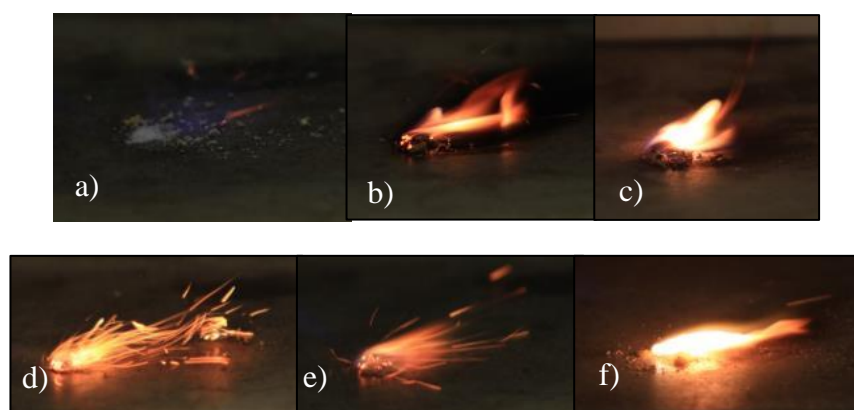
Figure 5.2.8 Burn Tests (fBDC MeOH) a) K_fBDC_2, b) Rb_BDC_2, c) Cs_fBDC_2,

d) Ca_fBDC_2, e) Sr_fBDC_2, f) Ba_fBDC_2

The burn tests shown below indicate the burn behaviours of all of the alkaline metals coupled with the various fluorinated acids; fBDC, isofBDC, and altfBDC, using DMF.
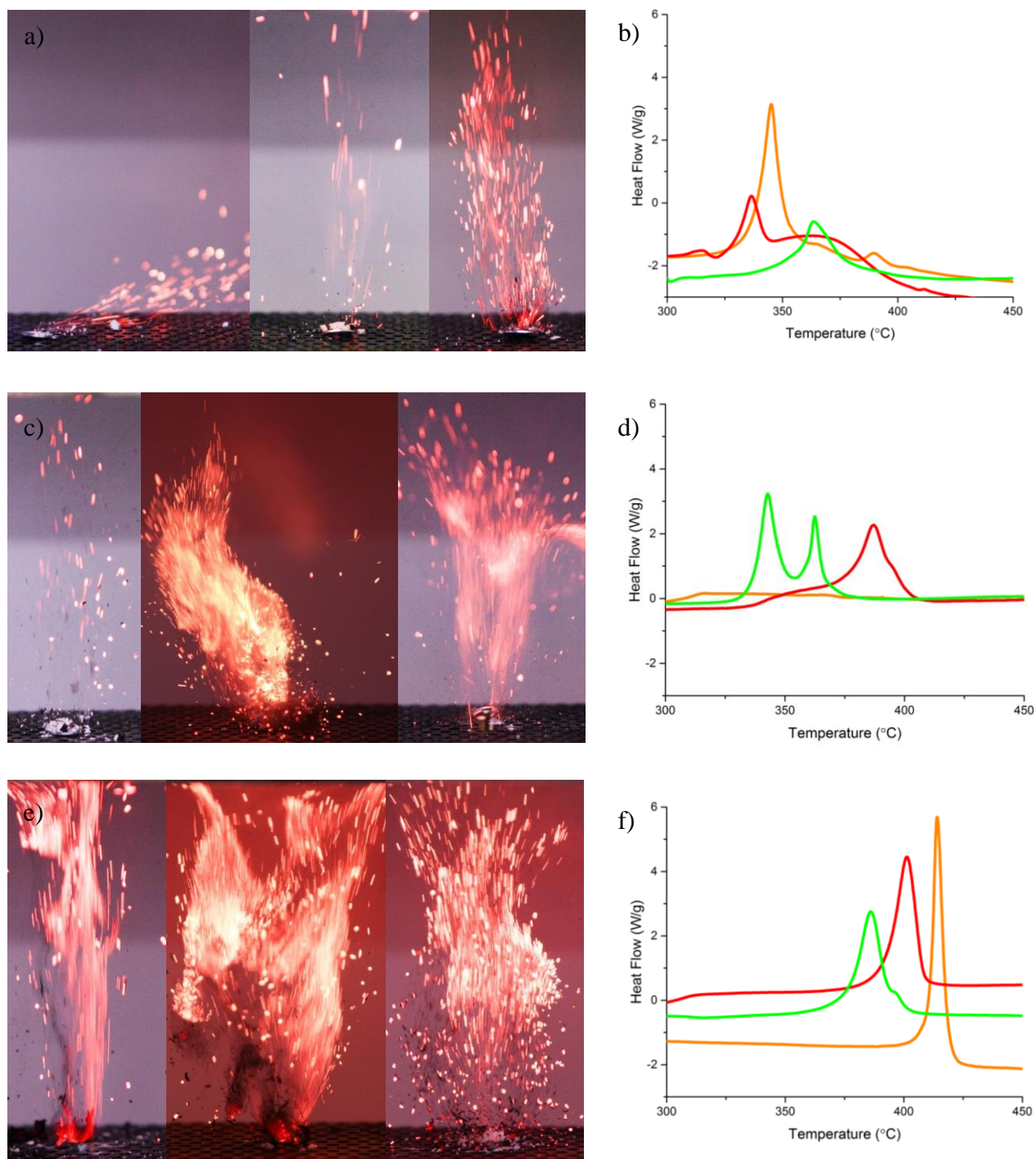
Figure 5.2.9 Burn Tests - a) Ca/Sr/Ba_fBDC_1, b) fBDC1 DSC Trace, c) Ca/Sr/Ba_isofBDC_1, d) isofBDC1 DSC Trace, e) Ca/Sr/Ba_altfBDC_1, f) altfBDC1 DSC Trace [Ca, orange, Sr, red, Ba, green]

The DSC results and the burn tests for fBDC show that Ba_fBDC is the most energetic. Burn tests for isofBDC MOFs show that both Sr and Ba are very energetic in comparison to Ca compounds. The DSC trace also suggests that Ca compound has negligible pyrotechnic potential. AltfBDC containing MOFs appear to have the most significant pyrotechnic potential. An interesting trend is observed within the DSC traces such that as the cation is changed from Ba through to Ca the position of the exothermic peak shifts steadily from 387.45°C to 416.08°C. The energy associated with these peaks is 250.85 J/g (Ca), 264.30 J/g (Sr), and 256.45 J/g (Ba).

DSC traces for the products which resulted from the MeOH synthesis show exothermic peaks occur at much lower temperatures than the DMF products mainly for the isofBDC and altfBDC containing MOFs.
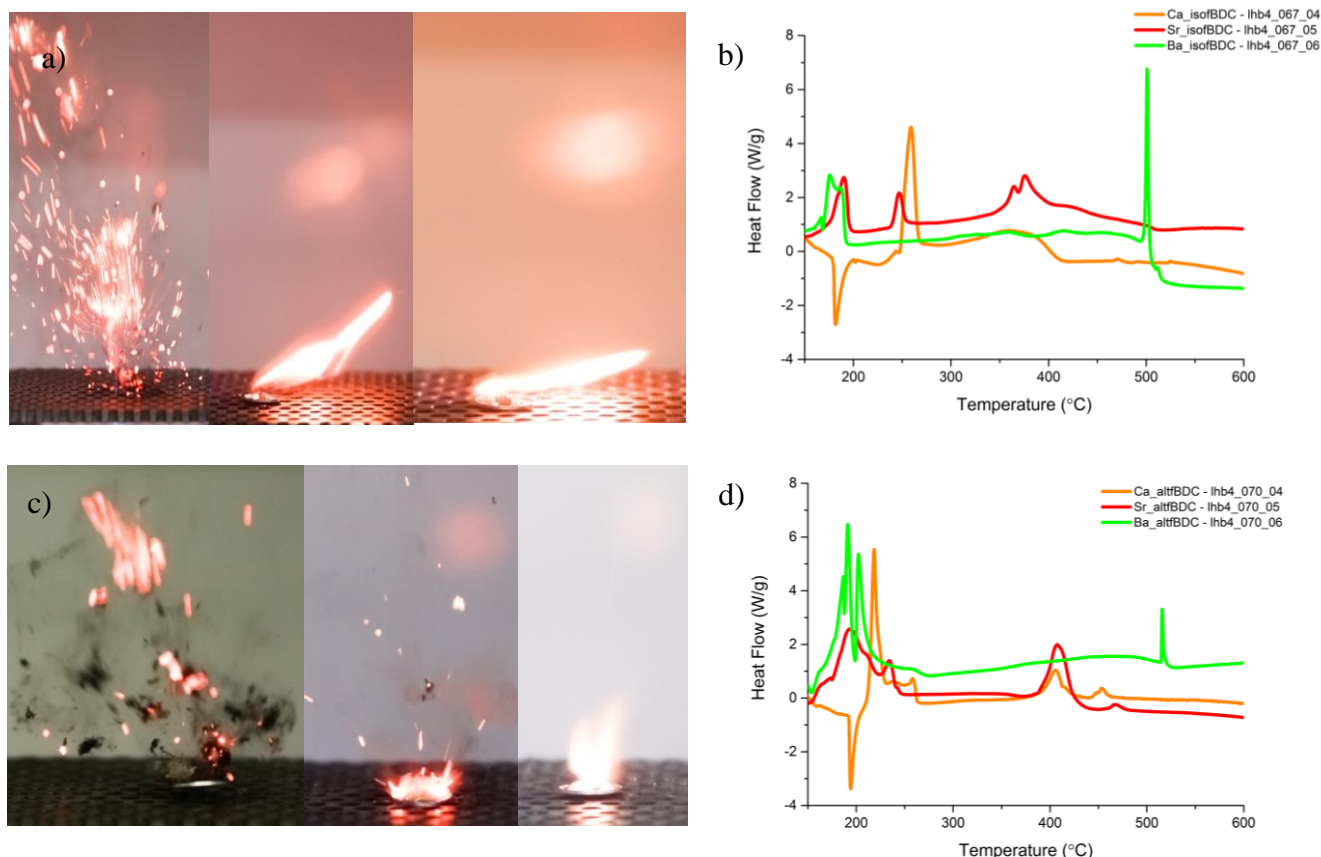
Figure 5.2.10 Burn Tests - a) Ca/Sr/Ba_isofBDC_2, b) isofBDC2 DSC Trace_2, c) Ca/Sr/Ba_altfBDC_2, d) altfBDC_2 DSC Trace [Ca, orange, Sr, red, Ba, green]

Similar patterns of thermal decomposition can be seen when comparing isofBDC and altfBDC MOFs with respect to the metal they are bound to.

Although crystal structures were not obtained for all combinations it was possible to notice a trend. The reduction in dimensionality appears to increase the materials pyrotechnic potential especially on moving from a 3D non-porous structure to either a 2D or 1D structure. This is particularly significant for pairings with either Ca or Sr as they do not appear to burn as well when combined with fBDC, the linker which generally produces 3D MOFs. Energetic material groups working towards the stabilisation of explosive materials have made similar findings.[18, 19, 24]

Only a couple of the non-fluorinated aromatic structures were resolvable. Ca and Sr when coupled with BDC resulted in two known structures in the CSD (CATPAL[25] and LOCCAH[26]). Both products form 1D chains. The coordination number for these structures are equivalent $(M(OH_2)_4(COO)_3))$ it is in the arrangement of the coordinated water molecules where these structures differ. Considering the metal carboxylate chain as a plane, Ca_BDC_2 has one water molecule above and three below this plane whereas Sr_BDC_2 has two water molecules above and two water molecules below. Each chain is hydrogen bonded to four other chains resulting in a 3D supramolecular network.
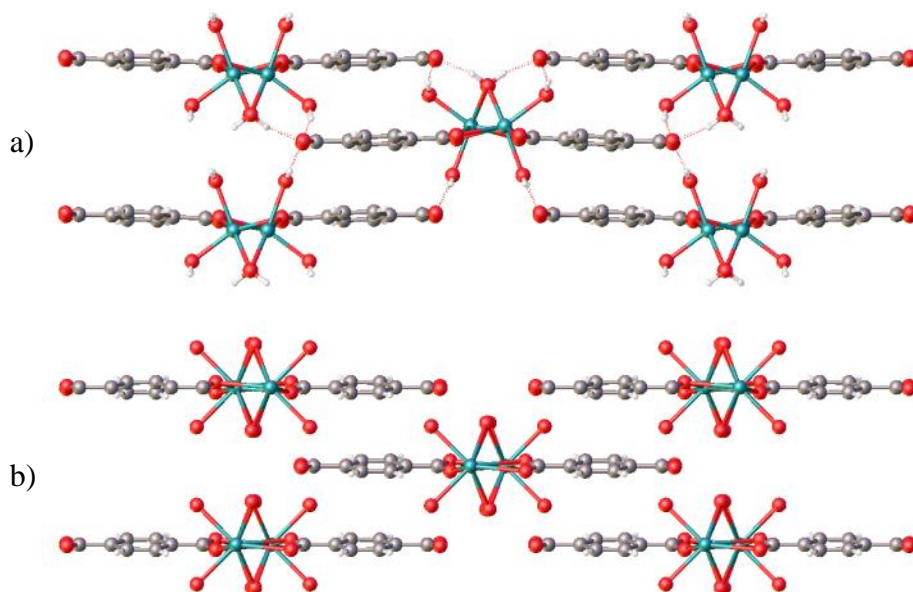
Figure 5.2.11 a) Ca_BDC_2, b) Sr_BDC_2

Sr_BDC_1 resulted in the formation of two known products, a) IJOVEJ[27] and b) NOCLOH[28]. The building units of Sr_BDC_1a are $Sr(OH_2)(COO)_5$ whereas for Sr_BDC_1b they are $Sr(DMF)(COO)_5$. Both crystal structures create 3D frameworks the main difference is how they arise. The 3D framework within Sr_BDC_1a is caused by the cross-linking of BDC ligands between sheets of $Sr(OH_2)(COO)_5$, whereas in Sr_BDC_1b several 1D chains are cross-linked to create a triangular arrangement as shown in Figure 5.2.12

a)   b)
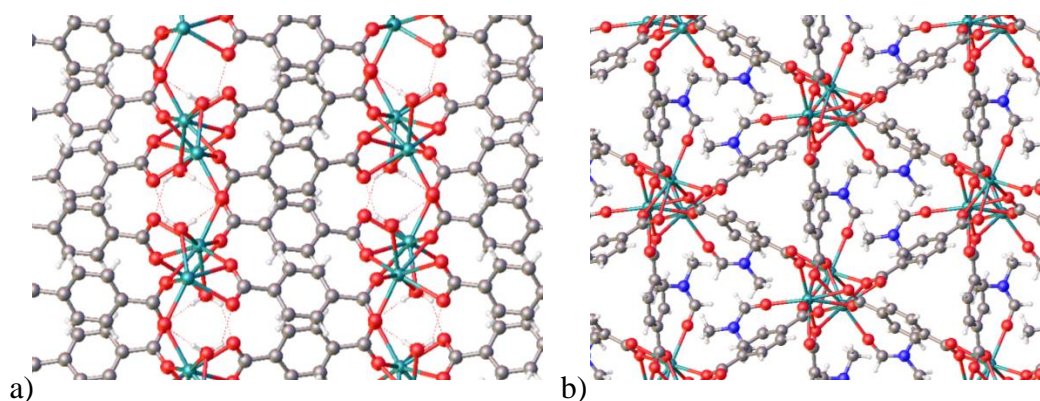
Figure 5.2.12 - a) Sr_BDC_1a b) Sr_BDC_1b

Ba_BDC_1 and Ba_BDC_2 were the only compounds found exhibiting an exothermic peak. Their crystal structures could not be determined. The peak was positioned at the same point (~500°C) as others identified in the fluorinated Ba containing coordination polymers. A decomposition product expected to result from heating these materials to high temperatures is barium oxide. This reacts at 500–600 °C with air to form barium peroxide, which decomposes at above 700 °C by releasing oxygen.[29] This may be the peak that is visible in several of the Ba structures. Ba_isoBDC_1 resulted in a decomposition product, Ba coupled with formic acid. Pyrotechnic potential was lacking for the non-fluorinated species with the exception of Ba containing materials. Based on this information it could be said that the incorporation of the non-fluorinated species into a MOF reduces its potential as a pyrotechnic product. However, the equivalent fluorinated structures show great potential but will require further investigation to assess their sensitivity values and to establish all other parameters necessary to allow its transport and production on a larger scale.

5.3   ALIPHATIC CRYSTAL STRUCTURES

This section assesses the use of aliphatic diacids as MOF linkers and the resulting pyrotechnic potential. The coordination geometries of the metal centres from the crystal structures obtained for the aliphatic products in this study are shown in Table 5.3.1. There are a total of 8 structures previously listed in the CSD[22] and 8 novel structures. The carboxylate moieties coordinate to metal cations typically by bridging, chelating, or via a combination of both as is highlighted by Scheme 5.3.1.

Similarly to BDC, OxA is also used as a fuel and a gassing agent. The question again follows; will the inclusion of the aliphatic diacids allow for an improved pyrotechnic product or will it be detrimental and minimise the required effect?
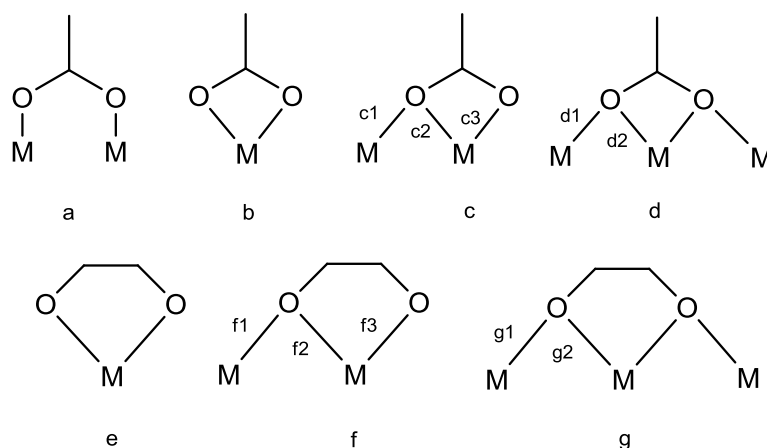
Scheme 5.3.1 - Schematic Diagram of Coordination Modes of the RCOO- Moiety a) bridging, b) chelating, c) chelating and bridging with one oxygen, d) chelating and bridging with two oxygens. e) chelating (OCCO-), f) chelating and bridging with one oxygen (OCCO-), g) chelating and bridging with two oxygens (OCCO-),

Ca_OxA_1 - (CALOXM13)
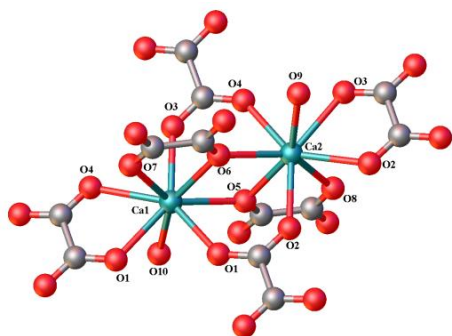
Ca1	Ca2
Ca1-O5(COO)f1	Ca2-O6(COO)f1
Ca1-O6(COO)f2	Ca2-O5(COO)f2
Ca1-O7(COO)f3	Ca2-O8(COO)f3
Ca1-O1(COO)g1	Ca2-O2(COO)g1
Ca1-O3(COO)g1	Ca2-O4(COO)g1
Ca1-O1(COO)g2	Ca2-O2(COO)g2
Ca1-O4(COO)g2	Ca2-O3(COO)g2
Ca1-O10(H2O)t	Ca2-O9(H2O)t

Sr_OxA_2
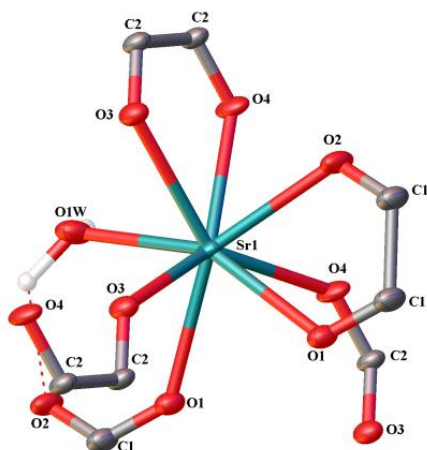
Sr1-O1(COO)f1
Sr1-O1(COO)f2
Sr1-O2(COO)f3
Sr1-O3(COO)g1
Sr1-O4(COO)g1
Sr1-O3(COO)g2
Sr1-O4(COO)g2
Sr1-O1W(H2O)t

Ba_OxA_1 (BALMUW)
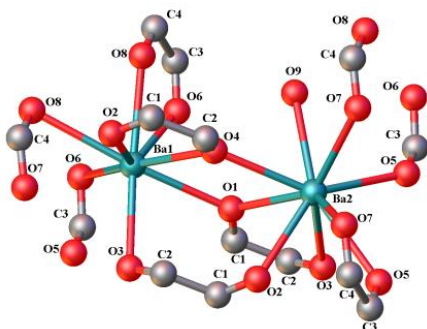
Ba1	Ba2
Ba1-O1(COO)g1	Ba2-O4(COO)g1
Ba1-O3(COO)g1	Ba2-O2(COO)g1
Ba1-O6(COO)g1	Ba2-O5(COO)g1
Ba1-O8(COO)g1	Ba2-O7(COO)g1
Ba1-O2(COO)g2	Ba2-O1(COO)g2
Ba1-O4(COO)g2	Ba2-O3(COO)g2
Ba1-O6(COO)g2	Ba2-O5(COO)g2
Ba1-O8(COO)g2	Ba2-O7(COO)g2
	Ba2-O9(H2O)t

Ba_OxA_2
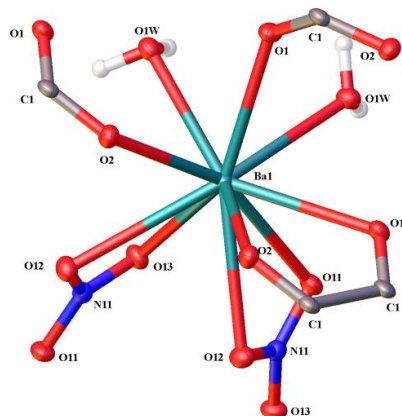
Ba1-O1(COO)g1
Ba1-O2(COO)g1
Ba1-O1(COO)g2
Ba1-O2(COO)g2
Ba1-O11(NO3)
Ba1-O12(NO3)
Ba1-O12(NO3)
Ba1-O13(NO3)
Ba1-O1W(H2O)br
Ba1-O1W(H2O)br

Na_OxA_2 - (NHOXAL)
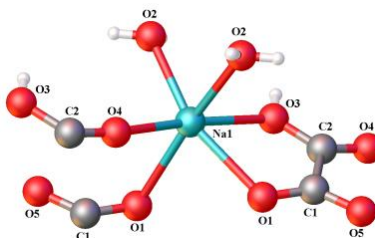
Na1-O4(COO)a
Na1-O1(COO)f1
Na1-O1(COO)f2
Na1-O3(COO)f3
Na1-O2(H2O)br
Na1-O2(H2O)br

Ca_MnA_2 - (CAMALD)
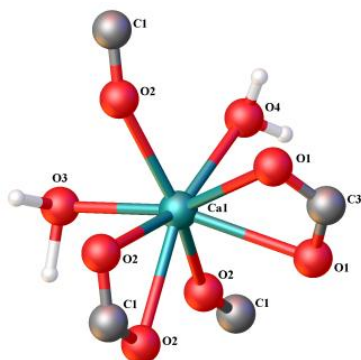
Ca1-O1(COO)a
Ca1-O1(COO)a
Ca1-O2(COO)d1
Ca1-O2(COO)d1
Ca1-O2(COO)d2
Ca1-O2(COO)d2
Ca1-O3(H2O)t
Ca1-O4(H2O)t

Sr_MnA_1 - (SRMALO)
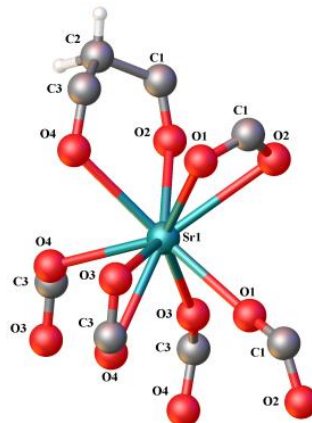
Sr1-O1(COO)d1
Sr1-O2(COO)d1
Sr1-O3(COO)d1
Sr1-O4(COO)d1
Sr1-O4(COO)d1
Sr1-O1(COO)d2
Sr1-O2(COO)d2
Sr1-O3(COO)d2
Sr1-O4(COO)d2

Sr_MnA_2 (Sr1)
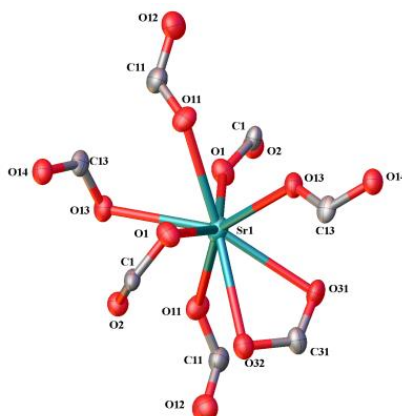
Sr1-O1(COO)a
Sr1-O1(COO)a
Sr1-O11(COO)a
Sr1-O11(COO)a
Sr1-O13(COO)d1
Sr1-O13(COO)d1
Sr1-O31(COO)d2
Sr1-O32(COO)d2

Sr_MnA_2 (Sr2)
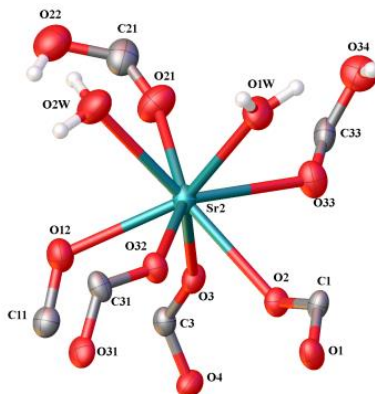
Sr2-O2(COO)a
Sr2-O12(COO)a
Sr2-O3(COO)d1
Sr2-O32(COO)d1
Sr2-O21(COO)*
Sr2-O33(COO)*
Sr2-O1W(H2O)t
Sr2-O2W(H2O)t

Sr_MnA_2 (Sr3)
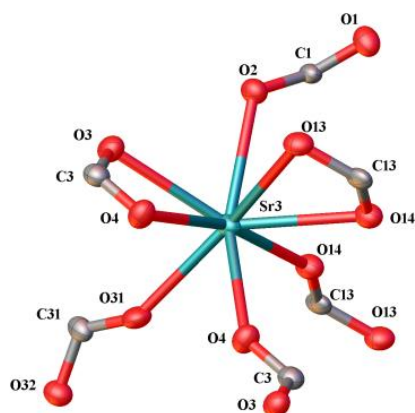
Sr3-O2(COO)a
Sr3-O4(COO)d1
Sr3-O14(COO)d1
Sr3-O31(COO)d1
Sr3-O3(COO)d2
Sr3-O4(COO)d2
Sr3-O13(COO)d2
Sr3-O14(COO)d2

Ca_GlA_1 - (YUDYAX)
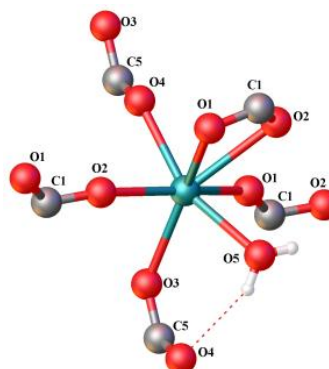
Ca1-O3(COO)a
Ca1-O4(COO)a
Ca1-O1(COO)d1
Ca1-O2(COO)d1
Ca1-O1(COO)d2
Ca1-O2(COO)d2
Ca1-O5(H2O)t

Sr_GlA_1
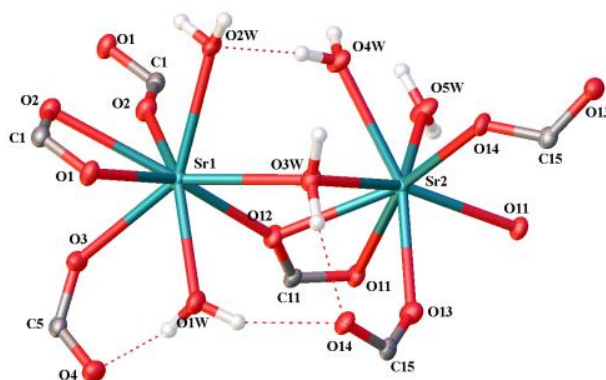
Sr1

Sr1-O2(COO)c1
Sr1-O2(COO)c2
Sr1-O1(COO)c3
Sr1-O12(COO)d1
Sr1-O3(COO)*
Sr1-O1W(H2O)t
Sr1-O2W(H2O)t
Sr1-O3W(H2O)br

Sr2

Sr2-O13(COO)a
Sr2-O14(COO)a
Sr2-O11(COO)d1
Sr2-O11(COO)d2
Sr2-O12(COO)d2
Sr2-O3W(H2O)br
Sr2-O4W(H2O)t
Sr2-O5W(H2O)t

Ba_GlA_1
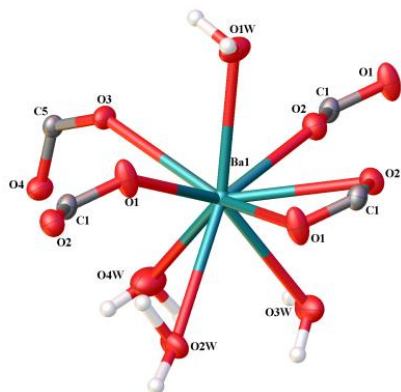
Ba1-O1(COO)d1
Ba1-O2(COO)d1
Ba1-O1(COO)d2
Ba1-O2(COO)d2
Ba1-O3(COO)*
Ba1-O1W(H2O)t
Ba1-O2W(H2O)t
Ba1-O3W(H2O)t
Ba1-O4W(H2O)t

Ca_AdA_1 - (LEGREU)
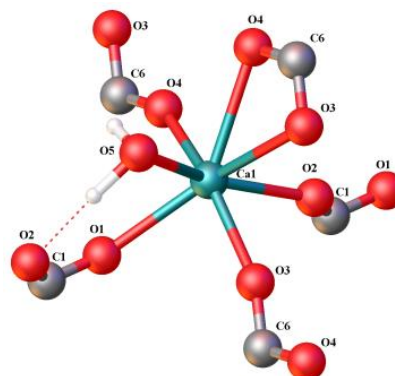
Ca1-O1(COO)a
Ca1-O2(COO)a
Ca1-O3(COO)d1
Ca1-O4(COO)d1
Ca1-O3(COO)d2
Ca1-O4(COO)d2
Ca1-O5(H2O)t

Ba_AdA_1 - (DEKZEA
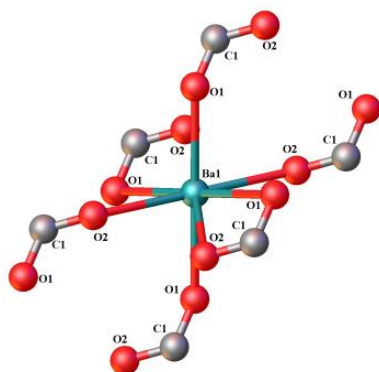
Ba1-O1(COO)d1
Ba1-O1(COO)d1
Ba1-O2(COO)d1
Ba1-O2(COO)d1
Ba1-O1(COO)d2
Ba1-O2(COO)d2
Ba1-O1(COO)d2
Ba1-O2(COO)d2

Ba_PmA_1
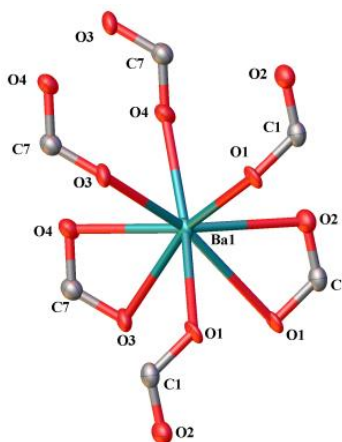
Ba1-O1(COO)c1
Ba1-O1(COO)c1
Ba1-O1(COO)c2
Ba1-O2(COO)c3
Ba1-O3(COO)d1
Ba1-O4(COO)d1
Ba1-O3(COO)d2
Ba1-O4(COO)d2

Sr_fScA_1
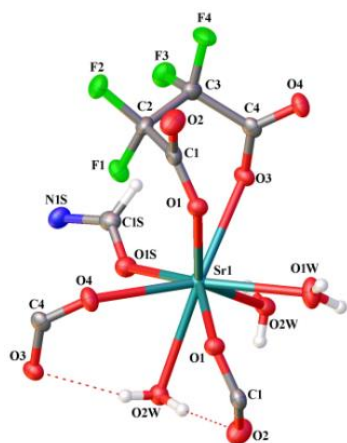
Sr1-O3(COO)a
Sr1-O4(COO)a
Sr1-O1(COO)*
Sr1-O1(COO)*
Sr1-O1S(DMF)t
Sr1-O1W(H2O)t
Sr1-O2W(H2O)br
Sr1-O2W(H2O)br

K_fScA_1
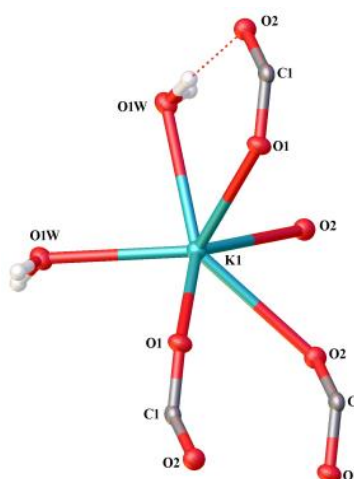
K1-O1(COO)a
K1-O1(COO)a
K1-O2(COO)a
K1-O2(COO)a
K1-O1W(H2O)br
K1-O1W(H2O)br

Table 5.3.1- Coordination geometries of the metal centres in potential pyrotechnic MOFs
(t = terminal, br = bridging, * = non-bridging M-O bond)

The majority of the crystal structures present in this series are 8-coordinate and similarly to the aromatic series most have biaugmented triangular prism coordination geometry. The other coordination geometries observed in these structures can be found in Table 5.3.2.

A compiled list of attributes of the aliphatic structures is found within Table 5.3.2. Most of the aliphatic structures form 3D frameworks with the exception of Ba_OxA_2, Na_OxA_2, Sr_MnA_2, Ba_GlA_1 and Sr_fScA_1 which each form 2D networks. A more detailed comparison of the aliphatic structures follows.

Product	*Building Units*	*Coordination Geometry*	*Linker Connectivity*	*Dimensionality*	*Carboxylate Torsion Angles/°*
Ca_OxA_1	Ca(OH$_2$)(COO)$_7$ (x2)	Biaugmented triangular prism (8)	f1, f2, f3, (g1, g2) x2, t	3D	-1.8(6), 0.9(7)
Sr_OxA_2	Sr(OH$_2$)(COO)$_7$	Biaugmented triangular prism (8)	f1, f2, f3, (g1, g2) x2, t	3D	19(3), 0.0(13)
Ba_OxA_1	Ba(COO)$_8$, Ba(OH$_2$)(COO)$_8$	Biaugmented triangular prism (8) Triaugmented triangular prism (9)	(g1, g2) x4 (g1, g2) x4, t	3D	31.0, 1.1
Ba_OxA_2	Ba(OH$_2$)$_2$(NO$_3$)$_2$(COO)$_4$	Pentagonal pyramid with square (10)	(g1, g2) x2, (br) x4	2D	0.5(5)
Na_OxA_2	Na(OH$_2$)$_2$(COO)$_4$	Octahedral (6)	a, f1, f2, f3, (br) x2	2D	13.4
Ca_MnA_2	Ca(OH$_2$)$_2$(COO)$_4$	Square antiprism (8)	(a, d1, d2, t) x2	3D	-88.8(2)
Sr_MnA_1	Sr(COO)$_7$	Triaugmented triangular prism (9)	(d1) x3 (a, d2, t) x2	3D	51.39, -63.72
Sr_MnA_2	Sr(COO)$_7$, Sr(OH$_2$)$_2$(COO)$_6$, Sr(COO)$_6$	Biaugmented triangular prism (8) Biaugmented triangular prism (8) Square pyramid with triangle (8)	(a) x4, (d1, d2) x2 (a, d1, *, t) x2 a, (d1) x3, (d2) x2	2D	32.5(9), 39.8(10), 6.9(9), 89.9(8), 93.3(11), 6.4(13)
Ca_GlA_1	Ca(OH$_2$)(COO)$_5$	Pentagonal bypyramidal (7)	(a, d1, d2) x2, t	3D	-59.4(2), -30.4(3)
Sr_GlA_1	Sr(OH$_2$)$_3$(COO)$_4$ (x2)	Biaugmented triangular prism (8)	c1, c2, c3, d1, *, (t) x2, br d1, (a, d2, t) x2, br	3D	-22.8(4), 33.6(4), 62.4(4), -78.2(3)
Ba_GlA_1	Ba(OH$_2$)$_4$(COO)$_4$	Triaugmented triangular prism (9)	(d1, d2, t x2) x2, *	2D	-82(2), 0(2)
Ca_AdA_1	Ca(OH$_2$)(COO)$_5$	Pentagonal bypyramidal (7)	(a, d1, d2) x2, t	3D	-17.7(4), -52.1(3)
Ba_AdA_1	Ba(COO)$_6$	Square antiprism (8)	(d1, d2) x4	3D	-17.6(18)
Ba_PmA_1	Ba(COO)$_6$	Biaugmented triangular prism (8)	c2, c3, (c1, d1, d2) x2	3D	21.8(13), -31.2(13)
Sr_fScA_1	Sr(OH$_2$)$_3$(DMF)(COO)$_4$	Square antiprism (8)	(a, *, t, br) x2	2D	85.7(3), 116.8(3)
K_fScA_1	K(OH$_2$)$_2$(COO)$_4$	Distorted trigonal prism (6)	(a) x4, (br) x2	3D	92.1(2)

Table 5.3.2 - Aliphatic Structures: List of MOF building units, coordination geometry, linker connectivity, dimensionality and carboxylate torsional angles.

Ca_OxA_1 (CALOXM)[30] formed a 3D MOF consisting of $Ca(OH_2)(COO)_7$ units. Sr_OxA_2 also formed a similar 3D framework composed of the same building units substituting Ca for Sr. The arrangement of the second OxA linker is what sets them apart. One carboxylate bridges two Ca cations (O1C1O2), whereas the second OxA within Sr_OxA_2 is chelated to one Sr cation by both of its carboxylates (O1C1C1O2). The second oxygen (O2) from the carboxylates is blocked from coordinating to another Sr cation due to a coordinated water molecule to which it hydrogen bonds.

a)   b)
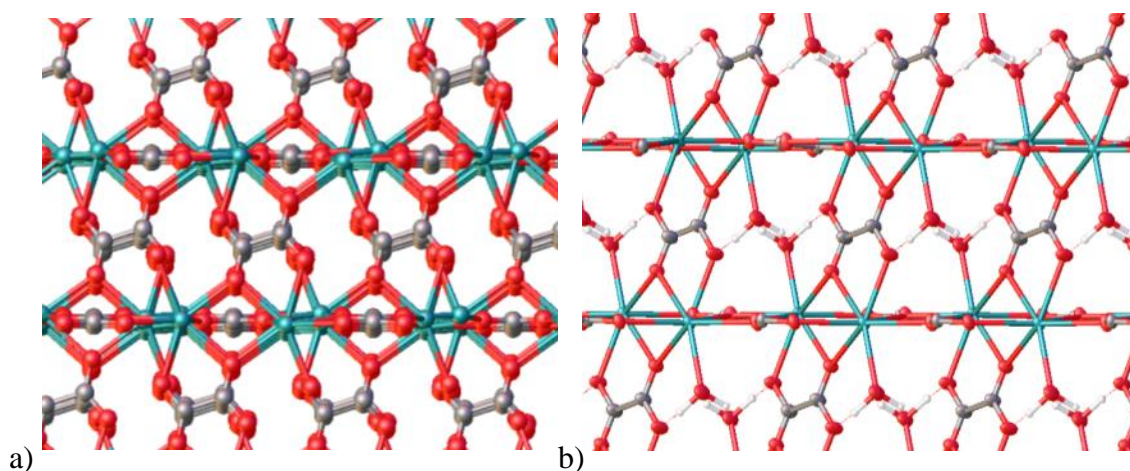
Figure 5.3.1 a) Ca_OxA_1 b) Sr_OxA_2

Ba_OxA_1 (BALMUW)[31] also has the same building units as the structures above and forms a 3D MOF. A table listing the torsion angles of the carboxylates for OxA is listed in Table 5.3.2 to highlight the difference in OxA arrangement. Ba_OxA_2 instead forms 2D sheets with building units $Ba(OH_2)_2(NO_3)_2(COO)_3$. Each 2D sheet is hydrogen bonded to one another through coordinated water molecules and nitrate anions.

a)   b)
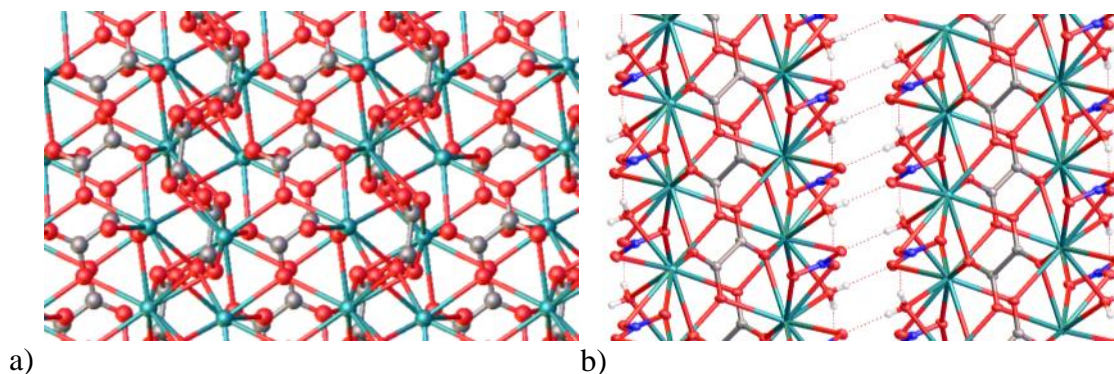
Figure 5.3.2 a) Ba_OxA_1, b) Ba_OxA_2

Ca_MnA_2 (CAMALD)[32] forms 2D sheets through $Ca(OH_2)_2(COO)_4$ units. Each sheet is hydrogen bonded to one another to create a 3D supramolecular network. Sr_MnA_1 (SRMALO)[33] does not coordinate to any water molecules and therefore the dimensionality has increased to form a 3D network. Sr_MnA_2 instead forms a structure composed of 2D sheets which are created by three different building units; $Sr(COO)_7$, $Sr(OH_2)(COO)_6$, $Sr(COO)_6$. The polymeric structure is prevented from forming a 3D network as one of the MnA molecules acts as a terminal unit. An oxygen from one carboxylate binds to a Sr cation and the other carboxylate of the diacid is instead hydrogen bonded to a water molecule.

a)

b)   c)
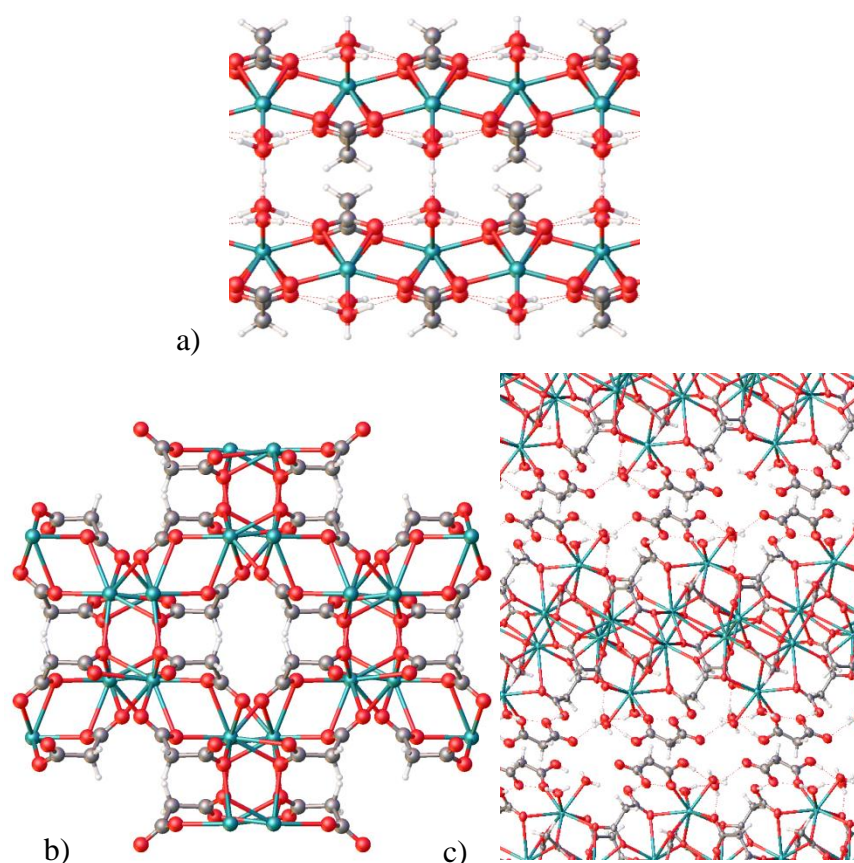
Figure 5.3.3 a) Ca_MnA_2, b) Sr_MnA_1, c) Sr_MnA_2

Ca_GlA_1 (YUDYAX)[34] is a 3D framework consisting of $Ca(OH_2)(COO)_5$ units. Sr_GlA_1 maintains a 3D framework although the building units change to $Sr(OH_2)_3(COO)_4$. This structure forms a somewhat similar arrangement to Sr_MnA_1. The Ba crystal structure contains an additional coordinated water, producing $Ba(OH_2)_4(COO)_4$. Ba_GlA_1 generates 2D sheets held together by hydrogen bonding

between water molecules, both coordinated (O1W) and uncoordinated (O101), to uncoordinated carboxylate oxygens (O4). Ca_BDC_2 has the same arrangement of water molecules (one water molecule above the metal carboxylate chain and three below).
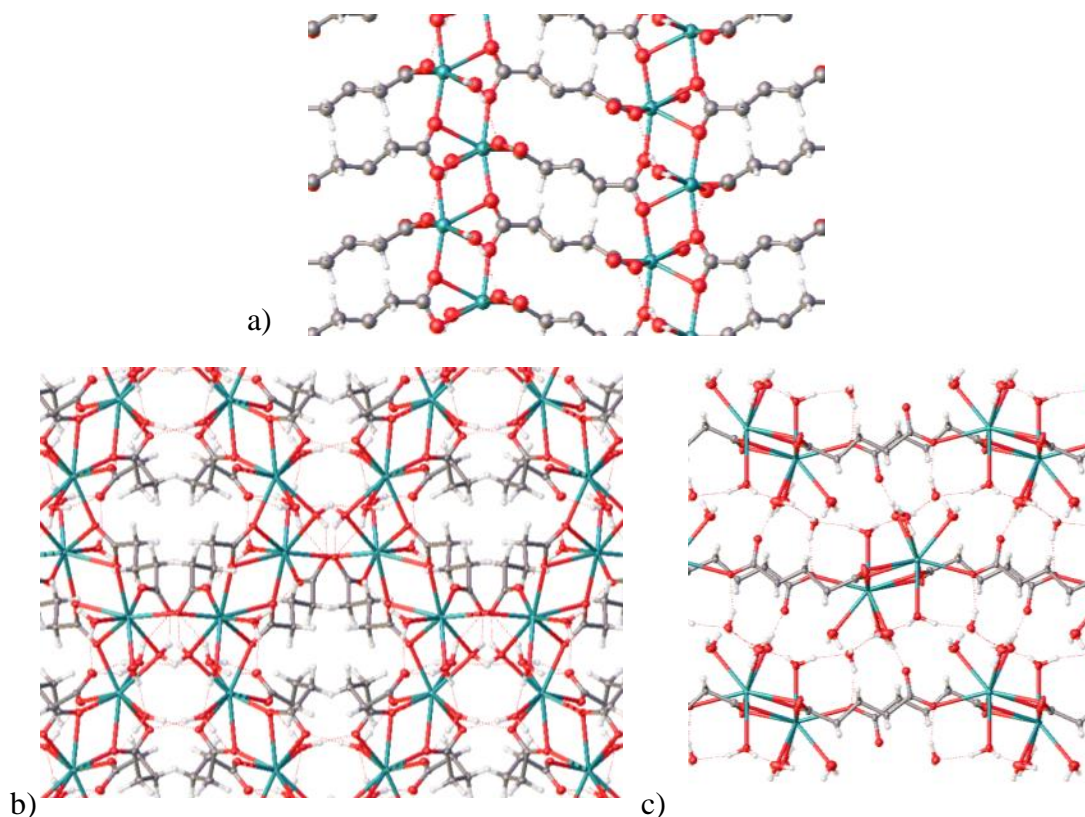
Figure 5.3.4 a) Ca_GlA_1, b) Sr_GlA_1, c) Ba_GlA_1

Ca_AdA_1 (LEGREU)[35] is a 3D framework consisting of $Ca(OH_2)(COO)_5$ units. The Ba equivalent, Ba_AdA_1 (DEKZEA)[36], has a similar arrangement, they both consist of 2D sheets which are cross-linked by AdA linkers. The Ba building units are $Ba(COO)_6$. The main difference between the structures comes about from the additional water within the Ca structure which causes a single carboxylate to bridge two Ca cations, rather than forming a bridge and binding in a bidentate fashion. Both carboxylates within the Ba structure form the latter type of binding.
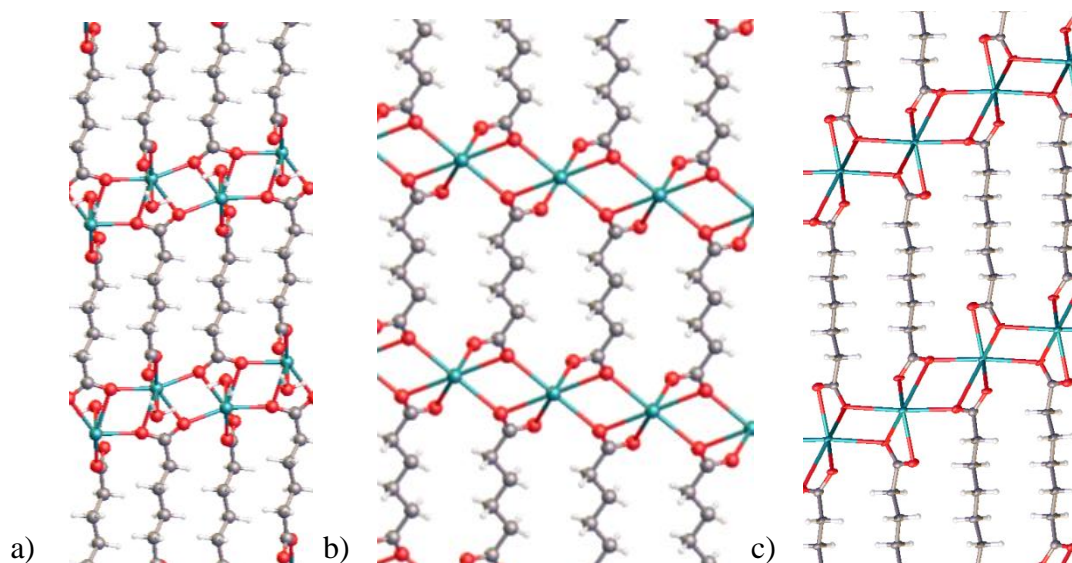
Figure 5.3.5 a) Ca_AdA_1, b) Ba_AdA_1, c) Ba_PmA_1

Ba_PmA_1, also consisting of Ba(COO)$_6$ units, has a similar packing arrangement to Ba_AdA_1. The linkers bind in the exact same manner in both cases. The carboxylate torsion angle is -17.6° for one linker, the other carboxylate (Ba_AdA_1) is equivalent as it is generated by symmetry. The PmA ligand possesses one additional carbon which causes the carboxylate torsion angle to extend further to -52.1° for Ba_PmA_1.
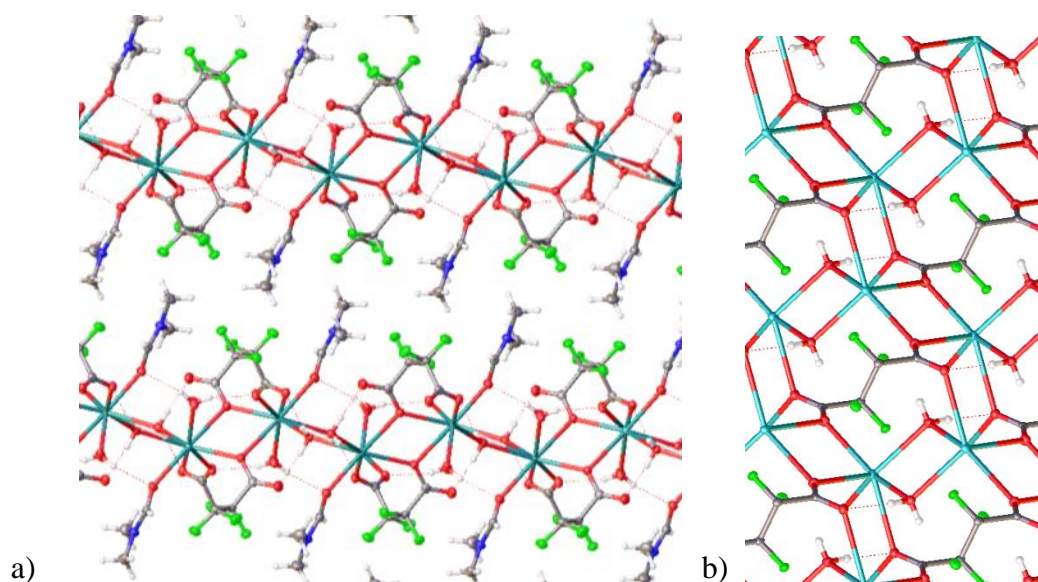
Figure 5.3.6 - a)Sr_fScA_1, b) K_fScA_1

fScA only formed a product when combined with Sr. The 2D sheet network is made up of $Sr(OH_2)_3(DMF)(COO)_4$ units. It creates a similar arrangement to the fluorinated aromatic structures containing isofBDC or altfBDC. It is most like Sr_altfBDC_1. The DMF to diacid ratio is the same and again appears to act as a 'spacer' between each of the diacids above and below the 2D sheets. One of the oxygens potentially available to bind to the Sr cation to help generate a 3D structure has instead hydrogen bonded to a water molecule. Similar findings were made when coupling this material with alkali metals such that only one resulted was with potassium, which formed a 3D framework. There were no terminal units within the structure compared to its Sr equivalent, thereby allowing it to generate a 3D structure. Each coordinated oxygen from both the carboxylates and the coordinated water molecules act to solely bridge several K^+ ions.

In comparison to the aromatic structures the aliphatic structures show a lesser degree of pyrotechnic potential and in some cases showed none. The DSC results can be found on the Appendix DVD in addition to the burn test photographs.

a)

b)
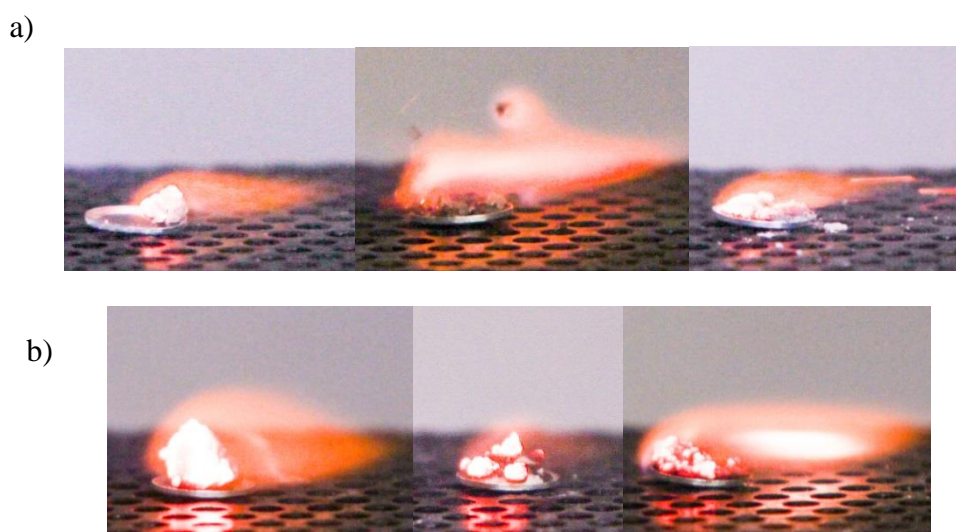
Figure 5.3.7 - Burn Tests a) Ca/Sr/Ba_OxA_1, b) Ca/Sr/Ba_GlA_1,

5.4   HYDROXYL & ALKENE CRYSTAL STRUCTURES

The coordination geometries of the metal centres from the crystal structures obtained for the hydroxyl and alkene products in this study are shown in Table 5.4.1. There are a total of 5 structures previously listed in the CSD[22] and 2 novel structures. The carboxylate moieties coordinate to metal cations typically by bridging, chelating, or via a combination of both as is highlighted by Scheme 5.4.1.

Each of these diacids are more rigid. They are comparable to the aromatic diacids which have a decreased flexibility compared to the aliphatic ligands. The pyrotechnic potential will be compared to each of the other series to highlight which series produced the most significant result.
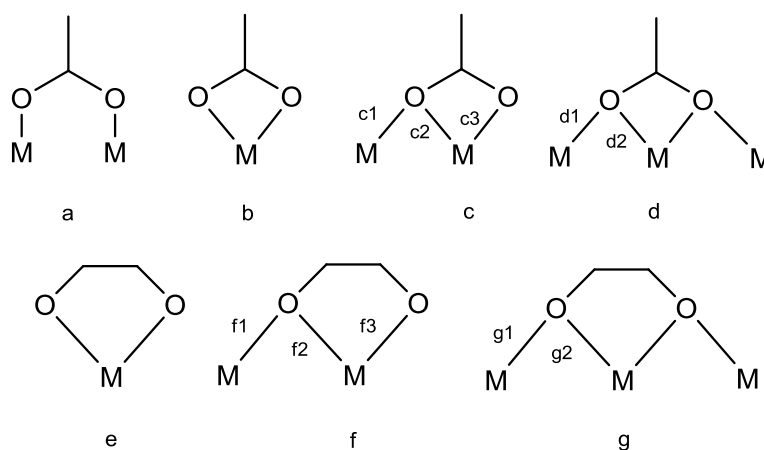
Scheme 5.4.1 - Schematic Diagram of Coordination Modes of the RCOO- Moiety a) bridging, b) chelating, c) chelating and bridging with one oxygen, d) chelating and bridging with two oxygens. e) chelating (OCCO-), f) chelating and bridging with one oxygen (OCCO-), g) chelating and bridging with two oxygens (OCCO-)

Ca_LTA_1/2 - (CATART)
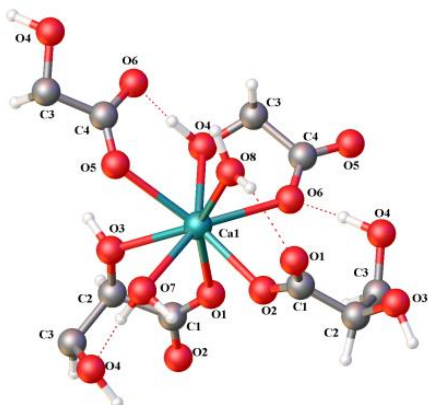
Ca1-O2(COO)a
Ca1-O5(COO)a
Ca1-O1(COO)e
Ca1-O3(COH)e
Ca1-O4(COH)e
Ca1-O6(COO)e
Ca1-O7(H2O)t
Ca1-O8(H2O)t

Sr_LTA_2a - (CUGSUT)
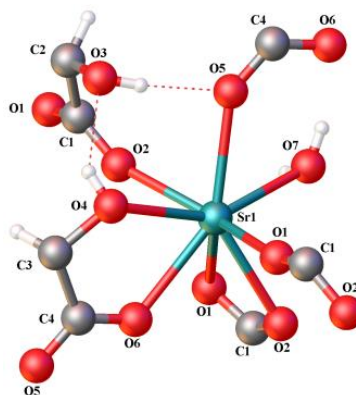
Sr1-O5(COO)a
Sr1-O6(COO)a/e
Sr1-O1(COO)d1
Sr1-O2(COO)d1
Sr1-O1(COO)d2
Sr1-O2(COO)d2
Sr1-O4(COH)e
Sr1-O7(H2O)t

Sr_LTA_2b - (QALNIA)
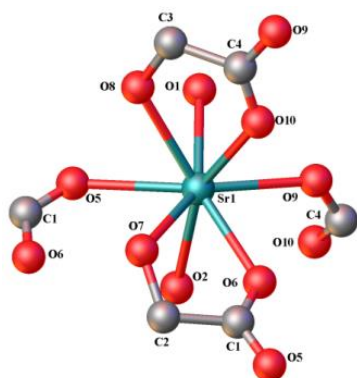
Sr1-O5(COO)a
Sr1-O9(COO)a
Sr1-O6(COO)a/e
Sr1-O10(COO)a/e
Sr1-O7(COH)e
Sr1-O8(COH)e
Sr1-O1(H2O)t
Sr1-O2(H2O)t

Ba_LTA_1/2 - (HIXZOD)
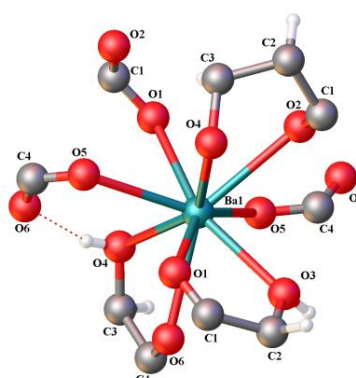
Ba1-O5(COO)a
Ba1-O5(COO)a
Ba1-O1(COO)a/f2
Ba1-O2(COO)a
Ba1-O6(COO)a/f3
Ba1-O1(COO)a/f1
Ba1-O4(COH)f1
Ba1-O4(COH)f2
Ba1-O3(COH)f3

Sr_MeA_1 - Sr1
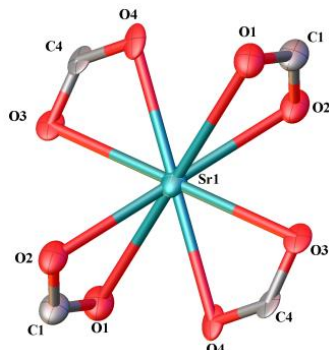
Sr1-O1(COO)d2
Sr1-O1(COO)d2
Sr1-O2(COO)d2
Sr1-O2(COO)d2
Sr1-O3(COO)d2
Sr1-O3(COO)d2
Sr1-O4(COO)d2
Sr1-O4(COO)d2

Sr_MeA_1 - Sr2
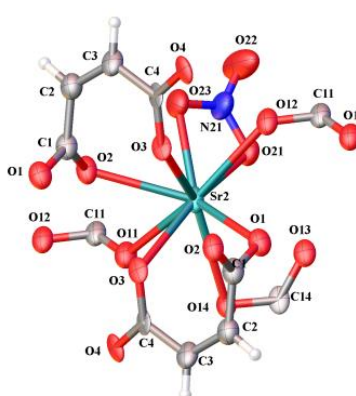
Sr2-O11(COO)a
Sr2-O12(COO)a
Sr2-O14(COO)a
Sr2-O1(COO)d1
Sr2-O2(COO)d1
Sr2-O3(COO)d1
Sr2-O3(COO)d1
Sr2-O21(NO3)
Sr2-O23(NO3)

216

Sr_MeA_1 - Sr3
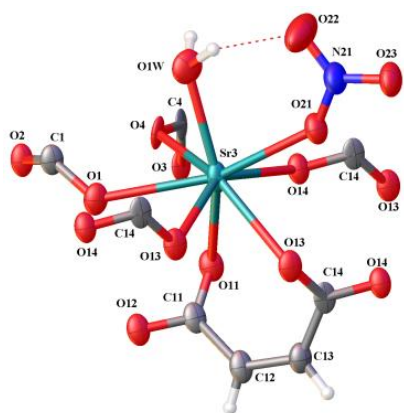
Sr3-O11(COO)a
Sr3-O13(COO)a
Sr3-O13(COO)a
Sr3-O14(COO)a
Sr3-O1(COO)d1
Sr3-O4(COO)d1
Sr3-O21(NO3)
Sr3-O1W(H2O)t

Ca_FmA_1
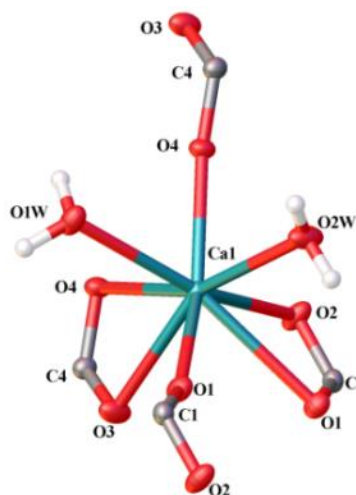
Ca1-O1(COO)c1
Ca1-O4(COO)c1
Ca1-O1(COO)c2
Ca1-O4(COO)c2
Ca1-O2(COO)c3
Ca1-O3(COO)c3
Ca1-O1W(H2O)t
Ca1-O2W(H2O)t

Sr_FmA_1/2 - (DUCLUJ)
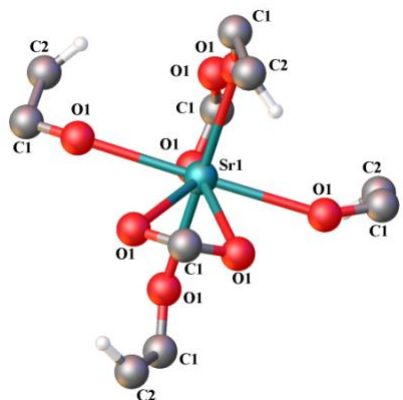
Sr1-O1(COO)d1
Sr1-O1(COO)d1
Sr1-O1(COO)d1
Sr1-O1(COO)d1
Sr1-O1(COO)d2
Sr1-O1(COO)d2
Sr1-O1(COO)d2
Sr1-O1(COO)d2

Table 5.4.1- Coordination geometries of the metal centres in potential pyrotechnic MOFs

(t = terminal, br = bridging, * = non-bridging M-O bond)

Most of the crystal structures within the hydroxyl and alkene series were found to be 8-coordinate and the remaining were 9-coordinate.

The structures containing FmA ligands are the only structures within this series which do not bridge two metal cations and instead favour modes c1, c2, c3, d1, and d2. All of the structures form 3D frameworks with the exception of Sr_MeA_1 which forms a 2D network where DMF resides in the channels between the 2D sheets. This arrangement is favoured because of the presence of the coordinated nitrate anions which block potential ligand binding sites.

Product	*Building Units*	*Coordination Geometry*	*Linker Connectivity*	*Dimensionality*	*Carboxylate Torsion Angles/°*
Ca_LTA_1/2	$Ca(OH_2)_2(COO)_4$	Biaugmented triangular prism (8)	(a, e x2, t) x2	3D	-7.2(6), 56.0(5), -28.3(6), 34.5(6)
Sr_LTA_2a	$Sr(OH_2)(COO)_5$	Biaugmented triangular prism (8)	(a, d1, d2) x2, e, t	3D	55.7(8), -8.8(8), -8.4(9), 53.0(8)
Sr_LTA_2b	$Sr(OH_2)_2(COO)_4$	Biaugmented triangular prism (8)	(a) x4, (e, t) x2	3D	-30.0(4), 27.6(4), -3.2(5), 54.8(4)
Ba_LTA_1/2	$Ba(COO)_6$	Triaugmented triangular prism (9)	(a) x6, f1, f2, f3	3D	0.6(5), 56.0(4), 4.0(5), 58.7(4)
Sr_MeA_1	$Sr(COO)_4$, $Sr(NO_3)(COO)_7$, $Sr(OH_2)(NO_3)(COO)_6$	Rhombohedral (8) Triaugmented triangular prism (9) Biaugmented triangular prism (8)	(d2) x8 (a) x3, (d1) x4 (a) x4, (d1) x2	2D	-97(2), 16(2), 46(2), 45(2)
Ca_FmA_1	$Ca(OH_2)_2(COO)_4$	Biaugmented triangular prism (8)	(c1, c2, c3) x2	3D	7.2(3), -2.2(3)
Sr_FmA_1/2	$Sr(COO)_6$	Distorted dodecahedron (8)	(d1, d2) x4	3D	75.1(3)

Table 5.4.2 - Hydroxyl and Alkene Structures: List of MOF building units, coordination geometry, linker connectivity,

dimensionality and carboxylate torsional angles.

Ca_LTA_1/2 (CATART)[37] formed a 3D MOF consisting of $Ca(OH_2)_2(COO)_4$ units. Ba_LTA_1/2(HIXZOD)[38] also formed a 3D framework composed of $Ba(COO)_6$ building units.
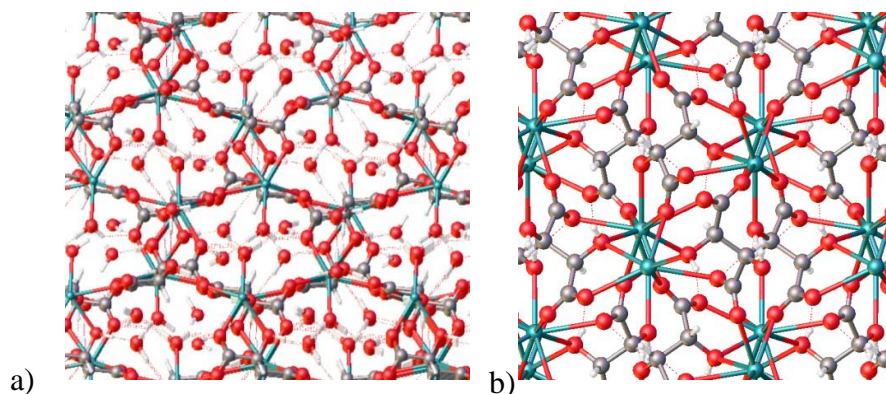
Figure 5.4.1 a) Ca_LTA_1/2, b) Ba_LTA_1/2

It appears that the products resulting from combining Group 2 metals with LTA are independent of the synthetic procedure followed to create them, Sr being the exception. The DMF approach produced microcrystalline material not suitable for SXRD analysis. The MeOH method resulted in two separate products within the same reaction. Sr_LTA_2a (CUGSUT)[39] utilises $Sr(OH_2)(COO)_5$ units whereas Sr_LTA_2b (QALNIA)[40] is constructed using $Sr(OH_2)_2(COO)_4$ units.   Sr_LTA_2b has a near isostructural similarity to Ca_LTA_1/2 (root mean square deviation 0.318). Both have two water solvent molecules contained in its pores which hydrogen bond to both coordinated water molecules.
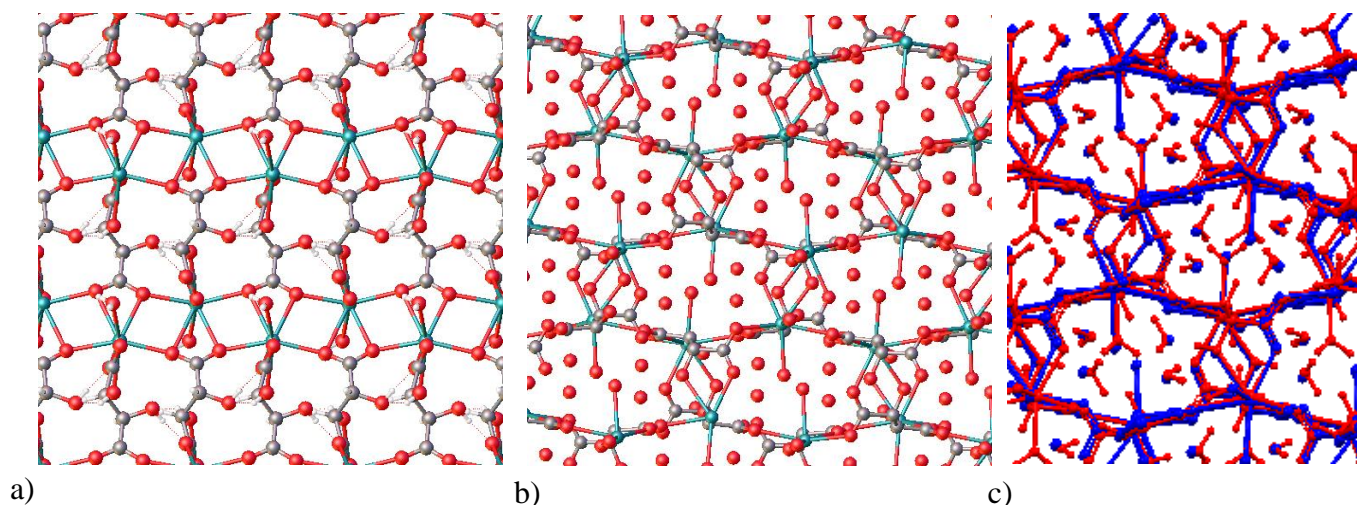
Figure 5.4.2 a) Sr_LTA_2a b) Sr_LTA_2b c) Mercury overlay of Ca_LTA_1/2 and Sr_LTA_2b

Sr_MeA_1 is made up of multiple building units which include $Sr(COO)_4$, $Sr(NO_3)(COO)_7$, and $Sr(OH_2)(NO_3)(COO)_6$. Disordered DMF was found residing in the channels between the 2D sheets. The DMF solvent molecules hydrogen bond to both the coordinated nitrate anions and the coordinated water molecules.
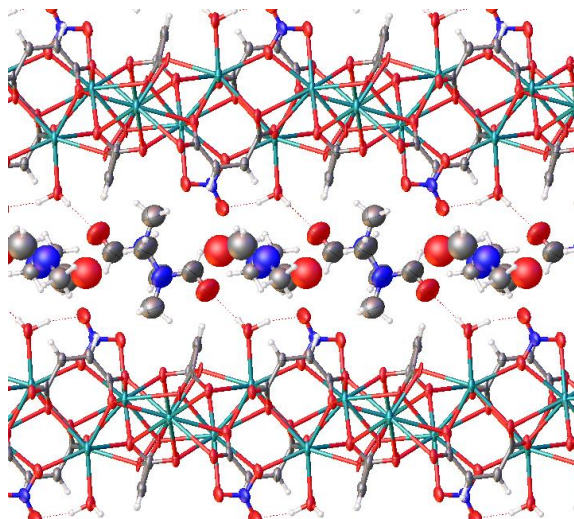
Figure 5.4.3 - Sr_MeA_1

Ca_FmA_1 utilises $Ca(OH_2)_2(COO)_4$ building units. DMF acted as a template. It can be found residing within the pores which resulted from the combination of the Ca metal nodes and FmA linkers. Sr_FmA_1/2 (DUCLUJ)[41], is comprised of $Sr(COO)_6$ building units. As Sr_FmA_1/2 is highly disordered, it is difficult to compare structures with relation to carboxylate torsion angles. The disorder within the structure prevents the true assessment of void space within the structure. It is likely that the system alternates between different pore types.

a)   b)
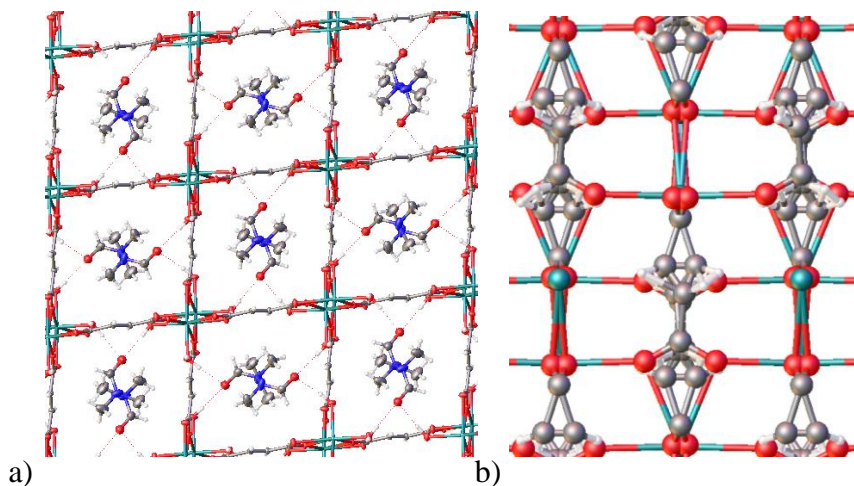
Figure 5.4.4 a) Ca_FmA_1, b) Sr_FmA_1/2

To summarize, these linkers are structurally more rigid therefore allowing on numerous occasions for the same product to precipitate out of the reaction irrespective of the synthetic method chosen. The alkene linkers allow the presence of solvent within their associated frameworks whether it is within their channels (2D) or pores (3D).

Out of this set of structures the alkene diacid MOFs showed the most promise as pyrotechnic materials. Their burn tests are highlighted in Figure 5.4.5
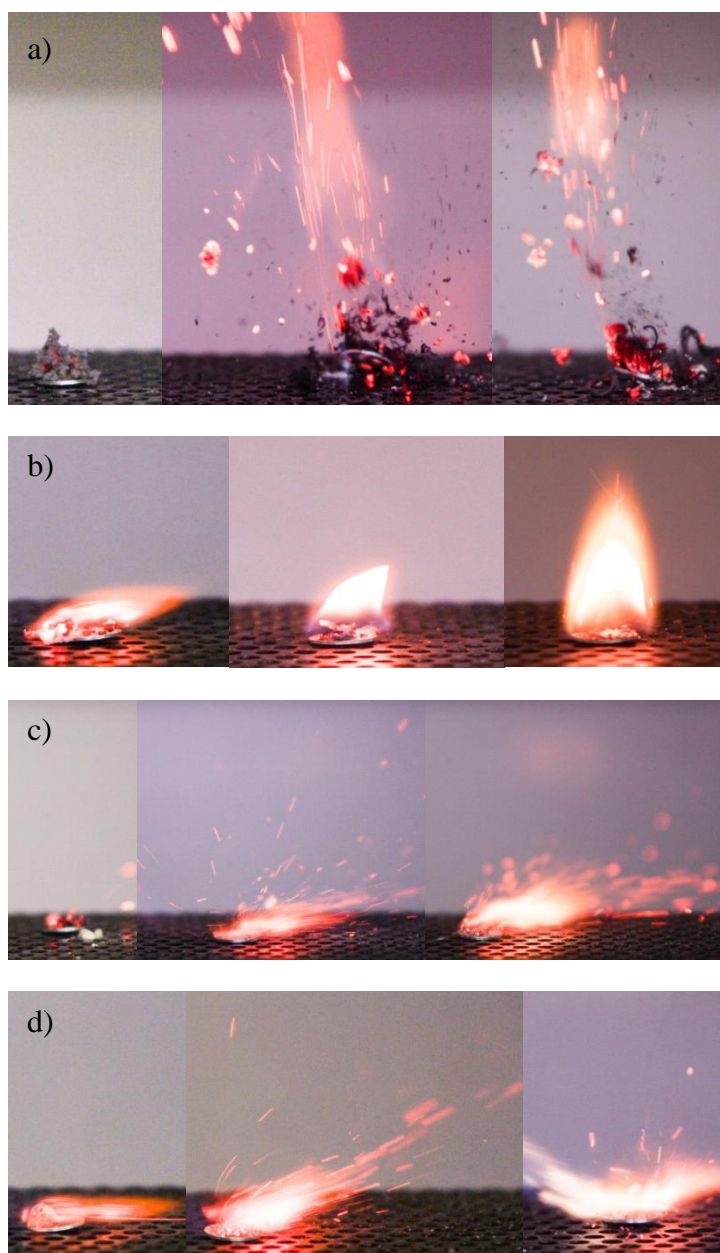
Figure 5.4.5 - Burn Tests a) Ca/Sr/Ba_MeA_1, b) Ca/Sr/Ba_MeA_2,
c) Ca/Sr/Ba_FmA_1, d) Ca/Sr/Ba FmA_2

5.5   CONCLUSION

A total of 40 crystal structures were discussed (of which 21 are novel) and assessed for their pyrotechnic properties. The majority of the crystal structures discovered from this work were found when diacid ligands were coupled with $Sr(NO_3)_2$.

Ca^{2+} cations are 7- or 8-coordinate. Sr^{2+} cations are 8-coordinate or 9- coordinate whist Ba^{2+} cations are 8-, 9-, or 10-coordinate. As would be expected, the length of the metal-oxygen (M-O) bond increases as the radius of the metal cation increases, with an average M-O bond length 2.445, 2.624, 2.814Å for Ca^{2+}, Sr^{2+}, and Ba^{2+} compounds, respectively. As the coordination number increases for each of the metal cations so too does the average bond length: Ca-O (7=2.40Å, 8=2.44Å), Sr-O (8=2.60Å, 9=2.65Å), Ba-O (8=2.82Å , 9=2.84Å , 10=2.86Å). A bond length table for these structures has been provided and can be found in Appendix A7. The metal cations are bridged by carboxylate ligands and in some cases solvent molecules to form polymeric metal-carboxylate chain (1D), sheet (2D), or framework (3D) motifs.

Group 1 metals all coordinate with a distorted trigonal prism geometry and form 3D topologies with the exception of Na_OxA_2 which forms 2D sheets and has octahedral coordination geometry. Two of the Ca products had pentagonal bypyramidal geometry. The majority of the structures are 8-coordinate. More than half of the group 2 metal structures coordinate with biaugmented trigonal prism geometry. There were four cases where a square antiprism was observed and four other cases where other unique 8 coordinate environments were discovered: pentagonal-triangle prismatoid, square pyramid with triangle, and rhombohedral. There were six instances where both Sr and Ba were both 9-coordinate resulting in a triaugmented triangular prism environment and only one case where a pentagonal biwedge was observed. Only one 10-coordinate system existed which had pentagonal pyramid with square geometry.

Modes c (c1, c2, and c3) are most prevalent for the aromatic crystal structures although their presence seems to affect fluorinated and non-fluorinated structures differently. When found in fluorinated structures the dimensionality is 1D with the exception of Sr_altfBDC_2 which instead is 2D. However, this crystal structure possessed two unique Sr environments. The non-fluorinated structures which include BDC ligands

with mode c connectivity result in 3D frameworks. The other BDC crystal structures are 1D; these have a higher coordinated water content which occupies sites on the metal centres, preventing the formation of covalent constructs with higher dimensionality. The additional water content does allow for a supramolecular 3D framework to form. Typically when the metal cations are coordinated to more than two water molecules the dimensionality is reduced to either 2D or 1D. There was only one product which was coordinated to three water molecules that was still able to maintain a 3D framework Sr_GlA_1. This comprised of two unique Sr environments which had the same coordination environment and geometry, however possessed different coordination modes. Similarly to the aromatic structures c1, c2, and c3 carboxylate arrangements were observed within the aliphatic systems which were studied. When the c modes were present a 3D framework was found.

The incorporation of DMF molecules and nitrate anions within the structures can cause reduced dimensionality, as they block metal centre sites. Whilst 3D constructs were desirable they were not necessary, and 2D and 1D constructs would equally be acceptable. Also the inclusion of DMF and nitrate anions could be seen to enhance the pyrotechnic reaction, however, this could not be proven with absolute certainty as there was only a subset which contained either of these species. Nitrate anions were mainly found within structures created by method 2. The presence of these molecules also influence the carboxylate torsional angles within the crystal structures as can be seen specifically within the fluorinated aromatic and non-fluorinated aromatic structures. An fBDC ligand in its uncoordinated state has carboxylate torsion angles of -18.8° and 20.5° but when they are coordinated in a MOF the carboxylates twist to a greater extent. When coupled with either Ca or Sr the presence of the coordinated nitrate anions in addition to pyridine solvent they twist to 61.8(4)° and -58.5(4)° for Ca and 62.2(6)° and -59.4(6)° for Sr. The Ba crystal structure has torsional angles of 42.8(4)° and 34.4(4)°. The latter torsion angle was also found within the K structure. The fBDC ligand within the Ba structure bridges two metal centres and is hydrogen bonded to a coordinated water molecule. The other is bound in a bidentate fashion to one metal centre and bridged to two others. Weak M-F contacts can be seen for both structures. The structures which incorporate the other fluorinated acids, isofBDC and altfBDC, also

show significant deviations in the carboxylate torsional angles from their uncoordinated states; 37.85° and 39.25° isofBDC and -14.18° and 94.28°.

A variety of 3D, 2D and 1D topologies have been observed. The majority of the combinations which were identified by SXRD or PXRD were found to be 3D frameworks making up twenty-five out of the forty crystal structures uncovered from this work. Achieving 3D structures was not vital for this work nor was it essential for the structures to be porous. The products which were less structurally stable i.e. 2D or 1D were found to perform better. There were two cases of isostructurality discovered in this work both involving the same fluorinated diacid linker, fBDC (Ca_fBDC_2 with Sr_fBDC_2, Rb_fBDC_2 with Cs_fBDC_2). Although these structures were identical their thermal properties were dissimilar as was shown by their DSC traces and their associated burn behaviour. Ca_LTA_1/2 and Sr_LTA_2b were near isostructural but had negligible pyrotechnic properties.

The MOFs which showed the greatest pyrotechnic potential were the fluorinated aromatic structures. Their energetic properties were enhanced when their dimensionality was reduced to either 2D or 1D. The aromatic ligands and the alkene ligand containing MOFs were second best whilst the aliphatic ligands showed the least promise.

Although a structure solution was not found for each combination of fuel and oxidiser there were similarities found within their DSC traces. Numerous comparisons were made to highlight the effect of using different alkaline earth metals where it was found that a large number of the combinations resulted in similar decomposition patterns when comparing down the group. The thermal behaviour of the material was effectively independent of the diacid when comparing the products resulting from method 2 using isofBDC and altfBDC.

The first synthesis method yielded the most products with the majority of the combinations of fuel and oxidiser ingredients resulting in new products although not all could be confirmed by SXRD. It was observed that as the carbon count of the aliphatic diacid increased, the materials became more hydrophobic.

One of the disadvantages of the second synthesis method was the possibility of pyridine salt formation. This occurred on several occasions, mainly with the alkali metal materials. Both isofBDC and altfBDC had a greater propensity for forming pyridine salts rather than polymeric structures when paired with these metals.

Overall, the MOFs which showed the greatest pyrotechnic potential were the fluorinated aromatic structures. Their energetic properties were enhanced when their dimensionality was reduced to either 2D or 1D. The aromatic ligands and the alkene ligand containing MOFs were second best whilst the aliphatic ligands displayed the least pyrotechnic potential.

The incorporation of DMF molecules and nitrate anions within the structures led to reduced dimensionality as they blocked metal centre sites. Although not confirmed, their presence was also thought to increase the pyrotechnic potential of the compounds. Fluorinated structures and those which possess nitrate anions lead to an improved oxygen balance. In the case of the fluorinated structures the fluorine combines with the metal to form the metal fluoride instead of the metal oxide allowing more oxygen to be available for the rest of the system. An increased oxygen balance was also observed in other cases due to the contribution of oxygen from nitrate anions. The full set of results can be found in Appendix A8.

Potential improvements for this study and suggestions for the future directions of this work can be found in the next chapter.

References

1. Yaghi, O. M.; O'Keeffe, M.; Ockwig, N. W.; Chae, H. K.; Eddaoudi, M.; Kim, J., *Nature* **2003,** *423* (6941), 705-714.

2. Bradshaw, D.; Claridge, J. B.; Cussen, E. J.; Prior, T. J.; Rosseinsky, M. J., *Acc. Chem. Res.* **2005,** *38* (4), 273-282.

3. Furukawa, H.; Kim, J.; Ockwig, N. W.; O'Keeffe, M.; Yaghi, O. M., *J. Am. Chem. Soc.* **2008,** *130* (35), 11650-11661.

4. Mueller, U.; Schubert, M.; Teich, F.; Puetter, H.; Schierle-Arndt, K.; Pastre, J., *J. Mater. Chem.* **2006,** *16* (7), 626-636.

5. Hawxwell, S. M.; Espallargas, G. M.; Bradshaw, D.; Rosseinsky, M. J.; Prior, T. J.; Florence, A. J.; van de Streek, J.; Brammer, L., *Chem. Commun.* **2007,** (15), 1532-1534.

6. Czaja, A. U.; Trukhan, N.; Muller, U., *Chem. Soc. Rev.* **2009,** *38* (5), 1284-1293.

7. Banerjee, D.; Hu, Z.; Pramanik, S.; Zhang, X.; Wang, H.; Li, J., *CrystEngComm* **2013,** *15* (45), 9745-9750.

8. Gong, Y.-N.; Jiang, L.; Lu, T.-B., *Chem. Commun.* **2013,** *49* (94), 11113-11115.

9. Lee, J. H.; Kang, S.; Lee, J. Y.; Jaworski, J.; Jung, J. H., *Chem. Eur. J.* **2013,** *19* (49), 16665-16671.

10. Li, L.; Zhang, S.; Xu, L.; Han, L.; Chen, Z.-N.; Luo, J., *Inorg. Chem.* **2013,** *52* (21), 12323-12325.

11. Nagarkar, S. S.; Joarder, B.; Chaudhari, A. K.; Mukherjee, S.; Ghosh, S. K., *Angew. Chem. Int. Ed.* **2013,** *52* (10), 2881-2885.

12. Pramanik, S.; Hu, Z.; Zhang, X.; Zheng, C.; Kelly, S.; Li, J., *Chem. Eur. J.* **2013,** *19* (47), 15964-15971.

13. Gole, B.; Bar, A. K.; Mukherjee, P. S., *Chem. Eur. J.* **2014,** *20* (8), 2276-2291.

14. Tian, D.; Li, Y.; Chen, R.-Y.; Chang, Z.; Wang, G.-Y.; Bu, X.-H., *J. Mater. Chem. A.* **2014,** *2* (5), 1465-1470.

15. Wang, G.-Y.; Song, C.; Kong, D.-M.; Ruan, W.-J.; Chang, Z.; Li, Y., *J. Mater. Chem. A.* **2014,** *2* (7), 2213-2220.

16. Zhang, S.-R.; Du, D.-Y.; Qin, J.-S.; Bao, S.-J.; Li, S.-L.; He, W.-W.; Lan, Y.-Q.; Shen, P.; Su, Z.-M., *Chem. Eur. J.* **2014,** *20* (13), 3589-3594.

17. Bushuyev, O. S.; Brown, P.; Maiti, A.; Gee, R. H.; Peterson, G. R.; Weeks, B. L.; Hope-Weeks, L. J., *J. Am. Chem. Soc.* **2011,** *134* (3), 1422-1425.

18. Bushuyev, O. S.; Peterson, G. R.; Brown, P.; Maiti, A.; Gee, R. H.; Weeks, B. L.; Hope-Weeks, L. J., *Chem. Eur. J.* **2013,** *19* (5), 1706-1711.

19.   Li, S.; Wang, Y.; Qi, C.; Zhao, X.; Zhang, J.; Zhang, S.; Pang, S., *Angew. Chem. Int. Ed.* **2013,** *52* (52), 14031-14035.

20.   Davies, N., *Pyrotechnics Handbook*. Cranfield University; Defence College of Management and Technology; Department of Applied Science, Security and Resilience: 2009.

21.   Saha, D.; Deng, S.; Yang, Z., *J. Porous Mater.* **2009,** *16* (2), 141-149.

22.   Allen, F. H., *Acta Crystallogr.* **2002,** *B58*, 380-388.

23.   Werker, M.; Dolfus, B.; Ruschewitz, U., *Z. Anorg. Allg. Chem.* **2013,** *639* (14), 2487-2492.

24.   Zhang, Q.; Shreeve, J. n. M., *Angew. Chem. Int. Ed.* **2014**, 2540-2542.

25.   Matsuzaki, T.; Iitaka, Y., *Acta Crystallogr. Sect. B* **1972,** *28* (7), 1977-1981.

26.   Groeneman, R. H.; Atwood, J. L., *Cryst. Eng.* **1999,** *2* (4), 241-249.

27.   Yang, L.; Zhao, D.; Li, G., *Acta Crystallogr. Sect. E* **2011,** *67* (2), m282.

28.   Williams, C. A.; Blake, A. J.; Wilson, C.; Hubberstey, P.; Schröder, M., *Cryst. Growth Des.* **2008,** *8* (3), 911-922.

29.   Jensen, W. B., *J. Chem. Educ.* **2009,** *86* (11), 1266.

30.   Tadokoro, M.; Ozawa, Y.; Mitsumi, M.; Toriumi, K.; Ogura, T., *Chem. Lett.* **2005,** *34* (2), 236-237.

31.   Mutin, J. C.; Dusausoy, Y.; Protas, J., *J. Solid State Chem.* **1981,** *36* (3), 356-364.

32.   Albertsson, J.; Oskarsson, A.; Svensson, C., *Acta Crystallogr. Sect. B* **1978,** *34* (9), 2737-2743.

33.   Briggman, B.; Oskarsson, A., *Acta Crystallogr. Sect. B* **1977,** *33* (6), 1900-1906.

34.   Mathew, M.; Takagi, S., *Z.Kristallogr.* **1995,** *210*, 199.

35.   Mathew, M.; Takagi, S.; Ammon, H. L., *J. Crystallogr. Spectrosc. Res.* **1993,** *23*, 617.

36.   Grzesiak, M.; Nitek, W.; Rafalska-Łasocha, A.; Łasocha, W., *Z. Krist. New Cryst. St.* **2012,** *227* (9), 629-634.

37.   Ambady, G., *Acta Crystallogr. Sect. B* **1968,** *24* (11), 1548-1557.

38.   Gonzalez-Silgo, C.; Gonzalez-Platas, J.; Ruiz-Perez, C.; Lopez, T.; Torres, M., *Acta Crystallogr. Sect. C* **1999,** *55* (5), 740-742.

39.   Appelhans, L. N.; Kosa, M.; Radha, A. V.; Simoncic, P.; Navrotsky, A.; Parrinello, M.; Cheetham, A. K., *J. Am. Chem. Soc.* **2009,** *131* (42), 15375-15386.

40.   Starynowicz, P.; Meyer, G., *Z. Anorg. Allg. Chem.* **2000,** *626* (12), 2441-2442.

41.   Stahl, K.; Andersen, J. E. T.; Shim, I.; Christgau, S., *Acta Crystallogr. Sect. B* **2009,** *65* (4), 481-487.

CHAPTER 6

Conclusion and Further Work

6.1   CONCLUSION

It is important that pyrotechnic products work the way they were intended to, primarily for safety. As such, quality control is an issue. It is also important to optimise the pyrotechnic effect. The objectives of this research were to look at ways to bring industrial pyrotechnic production into the modern era. The initial stages of this research were exploratory, as there was a wide range of directions that could be taken.

The 'dry powder small mixes' pyrotechnic production line was assessed as it operates at present. It comprised the following steps:

1. Gathering raw materials and Quality Control (QC)
2. Preparation of appropriate materials E.g. milling, kibbling of oxidisers
3. Drying of appropriate materials E.g. oxidisers
4. Sieve mixing of powder ingredients
5. Drying of composition (QC test)
6. Pressing (hand or automation)
    (Additional step: Further processing, drilling, milling, to achieve a particular shape)
7. Packaging of pyrotechnic product

The current techniques still mimic those which would have been used by Guy Fawkes – placing a large amount of gunpowder into a confined space, lighting the fuse, and observing the 'known result'. In order to gain confidence in the production of a material the process must be well understood. If one of the steps of the production were to change, e.g. change in supplier of a raw material, one would have to be able to assess the effect on the whole process. The main problem areas noted in the

pyrotechnic industry are caused by inconsistencies in production. The two main questions which this study aimed to address were:

- What makes a good quality mixture?
- How could batch to batch variation be minimised?

A diverse range of characterisation techniques were utilised to provide as much information as possible about the pyrotechnic materials. This was done in order to probe techniques and find out which ones would be most useful in terms of the information they can provide. The techniques are listed in the following table along with a description of the information each provided.

Characterisation Technique	Information
PXRD	Material phase identification, unit cell dimensions, Purity, Morphology
SXRD	Molecular structure, Crystal structure
DSC	Melting behaviour, Purity, Polymorphism
Hot-stage Microscopy	Melting behaviour, Purity, Polymorphism
CT	Material phase identification, Particle size distribution, Particle distribution (specifically when combined with a tessellation tool)

Table 6.1.1 - Information from Characterisation Techniques

6.1.1   MACROSCOPIC CHARACTERISATION

The final burning assessment of each composition was affected by ageing as initially the compositions had behaved more like mini-flare signals (more flame) whereas on the day of assessment they behaved more like smoke compositions although several were still able to produce a flame. In spite of this we were still able to compare several features of the compositions based on the oxidiser used, its concentration and the composition mixing quality. The particle size effect was more difficult to ascertain as the distinct particle shapes became less clear as the particle size was reduced to 75 µm and 38 µm. It was impossible with the time required to obtain a scan with higher resolution to allow the full assessment of these mixtures.

Through visual inspections of the 3D datasets, associated with each mix, it was relatively easy to see when the quality of mixing was efficient *i.e.* each component was in intimate contact with the other. It was understood that one image analysis methodology would never suffice and as such information obtained from numerous tools was aquired in order to assess the arrangements of the particles within a given volume. These tools included grayscale averaging, particle counting, and tessellation coupled with statistical tools. Grayscale averaging provided a rough indication of the concentration of the oxidiser and fuel content within a particular area/volume. Particle counting tools were used to show the effect of changing particle size. The output from these tools included not only the number of particles but also their locations, areas/volumes and sphericity values. The summation of the particle volumes in relation to the total volume being assessed could be used to determine oxidiser concentration and consequently the volumes density. Assessment of mixing quality was carried out by utilising a tessellation tool coupled with CoV. This allowed the comparison of several mixtures based on the distribution of one component, namely the oxidiser. The main burn test result which verified the findings from the CT results were associated with $RbNO_3$ compositions. It was shown that BA-BC (1st, 2nd, and 3rd ratios manufactured using 7 mixing cycles) produced consistent results within the two samples which were burn tested whereas when BD ('poor' mix, 1 mixing cycle) was initiated there was a distinct difference between the two. One burned very well whilst the other briefly let off a small quantity of smoke. The burn tests identified that the fastest burn rates were associated with the second ratio for each

composition tying in well with the results from the pyro valency calculations which showed this mixture was closest to oxygen balance for each composition.

The use of CT analysis has proved useful in combination with various imaging analysis tools for the investigation of pyrotechnic compositions. As of yet no other tool has provided a means to visualise particle distributions and concentrations of each component within a pyrotechnic product.

6.1.2   MOLECULAR CONTROL

6.1.2.1   BINARY SYSTEMS

Though several crystal structures were found, only a subset of the thirty nine binary systems produced an exothermic event. These were mainly attributed to altfBDC when coupled with the majority of the azole series as well as NPy and DNPy. The decomposition mechanism of these binary systems needs to be further investigated. Thermal analysis of the binary systems indicated that they possessed minimal pyrotechnic potential, however, there were other interesting observations regarding the crystal structure analysis. Common packing motifs which formed were catomeric diacid chains and alternate diacid base chains. 2D or 3D supramolecular networks were found when base units acted as a link between these chains. Numerous similarities were observed across the crystal structures especially within the azole series specifically with Im, 2MI, and Tro.

Although not all of the fluorinated diacids produced the same exothermic response as altfBDC it is asserted that these materials could still be useful as pyrotechnic ingredients within other arrangements.

6.1.2.2   MOFs

A total of 40 crystal structures were assessed of which 21 are novel. Out of the several diacids used the fluorinated ligands were found to impart the greatest pyrotechnic potential followed by the alkenes. The incorporation of DMF molecules and nitrate anions within the structures caused reduced dimensionality as they blocked metal centre sites. Their inclusion could be seen to assist in the pyrotechnic reaction. However, this could not be proven with absolute certainty as there was only a subset which contained either of these species. Nitrate anions were mainly found within structures created by method 2. The inclusion of water solvent molecules was seen to be detrimental compared to the inclusion of DMF solvent molecules as water is known to be a desensitiser of most pyrotechnics, with the exception of those containing magnesium. DMF inclusion could be seen to be advantageous as it is a flammable solvent so it could act as an additional fuel. Whilst 3D constructs were desirable they were not necessary 2D and 1D constructs would equally be acceptable. In fact the energetic properties of these MOFs were enhanced when their dimensionality was reduced to either 2D or 1D.

There were two cases of isostructurality discovered in this work both involving the same fluorinated diacid linker, fBDC (Ca_fBDC_2 with Sr_fBDC_2, Rb_fBDC_2 with Cs_fBDC_2). Although these structures were identical their thermal properties were dissimilar as was shown by their DSC traces and their associated burn behaviour. Ca_LTA_1/2 and Sr_LTA_2b were near isostructural but had negligible pyrotechnic properties. The structurally rigid diacids, LTA and FmA, commonly formed the same product irrespective of the synthetic procedure used. Although when Sr was coupled with LTA it resulted in two products within the same reaction when using synthesis method 2. A similar finding was made when using synthesis method 1 with BDC, two products were found within the same pot. The purity of the end product was found to be affected by the synthetic method. The DMF approach appeared to result in a higher level of purity compared to the MeOH method where residual starting material was still remaining.

6.1.3   COMBINING STRATEGIES

The design philosophy for this study is highlighted below and shows the suggested way forward for the manufacture of pyrotechnic materials and other energetic material formulations.
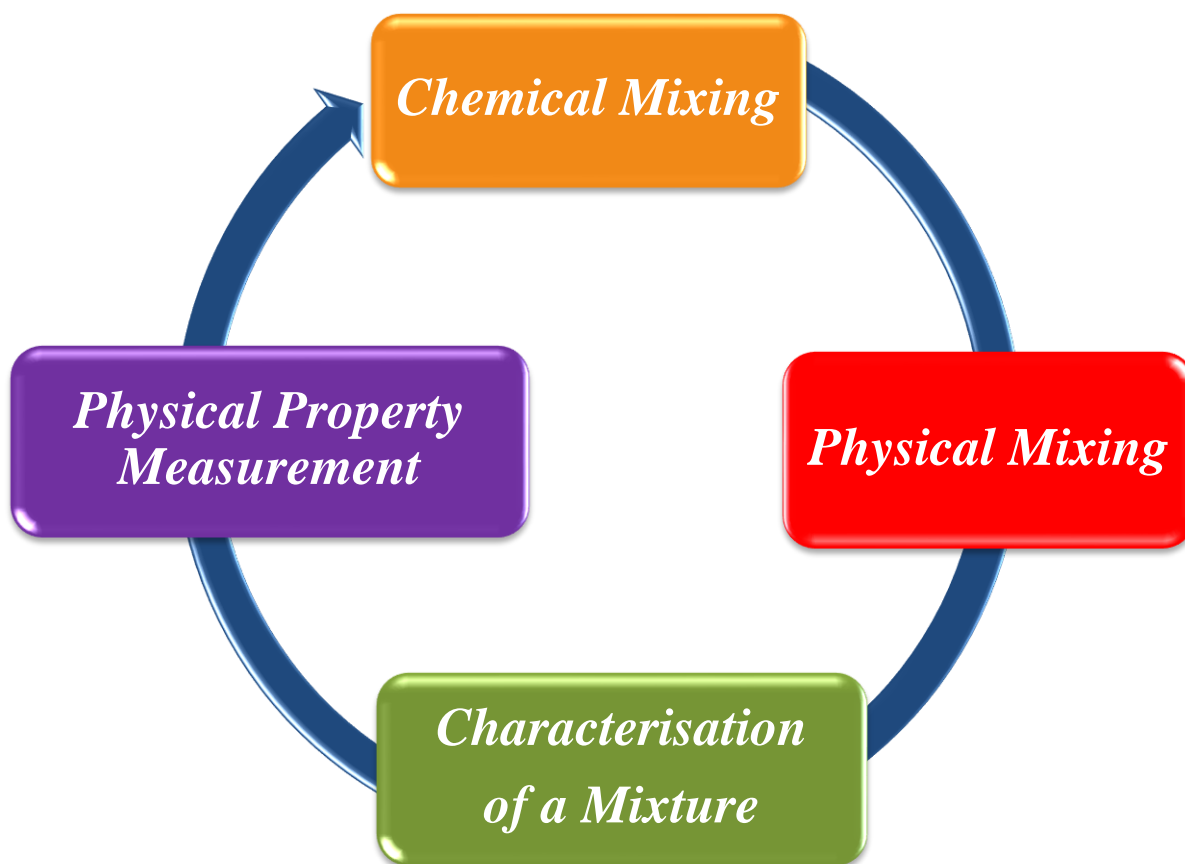
Figure 6.1.1 - Strategic Pyrotechnic Manufacturing Process

In this context chemical mixing mainly refers to the formation of co-crystals or MOFs. This step will involve the analysis of raw materials and utilising the fundamentals of crystal engineering. Crystal engineering will be considered both in terms of co-crystal and MOF formation and control of particle size via optimisation of the crystallisation method. Physical mixing refers to the mixing method employed (eg sieve mixing or dry powder dispensing) as well as the number of mixing cycles. Characterisation of a mixture refers to the results obtained from analysis of the mixtures through the use of PXRD and CT with the application of tessellation tools and statistical tools to describe

the homogeneity of the mixtures. Physical property measurements refer to the results acquired using DSC, bomb calorimetry, and burn rate assessment of the pyrotechnic mixtures by photography (normal and high-speed), radiometry, and photometry.

Each step of the process informs the other. It was understood that even if a co-crystal did form that it may not meet the performance criteria of a typical pyrotechnic. Whilst this was not necessarily desirable, information would have been gained from each step in the process in order to obtain the result. Results gathered from the physical property measurements of the mixtures can be related to the assessment of the properties of the individual components in crystal or co-crystal form. Characterisation of the mixture assessed the degree of physical mixing. These results were used to partly explain physical property measurements.

Most compositions in use today are legacy formulations. In order for changes to be made to a process, say when an ingredient is no longer available, an understanding of each ingredients purpose is required as well as its manufacturability. Using this approach would provide a more complete understanding of the manufacture of a pyrotechnic product compared to what is known at present.

6.2   FURTHER WORK

This section describes potential improvements which could be made for the work carried out in this study as well as possible routes of investigation for the future for energetic materials.

6.2.1   MACROSCOPIC CHARACTERISATION

6.2.1.1   *ANALYSIS DEVELOPMENTS*

An alternative setup for analysis of energetic materials using CT would be to use multiple scans of longer lengths of composition to build up a 3D volume of the complete composition. Thicker path lengths are more difficult to penetrate as there is more of the material for X-rays to pass through.

Another use for CT would be for investigating the application of different pressure loads to various pyrotechnic materials to assess the stress and strain values associated with specific compositions. It could help identify the most appropriate press load for any given pyrotechnic composition.

Thermal imaging of burn tests would be advisable to ascertain the heat output attributed to each composition to allow further comparison between each sample. Other tests which are required are the EMTAP (Energetic Materials Testing Assessment Policy) tests which measure the sensitivity and explosiveness of each sample.

6.2.1.2   *MANUFACTURING IMPROVEMENTS*

There are several improvements which could be realised by implementing a dry powder dispensing system in place of sieve mixing. Homogeneous mixing is achieved by the gradual build-up of layers composed of both oxidiser and fuel components. This approach is known as 'Additive Manufacturing'. Each material is dropped down onto an XY rotating table which is moved to a desired position which then shifts once the layer of mixed components have been deposited in a specific area. It will then move to its next programmed position until the desired width and height of material is

achieved. The main benefits attributed to dry powder dispensing would be the reduced mixing time required as only one cycle would be necessary compared to the sieve mixing process. This would mean significant reductions in process time and consequently reduced labour costs. Another benefit would be reducing human exposure to any hazardous material during the manufacturing process as the majority of this activity can be operated and controlled remotely.

Extending this approach one could look into the use of 3D printing to generate pyrotechnic components containing multiple ingredients which could be formed into any desired shape. Utilising 3D printing as a means to manufacture pyrotechnics could revolutionise the industry. One of the last stages of pyrotechnic design is the shaping and packing of the pyrotechnic composition. Rather than spending lots of time creating intricate patterns/grooves within a pyrotechnic, a 3D printer could do this and more. The main benefits are again the reduction of manual labour as the process is computationally driven. Grooves and patterns tend to be created to make room for another component. They can also be used to alter the burn rate. Grooves create more surface area and allow the material to burn quicker at these points. More intricate patterns, created by 3D printers, could produce burn rate patterns which would otherwise be unachievable through standard machining methods. Furthermore by using 3D printing to create said grooves from the outset, and therefore removing any machining operation, material waste is kept to an absolute minimum.

6.2.2   MOLECULAR CONTROL

6.2.2.1   BINARY SYSTEMS

Although co-crystals which arose from this research did not possess significant pyrotechnic potential, co-crystals in general could still be valuable for the design of new energetic materials. It would be advisable to investigate systems which include N-containing heterocycles (fuels) similar to those used within this work and couple these with other organic molecules which possess multiple nitro groups (oxidiser).

6.2.2.2   MOFs

EMTAP tests which measure the sensitivity and explosiveness of each sample are required for each new pyrotechnic before it would be considered as a future product for manufacture and so it is recommended that these tests be carried out and each sample evaluated.

There are limitless possibilities to be realised with the use of MOFs given that there is such a varied range of possible metal nodes and organic linkers which can be used to manufacture them. The dimensionality of the final structure can be tuned depending on the combination of ingredients used. Post-modification of MOFs is also possible. A linker can be altered when it is already present within a framework to create a new structure allowing very different properties to be realised.

Not only can the organic linker be changed post-synthesis but so can the metal nodes. Brozek *et al.* discussed cation exchange within MOFs in a recent review highlighting its potential.[1] The MOFs which undergo this sort of change rely on the presence of metal sites which are coordinatively unsaturated, coordinated by at least one solvent molecule or have the potential to obtain higher coordination numbers. The work in this area tends to be restricted to the investigation of transition metals. The use of multiple alkaline earth metal oxidisers were briefly trialled within the research presented within this thesis to see whether they would both be incorporated within the same crystal structure, however, it was realised that there was a preference for one metal. By altering the metal within the MOF it would be possible to change properties such as the burn colour of the product. It may be necessary to include chlorine donors to intensify and fine-tune the colour output.

A very specific subset of organic linkers, the diacids, was investigated for this work it would be advisable to investigate the use of other bridging ligands used by the energetic materials industry for the purpose of manufacturing MOFs with energetic potential. Additionally it would be interesting to replace metal nitrates with metal chlorates/perchlorates as these are typically combined with organic fuels in physical mixtures as opposed to metallic fuels which are typically paired with metal nitrates.

Another aspect of work which would be interesting to investigate for the series of MOFs generated within this work would be pore size analysis by means of Langmuir

and BET (Brunauer–Emmett–Teller) Analysis. Depending on the pore size available it may be possible to place additional useful components within the volume available. This may be in the form of a dye or an additional oxidiser/fuel etc. The majority of the MOFs obtained were deemed to be very dense with limited void space available. These observations were based on PLATON results associated with crystal structure determinations.[2] If larger organic linkers were used it may be possible to create a greater amount of accessible void space.

6.2.2.3   *CRYSTAL ENERGY LANDSCAPES VS PERFORMANCE*

It is known that changes in crystal packing, and defects, in crystal formation alter the performances of pyrotechnic materials.[3] In the process of designing a new energetic material it is important to establish the level of energetic output associated with the new material and any of its potential polymorphs which may arise under various temperatures and/or pressures.[4] One way of establishing this may be to assess the energy associated with the crystal landscape and observe how it compares to the performance of the energetic material. Mapping crystal energy landscapes was initially seen to be desirable for industrial pharmaceutical development.[5] It is possible that it could provide further insight to the energetic materials industry given there are several parallels between these two research areas. This method of investigation could be used for explosives already in existence as well as for future co-crystal and MOF energetic materials.

References

1.   Brozek, C. K.; Dinca, M., *Chem. Soc. Rev.* **2014,** *43* (16), 5456-5467.

2.   Spek, A. L. *PLATON, A Multipurpose Crystallographic Tool*, Utrecht University, Utrecht, The Netherlands., 2002.

3.   Teipel, U., *Energetic Materials - Particle Processing and Characterization*. WILEY-VCH: 2005; p 621.

4.   Millar, D. I. A.; Marshall, W. G.; Oswald, I. D. H.; Pulham, C. R., *Cryst. Revs.* **2010,** *16* (2), 115-132.

5.   Ismail, S. Z.; Anderton, C. L.; Copley, R. C. B.; Price, L. S.; Price, S. L., *Cryst. Growth Des.* **2013,** *13* (6), 2396-2406.

APPENDIX

A.1   MACROSCOPIC CHARACTERISATION CASE STUDY

The aim of this project was to investigate the use of available imaging software to allow the characterisation of several pyrotechnic compositions and determine their degree of homogeneity.

After initial visual assessments were carried out a macro was developed in Fiji/ImageJ to ascertain average grayscale values within the datasets to provide a rough indication of the oxidiser and fuel concentration within the mixtures. The macro detailed below. The macro editor was opened up as well as a recorder. The recorder allows you to identify coordinates within the image as they are selected. These values can be copied into the macro which, when run, estimates the average grayscale value for each slice within the region of interest selected. The volume grayscale value was calculated by taking an average of grayscale values for the combined slices.
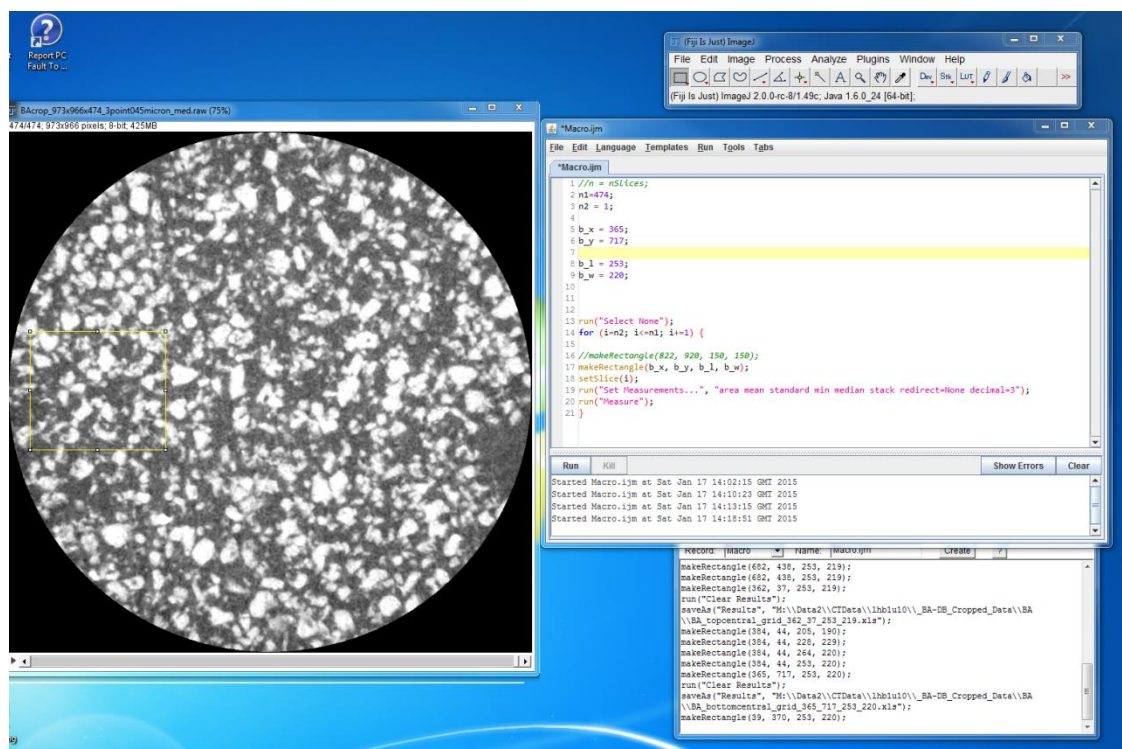
Figure A.1.1 - Grayscale Averaging Approach in Fiji/ImageJ

As particle size was of particular interest in this study it was advisable to look at software typically designed for the assessment of particles. One such tool was also incorporated within Fiji/ImageJ; a plugin called 'Analyze Particles'. Automatic particle analysis required a binary file input therefore the first step was to threshold the image as is shown in Figure A.1.2. The next step was to apply a watershed which helps to separate apparent touching particles. In the majority of cases this tool worked fairly well although in some cases particles were separated when they should have been connected and vice versa. We accepted that this tool would not work with 100% efficiency but it worked well enough for our needs. Once the particles were separated the edge particles were removed so as to only account for complete particles. The minimum pixel size and maximum size was selected to be 100-infinity as pixel counts less than 100 were considered to be spurious. Once set running a collection of images was provided such that within each slice each particle outline was provided along with a central label. In addition to the images was a collection of measurements which included particle number, location, size, feret diameter, circularity, solidity etc.
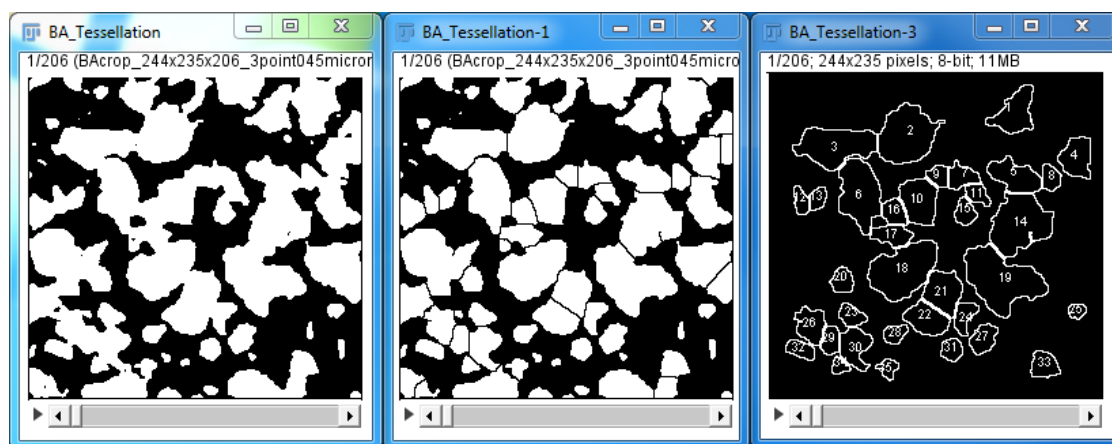
Figure A.1.2 'Analyze Particle' Fiji/ImageJ plugin image output

The disadvantage of using this tool was that as one moved on to the next slice the particle numbering would reinitiate and so it was found several particles were being over-counted. For this reason it was important to investigate tools which were capable of handling not only 2D data but 3D data as well. A tutorial was found within Avizo Fire which was able to address this requirement. It was able to output a list of oxidiser particles, their positions and their volumes. It was therefore useful for indicating both

the number of particles within a mixture but also determining the particle size distribution. The Avizo map of steps taken is shown in Figure A.1.4. The original grayscale image which this example was applied to is shown in Figure A.1.3.
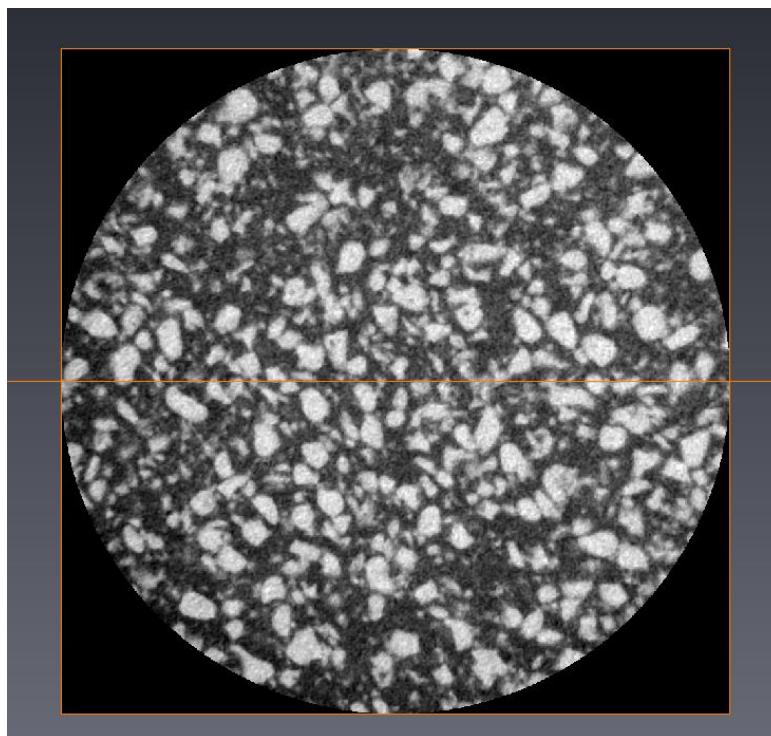
Figure A.1.3 - Original Grayscale Image
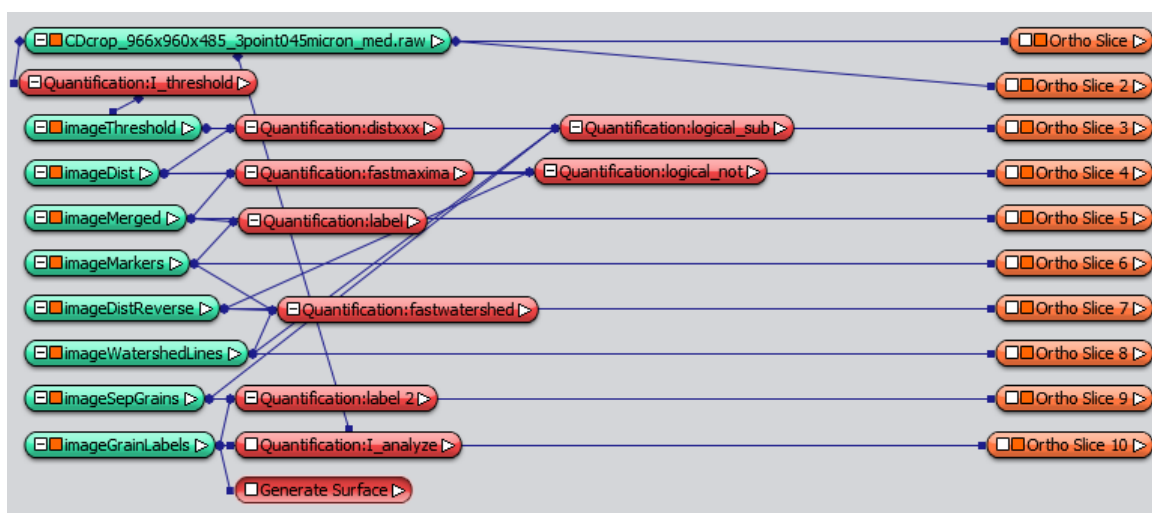
Figure A.1.4 - Avizo Map Workflow

| Step 1: Threshold | Step 2: Distance Transform | Step 3: Fast Maxima | Step 4: Labelling |

| Step 5: Inverse Distance Transform | Step 6: Watershed Line Creation | Step 7: Grain Separation | Step 8: Labelling |
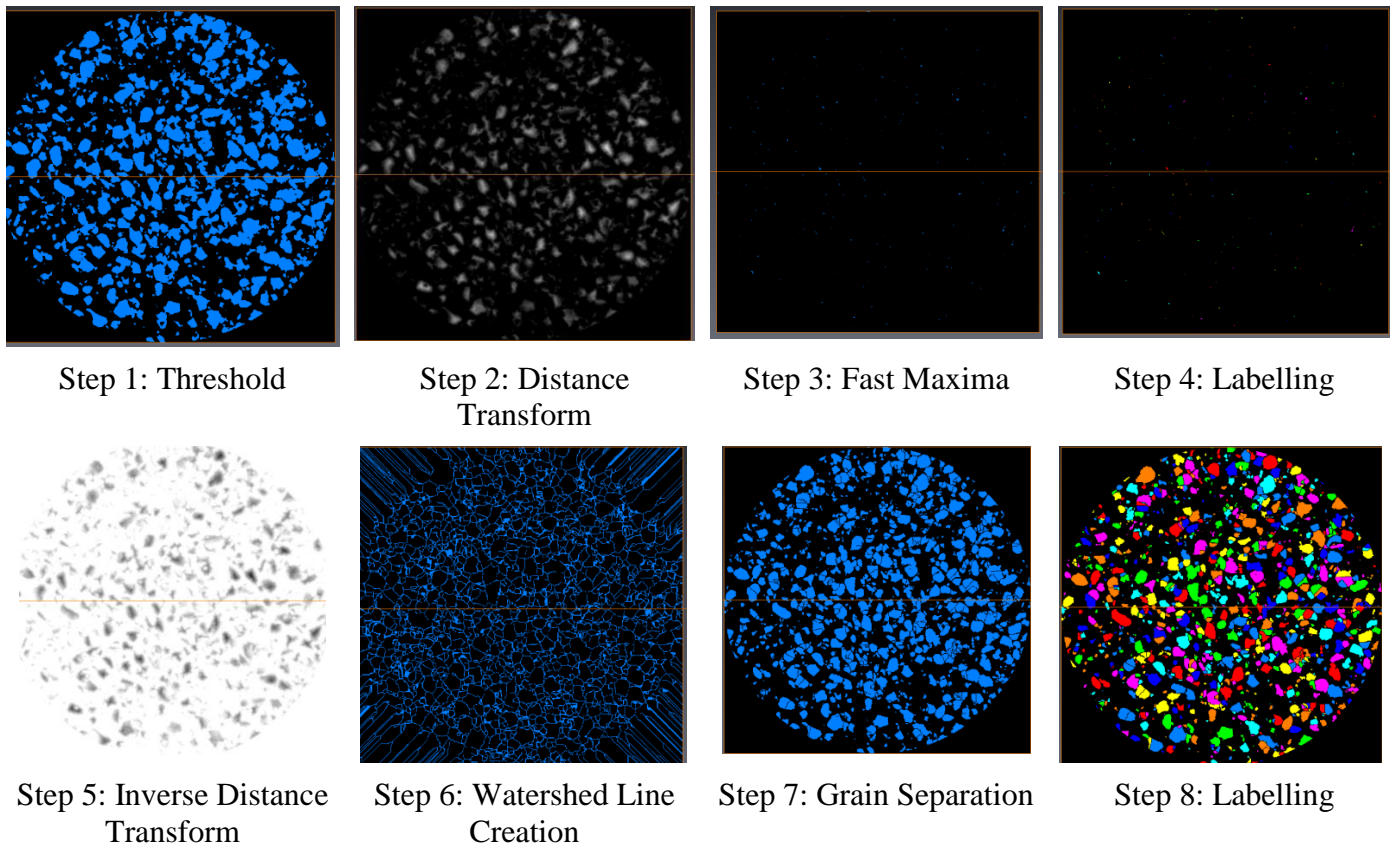
Figure A.1.5 - Avizo Map Workflow Output Step by Step

Step 1: Original Grayscale image segmented/binarised to assess only the oxidiser particles.

Step 2: Application of the distance transform

Step 3: Fast Maxima - Searches for the centroids of each particle and displays them

Step 4: Labelling of centroids

Step 5: Inverse Distance Transform to assess the correct separation points between particles

Step 6: Watershed uses Inverse distance transform coupled with the information obtained for the labelled centroids to create mesh used to create particle separations during the next step

Step 7: Grain Separation

Step 8: Labelling of particles.

A5

Derived CT data, all of which are 8 bit raw files, can be found on the Appendix CD along with a notepad file stating which software to use and how the labelling scheme of each dataset works. For anyone interested in CT analysis I would highly recommend that Fiji/Image J be used. This is free software which is constantly updated with new plugins and also has the added benefit that the user can create their own macros within the software.

The original CT Data used for the construction of this thesis can be requested via email to i.sinclair@soton.ac.uk.

A.2 BINARY SYSTEM RESULTS

	N-CONTAINING SATURATED HETEROCYCLES						N-CONTAINING HETEROCYCLES (6-MEMBERED RINGS)							
	Pyr	*MPyr*	*Idn*	*DMIdn*	*Mo*	*AMo*	*NPy*	*DNPy*	*3NONPy*	*5NONPy*	*DMNPym*		*Az*	*Tri*
fBDC	2014lhb114	2014lhb111	2014lhb043	2014lhb108	2014lhb082	2014lhb085b	2014lhb039	2014lhb041	2014lhb018a	2014lhb019b	2014lhb020	2014lhb022		
iso fBDC			2014lhb077		2014lhb115			2014lhb076	2014lhb126	2014lhb026d	2014lhb034			
alt fBDC	2014lhb109		2014lhb079		2014lhb113		2014lhb123	2014lhb078	2014lhb027	2014lhb029	2014lhb028			

	N-CONTAINING HETEROCYLIC AZOLES									DYES		
	Im	*2MI*	*4MI*	*1AI*	*4NOI*	*DMI*	*Tro*	*3NTro*	*5NOIn*	*MR*	*S3*	*MO1*
fBDC	2014lhb125	2014lhb046	2014lhb047	2014lhb050		2014lhb048	2014lhb105	2014lhb052				
iso fBDC			2014lhb093c				2014lhb101					
alt fBDC	2014lhb104	2014lhb087	2014lhb094	2014lhb117		2014lhb096	2014lhb103					

Table A.2.1 – Co-crystallisations Results

Key:

Salt	Salt hydrate	Co-crystal	Components reacted	Amorphous
Starting material	Starting material solvate	Microcrystalline	Decomposition Product	

A.3   GROUP 2 MOF RESULTS

	ALKANE DIACIDS							FLUORINATED ALKANE DIACIDS		
	OxA	*MnA*	*ScA*	*GlA*	*AdA*	*PmA*	*SbA*	*fScA*	*fGlA*	*fAdA*
Ca(NO₃)₂.4H₂0	CALOXM			YUDYAX	LEGREU					
		CAMALD								
Sr(NO₃)₂		SRMALO		2013lhb015				2014lhb095		
	2014lhb064	2014lhb066								
Ba(NO₃)₂	BALMUW			2013lhb040	DEKZEA	2014lhb010				
	2014lhb062b									

	HYDROXY DIACIDS & ALKENE DIACIDS			AROMATIC ACIDS			FLUORINATED AROMATIC DIACIDS		
	LTA	*MeA*	*FmA*	*BDC*	*iso BDC*	*alt BDC*	*fBDC*	*iso fBDC*	*alt fBDC*
Ca(NO₃)₂.4H₂0	CATART03		2013lhb017						
	CATART03			CATPAL03			2014lhb054b		2014lhb124
Sr(NO₃)₂		2013lhb018	DUCLUJ01	IJOVEJ				2014lhb127	2013lhb042
	CUGSUT		DUCLUJ01	NOCLOH			2014lhb055	2014lhb067	2014lhb061
	QALNIA		DUCLUJ01	LOCCAH			2014lhb055	2014lhb067	2014lhb061
Ba(NO₃)₂	HIXZOD				2014lhb013		2013lhb014		
	HIXZOD						2014lhb053		2014lhb060c

Table A.3.1 – Group 1 MOF Results (* = Synthesis Method 1, ** = Synthesis Method 2)

Key:

Starting material	1D MOF	2D MOF	3D MOF	Microcrystalline	Decomposition Product	Amorphous	No Precipitate

A.4   CELL PARAMETERS FOR BINARY COMPOUNDS

Sample ID	A-B	Asymmetric unit	R-Factor/%	Space Group	Z	Study Temp/ K	a/Å	b/Å	c/Å	Alpha/°	Beta/°	Gamma/°	Cell Volume/Å³
2014lhb020	fBDC - DMNPym	$0.5A^-\text{-}B^+.H_2O$	3.33	$P2_1/n$	2	150	10.7556(8)	6.7291(5)	15.6457(11)	90	102.236(2)	90	1106.64(14)
2014lhb022	fBDC - DMNPym	0.5A-0.5B	9.19	Pnma	4	100	14.5325(11)	25.4428(19)	3.8068(2)	90	90	90	1407.55(17)
2014lhb026d	isofBDC - 5NONPy	A-2B	4.23	C2/c	8	150	40.957(3)	5.5165(4)	17.5477(11)	90	94.334(2)	90	3953.4(5)
2014lhb027	altfBDC - 3NONPy	$0.5A^-\text{-}B^+$	4.51	Pbcn	4	100	18.9915(13)	14.7926(10)	6.9717(5)	90	90	90	1958.6(2)
2014lhb028	altfBDC - DMNPym	$A^-\text{-}B^+$	5.20	P-1	2	150	8.7030(5)	9.0169(5)	10.7766(8)	81.583(11)	73.347(1)	66.528(9)	742.67(10)
2014lhb029	altfBDC - 5NONPy	$2A^-\text{-}B^+$	5.50	Pbca	8	100	27.7330(19)	15.5833(11)	10.5778(7)	90	90	90	4571.4(5)
2014lhb030	fBDC - 3NONPy	$0.5A^-\text{-}B^+$	3.26	$P2_1/n$	2	150	11.9443(8)	5.7289(4)	14.2882(10)	90	98.028(3)	90	968.12(12)
2014lhb032	fBDC - 5NONPy	$0.5A^-\text{-}B^+$	3.22	$P2_1/n$	2	100	11.0340(8)	5.7413(4)	15.0758(11)	90	99.084(3)	90	943.07(12)
2014lhb034	isofBDC - DMNPym	$A^-\text{-}B^+$	15.01	$P2_1/c$	4	100	4.0171(2)	20.2136(14)	17.2161(11)	90	95.393(5)	90	1422.94(15)
2014lhb039	fBDC - 2NPy	$A^-\text{-}B^+$	3.19	$P2_1/c$	4	100	9.7001(7)	17.4712(11)	8.2971(15)	90	112.68(1)	90	1297.39(15)
2014lhb041	fBDC - DNPy	$2(0.5)A^-\text{-}B^+$	3.24	P-1	2	100	7.5134(5)	9.6553(7)	9.6897(7)	87.589(5)	78.010(5)	88.793(6)	686.93(9)
2014lhb043	fBDC - Idn	0.5A-B	4.08	$P2_1/n$	2	20	5.6187(4)	5.7526(4)	26.2334(18)	90	93.019(2)	90	846.74(10)
2014lhb046	fBDC - 2MI	$0.5(A^-\text{-}B^+)$	6.37	$P2_1/c$	2	20	9.2084(5)	7.3851(5)	9.6353(7)	90	97.547(2)	90	649.57(7)
2014lhb047	fBDC - 4MI	$A^-\text{-}B^+$	9.38	$P2_12_12_1$	4	20	7.2233(5)	9.6951(7)	18.3487(13)	90	90	90	1284.97(16)
2014lhb048	fBDC - DMI	$A^-\text{-}B^+.H_2O$	3.42	$P2_1/c$	4	100	8.0471(5)	18.6519(13)	9.5052(7)	90	91.257(2)	90	1426.33(17)
2014lhb052	fBDC - NTro (-NH₂)	$A^-\text{-}B^+.H_2O$	3.19	P-1	1	100	5.6137(4)	8.0917(5)	8.9568(7)	77.613(7)	78.978(7)	82.252(7)	388.18(5)
2014lhb076	isofBDC - DNPy	$A^-\text{-}B^+$	2.65	Pc	2	100	5.4774(4)	8.6080(5)	14.5149(10)	90	95.254(2)	90	681.49(8)
2014lhb077	isofBDC - Idn	A-B	7.03	$P2_1$	2	100	5.5381(4)	9.4554(7)	11.7661(8)	90	90.558(4)	90	616.10(8)
2014lhb078	altfBDC - DNPy	$2(A^-\text{-}B^+)$	11.15	P-1	4	100	8.9965(5)	11.6354(8)	13.4821(9)	84.070(8)	89.336(9)	89.221(9)	1403.52(16)
2014lhb079	altfBDC - Idn	2A-3B	6.17	$P2_1/n$	2	100	10.2841(7)	26.8071(19)	10.7871(8)	90	102.211(2)	90	2906.6(4)
2014lhb080	altfBDC - NPy	$A^-\text{-}B^+$	6.39	$Pca2_1$	4	100	7.5087(6)	13.3571(10)	12.9653(9)	90	90	90	1300.35(17)

Sample ID	A-B	Asymmetric unit	R-factor/%	Space Group	Z	Study Temp/ K	a/Å	b/Å	c/Å	Alpha/°	Beta/°	Gamma/°	Cell Volume/Å³
2014lhb082b	fBDC - Mo	A^--B^+	5.25	Ia	4	100	7.6822(5)	17.8120(13)	9.6799(6)	90	106.992(4)	90	1266.73(15)
2014lhb085b	fBDC - AMo	$0.5\,A^--B^+$	9.18	C2/c	4	100	17.4048(11)	6.3536(4)	20.4021(14)	90	106.955(3)	90	2158.1(3)
2014lhb087b	alt fBDC - 2MI	$0.5(A^--B^+)$	10.07	C2/c	4	100	12.1886(11)	12.3727(11)	9.4275(7)	90	112.570(11)	90	1312.8(2)
2014lhb093e	iso fBDC - 4MI	A^--B^+	8.06	P2$_1$/c	4	100	12.4952(9)	14.5165(10)	7.0035(5)	90	98.090(3)	90	1257.70(15)
2014lhb094	alt fBDC - 4MI	$2(A^--B^+)$	4.84	P-1	4	100	7.5331(5)	11.0533(8)	15.5493(11)	80.509(6)	79.044(5)	80.805(6)	1242.64(15)
2014lhb096	alt fBDC - DMI	A^--B^+	4.30	Pca2$_1$	4	100	7.6757(5)	13.4117(9)	13.0049(9)	90	90	90	1338.78(16)
2014lhb101	iso fBDC - Tro	A^--B^+	4.27	P-1	2	100	4.6416(2)	11.3274(8)	11.3941(8)	72.150(5)	89.610(6)	84.359(6)	567.30(6)
2014lhb103	alt fBDC - Tro	A^--B^+	4.42	P2/c	24	100	26.6344(19)	7.7400(5)	33.874(2)	90	106.651(1)	90	6690.3(8)
2014lhb104	alt fBDC - Im	A^--B^+	9.66	C2/c	8	100	17.0193(15)	7.7530(5)	17.1572(11)	90	92.472(10)	90	2261.8(3)
2014lhb105	fBDC - Tro	A^--B^+	3.45	P-1	2	100	7.6932(5)	8.1306(5)	9.5538(7)	73.924(8)	84.624(9)	70.797(8)	542.27(7)
2014lhb108	fBDC - DMIdn	$0.5(A^--B^+)$	4.37	C2/c	4	100	10.7847(8)	12.0847(8)	10.8783(8)	90	98.107(2)	90	1403.60(17)
2014lhb109	alt fBDC - Pyr	A-B	6.03	P2$_1$/n	4	100	11.6267(8)	6.9266(5)	16.4226(11)	90	104.992(2)	90	1277.55(15)
2014lhb111	fBDC - MPyr	A^--B^+	5.99	P-1	2	100	8.4868(5)	8.5397(5)	9.7164(7)	96.033(7)	104.841(8)	95.630(7)	671.18(8)
2014lhb113	alt fBDC - Mo	A^--B^+	6.28	P-1	2	100	7.8849(5)	8.9876(5)	9.5444(7)	85.128(11)	68.953(9)	78.823(11)	619.19(8)
2014lhb114	fBDC - Pyr	0.5A-B	7.98	P-1	1	100	6.9399(5)	6.9624(5)	9.8741(7)	69.472(13)	70.986(13)	85.597(15)	422.05(7)
2014lhb115c	iso fBDC - Mo	$2(A^--B^+)$	5.38	Pc	4	100	10.9814(8)	5.9090(4)	20.5436(14)	90	99.012(2)	90	1316.60(16)
KURBUV	fBDC - Im	A^--B^+	2.59	Pna2$_1$	4	100	9.7144(7)	7.0323(5)	17.4728(11)	90	90	90	1193.65(14)

Table A.4.1 – Binary Compounds Cell Parameters

A.5   CELL PARAMETERS FOR MOFS

Sample ID	Metal-Acid (M-A)	Contents of asymmetric unit	R-factor	Space Group	Z	Study Temp/K	a/Å	b/Å	c/Å	Alpha/°	Beta/°	Gamma/°	Cell Volume/Å³
2013lhb014	Ba fBDC	Ba(0.5fBDC)$_2$(H$_2$O)	2.22	C2/c	4	100	12.5647(9)	7.1406(5)	19.8230(14)	90	101.663(2)	90	1741.8(2)
2013lhb015	Sr GlA	Sr$_2$(GlA)$_2$(H$_2$O)$_5$	3.53	P2$_1$/c	4	100	13.9278(10)	14.3557(10)	9.1645(5)	90	104.908(2)	90	1770.7(2)
2013lhb017	Ca FmA	Ca(FmA)(H$_2$O)$_2$(DMF)	3.50	P2$_1$/n	4	100	7.7776(5)	12.8231(9)	12.0005(8)	90	107.042(2)	90	1144.29(13)
2013lhb018a	Sr MeA	Sr$_3$(MeA)$_2$(NO$_3$)(H$_2$O)(DMF)$_2$	9.95	P-1	1	100	6.9817(5)	10.2735(7)	14.5774(10)	92.682(16)	103.369(17)	103.264(17)	984.60(16)
2013lhb040	Ba GlA	Ba(GlA)(H$_2$O)$_5$	10.33	P2$_1$/n	4	100	7.3029(2)	12.1368(4)	13.2043(5)	90	92.323(3)°	90	1169.39(7)
2013lhb042	Sr alt fBDC	Sr(altfBDC)(H$_2$O)(DMF)	9.99	P-1	2	100	6.1469(4)	7.0452(5)	16.1438(11)	94.495(16)	96.741(16)	101.639(17)	676.26(10)
2014lhb010_a	Ba PmA	Ba(PmA)	5.26	P-1	2	100	4.5640(4)	8.5890(8)	11.4668(17)	96.49(2)	101.413(18)	104.286(19)	420.74(10)
2014lhb013_f	Ba isoBDC	Ba formic acid	4.48	P2$_1$2$_1$2$_1$	4	100	6.8001(15)	7.6342(5)	8.8092(7)	90	90	90	457.31(16)
2014lhb054b	Ca fBDC	Ca(fBDC)(NO$_3$)(H$_2$O)(Pyridine)	3.54	Pna2$_1$	4	100	14.2384(10)	16.3862(11)	6.8450(5)	90	90	90	1597.03(19)
2041lhb055	Sr fBDC	Sr(fBDC)(NO$_3$)(H$_2$O)(Pyridine)	3.72	Pna2$_1$	4	100	14.2686(10)	16.7326(11)	7.0181(5)	90	90	90	1675.6(2)
2014lhb060c	Ba altfBDC	Ba(altfBDC)(H$_2$O)(Pyridine)	3.60	P2$_1$/n	4	100	7.0904(5)	32.270(2)	7.2698(5)	90	117.997(2)	90	1468.72(17)
2014lhb061d	Sr altfBDC	Sr$_2$(altfBDC)$_2$(H$_2$O)$_2$(Pyridine)	8.38	C2	2	100	32.076(3)	6.1638(4)	11.5618(7)	90	97.569(7)	90	2266.0(3)
2014lhb062	Ba OxA	Ba(0.5OxA)(NO$_3$)(H$_2$O)	3.91	P2$_1$/c	4	100	10.9844(8)	8.0932(5)	6.3740(4)	90	104.434(2)	90	548.76(6)
2014lhb064	Sr OxA	Sr(OxA)(H$_2$O)	7.67	P-1	2	100	6.4409(5)	6.4876(5)	6.5196(5)	77.90(2)	71.32(2)	69.66(2)	240.50(5)
2014lhb066	Sr MnA	Sr$_3$(MnA)$_4$(H$_2$O)$_3$	6.57	P2$_1$/c	4	100	17.9793(13)	7.4845(5)	16.9582(11)	90	113.283(2)	90	2096.2(3)
2014lhb067	Sr isofBDC	Sr(isofBDC)(H$_2$O)(Pyridine)	5.84	P-1	2	100	7.3008(5)	9.1264(5)	13.1904(9)	101.118(6)	93.830(5)	110.526(6)	798.95(10)
2014lhb095	Sr fScA	Sr(fScA)(H$_2$O)$_2$(DMF)	3.67	C2/c	8	100	25.6904(18)	6.2503(4)	15.8437(11)	90	98.581(3)	90	2515.6(3)
2014lhb124	Ca altfBDC	Ca(altfBDC)(NO$_3$)(Pyr)	5.94	P2$_1$/n	4	100	4.4398(3)	23.0380(18)	14.3878(9)	90	96.661(6)	90	1461.69(17)

Sample ID	Metal-Acid (M-A)	Contents of asymmetric unit	R-factor	Space Group	Z	Study Temp/K	a/Å	b/Å	c/Å	Alpha/°	Beta/°	Gamma/°	Cell Volume/Å³
2014lhb127	Sr isofBDC	Sr(isofBDC)(H$_2$O)$_3$(DMF).H$_2$O	8.58	P-1	2	100	8.8263(7)	8.9293(7)	10.8630(9)	92.612(16)	93.939(17)	100.991(18)	836.95(13)
2014ac013	Rb fBDC	Rb(0.5fBDC)	8.02	I2/a	4	293	9.2821(7)	9.7189(7)	10.9837(8)	90	110.340(5)	90	929.08(12)
2014ac012b	Cs fBDC	Cs(0.5fBDC)	2.14	I2/a	4	293	9.3605(7)	9.6918(7)	11.0752(7)	90	108.566(5)	90	952.45(12)
2014ac032	K fScA	K(0.5fScA). H$_2$O	2.76	P-1	2	100	5.8968(4)	6.1582(4)	7.0496(5)	67.778(9)	70.943(9)	84.760(11)	223.84(3)
BALMUW	Ba OxA	2(Ba(OxA)).H$_2$O	6.50	P-1	2	283	9.312(1)	9.649(1)	6.188(1)	90.13(2)	95.36(2)	125.18(2)	451.382
CALOXM13	Ca OxA	2(Ca(OxA)(H$_2$O))	7.72	P2$_1$/a	4	200	10.090(2)	14.549(4)	6.270(3)	90	109.53(2)	90	867.477
CAMALD	Ca MnA	Ca(MnA)(H$_2$O)$_2$	3.20	C2/m	2	283	13.8707(4)	6.8120(2)	6.8040(2)	90	106.289(4)	90	617.085
CATART	Ca LTA	Ca(LTA)$_2$(H$_2$O)$_2$.2H$_2$O	3.52	P2$_1$2$_1$2$_1$	4	283	9.62282(5)	10.56490(5)	9.21970(5)	90	90	90	937.313
CATPAL	Ca BDC	Ca(BDC) (H$_2$O)$_3$	4.85	P2$_1$/c	4	283	7.0982(5)	21.6400(15)	6.5856(5)	90	92.217(7)	90	1010.82
CUGSUT	Sr LTA	Sr(LTA)(H$_2$O)	5.54	P2$_1$	2	283	6.6143(5)	7.1191(5)	7.8433(6)	90	98.334(2)	90	365.424
DEKZEA	Ba AdA	Ba(0.5AdA)	4.57	P-1	1	283	4.5948(4)	9.9469(3)	4.4595(3)	99.486(6)	97.037(9)	96.840(5)	197.486
DUCLUJ	Sr FmA	Sr(0.5FmA)	3.40	Fddd	8	105	10.5980(1)	9.81628(9)	10.00739(8)	90	90	90	1041.1
HIXZOD	Ba LTA	Ba(LTA)	1.90	P2$_1$2$_1$2$_1$	4	283	8.181(2)	9.036(2)	8.392(1)	90	90	90	620.366
IJOVEJ	Sr BDC	Sr(BDC)(H$_2$O)	2.70	Pbca	8	283	11.8724(3)	7.13080(10)	20.0592(4)	90	90	90	1698.21
LEGREU	Ca AdA	Ca(AdA)(H$_2$O)	4.00	P-1	2	283	5.8990(3)	6.7985(5)	10.8212(6)	78.999(5)	81.831(5)	82.971(5)	419.649
LOCCAH	Sr BDC	Sr(0.5BDC)(H$_2$O)$_2$	7.88	C2/c	4	173	9.6245(9)	22.101(2)	6.7682(6)	90	129.893(1)	90	1104.58
NHOXAL	Na OxA	Na(OxA)(H$_2$O)	3.31	P-1	2	273	5.6982(11)	6.5040(12)	6.6647(13)	75.040(2)	84.990(3)	70.072(3)	224.34
NOCLOH	Sr BDC	Sr(BDC)(DMF)	2.38	P3$_2$	3	150	10.599(1)	10.599(1)	9.806(2)	90	90	120	954.009
PIPDOJ	K fBDC	K(0.25fBDC)	5.37	I2/m	2	283	4.0394(9)	19.953(3)	6.0480(13)	90	91.25(3)	90	487.342
QALNIA	Sr LTA	Sr(LTA)(H$_2$O)$_2$.2H$_2$O	2.97	P2$_1$2$_1$2$_1$	4	283	9.4921(10)	9.5394(13)	11.0134(13)	90	90	90	997.252
SRMALO	Sr MnA	Sr(MnA)	2.60	Pnan	8	283	6.7538(4)	10.6270(8)	12.6744(11)	90	90	90	909.675
YUDYAX	Ca GlA	Ca(GlA)(H$_2$O)	1.90	P2$_1$2$_1$2$_1$	4	283	6.805(1)	18.486(2)	5.884(1)	90	90	90	740.191

Table A.5.1 – MOF Structures Cell Parameters

A.6   SXRD MOF BOND LENGTHS

Ca_fBDC_2	
Ca1-O3(COO)b	2.502(2)
Ca1-O4(COO)b	2.566(2)
Ca1-O1(COO)d1	2.395(2)
Ca1-O2(COO)d1	2.395(2)
Ca1-O1(COO)d2	2.558(2)
Ca1-O2(COO)d2	2.618(2)
Ca1-O13(NO3)	2.444(2)
Ca1-O1W(H2O)t	2.423(2)
average	2.488

Sr_fBDC_2	
Sr1-O3(COO)b	2.661(3)
Sr1-O4(COO)b	2.630(3)
Sr1-O1(COO)d1	2.491(4)
Sr1-O2(COO)d1	2.488(4)
Sr1-O1(COO)d2	2.726(3)
Sr1-O2(COO)d2	2.686(4)
Sr1-O13(NO3)	2.597(3)
Sr1-O1W(H2O)t	2.569(3)
average	2.606

Ba_fBDC_1/2	
Ba1-O11(COO)a	2.813(2)
Ba1-O11(COO)a	2.791(2)
Ba1-O12(COO)a	2.957(2)
Ba1-O1(COO)d1	2.691(2)
Ba1-O1(COO)d2	2.807(2)
Ba1-O2(COO)d1	2.686(2)
Ba1-O2(COO)d2	2.939(2)
Ba1-O1W(H2O)br	2.892(2)
average	2.822

K_fBDC_2 (PIPDOJ)	
K1-O1(COO)d1	2.862(2)
K1-O1(COO)d1	2.862(2)
K1-O1(COO)d1	2.716(2)
K1-O1(COO)d1	2.716(2)
K1-O1(COO)d2	2.856(2)
K1-O1(COO)d2	2.856(2)
K1-F1(COO)	2.840(2)
K1-F1(COO)	2.840(2)
average	2.811

Rb_fBDC_2	
Rb1-O1(COO)a	3.049(3)
Rb1-O1(COO)a	3.049(3)
Rb1-O2(COO)a	3.061(5)
Rb1-O2(COO)a	3.061(5)
Rb1-O2(COO)a	3.070(4)
Rb1-O2(COO)a	3.070(4)
Rb1-F1(COO)	3.179(3)
Rb1-F1(COO)	3.179(3)
average	3.060

Cs_fBDC_2	
Cs1-O1(COO)a	3.196(2)
Cs1-O1(COO)a	3.196(2)
Cs1-O2(COO)a	3.127(2)
Cs1-O2(COO)a	3.127(2)
Cs1-O2(COO)a	3.159(2)
Cs1-O2(COO)a	3.159(2)
Cs1-F1(COO)	3.277(2)
Cs1-F1(COO)	3.277(2)
average	3.161

Sr_isofBDC_1	
Sr1-O1(COO)c1	2.485(5)
Sr1-O1(COO)c2	2.750(5)
Sr1-O2(COO)c3	2.668(5)
Sr1-O3(COO)*	2.586(5)
Sr1-O1S(DMF)t	2.499(5)
Sr1-O1W(H2O)t	2.564(5)
Sr1-O2W(H2O)t	2.611(5)
Sr1-O3W(H2O)t	2.544(5)
average	2.588

Sr_isofBDC_2	
Sr1-O3(COO)a	2.634(3)
Sr1-O4(COO)a	2.572(3)
Sr1-O1(COO)d1	2.659(2)
Sr1-O2(COO)d1	2.579(2)
Sr1-O1(COO)d2	2.780(2)
Sr1-O2(COO)d2	2.671(2)
Sr1-O1W(H2O)t	2.616(3)
Sr1-O11(NO3)	2.692(2)
Sr1-O12(NO3)	2.736(3)
average	2.660

Ca_altfBDC_2	
Ca1-O1(COO)a	2.373(3)
Ca1-O2(COO)a	2.427(3)
Ca1-O2(COO)a	2.387(3)
Ca1-O4(COO)c1	2.382(3)
Ca1-O4(COO)c2	2.501(3)
Ca1-O3(COO)c3	2.529(3)
Ca1-O11(NO3)	2.502(3)
Ca1-O12(NO3)	2.509(3)
average	2.451

Sr_altfBDC_1		Sr_altfBDC_2 (Sr1)		Sr_altfBDC_2 (Sr2)	
Sr1-O3(COO)a	2.605(7)	Sr1-O3(COO)a	2.583(11)	Sr2-O1(COO)a	2.541(10)
Sr1-O4(COO)a	2.611(8)	Sr1-O3(COO)a	2.583(11)	Sr2-O2(COO)a	2.609(13)
Sr1-O1(COO)d1	2.501(7)	Sr1-O12(COO)a	2.560(11)	Sr2-O4(COO)a	2.685(13)
Sr1-O2(COO)d1	2.480(7)	Sr1-O12(COO)a	2.560(11)	Sr2-O11(COO)a	2.520(12)
Sr1-O2(COO)d2	2.777(7)	Sr1-O14(COO)c1	2.535(11)	Sr2-O14(COO)c2	2.654(12)
Sr1-O1(COO)d2	2.752(8)	Sr1-O14(COO)c1	2.535(11)	Sr2-O13(COO)c3	2.708(13)
Sr1-O1W(H2O)t	2.550(8)	Sr1-O1W(H2O)br	2.617(12)	Sr2-O1W(H2O)br	2.675(10)
Sr1-O1S1(DMF)t	2.637(9)	Sr1-O1W(H2O)br	2.617(12)	Sr2-O2W(H2O)t	2.631(10)
average	2.614	average	2.574	average	2.628

Ba_altfBDC_2		Ca_BDC_2 (CATPAL)		Sr_BDC_1a (IJOVEJ)	
Ba1A-O3(COO)a	2.615(3)	Ca1-O2(COO)d1	2.349	Sr1-O1(COO)a	2.553
Ba1A-O4(COO)a	2.974(3)	Ca1-O3(COO)d1	2.362	Sr1-O1(COO)a	2.660
Ba1A-O1(COO)d1	2.611(2)	Ca1-O3(COO)d2	2.490	Sr1-O5(COO)a	2.532
Ba1A-O2(COO)d1	2.852(3)	Ca1-O2(COO)d2	2.528	Sr1-O3(COO)c1	2.475
Ba1A-O1(COO)d2	2.952(2)	Ca1-O4(H2O)br	2.522	Sr1-O3(COO)c2	2.831
Ba1A-O2(COO)d2	2.934(3)	Ca1-O4(H2O)br	2.633	Sr1-O4(COO)c3	2.554
Ba1A-O1WA(H2O)br	2.852(5)	Ca1-O1(H2O)t	2.372	Sr1-O2(H2O)br	2.639
Ba1A-O1WA(H2O)br	2.927(5)	Ca1-O6(H2O)t	2.394	Sr1-O2(H2O)br	2.645
Ba1A-O2WA(H2O)t	2.810(5)				
average	2.836	average	2.456	average	2.611

Sr_BDC_1b (NOCLOH)		Sr_BDC_2 (LOCCAH)		Ba_isoBDC_2 (Ba_form)	
Sr1-O4(COO)c1	2.497	Sr1-O1(COO)d1	2.503	Ba1-O1(COO)a	2.768(11)
Sr1-O4(COO)c2	2.744	Sr1-O1(COO)d1	2.503	Ba1-O1(COO)a	2.884(11)
Sr1-O3(COO)c3	2.554	Sr1-O1(COO)d2	2.812	Ba1-O2(COO)a	2.779(11)
Sr1-O1(COO)d1	2.537	Sr1-O1(COO)d2	2.812	Ba1-O2(COO)a	2.740(10)
Sr1-O2(COO)d1	2.519	Sr1-O3(H2O)t	2.669	Ba1-O11(COO)a	2.782(10)
Sr1-O1(COO)d2	2.703	Sr1-O3(H2O)t	2.669	Ba1-O11(COO)a	2.788(10)
Sr1-O2(COO)d2	2.684	Sr1-O4(H2O)t	2.637	Ba1-O12(COO)a	2.748(10)
Sr1-O5(DMF)t	2.485	Sr1-O4(H2O)t	2.637	Ba1-O12(COO)a	2.737(11)
				average	2.778
average	2.574	average	2.655		

Table A.6.1 - M-O Interatomic Distances in the Metal Coordination Spheres of Potential Pyrotechnic MOFs

(t = terminal, br = bridging, * = non-bridging M-O bond)

Ca_OxA_1 (CALOXM13) Ca1		Ca_OxA_1 (CALOXM13) Ca2		Sr_OxA_2	
Ca1-O5(COO)f1	2.435	Ca2-O6(COO)f1	2.428	Sr1-O1(COO)f1	2.554(7)
Ca1-O6(COO)f2	2.444	Ca2-O5(COO)f2	2.407	Sr1-O1(COO)f2	2.593(7)
Ca1-O7(COO)f3	2.448	Ca2-O8(COO)f3	2.430	Sr1-O2(COO)f3	2.560(18)
Ca1-O1(COO)g1	2.445	Ca2-O2(COO)g1	2.424	Sr1-O3(COO)g1	2.570(7)
Ca1-O3(COO)g1	2.431	Ca2-O4(COO)g1	2.448	Sr1-O4(COO)g1	2.588(7)
Ca1-O1(COO)g2	2.450	Ca2-O2(COO)g2	2.429	Sr1-O3(COO)g2	2.577(7)
Ca1-O4(COO)g2	2.481	Ca2-O3(COO)g2	2.470	Sr1-O4(COO)g2	2.560(7)
Ca1-O10(H2O)t	2.433	Ca2-O9(H2O)t	2.542	Sr1-O1W(H2O)t	2.591(17)
average	2.446	average	2.447	average	2.574

Ba_OxA_1 (BALMUW) Ba1		Ba_OxA_1 (BALMUW) Ba2		Ba_OxA_2	
Ba1-O1(COO)g1	2.778	Ba2-O4(COO)g1	2.791	Ba1-O1(COO)g1	2.726(2)
Ba1-O3(COO)g1	2.859	Ba2-O2(COO)g1	2.866	Ba1-O2(COO)g1	2.777(3)
Ba1-O6(COO)g1	2.906	Ba2-O5(COO)g1	2.761	Ba1-O1(COO)g2	2.762(3)
Ba1-O8(COO)g1	2.903	Ba2-O7(COO)g1	2.758	Ba1-O2(COO)g2	2.736(3)
Ba1-O2(COO)g2	2.903	Ba2-O1(COO)g2	2.754	Ba1-O11(NO3)	2.958(4)
Ba1-O4(COO)g2	2.760	Ba2-O3(COO)g2	2.900	Ba1-O12(NO3)	2.932(3)
Ba1-O6(COO)g2	2.751	Ba2-O5(COO)g2	2.822	Ba1-O12(NO3)	2.966(3)
Ba1-O8(COO)g2	2.762	Ba2-O7(COO)g2	2.828	Ba1-O13(NO3)	2.954(3)
		Ba2-O9(H2O)t	2.939	Ba1-O1W(H2O)br	2.870(3)
				Ba1-O1W(H2O)br	2.885(3)
average	2.828	average	2.824	average	2.8566

Na_OxA_2 (NHOXAL)		Ca_MnA_2 (CAMALD)		Sr_MnA_1 (SRMALO)	
Na1-O4(COO)a	2.327	Ca1-O1(COO)a	2.530	Sr1-O1(COO)d1	2.522
Na1-O1(COO)f1	2.477	Ca1-O1(COO)a	2.530	Sr1-O2(COO)d1	2.512
Na1-O1(COO)f2	2.357	Ca1-O2(COO)d1	2.392	Sr1-O3(COO)d1	2.532
Na1-O3(COO)f3	2.454	Ca1-O2(COO)d1	2.392	Sr1-O4(COO)d1	2.628
Na1-O2(H2O)br	2.311	Ca1-O2(COO)d2	2.523	Sr1-O4(COO)d1	2.664
Na1-O2(H2O)br	2.399	Ca1-O2(COO)d2	2.523	Sr1-O1(COO)d2	2.639
		Ca1-O3(H2O)t	2.366	Sr1-O2(COO)d2	2.796
		Ca1-O4(H2O)t	2.392	Sr1-O3(COO)d2	2.770
				Sr1-O4(COO)d2	2.706
average	2.388	average	2.456	average	2.646

Sr_MnA_2 (Sr1)		Sr_MnA_2 (Sr2)		Sr_MnA_2 (Sr3)	
Sr1-O1(COO)a	2.519(5)	Sr2-O2(COO)a	2.577(5)	Sr3-O2(COO)a	2.587(5)
Sr1-O1(COO)a	2.554(5)	Sr2-O12(COO)a	2.498(5)	Sr3-O4(COO)d1	2.610(5)
Sr1-O11(COO)a	2.695(5)	Sr2-O3(COO)d1	2.555(5)	Sr3-O14(COO)d1	2.572(5)
Sr1-O11(COO)a	2.603(5)	Sr2-O32(COO)d1	2.663(5)	Sr3-O31(COO)d1	2.481(5)
Sr1-O13(COO)d1	2.752(5)	Sr2-O21(COO)*	2.552(6)	Sr3-O3(COO)d2	2.547(5)
Sr1-O13(COO)d1	2.868(5)	Sr2-O33(COO)*	2.718(6)	Sr3-O4(COO)d2	2.759(5)
Sr1-O31(COO)d2	2.549(5)	Sr2-O1W(H2O)t	2.501(6)	Sr3-O13(COO)d2	2.718(5)
Sr1-O32(COO)d2	2.747(6)	Sr2-O2W(H2O)t	2.625(7)	Sr3-O14(COO)d2	2.592(5)
average	2.661	average	2.586	average	2.608

Ca_GlA_1 (YUDYAX)		Sr_GlA_1 (Sr1)		Sr_GlA_1 (Sr2)	
Ca1-O3(COO)a	2.372	Sr1-O2(COO)c1	2.497(2)	Sr2-O13(COO)a	2.592(2)
Ca1-O4(COO)a	2.357	Sr1-O2(COO)c2	2.682(2)	Sr2-O14(COO)a	2.546(2)
Ca1-O1(COO)d1	2.355	Sr1-O1(COO)c3	2.604(2)	Sr2-O11(COO)d1	2.567(2)
Ca1-O2(COO)d1	2.340	Sr1-O12(COO)d1	2.551(2)	Sr2-O11(COO)d2	2.710(2)
Ca1-O1(COO)d2	2.520	Sr1-O3(COO)*	2.585(2)	Sr2-O12(COO)d2	2.597(2)
Ca1-O2(COO)d2	2.535	Sr1-O1W(H2O)t	2.639(3)	Sr2-O3W(H2O)br	2.710(2)
Ca1-O5(H2O)t	2.376	Sr1-O2W(H2O)t	2.599 (3)	Sr2-O4W(H2O)t	2.575 (2)
		Sr1-O3W(H2O)br	2.707(2)	Sr2-O5W(H2O)t	2.521(3)
average	2.408	average	2.608	average	2.602

Ba_GlA_1		Ca_AdA_1 (LEGREU)		Ba_AdA_1 (DEKZEA)	
Ba1-O1(COO)d1	2.713(14)	Ca1-O1(COO)a	2.358	Ba1-O1(COO)d1	2.645
Ba1-O2(COO)d1	2.717(13)	Ca1-O2(COO)a	2.348	Ba1-O1(COO)d1	2.645
Ba1-O1(COO)d2	2.905(13)	Ca1-O3(COO)d1	2.340	Ba1-O2(COO)d1	2.732
Ba1-O2(COO)d2	2.868(13)	Ca1-O4(COO)d1	2.353	Ba1-O2(COO)d1	2.732
Ba1-O3(COO)*	2.886(12)	Ca1-O3(COO)d2	2.543	Ba1-O1(COO)d2	2.967
Ba1-O1W(H2O)t	2.828(13)	Ca1-O4(COO)d2	2.493	Ba1-O2(COO)d2	2.743
Ba1-O2W(H2O)t	2.879(14)	Ca1-O5(H2O)t	2.387	Ba1-O1(COO)d2	2.967
Ba1-O3W(H2O)t	2.826(14)			Ba1-O2(COO)d2	2.743
Ba1-O4W(H2O)t	2.820(15)				
average	2.827	average	2.403	average	2.772

Ba_PmA_1		Sr_fScA_1		K_fScA_1	
Ba1-O1(COO)c1	2.757(6)	Sr1-O3(COO)a	2.644(2)	K1-O1(COO)a	2.777(2)
Ba1-O1(COO)c1	2.792(6)	Sr1-O4(COO)a	2.580(2)	K1-O1(COO)a	2.859(2)
Ba1-O1(COO)c2	2.961(6)	Sr1-O1(COO)*	2.597(2)	K1-O2(COO)a	2.760(2)
Ba1-O2(COO)c3	2.716(7)	Sr1-O1(COO)*	2.710(2)	K1-O2(COO)a	2.930(2)
Ba1-O3(COO)d1	2.714(6)	Sr1-O1S(DMF)t	2.554(2)	K1-O1W(H2O)br	2.733(2)
Ba1-O4(COO)d1	2.674(7)	Sr1-O1W(H2O)t	2.523(3)	K1-O1W(H2O)br	2.814(2)
Ba1-O3(COO)d2	2.804(6)	Sr1-O2W(H2O)br	2.717(2)		
Ba1-O4(COO)d2	2.842(7)	Sr1-O2W(H2O)br	2.662(2)		
average	2.783	average	2.623	average	2.812

Table A.6.2 - M-O Interatomic Distances in the Metal Coordination Spheres of Potential Pyrotechnic MOFs

(t = terminal, br = bridging, * = non-bridging M-O bond)

Ca_LTA_1/2 (CATART)		Sr_LTA_2a (CUGSUT)		Sr_LTA_2b (QALNIA)	
Ca1-O2(COO)a	2.437	Sr1-O5(COO)a	2.560	Sr1-O5(COO)a	2.611
Ca1-O5(COO)a	2.507	Sr1-O6(COO)a/e	2.562	Sr1-O9(COO)a	2.562
Ca1-O1(COO)e	2.350	Sr1-O1(COO)d1	2.511	Sr1-O6(COO)a/e	2.555
Ca1-O3(COH)e	2.481	Sr1-O2(COO)d1	2.526	Sr1-O10(COO)a/e	2.532
Ca1-O4(COH)e	2.533	Sr1-O1(COO)d2	2.788	Sr1-O7(COH)e	2.688
Ca1-O6(COO)e	2.391	Sr1-O2(COO)d2	2.600	Sr1-O8(COH)e	2.626
Ca1-O7(H2O)t	2.482	Sr1-O4(COH)e	2.653	Sr1-O1(H2O)t	2.649
Ca1-O8(H2O)t	2.387	Sr1-O7(H2O)t	2.641	Sr1-O2(H2O)t	2.612
average	2.446	average	2.605	average	2.604

Ba_LTA_1/2 (HIXZOD)		Sr_MeA_1 - Sr1		Sr_MeA_1 - Sr2	
Ba1-O5(COO)a	2.773	Sr1-O1(COO)d2	2.799(11)	Sr2-O11(COO)a	2.710(11)
Ba1-O5(COO)a	2.876	Sr1-O1(COO)d2	2.799(11)	Sr2-O12(COO)a	2.671(11)
Ba1-O1(COO)a/f2	2.798	Sr1-O2(COO)d2	2.609(11)	Sr2-O14(COO)a	2.751(11)
Ba1-O2(COO)a	2.805	Sr1-O2(COO)d2	2.609(11)	Sr2-O1(COO)d1	2.669(11)
Ba1-O6(COO)a/f3	2.805	Sr1-O3(COO)d2	2.757(10)	Sr2-O2(COO)d1	2.668(11)
Ba1-O1(COO)a/f1	2.838	Sr1-O3(COO)d2	2.757(10)	Sr2-O3(COO)d1	2.633(11)
Ba1-O4(COH)f1	2.870	Sr1-O4(COO)d2	2.671(11)	Sr2-O3(COO)d1	2.714(10)
Ba1-O4(COH)f2	2.809	Sr1-O4(COO)d2	2.671(11)	Sr2-O21(NO3)	2.614(11)
Ba1-O3(COH)f3	2.769			Sr2-O23(NO3)	2.692(13)
average	2.816	average	2.709	average	2.680

Sr_MeA_1 - Sr3		Ca_FmA_1		Sr_FmA_1/2 (DUCLUJ01)	
Sr3-O11(COO)a	2.547(11)	Ca1-O1(COO)c1	2.361(2)	Sr1-O1(COO)d1	2.569
Sr3-O13(COO)a	2.587(11)	Ca1-O4(COO)c1	2.367(2)	Sr1-O1(COO)d1	2.569
Sr3-O13(COO)a	2.708(11)	Ca1-O1(COO)c2	2.563(2)	Sr1-O1(COO)d1	2.569
Sr3-O14(COO)a	2.617(10)	Ca1-O4(COO)c2	2.578(2)	Sr1-O1(COO)d1	2.569
Sr3-O1(COO)d1	2.638(11)	Ca1-O2(COO)c3	2.464(2)	Sr1-O1(COO)d2	2.777
Sr3-O4(COO)d1	2.569(10)	Ca1-O3(COO)c3	2.470(2)	Sr1-O1(COO)d2	2.777
Sr3-O21(NO3)	2.588(11)	Ca1-O1W(H2O)t	2.409(2)	Sr1-O1(COO)d2	2.777
Sr3-O1W(H2O)t	2.529(12)	Ca1-O2W(H2O)t	2.396(2)	Sr1-O1(COO)d2	2.777
average	2.598	average	2.451	average	2.673

Table A.6.3 - M-O Interatomic Distances in the Metal Coordination Spheres of Potential Pyrotechnic MOFs

(t = terminal, br = bridging, * = non-bridging M-O bond)

A.7   BINARY SYSTEM OXYGEN BALANCES

The equation used to estimate the oxygen balance associated with each of the crystal structures determined for the binary systems is shown below. A simplistic version of this equation can be found in Section 1.1.1, equation 4. This equation also takes into account the presence of fluorine within the binary systems.

$$C_bH_cN_fO_aX_d \text{ ------ } bCO_2 + 0.5(c-d)H_2O + f/2 \text{ } N_2 + dHX + [(b)+ 0.25 \text{ } (c - d) - a/2]O_2$$
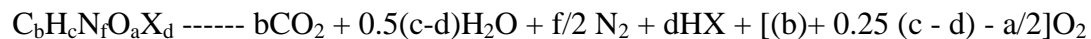
$$\text{where } X = \text{Halogen}$$

$$\Omega = ((aO - 2bC - 0.5(c-d)H)*1600/\text{Molecular Weight})$$

A-B	Asymmetric Unit	Co-crystal Formula	Molecular Weight (GFW)	Oxygen Balance, Ω
fBDC - Im	A--B+	$C_{11}H_6F_4N_2O_4$	306.1697	-5.285
fBDC - DMNPym	0.5A--B+.H$_2$O	$C_{20}H_{24}F_4N_6O_6$	260.2169	-30.809
fBDC - DMNPym	0.5A-0.5B	$C_{14}H_{10}F_4N_3O_4$	201.1499	-19.955
isofBDC - 5NONPy	A-2B	$C_{18}H_{12}F_4N_6O_8$	516.3164	-12.450
altfBDC - 3NONPy	0.5A--B+	$C_{18}H_{12}F_4N_6O_8$	258.1582	-12.450
altfBDC - DMNPym	A--B+	$C_{14}H_{11}F_4N_3O_4$	361.248	-15.568
altfBDC - 5NONPy	2A--B+	$C_{21}H_9F_8N_3O_{10}$	615.2971	-1.352
fBDC - 3NONPy	0.5A--B+	$C_{18}H_{12}F_4N_6O_8$	258.1582	-12.450
fBDC - 5NONPy	0.5A--B+	$C_{18}H_{12}F_4N_6O_8$	258.1582	-12.450
isofBDC - DMNPym	A--B+	$C_{14}H_{11}F_4N_3O_4$	361.248	-15.568
fBDC - 2NPy	A--B+	$C_{13}H_8F_4N_2O_4$	332.2069	-9.699
fBDC - DNPy	2(0.5)A--B+	$C_{13}H_9F_4N_3O_4$	347.2215	-12.690
fBDC - Idn	0.5A-B	$C_{14}H_{14}F_4N_4O_6$	205.1386	-21.045
fBDC - 2MI	0.5(A--B+)	$C_{12}H_8F_4N_2O_4$	160.0981	-10.056
fBDC - 4MI	A--B+	$C_{12}H_8F_4N_2O_4$	320.1962	-10.056
fBDC - DMI	A--B+.H$_2$O	$C_{13}H_{12}F_4N_2O_5$	352.2379	-18.229
fBDC - NTro (-NH$_2$)	A--B+.H$_2$O	$C_{12}H_{12}F_4N_6O_6$	206.1267	-15.568
isofBDC - DNPy	A--B+	$C_{13}H_9F_4N_3O_4$	347.2215	-11.583
isofBDC - Idn	A-B	$C_{11}H_8F_4N_2O_5$	324.1849	-9.923
altfBDC - DNPy	2(A--B+)	$C_{13}H_9F_4N_3O_4$	694.443	-11.583
altfBDC - Idn	2A-3B	$C_{25}H_{22}F_8N_6O_{11}$	734.4621	-15.302
altfBDC - NPy	A--B+	$C_{13}H_8F_4N_2O_4$	332.2069	-9.699
fBDC - Mo	A--B+	$C_{12}H_{11}F_4NO_5$	325.2126	-17.280
fBDC - AMo	0.5 A--B+	$C_{18}H_{16}F_4N_2O_{10}$	248.16	-19.395
alt fBDC - 2MI	0.5(A--B+)	$C_{12}H_8F_4N_2O_4$	160.0981	-10.056
iso fBDC - 4MI	A--B+	$C_{12}H_8F_4N_2O_4$	320.1962	-10.056
alt fBDC - 4MI	2(A--B+)	$C_{12}H_8F_4N_2O_4$	640.3922	-10.056
alt fBDC - DMI	A--B+	$C_{13}H_{10}F_4N_2O_4$	334.2227	-14.428
iso fBDC - Tro	A--B+	$C_{10}H_5F_4N_3O_4$	307.1578	-2.657
alt fBDC - Tro	A--B+	$C_{10}H_5F_4N_3O_4$	1842.9468	-2.657
alt fBDC - Im	A--B+	$C_{11}H_6F_4N_2O_4$	306.1697	-5.285
fBDC - Tro	A--B+	$C_{10}H_5F_4N_3O_4$	307.1578	-2.657
fBDC - DMIdn	0.5(A--B+)	$C_{13}H_{12}F_4N_2O_5$	190.124	-16.889
alt fBDC - Pyr	A-B	$C_{12}H_9F_4NO_5$	323.1968	-12.435
fBDC - MPyri	A--B+	$C_{13}H_{13}F_4NO_4$	323.2397	-22.343
alt fBDC - Mo	A--B+	$C_{12}H_{11}F_4NO_5$	325.2126	-17.280
fBDC - Pyr	0.5A-B	$C_{16}H_{16}F_4N_2O_6$	204.1505	-23.576
iso fBDC - Mo	2(A--B+)	$C_{12}H_{11}F_4NO_5$	650.4252	-17.280

Table A.7.1 - Binary System Oxygen Balance Results

A.8   MOFS OXYGEN BALANCES

The equations used to estimate the oxygen balance associated with each MOF crystal structure is shown highlighted below. These equations were derived based on the knowledge of the end products which were likely to form as a result of each material decomposing.

Group 2 Fluorinated Crystal Structures:
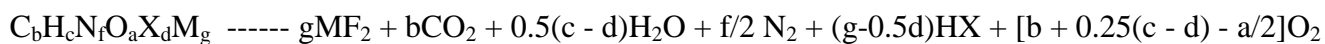
$$C_bH_cN_fO_aX_dM_g \ \text{------} \ gMF_2 + bCO_2 + 0.5(c - d)H_2O + f/2 \ N_2 + (g-0.5d)HX + [b + 0.25(c - d) - a/2]O_2$$

$$\Omega = ((aO - 2bC - 0.5cH)*1600/\text{Molecular Weight})$$

Group 2 Non-Fluorinated Crystal Structures:

$$C_bH_cN_fO_aX_dM_g \ \text{------} \ gMF + bCO_2 + 0.5(c - d)H_2O + f/2 \ N_2 + (g-d)HX + [b + 0.25(c - d) - a/2]O_2$$

$$\Omega = ((aO - 2bC - 0.5cH)*1600/\text{Molecular Weight})$$

Group 2 Non-Fluorinated Crystal Structures:

$$C_bH_cN_fO_aM_g \ \text{------} \ gMO + bCO_2 + 0.5cH_2O + f/2 \ N_2 + [b + 0.25(c + 2g) - a/2]O_2$$
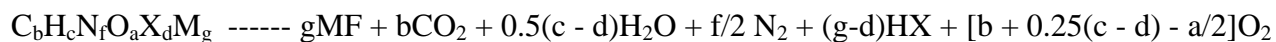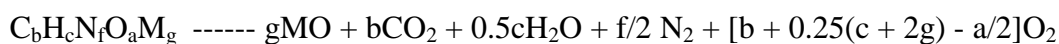
$$\Omega = ((aO - gM - 2bC - 0.5cH)*1600/\text{Molecular Weight})$$

Group 1 Non-Fluorinated Crystal Structures:

$$C_bH_cN_fO_aM_g \ \text{------} \ gM_2O + bCO_2 + 0.5cH_2O + f/2 \ N_2 + [b + 0.25(c + g) - a/2]O_2$$
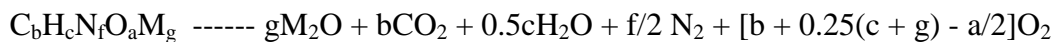
$$\text{where X = Halogen, M = Na, K, Rb, Cs, Ca, Sr, Ba}$$

$$\Omega = ((aO - 2bC - 0.5(c + d)H)*1600/\text{Molecular Weight})$$

Metal-Acid	Asymmetric Unit	MOF Formula	Molecular Weight (GFW)	Oxygen Balance, Ω
Ba fBDC	Ba(0.5fBDC)$_2$(H$_2$O)	C$_{16}$H$_2$Ba$_2$F$_8$O$_9$	764.823	-2.122
Sr GlA	Sr$_2$(GlA)$_2$(H$_2$O)$_5$	C$_{10}$H$_{22}$O$_{13}$Sr$_2$	525.51	-33.508
Ca FmA	Ca(FmA)(H$_2$O)$_2$(DMF)	C$_7$H$_{13}$CaNO$_7$	263.258	-39.535
Sr MeA	Sr$_3$(MeA)$_2$(NO$_3$)(H$_2$O)(DMF)$_2$	C$_{25}$H$_{33}$N$_5$O$_{27}$Sr$_5$	715.16	-20.159
Ba GlA	Ba(GlA)(H$_2$O)$_5$	C$_5$H$_{16}$BaO$_9$	357.501	-35.810
Sr alt fBDC	Sr(altfBDC)(H$_2$O)(DMF)	C$_{11}$H$_{10}$F$_4$NO$_6$Sr	415.81	-19.278
Cs fBDC	Cs(0.5fBDC)	C$_8$F$_4$O$_4$Cs	250.9429	6.352
Rb fBDC	Rb(0.5fBDC)	C$_8$F$_4$O$_4$Rb	203.5062	7.832
K fScA	K(0.5fScA).H$_2$O	C$_2$H$_2$F$_2$KO$_3$	151.1305	-0.007
Ba PmA	Ba(PmA)	C$_7$H$_{10}$BaO$_4$	295.478	-27.112
Ba isoBDC	Ba formic acid	C$_2$H$_2$BaO$_4$	227.362	-7.042
Ca fBDC	Ca(fBDC)(NO$_3$) (H$_2$O)(Pyridine)	C$_{13}$H$_8$CaF$_4$N$_2$O$_8$	436.283	-14.711
Ba altfBDC	Ba(altfBDC) (H$_2$O)(Pyridine)	C$_{26}$H$_{18}$Ba$_2$F$_8$N$_2$O$_{11}$	472.535	-15.280
Sr altfBDC	Sr$_2$(altfBDC)$_2$(H$_2$O)$_2$(Pyridine)	C$_{42}$H$_{20}$F$_{16}$N$_2$O$_{20}$Sr$_3$	763.53	-10.520
Ba OxA	Ba(0.5OxA)(NO$_3$)(H$_2$O)	CH$_2$BaNO$_6$	261.357	-6.110
Sr OxA	Sr(OxA)(H$_2$O)	C$_2$H$_2$O$_5$Sr	193.65	-8.262
Sr MnA	Sr$_3$(MnA)$_4$(H$_2$O)$_3$	C$_{12}$H$_{16}$O$_{19}$Sr$_3$	727.1	-17.615
Sr isofBDC	Sr(isofBDC) (H$_2$O)(Pyridine)	C$_{13}$H$_8$F$_4$N$_2$O$_8$Sr	483.82	-13.265
Sr fScA	Sr(fScA)(H$_2$O)$_2$(DMF)	C$_7$H$_{11}$F$_4$NO$_7$Sr	384.78	-22.888
Ca altfBDC	Ca(altfBDC)(NO$_3$)(Pyr)	C$_{13}$H$_6$CaF$_4$N$_2$O$_7$	418.267	-11.521
Sr isofBDC	Sr(isofBDC)(H$_2$O)$_3$(DMF).H$_2$O	C$_{11}$H$_{15}$F$_4$NO$_9$Sr	469.85	-25.568
Sr fBDC	Sr(fBDC)(NO$_3$) (H$_2$O)(Pyridine)	C$_{13}$H$_8$F$_4$N$_2$O$_8$Sr	483.82	-13.265
Ba OxA	2(Ba(OxA)).H$_2$O	C$_4$H$_2$Ba$_2$O$_9$	468.707	-3.416
Ca OxA	2(Ca(OxA)(H$_2$O))	C$_4$H$_4$Ca$_2$O$_{10}$	292.224	-10.951
Ca MnA	Ca(MnA)(H$_2$O)$_2$	C$_3$H$_6$CaO$_6$	178.154	-26.949
Ca LTA	Ca(LTA)$_2$(H$_2$O)$_2$.2H$_2$O	C$_4$H$_{12}$CaO$_{10}$	260.21	-36.889
Ca BDC	Ca(BDC) (H$_2$O)$_3$	C$_8$H$_{10}$CaO$_7$	258.238	-31.018
Sr LTA	Sr(LTA)(H$_2$O)	C$_4$H$_6$O$_7$Sr	253.71	-18.927
Ba AdA	Ba(0.5AdA)	C$_6$H$_8$BaO$_4$	281.452	-22.771
Sr FmA	Sr(0.5FmA)	C$_4$H$_2$O$_4$Sr	201.68	-7.958
Ba LTA	Ba(LTA)	C$_4$H$_4$BaO$_6$	285.398	-11.223
Sr BDC	Sr(BDC)(H$_2$O)	C$_8$H$_6$O$_5$Sr	269.75	-17.838
Ca AdA	Ca(AdA)(H$_2$O)	C$_6$H$_{10}$CaO$_5$	202.218	-39.601
Sr BDC	Sr(0.5BDC)(H$_2$O)$_2$	C$_8$H$_{12}$O$_8$Sr	323.8	-29.676
Na OxA	Na(OxA)(H$_2$O)	C$_2$H$_3$NaO$_5$	130.0319	-24.6017
Sr BDC	Sr(BDC)(DMF)	C$_{11}$H$_{11}$NO$_5$Sr	324.83	-27.146
K fBDC	K(0.25fBDC)	C$_4$F$_2$KO$_2$	98.1175	8.130
Sr LTA	Sr(LTA)(H$_2$O)$_2$.2H$_2$O	C$_4$H$_{12}$O$_{10}$Sr	307.75	-31.191
Sr MnA	Sr(MnA)	C$_3$H$_2$O$_4$Sr	189.67	-8.452
Ca GlA	Ca(GlA)(H$_2$O)	C$_5$H$_7$CaO$_5$	187.184	-29.949

Table A.8.1 - MOF Oxygen Balance Results